Title
Discovery and Demographics of Hot Planets Orbiting Hot Stars

Author
Giacalone, Steven Anthony

Publication Date
2023

Peer reviewed|Thesis/dissertation

Discovery and Demographics of Hot Planets Orbiting Hot Stars

by

Steven Anthony Giacalone

A dissertation submitted in partial satisfaction of the

requirements for the degree of

Doctor of Philosophy

in

Astrophysics

in the

Graduate Division

of the

University of California, Berkeley

Committee in charge:

Assistant Professor Courtney Dressing, Chair
Professor Eugene Chiang
Professor Burkhard Militzer
Professor Uroš Seljak

Spring 2023

Discovery and Demographics of Hot Planets Orbiting Hot Stars

Abstract

Discovery and Demographics of Hot Planets Orbiting Hot Stars

by

Steven Anthony Giacalone

Doctor of Philosophy in Astrophysics

University of California, Berkeley

Assistant Professor Courtney Dressing, Chair

Surveys dedicated to detecting exoplanets via the transit and radial velocity methods have revolutionized our understanding of planet formation and evolution by revealing the the prevalence of planets orbiting close to their stars. Transit surveys have been especially groundbreaking due to their abilities to discover large quantities of planets with small orbital separations, which can they be further characterized via transmission spectroscopy, emission spectroscopy, and thermal phase curve observations to reveal details about their atmospheres and surfaces. In recent years, the Transiting Exoplanet Survey Satellite (*TESS*) has provided the opportunity to expand these techniques into entirely new regimes, due to its ability to search for transiting planets around a greater variety of stars and around brighter stars that are more amendable to follow-up observations. This thesis focuses on the utilization of *TESS* data to search for and study the demographics of these planets.

First, I present `TRICERATOPS`, a tool designed to statistically validate transiting exoplanets and identify likely astrophysical false positives in *TESS* data. To statistically validate a transiting exoplanet is to confirm its planetary nature by ruling out plausible false positive scenarios, such as those that arise when multiple stars are blended together in the data. This is a particularly pertinent problem for *TESS*, which is equipped with relatively low-resolution cameras that often cannot distinguish light originating from individual stars, especially in crowded fields. I discuss the design and efficacy of `TRICERATOPS`, demonstrating that it is an effective tool for identifying the most promising planet candidates detected by *TESS* and prioritizing follow-up observations with both ground-based and space-based telescopes.

Next, I use `TRICERATOPS` and an array of ground-based follow-up observations to validate 13 hot and potentially terrestrial planets detected by *TESS*. These planets are unlike any rocky bodies in the Solar System; they orbit their stars at distances of only a few stellar radii and are so highly irradiated that many are expected to have molten surfaces. Their high temperatures also mean that they emit infrared light at levels detectable by *JWST*. Emission spectroscopy and thermal phase curve observations of these worlds can reveal the presence

and composition of an atmosphere, measure Bond albedo, and calculate heat redistribution properties. Prior to *TESS*, very few of these types of planets were known around bright stars amenable to *JWST* observations. This sample therefore facilitates the investigation of hot Earth-size worlds at a population level.

Finally, I conduct a search for planets smaller than Saturn orbiting A-type stars. A-type stars, which are roughly twice as massive and nearly twice as hot as Sun-like stars, have historically been avoided by transit and radial velocity surveys due to their large radii and rapid rotation rates, which hinder our ability to detect planets around them. As a consequence, early transit surveys like the *Kepler* mission acquired very little data of these stars, limiting our understanding of planet demographics to stars like the Sun and cooler. By observing all bright stars across nearly the entire sky, *TESS* has provided the best opportunity yet to search for small planets orbiting relatively hot stars. Through this search, I discover and validate a single planet: HD 56414 b, a Neptune-size planet orbiting one of the hottest planet-hosting stars known to date on a 29-day orbital period. The orbital period of this planet is long compared to the typical planet detected by *TESS*, suggesting that Neptune-size planets with smaller orbital separations may not exist around A-type stars. I display that atmospheric photoevaporation due to high levels of near-ultraviolet radiation offers one possible explanation for this phenomenon.

To test this hypothesis more robustly, I calculate the occurrence rate of small planets with orbital periods under 10 days around A-type stars. I demonstrate, for the first time, that sub-Saturns and sub-Neptunes are rarer around A-type stars than they are around their cooler counterparts. I also find evidence that super-Earths are as common or less common around A-type stars than cooler stars. These results suggest that small planets are unable to form at, migrate to, or survive at the small orbital separations probed by *TESS* around these hot stars. Overall, these findings significantly advance our understanding of how planets form and evolve around stars hotter than the Sun, providing a more holistic picture of planetary populations throughout the galaxy.

Contents

Contents **i**

List of Figures **iii**

List of Tables **vi**

1 Background Information **1**
1.1 Detecting and Confirming Close-in Planets 1
1.2 Terrestrial Exoplanets 4
1.3 Planet Occurrence Rates 6
1.4 Thesis Summary 8
1.5 Other Work 8

2 TRICERATOPS: A Validation Tool for Transiting Planets **10**
2.1 Introduction 10
2.2 Procedure 15
2.3 Examples 27
2.4 Planet Vetting and Validation 33
2.5 Nearby False Positive Identification 40
2.6 Results 50
2.7 Discussion 52
2.8 Conclusions 55

3 Validation of 13 Hot and Potentially Terrestrial Planets **65**
3.1 Introduction 66
3.2 Sample 68
3.3 Vetting Procedure 75
3.4 Follow-Up Observations 77
3.5 Results 91
3.6 Discussion 108
3.7 Conclusions 114

4 HD 56414 b: A Warm Neptune Transiting an A-type Star **116**

4.1 Introduction 116
4.2 Observations 119
4.3 Data Analysis 120
4.4 Planet Validation 123
4.5 Discussion and Conclusions 125

5 The Frequency of Small Close-In Planets Around A-type Stars 130
5.1 Introduction 130
5.2 Preliminary Vetting of Planet Candidates 132
5.3 Sample Selection 133
5.4 Occurrence Rate Calculation 145
5.5 Discussion 152
5.6 Remaining Work 155
5.7 Conclusions 157

6 Future Work 159

Bibliography 164

List of Figures

2.1 Comparison of target star flux ratios reported by TRICERATOPS and the *TESS* SPOC pipeline for a 228 TOIs. 17
2.2 $R_\star - M_\star$ and $T_{\rm eff} - M_\star$ relations used in the TRICERATOPS calculations. 19
2.3 Visualizations of the distributions used to determine model priors and sample parameters in TRICERATOPS calculations. 22
2.4 Δ *TESS* magnitude between a star of mass $M_\star$ and a 10th magnitude, $1M_\odot$ star. 27
2.5 Visualization of the TIC querying performed by TRICERATOPS to identify possible nearby sources of the transit-like event associated with TOI 465.01. 28
2.6 Fit of each transit-producing scenario tested by TRICERATOPS for TOI 465.01. . 29
2.7 High-resolution image of TOI 465 obtained with ShARCS/ShaneAO in K_s band and corresponding contrast curve. 31
2.8 Visualization of the TIC querying performed by TRICERATOPS to identify possible nearby sources of the transit-like event associated with TOI 529.01. 31
2.9 Fit of each transit-producing scenario tested by TRICERATOPS for TOI 529.01. . 32
2.10 Host star and planet properties of confirmed planets and false positives used in the TRICERATOPS performance analysis. 34
2.11 SNR vs FPP for all false positives and confirmed planets used in the TRICERATOPS performance analysis on 2-min cadence data. 35
2.12 NFPP vs FPP for returned by TRICERATOPS for confirmed planet and false positives, analyzed with 2-minute-cadence data. 36
2.13 VESPA FPP vs TRICERATOPS FPP for the confirmed planets and false positives analyzed previously. 37
2.14 SNR vs FPP for all false positives and confirmed planets used in the TRICERATOPS performance analysis on 30-min-cadence data. 39
2.15 NFPP vs FPP for returned by TRICERATOPS for confirmed planets and false positives, analyzed with 30-minute-cadence data. 39
2.16 Host star properties and planet properties of unclassified TOI systems analyzed in this chapter. 51
2.17 NFPP versus number of nearby stars bright enough to be an NFP for each of the 384 TOIs tested in Section 2.6. 54

3.1 Phase-folded *TESS* data and best-fit transit models for each TOI. 76

3.2 Contrast curves extracted from the high-resolution follow up summarized in Table 3.4. 80
3.3 Phase-folded ground-based data and best-fit model of the transit of TOI-206.01. 94
3.4 Phase-folded ground-based data and best-fit model of the transit of TOI-1075.01. 98
3.5 Phase-folded ground-based data and best-fit model of the transit of TOI-1442.01. 102
3.6 Phase-folded ground-based data and best-fit model of the transit of TOI-1693.01. 103
3.7 *TESS* light curves and Lomb-Scargle periodograms for TOI-1860 and TOI-2260, which enable the calculations of the rotation periods of the young stars. 104
3.8 Phase-folded ground-based data and best-fit model of the transit of TOI-2411.01. 107
3.9 Phase-folded ground-based data and best-fit model of the transit of TOI-2427.01. 108
3.10 Phase-folded ground-based data and best-fit model of the transit of TOI-2445.01. 109
3.11 Planet radii, planet orbital periods, planet equilibrium temperatures, and stellar effective temperatures of the planets validated in this chapter. 110
3.12 Coordinates and ESM values of the planets validated in this chapter. 113

4.1 Full *TESS* lightcurve, phase-folded *TESS* lightcurve, and SED fit for HD 56414. 118
4.2 Visualizations of the vetting measures used to validate HD 56414 b. 124
4.3 HD 56414 b compared to other confirmed transiting planets in various parameter spaces. 126
4.4 Simulated atmospheric mass loss rates as a function of orbital separation for planets with the same size as HD 56414 b orbiting a star identical to HD 56414. 128

5.1 Follow-up observations displaying that TOI-998.01 is a false positive caused by a nearby eclipsing binary. 134
5.2 Follow-up observations displaying that TOI-1360.01 is a false positive caused by a nearby eclipsing binary. 135
5.3 Follow-up observations displaying that TOI-1497.01 is a false positive caused by a nearby eclipsing binary. 136
5.4 Follow-up observations displaying that TOI-1522.01 is a false positive caused by a nearby eclipsing binary. 137
5.5 Follow-up observations displaying that TOI-1570.01 is a false positive caused by a nearby eclipsing binary. 138
5.6 Follow-up observations displaying that TOI-2059.01 is a false positive caused by a nearby eclipsing binary. 139
5.7 Follow-up observations displaying that TOI-2248.01 is a false positive caused by a transiting planet around a nearby star. 140
5.8 Follow-up observations displaying that TOI-3380.01 is a false positive caused by a nearby eclipsing binary. 141
5.9 Follow-up observations displaying that TOI-4268.01 is a false positive caused by a nearby eclipsing binary. 142
5.10 Follow-up observations displaying that TOI-5429.01 is a false positive caused by a nearby eclipsing binary. 143

5.11 Properties of the 20,652 A-type stars that are used in the occurrence rate calculation in this chapter. 144
5.12 Pipeline sensitivity to small close-in planets around the sample of A-type stars described in Section 5.3. 147
5.13 Completeness of the transit detection pipeline to planets of various sizes and orbital periods around the sample of A-type stars described in Section 5.3. . . . 149
5.14 Calculated 3σ upper limits on the occurrence rates of planets orbiting A-type stars, as a function of both planet radius and orbital period. 151
5.15 The occurrence rates of sub-Saturns, sub-Neptunes, and super-Earths with $P_{\rm orb} <$ 10 days for FGKM-type stars compared to the results from the calculation for A-type stars in this chapter. 154

List of Tables

2.1 False positive scenarios tested by TRICERATOPS. 14
2.2 The probability of each TRICERATOPS scenario j ($\mathcal{P}_j$) for TOI 465.01. 30
2.3 The probability of each TRICERATOPS scenario j ($\mathcal{P}_j$) for TOI 529.01. 33
2.4 TFOP SG1 false-positive identification compared to TRICERATOPS predictions. . 41
2.5 Facilities used for TFOP SG1 followup. 42
2.6 TOIs statistically validated with TRICERATOPS. 52
2.7 TRICERATOPS predictions for undesignated TOIs. 64

3.1 TOI parameters from TICv8.1 and ExoFOP. 70
3.2 Best fit planet parameters. 71
3.3 Adopted stellar parameters. 73
3.4 Summary of high-resolution imaging follow up. 79
3.5 Summary of reconnaissance spectroscopy follow up and derived stellar parameters. 84
3.6 Elemental abundances derived with KeckSpec. 86
3.7 Summary of time-series photometry follow up. 91
3.8 Facilities used for TFOP SG1 follow up. 92
3.9 Vetting results. 93
3.10 Previously confirmed and validated planets with $R_{\rm p} < 2\,R_\oplus$ and ESM > 7.5. . . 112

4.1 Adopted stellar and planet parameters for the HD 56414 b system. 122

5.1 Summary of the planet candidate follow-up observing program conducted with the 1 m Nickel and LCOGT telescopes. 132
5.2 Predicted properties of TOIs in the stellar sample used in this chapter. 150

Acknowledgments

The work in this thesis was largely supported by various NASA grants, including NASA *TESS* Guest Investigator Program award 80NSSC18K1583 (awarded to Dr. Courtney Dressing), NASA Exoplanet Research Program (XRP) award 80NSSC20K0250 (awarded to Dr. Courtney Dressing), and NASA FINESST award 80NSSC20K1549 (awarded to Steven Giacalone and Dr. Courtney Dressing). Portions of the thesis were also supported by the Hellman Fellows Fund, the Alfred P. Sloan Foundation, and the David and Lucile Packard Foundation (awarded to Dr. Courtney Dressing).

This thesis make use of data from the NASA *TESS* mission, which are publicly available from the Mikulski Archive for Space Telescopes (MAST). Funding for the *TESS* mission is provided by NASA's Science Mission directorate. I acknowledge the use of public *TESS* Alert data from pipelines at the *TESS* Science Office and *TESS* Science Processing Operations Center. Resources supporting this work were provided by the NASA High-End Computing (HEC) Program through the NASA Advanced Supercomputing (NAS) Division at Ames Research Center for the production of the Science Processing Operations Center (SPOC) data products. This thesis also makes use of the Exoplanet Follow-up Observation Program website, which is operated by the California Institute of Technology, under contract with the National Aeronautics and Space Administration under the Exoplanet Exploration Program.

Chapters 2-4 of this thesis feature results contributed by various collaborators. I am most grateful for their contributions. I refer the reader to the peer-reviewed publication corresponding to each chapter for appropriate acknowledgements of their funding resources.

Research at UC Berkeley is conducted on the territory of Huichin, the ancestral and unceded land of the Chochenyo-speaking Ohlone people, the successors of the sovereign Verona Band of Alameda County. The results in this thesis would not be possible without the sacrifices they have made and continue to make.

This thesis features data acquired with telescopes in the United States that are located on land taken from indigenous peoples. Lick Observatory is located on the land of the Ohlone (Costanoans), Tamyen, and Muwekma Ohlone tribes. McDonald Observatory is located on the land of the Chiricahua Apache, Mescalero Apache, Lipan Apache, and Jumanos tribes. Whipple Observatory is located on the land of the Tohono O'odham nation, the Hia-Ced O'odham nations, the Ak-Chin Indian community, and Hohokam people. Palomar Observatory is located on the land of the Pauma tribe, the Cupeño tribe, the Kumeyaay Nation, and the Payómkawichum (Luiseño) people. Kitt Peak Observatory is located on the land of the Tohono O'odham nation, the Hia-Ced O'odham nation, the Ak-Chin Indian community, and the Hohokam people. Maunakea Observatory is located on the land of the kānaka ʻōiwi people. I stand in solidarity with the Puʻuhonua o Puʻuhuluhulu Maunakea in their effort to preserve this sacred space for native Hawaiʻians. I wish to recognize and acknowledge the very significant cultural role and reverence that these lands have within these indigenous communities.

This thesis would have never existed without my research advisors: my primary doctoral research advisor Dr. Courtney Dressing, my primary undergraduate research advisors Dr. Arieh Königl and Dr. Titos Matsakos, and my first ever research advisor Dr. Daniel Fabrycky. I don't know how I would have made it this far without their patience and mentorship. I am also extremely grateful for the guidance and career advice provided by my graduate academic advisors, Dr. Imke de Pater and Dr. Eugene Chiang, and the remaining members of my thesis committee, Dr. Burkhard Militzer and Dr. Uroš Seljak. In addition, I thank my teachers and mentors over the years for inspiring me to pursue degrees in physics and astronomy: Dr. Fred Ciesla, Dr. Sebastiaan Krijt, Paul Lang, and Jane Schoch.

I am greatly indebted to the many members of the UC Berkeley Astronomy Department for fostering a rich and supportive academic environment. I am especially grateful for the department staff – Dexter Stewart, Nina Ruyemaker, Lochland Trotter, Cara-Lyn Giovanniello, Amber Banayat, Yasasha Ridel, Maria Kies, Brandye Johnson, Brianna Franklin, and Bill Boyd – for keeping everything running during my time at Berkeley. I thank my fellow graduate students for making the department a place of community, rather than just a place of work. And of course, a special thanks to the members of the PALS research group for being a source of collaboration and helping me with my many proposals over the years.

I thank my family – Mom, Dad, and Sydney – for their unwavering love and encouragement. Even if they haven't understood what I've been doing for the past six years, they've consistently cheered me on from the east coast, which means more than they probably realize.

Lastly, I thank my friends and companions – Jordan Fleming, Grace Shipton, Nathan Sandford, Sarafina Nance, Daniel Hernandez, David Matesanz, Andrew Johnstone, Nicole Martinez, Michelle Bueno, Matt Ehrlich, and Sean Greer – for being an incredible support network and sticking with me through the thick and thin. You kept me grounded after the sleepless nights (literally sleepless, I did a lot of observing) and during the stressful deadline sprints. I wouldn't have been able to do it without you.

Chapter 1

Background Information

Close-in, transiting exoplanets currently provide the best opportunity to learn about the properties and demographics of planetary systems. The main chapters of this thesis are primarily concerned with the discovery of transiting extrasolar planets (which I interchangeably refer to as "exoplanets" and "planets" throughout the document) and how we use these discoveries to learn about planetary populations as a whole. In this introductory chapter, I provide context for the subjects discussed in the remainder of the thesis.

1.1 Detecting and Confirming Close-in Planets

There are a number of methods for detecting planets orbiting other stars, although two methods – the radial velocity and transit methods – are responsible for discovering the vast majority of the over 5,000 currently known exoplanets.[1] The radial velocity method detects a planet by measuring the reflex motion of a star with a planetary companion as they orbit their common center of mass (e.g., Lovis and Fischer 2010; Mayor and Queloz 1995; Struve 1952). The transit method detects a planet by observing periodic dips in the brightness of a star as an orbiting planet obscures part of the luminous stellar surface (e.g., Charbonneau et al. 2000; Winn 2010). Both of these techniques are biased towards planets that are close to their stars. The radial velocity amplitude of a star caused by an orbiting planet scales as $P_{\rm orb}^{-1/3}$, or $a^{-1/2}$, where $P_{\rm orb}$ and a are the orbital period and semi-major axis of the planet, respectively. The probability of planet being oriented such that we can detect its transit scales as $P_{\rm orb}^{-2/3}$, or a^{-1}, due to the fact that the orientations of planetary systems along our line of sight are randomly distributed. In addition, both of these techniques require longer observational baselines to confidently detect the signals of planets with longer $P_{\rm orb}$. As a consequence, nearly 80% of known planets are closer to their stars than Mercury is to the Sun.[1] In this thesis, I focus mainly on the transit method, although discussions of the radial velocity method appear throughout in the various chapters.

[1] `https://exoplanetarchive.ipac.caltech.edu/index.html`, accessed 8 May 2023.

The first transiting exoplanets were discovered by ground-based surveys that utilized moderate-aperture telescopes, such as the Trans-Atlantic Exoplanet Survey (TrES; Alonso et al. 2004), the Hungarian-made Automated Telescope Network (HATNet; Bakos et al. 2004), the Wide Angle Search for Planets (SuperWASP; Pollacco et al. 2006), the Optical Gravitational Lensing Experiment (OGLE; Konacki et al. 2003), and the XO project (McCullough et al. 2005). These surveys discovered several dozen transiting planets between 2000 and 2007, but had largely limited capabilities due to the long baselines and high photometric precisions needed to detect transiting planets, which can most easily be achieved from space. The CoRoT mission, a joint endeavor by the French Space Agency and European Space Agency, was the first space-based survey to search for transiting planets (Auvergne et al. 2009). Due to its ability to observe stars in a continuous fashion for long periods of time, the mission was able to detect an additional 29 transiting planets between 2007 and 2013. In 2009, NASA launched the *Kepler* Space Telescope with the objective of determining the frequency of Earth-like planets orbiting Sun-like stars (Borucki et al. 2010). In an Earth-trailing heliocentric orbit, *Kepler* was designed to stare continuously at a 115 square degree patch of sky (over 10× the area of the CoRoT field of view) near the constellations Cygnus and Lyra. In doing so, it searched for transiting planets around over 500,000 stars for four consecutive years. To this day, *Kepler* wears the crown as the most successful planet-hunting mission, having detected over 2,700 planets (and another 2,000 planet candidates that have yet to be confirmed). The *Kepler* mission continued until 2013, when the second of its four reaction wheels failed, making it impossible for the spacecraft to continue staring at the originally targeted field. However, the mission was repurposed to into the *K2* mission, which was able to achieve temporary stable pointing by balancing radiation pressure from the Sun with periodic thruster firings and its two remaining reaction wheels (Howell et al. 2014). With this strategy, *K2* searched for transiting planets in different areas of the ecliptic plane in roughly 80-day increments, discovering hundreds (Crossfield et al. 2016; Mayo et al. 2018) before the spacecraft was retired in 2018 due to fuel depletion. All the while, several new ground-based transit surveys continued to search bright stars for transiting planets, including HATSouth (Bakos et al. 2013), WASP-South (Pollacco et al. 2006), Kilodegree Extremely Little Telescope survey (KELT; Pepper et al. 2007), the MEarth project (Irwin et al. 2015; Nutzman and Charbonneau 2008), the TRAnsiting Planets and PlanetesImals Small Telescope survey (TRAPPIST; Jehin et al. 2011), the Qatar Exoplanet Survey (Alsubai et al. 2013), the Multi-site All-Sky CAmeRA survey (MASCARA; Talens et al. 2017), and the Next-Generation Transit Survey (NGTS; Wheatley et al. 2018).

In 2018, NASA launched the Transiting Exoplanet Survey Satellite (*TESS*; Ricker et al. 2010), the successor to *Kepler*. Unlike *Kepler*, *TESS* does not stare at a single patch of sky. *TESS* scans nearly the entire sky over 26 month-long sectors (13 per hemisphere), each of which covers a wide area stretching from the ecliptic plane to the northern or southern ecliptic pole. As a result, *TESS* can search for planets around much brighter stars, which are highly amenable to follow-up observations that characterize their transiting planets, but is primarily sensitive to planets with shorter orbital periods than *Kepler* was. The primary objective of the *TESS* mission is to detect at least 50 planets smaller than Neptune that

can have their masses precisely determined with radial velocity observations, with less of a focus on planet demographics than its predecessor. The main chapters of this thesis focus on data from *TESS*, which is still in operation at the time of writing in Spring 2023.

The surveys described above have cumulatively detected over 10,000 transiting planet candidates, but only a fraction of those candidates are designated as bona fide planets today. Additional analyses are required to elevate a planet candidate to a true planet because signals resembling planet transits can often be produced by instrumental effects (e.g., Mullally et al. 2016) and astrophysical phenomena like stellar variability or eclipsing binary stars (e.g., Torres et al. 2004). The process of confirming the planetary nature of a transiting planet candidate is important for selecting targets for in-depth characterization and studying planet demographics.

The most robust way to determine if a transiting planet candidate is a true planet is by measuring the mass of the transiting object and verifying that it is consistent with that of a planet. This is most frequently done by measuring the radial velocity of the star over time as it is tugged by the planet. For a transiting multi-planet system in orbital resonance, planet masses can be constrained using transit-timing variations, or the deviations in the transit times of transiting planets resulting from the gravitational influence of the other planets in the system (Holman and Murray 2005). For large planets orbiting bright stars, mass can be constrained by quantifying out-of-transit brightness variations resulting from the beaming effect, tidal ellipsoidal distortions of the star, and reflection/heating off of the planet (e.g., Shporer et al. 2011).

Measuring the mass of a transiting planet is the preferred method of confirmation, as it reveals information about the bulk density and composition of the planet. However, this is not always feasible. Precise radial velocities are difficult to measure for stars with high activity levels, and small planets on relatively long-period orbits can induce radial velocity amplitudes too small to be detected by many current spectrographs. In addition, radial velocity monitoring requires often competitive telescope time. Transit-timing variations are most easily measured for resonant multi-planet systems, which are relatively rare. This method also requires a long observational baseline over which many transits of each planet are observed. Lastly, constraining planet mass using out-of-transit brightness variations can only be accomplished for the brightest stars and requires the photometric precision of a space-based telescope. Consequently, alternative methods of confirming the planetary natures of transiting planet candidates have been developed.

The process of determining that a transiting planet candidate is a true planet without measuring its mass is colloquially referred to as "planet validation." Put simply, validation involves conducting a statistical analysis to rule out plausible astrophysical false positives. The most common astrophysical false positive scenarios that produce transit-like events are the following:

1. The transit is caused by an eclipsing stellar-mass companion that eclipses the target star with a grazing orientation, such that the depth of the transit resembles that of a planet.

2. The transit is caused by a much larger object than predicted orbiting the target star, either because the size of the target star is being underestimated or because there are unknown sources diluting the flux of the target star.

3. The transit is caused by an pair of eclipsing binary stars that are spatially unresolved with and physically associated with the target star (i.e., a hierarchical stellar system).

4. The transit is caused by an foreground or background pair of eclipsing binary stars that are spatially unresolved with and physically unassociated with the target star (i.e., a chance-aligned binary system).

5. The transit is caused by a nearby pair of eclipsing binary stars that are spatially resolved from the target star but are close enough to contaminate the photometric aperture.

A number of techniques have been used to rule out these scenarios. The most common technique is model-based validation, which involves explicitly calculating the likelihood of each scenario and comparing them with the likelihood of the transiting planet scenario (e.g., Giacalone et al. 2021; Morton 2012; Torres et al. 2004). Others have validated planets by noting that planet candidates in multi-planet systems detected by *Kepler* have a higher probability of being real planets than those in single-planet systems (Lissauer et al. 2012). More recently, machine learning has been employed to validate transiting planets (Ansdell et al. 2018; Shallue and Vanderburg 2018; Valizadegan et al. 2022). Cumulatively, these techniques are responsible for over half of currently confirmed transiting planets (e.g., Morton et al. 2016), meaning that validation plays an important role of our understanding of the demographics of planetary systems. A more detailed discussion of transiting planet validation can be found in Chapter 2.

1.2 Terrestrial Exoplanets

One of the overall goals of exoplanet science is to determine the frequency and properties of terrestrial planets throughout the galaxy. This was the primary goal of the *Kepler* mission, which enabled estimates of how common Earth-like planets are in the habitable zones of Sun-like stars, although different estimates vary by orders of magnitude (e.g., Bryson et al. 2020; Hsu et al. 2019; Kunimoto and Matthews 2020; Petigura et al. 2013). Due to the bias of the transit method towards detecting planets with shorter orbital periods, *Kepler* was much more effective at characterizing the population of close-in terrestrial planets. For instance, Rogers (2015) showed that planets with radii larger than 1.6$\times$ the size of Earth tend to have volatile-rich envelopes, indicating that planets can only grow so large before they are no longer Earth-like. As the number of discovered terrestrial planets increased, it became possible to study the compositions of these planets in a statistical way. Measuring the radii and masses of those that transit, and therefore determining their bulk densities, provided insight into the diversity of compositions of these Earth-like worlds (Seager et al.

2007; Zeng et al. 2016). As the age of *JWST* drew near, another interesting prospect came into view: determining if close-in terrestrial planets have atmospheres like that of Earth.

Some of the most exciting targets for these atmospheric studies are terrestrial planets orbiting M dwarfs. M dwarfs are the most common type of star in the galaxy, and they commonly have close-in rocky planets (e.g., Dressing and Charbonneau 2013, 2015). Because these stars are relatively cool, their habitable zones are also located much closer in, meaning that many of these close-in worlds receive similar levels of irradiation as the Earth. In addition, these stars are often more amenable to atmosphere-characterizing observations than Sun-like stars due to their small radii and cool effective temperatures. Transmission spectroscopy observations can more easily probe the compositions of planet atmospheres when the ratio of stellar radius to atmospheric scale height is small. Emission from the planet is also easier to detect because the planet-to-star flux ratio is larger for a planet at a given orbital separation. Techniques that utilize both transmission and emission observations with *JWST* have been devised to study these planets (Lustig-Yaeger et al. 2019; Mansfield et al. 2019), although observations have yet to reveal the presence of an Earth-like atmosphere. For instance, Kreidberg et al. (2019) observed the thermal phase curve of the rocky planet LHS 3844 b with the *Spitzer* Space Telescope (Werner et al. 2004) and found its emission to be consistent with a bare-rock surface. Recently, Greene et al. (2023) obtained similar observations of TRAPPIST-1 b with *JWST* and found a consistent result. These studies indicate that short-period rocky worlds around M dwarfs may frequently be airless, potentially due to the high levels of X-ray and extreme ultraviolet (XUV) emission from their stars (e.g., Luger and Barnes 2015), although observations of more temperate planets may prove otherwise.

Close-in terrestrial planets orbiting hotter stars are far too highly irradiated to be habitable, but provide the opportunity to study the geochemistry of rocky worlds at extremely high temperatures. Planets with surface temperatures greater than 850 K, the temperature at which silicate rock begins to melt (Lutgens et al. 2014), are expected to have partially molten surface that constantly outgas atmospheres consisting of silicates and other volatiles (Schaefer et al. 2012), which can be detected in the mid infrared (Zilinskas et al. 2022). Kite et al. (2016) showed that we can gain insight into the geochemistries of these "lava worlds" by studying those with different surface temperatures, where hotter planets are more likely to have high-pressure outgassed atmospheres and chemically evolved surfaces that may be distinguishable in their refection and emission profiles. Today, only two lava worlds have been closely studied to understand their surface and atmospheric properties – 55 Cancri e (Demory et al. 2011; Demory et al. 2016) and K2-141 b (Malavolta et al. 2018; Zieba et al. 2022) – both of which have been targeted for observations with *Spitzer* and *JWST*. However, by searching for close-in transiting planets around bright stars, *TESS* is significantly expanding the list of lava worlds that can be characterized in this way. In Chapter 3, I provide a more detailed discussion of the observability of hot terrestrial planets with *JWST* and validate 13 planets that are particularly amenable to future observations.

1.3 Planet Occurrence Rates

The term "planet occurrence rate" denotes the fraction of stars with a given set of properties (e.g., mass, metallicity, age) that have a planet with a certain set characteristics (e.g., orbital period, radius, mass). These occurrence rates play a particularly unique role in planetary science, as they provide a window into the physics dictating planet formation and evolution that is free from the biases of the Solar System.

Early planet occurrence rate calculations utilized data from radial velocity surveys targeting close-in giant planets around FGK-type stars and found that these worlds are more common around stars with higher metallicities (Fischer and Valenti 2005) and masses (Johnson et al. 2010). A similar relationship between stellar mass and giant planet frequency was later found by exoplanet direct imaging surveys, but for planets on much wider orbits ($a > 10$ AU; Nielsen et al. 2019). These findings align with the core-accretion model of giant planet formation, in which the cores of giant planets coalesce from solids in the protoplanetary disk and a gaseous envelope is subsequently accreted (Pollack et al. 1996). More massive stars are known to have more massive protoplanetary disks, leading to more solid material with which to form giant planet cores (Ansdell et al. 2016).

Calculating the occurrence rates of small close-in planets became possible with the *Kepler* mission. *Kepler* primarily observed Sun-like stars, enabling planet occurrence rates for FGK-type stars (e.g., Howard et al. 2012) and early-type M dwarfs (e.g., Dressing and Charbonneau 2013, 2015). These studies revealed that at short orbital periods ($P_{\rm orb} < 50$ days) planets smaller than Neptune are over 10× more common than giant planets (Howard et al. 2012; Mulders et al. 2015b), become more common around stars with lower masses (Mulders et al. 2015a), and are spatially distributed such that they become more common when moving from orbital periods of 0 days to 10 days and are roughly constant in frequency at longer orbital periods (Mulders et al. 2015a). These findings carry important implications for how small planets form and evolve around different types of stars. For instance, the 10-day transitional period is believed to correspond to the co-rotation radius of a pre-main-sequence star and its protoplantery disk, at which the disk is truncated by the stellar magnetosphere. Lee and Chiang (2017) showed that the orbital period distribution of small planets can be explained by disk migration up to the edge of the truncated disk, followed by migration due to tidal interactions with the star.

Occurrence rate calculations have also revealed interesting features in the planet radius – orbital period plane that provide unique insight into how short-period planets form and evolve. For instance, Earth-size and Jupiter-size planets are known to exist with $P_{\rm orb} < 3$ days, but Neptune-size planets are distinctly rare at these periods, creating what is known as the "hot Neptune desert" (e.g., Mazeh et al. 2016). It is believed that this feature is caused by two processes: (1) atmospheric photoevaporation due to XUV radiation emitted from the pre-main-sequence star, and (2) tidal disruption of giant planets migrating inwards via high-eccentricity migration (Owen and Lai 2018; Thorngren et al. 2023). Some also suggest that the orbital period at which this desert begins should depend on stellar mass, with hot Neptunes able to exist more frequently at shorter periods for lower mass stars (Hallatt and

Lee 2022). Another interesting feature, the "radius valley," was identified by Fulton et al. (2017). The valley, which is described by a dip in the occurrence rates of planets $1.5-2\times$ the size of Earth, is evidence that super-Earths and sub-Neptunes experience distinct formation or evolution histories. The presence of the valley was first predicted by Lopez and Fortney (2013) as a consequence of XUV photoevaporation. Others have suggested that the valley can be explained by core-powered atmospheric loss, or atmospheric mass loss that occurs due to residual heat from planet formation (Ginzburg et al. 2016, 2018; Gupta and Schlichting 2019). Lastly, the valley could plausibly be created by atmospheric accretion during the gas-poor stage of protoplanetary disk evolution (Lee and Chiang 2016; Lee et al. 2022).

Due to biases in the types of stars that *Kepler* observed, *Kepler* occurrence rate studies were largely limited to main sequence stars. However, subsequent missions would permit the exploration of occurrence rates as a function of stellar age. Grunblatt et al. (2019) utilized data from the *K2* mission to calculate comparative occurrence rates for close-in giant planets between main-sequence stars and red-giant-branch stars, finding that these planets may become more common as stars age, possibly due to post-main-sequence star-planet interactions. David et al. (2021) derived stellar ages for the *Kepler* sample using data from the *Gaia* mission and showed that the location of the radius valley moves to larger planet radii as stars age, indicating that the smallest sub-Neptunes may become the largest super-Earths over billions of years. With the launch of *TESS*, which allows for the detection of transiting planets around stars in young clusters and moving groups, our understanding of the relationship between planet occurrence rate and stellar age has continued to improve (e.g., Fernandes et al. 2022; Grunblatt et al. 2022).

TESS also provides the opportunity to explore planet occurrence rate for a wider range of stellar spectral types than previously accessible. *Kepler* did not collect data for many late-type M dwarfs or A-type stars due to its objective to study planet demographics around Sun-like stars. Ground-based radial velocity surveys have historically avoided very cool stars because they are very faint, and avoided A-type stars because their rapid rotation rates greatly limit the precision of radial velocity measurements (Galland et al. 2005). By collecting data across nearly the entire sky, *TESS* permits the search for planets around a large number of both very cool and very hot stars for the first time (Kunimoto et al. 2022). The frequencies of hot Jupiters around these stars have already been explored using *TESS* data (Gan et al. 2023; Zhou et al. 2019b), but the demographics of smaller planets have yet to be studied. A-type stars are particularly interesting from the perspective of planet formation and evolution. It is know that these massive and hot stars host Jupiter-size planets more frequently than Sun-like stars (Johnson et al. 2010), likely as a result of having more massive protoplanetary disks (Ansdell et al. 2016), which may lead one to hypothesize that smaller planets are also more common around A-type stars. However, it is also known that the gas in disks surrounding more massive stars dissipates more rapidly, potentially providing too little time for sub-Jovian planets to accrete volatile envelopes or migrate inwards (Ribas et al. 2015). Lastly, A-type stars have relatively short pre-main-sequence lifetimes and largely radiative interiors, causing them to emit very little in the XUV (Schröder and Schmitt 2007). Because XUV photoevaporation is thought to sculpt

the population of small close-in planets, one might expect features like the hot Neptune desert or the radius valley to be absent. However, these hot stars have significant continuum emission in the near ultraviolet that may be able to drive atmospheric photoevaporation even more efficiently (García Muñoz and Schneider 2019). Using *TESS*, it is possible to test these hypotheses by measuring the occurrence rate of small close-in planets around A-type stars. This subject is further discussed in Chapters 4 and 5.

1.4 Thesis Summary

This thesis is organized as follows. In Chapter 2, I present `TRICERATOPS`, a tool designed to statistically validate transiting planet candidates detected by *TESS*. I demonstrate that the tool is able to reliably determine when planet candidates are true planets or false positives originating from nearby stars in the field. I run `TRICERATOPS` on a several hundred *TESS* planet candidates and assign them designations based on the results of the analysis. In Chapter 3, I use `TRICERATOPS` and several different types of ground-based follow-up observations to validate 13 hot *TESS* planets that are consistent with having terrestrial compositions based on their sizes and are ideal targets for observations with *JWST*. In Chapter 4, I perform a similar analysis to validate the planet HD 56414 b, a Neptune-size planet on a 29-day orbit around an A-type star. Sub-Jovian planets orbiting A-type stars are difficult to detect due to the sizes and rapid rotation rates of these stars, and the fact that the first one discovered in *TESS* data has a relatively long orbital period suggests that they may be especially uncommon at smaller orbital separations. I also present simulation results showing that photoevaporation due to high levels of near-ultraviolet continuum emission from A-type stars is capable of stripping short-period Neptune-size planets of their atmospheres, potentially causing a dearth of these worlds around hot stars. In Chapter 5, I perform an occurrence rate calculation for planets smaller than Saturn with orbital periods under 10 days around A-type stars. I show, for the first time, that planets of this size are rarer around A-type stars than they are around cooler stars, providing new insight into how planet formation and evolution varies based on stellar properties. Lastly, in Chapter 6, I provide concluding remarks and a brief discussion of what lies ahead in exoplanet science.

Note that many of the chapters of this thesis are based on works written prior to the launch of *JWST*, and therefore refer to the mission in the future tense. I have left this text in its original form, but the reader should be aware that the flagship mission has begun operations at the time of the writing of this thesis.

1.5 Other Work

I keep the chapters in this thesis mostly thematically consistent, but in doing so I exclude discussions of a number of other projects I have been a part of during graduate school. Here, I briefly acknowledge this other work.

I have participated in several *TESS* follow-up programs that aim to characterize transiting planets detected by *TESS* as well as their host stars. My first experience collecting ground-based observations was with the 3 m NASA Infrared Telescope Facility through a program lead by my graduate research advisor, Dr. Courtney Dressing. The goal of the program was to collect near-infrared spectra of M dwarfs with planet candidates in order to measure their metallicities and calculate their masses and radii with a better precision. Later, I led my own program to collect similar observations in order to explore the relationship between system architecture and stellar metallicity for cool stars. These data will soon be submitted for publication in a paper led by a former Berkeley undergraduate student I am advising. We have also contributed this data to other papers that confirm and characterize *TESS* planets (Mori et al. 2022; Wells et al. 2021).

I also participated in a program with the 3 m Shane telescope at Lick Observatory, also lead by Dr. Dressing, to collect adaptive optics images of potential planet-hosting stars to search for unknown stellar-mass companions in the systems. I assisted with the collection of data over dozens of nights, in addition to its reduction, analysis, and dissemination to the broader exoplanet community. These data have been included in several *TESS* planet discovery papers (Cloutier et al. 2021; de Leon et al. 2021; Demory et al. 2020; Dong et al. 2022; Gan et al. 2022; Lillo-Box et al. 2023; Newton et al. 2022; Rodriguez et al. 2021; Savel et al. 2020; Yee et al. 2022) and are being compiled into a paper lead by Dr. Dressing.

Lastly, for the last several years I have collected data for the *TESS*-Keck Survey, a collaboration between several institutions to use the HIRES spectrograph on the 10 m Keck telescope to characterize stars with *TESS* planet candidates, measure the masses of planets detected by *TESS*, and characterize the architectures of systems with transiting planets. I have observed over 80 partial nights, contributing to multiple papers that characterize nearby planetary systems (Dai et al. 2020, 2021; Dalba et al. 2020, 2022; Lubin et al. 2022; MacDougall et al. 2021, 2022; Rubenzahl et al. 2021; Scarsdale et al. 2021; Turtelboom et al. 2022; Van Zandt et al. 2023; Weiss et al. 2021).

Chapter 2

TRICERATOPS: A Validation Tool for Transiting Planets

An earlier version of this article was published as: Giacalone, S., Dressing, C. D., Jensen, E. L. N., Collins, K. A., Ricker, G. R., Vanderspek, R., Seager, S., Winn, J. N., Jenkins, J. M., Barclay, T., Barkaoui, K., Cadieux, C., Charbonneau, D., Collins, K. I., Conti, D. M., Doyon, R., Evans, P, Ghachoui, M, Gillon, M, Guerrero, N. M., Hart, R., Jehin, E, Kielkopf, J. F., McLean, B., Murgas, F., Palle, E., Parviainen, H., Pozuelos, F. J., Relles, H. M., Shporer, A., Socia, Q., Stockdale, C., Tan, T.-G., Torres, G., Twicken, J. D., Waalkes, W. C., Waite, I. A., 2021, *The Astronomical Journal*, 161, 24.

We present `TRICERATOPS`, a new Bayesian tool that can be used to vet and validate *TESS* Objects of Interest (TOIs). We test the tool on 68 TOIs that have been previously confirmed as planets or rejected as astrophysical false positives. By looking in the false positive probability (FPP) – nearby false positive probability (NFPP) plane, we define criteria that TOIs must meet to be classified as validated planets (FPP < 0.015 and NFPP $< 10^{-3}$), likely planets (FPP < 0.5 and NFPP $< 10^{-3}$), and likely nearby false positives (NFPP $> 10^{-1}$). We apply this procedure for 384 unclassified TOIs. We statistically validate 12, classify 125 as likely planets, and classify 52 as likely nearby false positives. Of the 12 statistically validated planets, 9 are newly validated. `TRICERATOPS` is currently the only *TESS* vetting and validation tool that models transits from nearby contaminant stars in addition to the target star. We therefore encourage use of this tool to prioritize follow-up observations that confirm bona fide planets and identify false positives originating from nearby stars.

2.1 Introduction

Over the last decade, the *Kepler* Space Telescope has revolutionized our understanding of exoplanets by facilitating the discovery of thousands of planets that transit in front of their host stars. Among other things, these planets have been useful for investigating the frequency of planets as a function of size and orbital period (e.g., Burke et al. 2015; Dong and Zhu 2013; Dressing and Charbonneau 2013, 2015; Foreman-Mackey et al. 2014; Fressin

et al. 2013; Fulton et al. 2017; Howard et al. 2012; Hsu et al. 2018; Morton and Swift 2014; Mulders et al. 2015a,b; Petigura et al. 2013; Sanchis-Ojeda et al. 2014), as well as testing theories of planet formation and evolution (e.g., Giacalone et al. 2017; Königl et al. 2017; Lee and Chiang 2017; Lopez and Fortney 2013; Swift et al. 2013). To ensure the veracity of their results, studies that utilized the *Kepler* dataset required that: (1) the measured radii of these planets were accurate, and (2) that the discovered objects were actually planets. However, due to the limited $4''$/pixel resolution of the camera used by *Kepler*, these two requirements could not always be assumed true. Because it was not uncommon for *Kepler* field stars of comparable brightness to reside $< 4''$ apart, the presence of multiple unresolved stars within a given set of pixels could not be discounted. This uncertainty was problematic because the existence of unresolved stars could cause an underestimation of the radius of a transiting object, sometimes to the extent that an eclipsing binary star could be mistaken for a transiting planet with a fraction of the size.

A number of methods have been used to constrain the possibility of an unresolved star residing within a given pixel. One method used is to search for offsets in the centroid of the source during transit, a signal indicative of another star residing elsewhere in the pixel (e.g., Bryson et al. 2013; Coughlin et al. 2014). Multi-band time-series photometry has also been used to search for unresolved stars, as one would expect a different transit depth in different photometric bands if the transiting object is around a star of a different color than the target (e.g., Alonso et al. 2004). Spectra of the target star can also be useful in this vetting process. High-precision radial velocities can rule out bound stellar companions by measuring the masses of transiting objects and monitoring for longer-period secondaries (e.g., Errmann et al. 2014), and reconnaissance spectroscopy can rule out bright unresolved stars by searching for additional lines in the spectrum of the target star (e.g., Kolbl et al. 2015; Santerne et al. 2012). Finally, high-resolution imaging can rule out unresolved stars beyond a fraction of an arcsecond from the target star (e.g., Crossfield et al. 2016; Mayo et al. 2018). Unfortunately, these techniques do not cover the full allowed parameter space individually, and *Kepler* planet candidate hosts were often too faint for precise radial velocity measurements. For this reason, it was common to turn to vetting and statistical validation to assess the genuineness of *Kepler* planet candidates.

When speaking of vetting, we refer to the process of scrutinizing the photometry of threshold-crossing events (TCEs, periodic transit-like signals originating from target stars) and classifying them as planet candidates and false positives of instrumental or astrophysical origin. Vetting procedures typically make use of automated decision-making algorithms to determine the natures of these events. Autovetter (Catanzarite 2015; McCauliff et al. 2015) and Robovetter (Thompson et al. 2018) are a *Kepler*-era vetting procedures that classify TCEs based on *Kepler* data using a random-forest and decision tree algorithms. `DAVE` (Kostov et al. 2019) is a vetting tool that calculates metrics based on centroid position and transit shape to classify *K*2 and *TESS* TCEs. Lastly, Exonet (Shallue and Vanderburg 2018) and Astronet (Ansdell et al. 2018) make use of convolutional neural networks to classify TCEs based on transit shape. By distinguishing planet candidates from false positives, these tools have allowed others to focus planetary confirmation and characterization efforts on the

most promising targets.

When speaking of statistical validation, we refer to the process of statistically ruling out astrophysical false positive scenarios to a degree of certainty high enough to advance the status of a planet candidate to one similar to that of a planet confirmed via mass measurement. In addition to information gleaned from the light curve of a planet candidate, validation algorithms typically incorporate constraints obtained from follow-up observations like those described previously. A number of statistical validation algorithms were used during the *Kepler* era in order to grow the dataset with which large-scale studies of planetary system properties could be conducted.

The first *Kepler*-era validation framework was `BLENDER` (Torres et al. 2004, 2005, 2011). `BLENDER` begins by generating synthetic light curves using models of transiting planets and astrophysical false positives involving blended eclipsing binaries. Next, it calculates the χ^2 of the best-fit planetary scenario and the χ^2 values for several false positive scenarios over a grid of model parameters. For each false positive scenario, the region of parameter space where the scenario is viable (defined by where χ^2 differs from the best-fit planetary χ^2 with a confidence level $< 3\sigma$) is identified. The properties of the blended stars in these viable instances are then compared to constraints obtained from supplementary follow-up, such as high-resolution imaging and spectroscopy, to determine if they are physically possible. In addition to this light curve analysis, `BLENDER` calculates the multi-color photometry one would expect to measure for each false positive scenario to compare to the actual observed colors. If the properties of all viable false positive scenarios are ruled out by the information from these external observations, the planet candidate is considered validated.

`BLENDER` offered a robust option for the statistical validation of transiting planet candidates during the *Kepler* era. However, the hands-on nature of the algorithm and the long computation times required to simulate the many false positive scenarios involved in its analysis made it inefficient for validating planet candidates in bulk. This led to the formulation of a different validation procedure by the name of `VESPA` (Morton 2015; Morton 2012). In addition to being fully automated, `VESPA` provides a more computationally expedient option for validating planet candidates by replacing the physical transit models employed in `BLENDER` with a simpler trapezoidal model, which can capture the most important features of the transit shape with fewer free parameters.

`VESPA` works in a Bayesian framework where the probabilities of several transit-producing scenarios are computed. For every scenario, `VESPA` uses the TRILEGAL galactic model (Girardi et al. 2005) to simulate a population of stars with properties consistent with the target star in a cone around the line of sight to the target. The properties of these simulated stars are inferred using archival photometry of the target star and isochrone interpolation, which ensures agreement with observational constraints. For each instance of each population, the transit shape is characterized using a trapezoidal model, which allows for the generation of a trapezoidal parameter prior distribution for each scenario. `VESPA` then uses a Markov Chain Monte Carlo routine to fit the *Kepler* light curve to the same trapezoidal model to determine the region of parameter space the target occupies. Next, the marginal likelihood is calculated for every scenario by integrating the product of the trapezoidal likelihood and

parameter prior over the predetermined region of parameter space. These marginal likelihoods are multiplied by model priors based on the geometries of simulated systems and assumptions relating to the occurrence of planets and close binaries. Lastly, the probability of the transiting planet scenario is assessed by comparing this product for the transiting planet scenario with those of all false positive scenarios, with the planet candidate being validated if the overall false positive probability is $< 1\%$. Like `BLENDER`, `VESPA` can also incorporate follow-up observations to obtain tighter constraints on this probability.

Another procedure used to validate exoplanet candidates is `PASTIS` (Dıaz et al. 2014; Santerne et al. 2015). `PASTIS` provides a rigorous option for the statistical validation of small planetary transits by calculating the Bayesian odds ratio between the transiting planet scenario and all possible false positive scenarios for a given target star. Prior probabilities are computed for each scenario by combining information about the target, including that contained within ground-based follow-up observations, with knowledge of stellar multiplicity and planet occurrence rates. In addition, for false positive scenarios that involve an unresolved foreground or background star, TRILEGAL is used to simulate a population of stars around the line of sight to target to calculate the prior probability of such a chance alignment. Like in `VESPA`, these priors are combined with marginal likelihoods, which `PASTIS` calculates using importance sampling. However, unlike `VESPA`, `PASTIS` additionally models the radial velocities of its targets and uses physical light curve models in its analysis. Like those utilized with `BLENDER`, these light curve models are more complex than the trapezoidal model, meaning `PASTIS` must sample over a wider parameter space when computing the marginal likelihood of each scenario. While ensuring that all possible parameter combinations for each scenario are considered, this method requires significantly more time to run for a given target than `VESPA` does.

Each of the aforementioned procedures was designed to work with minimal information about a given target star in order to argue for the existence of a transiting planet around it. This design mainly grew out of necessity, as information about many planet candidate hosts and the region of sky in which they were located was sparse in the absence of additional observations. For instance, the number of stars within each pixel was often unknown, and the stars that were known were not always precisely characterized. These facts imposed limitations on the functionalities of the procedures. Specifically, they restricted testable false positive scenarios to those involving the target star and a single unresolved star, even though there could have been a multitude of unknown stars in the group of pixels used to extract a given light curve. Additionally, poorly characterized target stars forced these procedures to use stellar models and isochrone interpolation to estimate host star properties, which comes at the cost of computation time.

These design features make previous validation algorithms poorly optimized for use on planet candidates identified by the Transiting Exoplanet Survey Satellite (*TESS*; Ricker et al. 2010). *TESS* differs from *Kepler* by being an all-sky survey that focuses on the nearest and brightest stars in order to find planets that are well-suited for mass measurement and atmospheric characterization. However, this increased sky coverage comes at the cost of resolution. The *TESS* cameras contain pixels that span $21''$, which means each pixel covers an

Scenario	Scenario Configuration	Parameter Vector, θ_j
TP	No unresolved companion. Transiting planet with $P_{\rm orb}$ around target star.	(i, R_p)
EB	No unresolved companion. Eclipsing binary with $P_{\rm orb}$ around target star.	(i, $q_{\rm short}$)
EBx2P	No unresolved companion. Eclipsing binary with $2 \times P_{\rm orb}$ around target star.	(i, $q_{\rm short}$)
PTP	Unresolved bound companion. Transiting planet with $P_{\rm orb}$ around primary star.	(i, R_p, $q_{\rm long}$)
PEB	Unresolved bound companion. Eclipsing binary with $P_{\rm orb}$ around primary star.	(i, $q_{\rm short}$, $q_{\rm long}$)
PEBx2P	Unresolved bound companion. Eclipsing binary with $2 \times P_{\rm orb}$ around primary star.	(i, $q_{\rm short}$, $q_{\rm long}$)
STP	Unresolved bound companion. Transiting planet with $P_{\rm orb}$ around secondary star.	(i, R_p, $q_{\rm long}$)
SEB	Unresolved bound companion. Eclipsing binary with $P_{\rm orb}$ around secondary star.	(i, $q_{\rm short}$, $q_{\rm long}$)
SEBx2P	Unresolved bound companion. Eclipsing binary with $2 \times P_{\rm orb}$ around secondary star.	(i, $q_{\rm short}$, $q_{\rm long}$)
DTP	Unresolved background star. Transiting planet with $P_{\rm orb}$ around target star.	(i, R_p, sim. star)
DEB	Unresolved background star. Eclipsing binary with $P_{\rm orb}$ around target star.	(i, $q_{\rm short}$, sim. star)
DEBx2P	Unresolved background star. Eclipsing binary with $2 \times P_{\rm orb}$ around target star.	(i, $q_{\rm short}$, sim. star)
BTP	Unresolved background star. Transiting planet with $P_{\rm orb}$ around background star.	(i, R_p, sim. star)
BEB	Unresolved background star. Eclipsing binary with $P_{\rm orb}$ around background star.	(i, $q_{\rm short}$, sim. star)
BEBx2P	Unresolved background star. Eclipsing binary with $2 \times P_{\rm orb}$ around background star.	(i, $q_{\rm short}$, sim. star)
NTP	No unresolved companion. Transiting planet with $P_{\rm orb}$ around nearby star.	(i, R_p)
NEB	No unresolved companion. Eclipsing binary with $P_{\rm orb}$ around nearby star.	(i, $q_{\rm short}$)
NEBx2P	No unresolved companion. Eclipsing binary with $2 \times P_{\rm orb}$ around nearby star.	(i, $q_{\rm short}$)

Table 2.1: Scenarios tested by `TRICERATOPS`. In the right-most column: i is orbital inclination, $R_{\rm p}$ is planet radius, $q_{\rm short}$ is the short-period stellar binary mass ratio, $q_{\rm long}$ is the long-period stellar binary mass ratio, and sim. star is the star simulated with the TRILEGAL code (which has a specified mass, radius, and effective temperature).

area of sky roughly 25× larger than those utilized by *Kepler* . Because of this, the assumption that there is at most one additional star contributing to the flux in a given aperture is unlikely to be true. In addition to scenarios involving a bound stellar companion or a chance alignment of a non-associated star near the target star, a *TESS* validation procedure must be capable of considering false positive scenarios involving a multitude of known stars near a given target.[1] While tools like `VESPA` have been used to validate planet candidates detected by *TESS* after ruling out false positives due to nearby stars with supplementary follow-up observations (e.g., Cloutier 2019; Cloutier et al. 2020b; Eisner et al. 2020; Gilbert et al. 2020; Günther et al. 2019; Huang et al. 2020; Quinn et al. 2019; Vanderspek et al. 2019), no tool exists as of yet that can perform a multi-star analysis on its own.

Luckily, the drawback of decreased resolution is counteracted by the wealth of information on nearby stars provided by the second *Gaia* data release (DR2; Gaia Collaboration et al. 2018). DR2 provides optical photometry, astrometry, and positions for over one billion of the nearest stars in the Galaxy. Perhaps most importantly, it is reported that DR2 consistently resolves individual point sources that reside more than 2.″2 apart, which allows for the identification of stars blended within a *TESS* pixel to levels previously only possible with supplementary follow-up. With this knowledge, one can test for false positive scenarios around known nearby stars and conduct more precise centroid analyses. In addition, the

[1]It should be noted that because *TESS* focuses on brighter stars than *Kepler* did and the field density of brighter stars is low compared to the field density of fainter stars, most of these contaminating stars will contribute only a small fraction of the total flux within the pixel. By contrast, stars blended within a *Kepler* pixel had a higher probability of having comparable brightnesses.

focus on nearby and bright stars means that most *TESS* planet candidate hosts can be more easily characterized using archival and follow-up data. In fact, the properties of millions of *TESS* targets have already been compiled in the *TESS* Input Catalog (TIC; Stassun et al. 2018b). It would benefit a validation procedure for *TESS* planet candidates to leverage these known stellar properties, rather than use stellar models to estimate them.

In this work, we present `TRICERATOPS` (**T**ool for **R**ating **I**nteresting **C**andidate **E**xoplanets and **R**eliability **A**nalysis of **T**ransits **O**riginating from **P**roximate **S**tars), a new Bayesian tool formulated to validate and vet *TESS* planet candidates.[2] The procedure calculates the probabilities of a wide range of transit-producing scenarios using the primary transit of the planet candidate, preexisting knowledge of its host and nearby stars, and the current understanding of planet occurrence and stellar multiplicity.

Our tool is designed to provide fast[3] and accurate calculations that can be used to not only validate transiting planet candidates, as validation tools have been used to do in the past, but also to serve as a metric for ranking targets of follow-up programs. Because a majority of *TESS* targets will be bright enough to be followed up with ground-based telescopes, there will inevitably be more planet candidate hosts to observe from the ground than time and resources allow for. We therefore encourage the use of our tool to identify targets that would benefit most from additional vetting.

The layout of this paper is as follows. In Section 2.2 we present our vetting and validation procedure, including how we determine the possible scenarios for a given target star and calculate the probability of each. In Section 2.3 we present detailed statistical validation results for a confirmed planet and for a known false positive. In Section 2.4 we present the results of our calculations for a sample of 68 TOIs that are known planets or false positives, conduct a performance assessment, and define the criteria a TOI must meet in order to be validated. In Section 2.5 we report observations that identify several TOIs as false positives originating from nearby stars and compare these observations with `TRICERATOPS` predictions. In Section 2.6 we apply our tool to 384 unclassified TOIs and statistically validate 12. In Section 2.7 we provide a discussion of our results, provide suggestions for how our tool can best be utilized, and present features that we plan on implementing in the future. Lastly, we provide concluding remarks in Section 2.8.

2.2 Procedure

Our validation procedure is initiated when the user inputs the ID a target star listed in the *TESS* Input Catalog (TIC) that has a transiting planet candidate. Using the MAST module of `astroquery` (Ginsburg et al. 2019), the tool queries the TIC for all stars within a circle of radius 10 pixels from the target. The positions, *TESS* magnitudes, and available stellar properties of each star are recorded for later use. Next, the user is required to specify

[2] Available at https://github.com/stevengiacalone/triceratops.

[3] Typical run time of about 5 minutes on a standard 2-core laptop for a single target.

the aperture used to extract the *TESS* light curve for each sector in which the target was observed. The remaining steps of the procedure are summarized as follows:

1. `TRICERATOPS` calculates the proportion of flux contributed to the aperture by each star near the target. Using the user-entered transit depth, the algorithm identifies the stars bright enough to produce the observed transit-like signal.

2. Using the user-entered primary transit of the planet candidate and light curve models of transiting planets and eclipsing binaries, `TRICERATOPS` calculates the marginal likelihood of each transit-producing scenario.

3. Given the marginal likelihood and prior probability of each scenario, the algorithm calculates the probability of each scenario.

4. The algorithm uses these probabilities to determine if the planet candidate can be classified as a validated planet, a likely planet, or a likely nearby false positive.

Flux Ratio Calculation

Initially, each star within 10 pixels of the target is considered a potential origin of the transit-like event. Because each star is contributing a different amount of flux to the aperture, the size that the transiting object must be to produce the observed transit depth is different for each star. Because the transiting object size is important for determining the probability of each scenario, the relative flux contributed by each star in the aperture is essential information.

We calculate the flux ratio contributed by each star using a method similar to that used in Stassun et al. (2018b) to determine the contamination ratios reported for candidate target stars in the TIC. Specifically, we assume the point spread function (PSF) of each star takes the form of a circular 2D Gaussian where the area under each Gaussian (i.e., the total flux) is determined using the *TESS* magnitudes reported in the TIC. We estimate the standard deviation of the Gaussian using the *TESS* pixel response function (PRF) models on MAST.[4] Due to effects relating to the design of the *TESS* optics, the exact PRF for a star is dependent on the location on the CCD on which it is observed. These models allow one to estimate the PRF for a given star by providing the size and shape of the *TESS* PRF at 25 locations on each CCD. We fit each PRF model to a circular 2D Gaussian and record the best-fit standard deviation, finding that it typically ranges between 0.6 and 0.9 pixels. For simplicity, we adopt a standard deviation of 0.75 pixels for all stars, regardless of CCD location. For each star, we integrate the flux in the aperture and divide by the total flux contributed to the aperture by all stars to determine its flux ratio, X_s. For targets that are observed in multiple sectors, we assume the flux ratio for a given star is the average of its flux ratios across each sector.

[4] `https://archive.stsci.edu/missions-and-data/transiting-exoplanet-survey-satellite-tess`

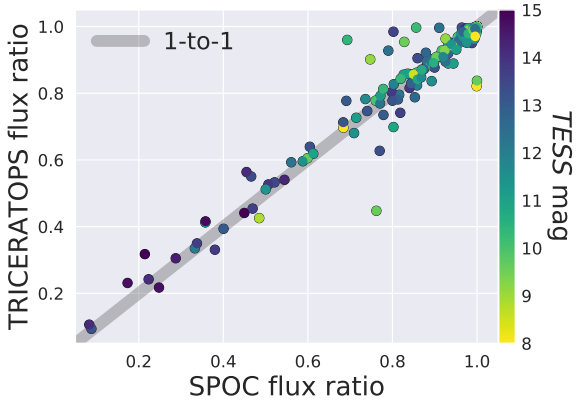

Figure 2.1: Comparison of target star flux ratios (i.e., the fraction of the flux in the aperture due to the target star) reported by `TRICERATOPS` and the *TESS* SPOC pipeline for a 228 TOIs. A 1-to-1 line is also shown for illustrative purposes. The two methods yield consistent results, with slightly larger discrepancies for brighter stars.

To ensure that our method provides reliable flux ratios, we compare in Figure 2.1 the target star flux ratios for 228 TOIs obtained using our method with those reported by the *TESS* Science Processing Operations Center (SPOC) pipeline (Jenkins et al. 2016), which calculates flux ratios using the actual PRF models discussed above.[5] Both of these calculations are carried out with the aperture used by the *TESS* SPOC pipeline to extract the light curve of the target star. The figure shows good agreement between the two calculations, with a slightly better agreement for fainter stars.

After flux ratios are determined, we eliminate stars that are too faint to be the source of the observed dimming event. If the observed transit depth is $\delta_{\rm obs}$, the relative transit depth for each star is simply $\delta_s = \delta_{\rm obs}/X_s$. For stars that contribute relatively little flux to the aperture, it is possible for δ_s to exceed unity. We exclude these stars from further analysis.

Transit Scenario Identification

After calculating the flux ratio for each star in the aperture, we determine the scenarios that can produce the observed transit-like event. Our procedure considers a total of fifteen scenarios for the target star and an additional three scenarios for each nearby star with $\delta_s < 1$. These scenarios are summarized in Table 2.1.

The fifteen target star scenarios can be classified into three configurations. The first is the case where the target star has no unresolved stellar companion (where we define "companion" to encompass both bound and foreground/background stars). In this case, we consider the

[5]Note that the decision to use Gaussian models rather than the actual *TESS* PRFs for our calculation was made in the interest of computational expediency.

scenarios of a transiting planet with the reported orbital period around the target star (TP), an EB with the reported orbital period around the target star (EB), and an EB with twice the reported orbital period around the target star (EBx2P). The last of these scenarios is meant to capture the possibility that the observed transit is caused by eclipsing binary stars of roughly equal size, such that the primary and secondary eclipses are mistaken for the primary transit of a smaller object with half the orbital period. The second configuration is that in which the target star has an unresolved bound stellar companion. In this case, we consider the scenarios of a transiting around the target star with the reported orbital period (Primary TP, or PTP), an eclipsing binary with the reported orbital period around the target star (Primary EB, or PEB), an eclipsing binary with twice the reported orbital period around the target star (Primary EBx2P, or PEBx2P), a transiting planet with the reported orbital period around the companion (Secondary TP, or STP), an eclipsing binary around the companion (Secondary EB, or SEB), and an eclipsing binary with twice the reported orbital period around the companion (Secondary EBx2P, or SEBx2P). The third configuration is that in which there there is an unresolved foreground or background star along the line of sight to the target star. In this case, we again consider the scenarios of a transiting planet with the reported orbital period around the target star (Diluted TP, or DTP), an eclipsing binary with the reported orbital period around the target star (Diluted EB, or DEB), an eclipsing binary with twice the reported orbital period around the target star (Diluted EBx2P, or DEBx2P), a transiting planet with the reported orbital period around the companion (Background TP, or BTP), an eclipsing binary with the reported orbital period around the companion (Background EB, or BEB), and an eclipsing binary with twice the reported orbital period around the companion (Background EBx2P, or BEBx2P).[6]

For nearby stars with $\delta_s < 1$, we also consider the scenarios of a transiting planet with the reported orbital period around that star (Nearby TP, or NTP), an eclipsing binary with the reported orbital period around that star (Nearby EB, or NEB), and an eclipsing binary with twice the reported orbital period around that star (Nearby EBx2P, or NEBx2P). Each of these scenarios operates under the assumption that the nearby star has no unresolved stellar companion. These scenarios can also be omitted by the calculation if false positives originating from the respective nearby stars have been ruled out through supplementary follow-up.

Stellar Property Estimation

Whenever possible, we use the stellar properties listed in the TIC in our calculations. However, for reasons that will be discussed, there are times in our procedure where we must estimate the properties (i.e., mass $M_\star$, radius $R_\star$, and effective temperature $T_{\rm eff}$) of a star in order to determine the probability of the corresponding scenario. We do so using the em-

[6]The BTP and BEB scenarios also include unresolved foreground stars, but the case where a background star is blended with the target star is typically the relevant one.

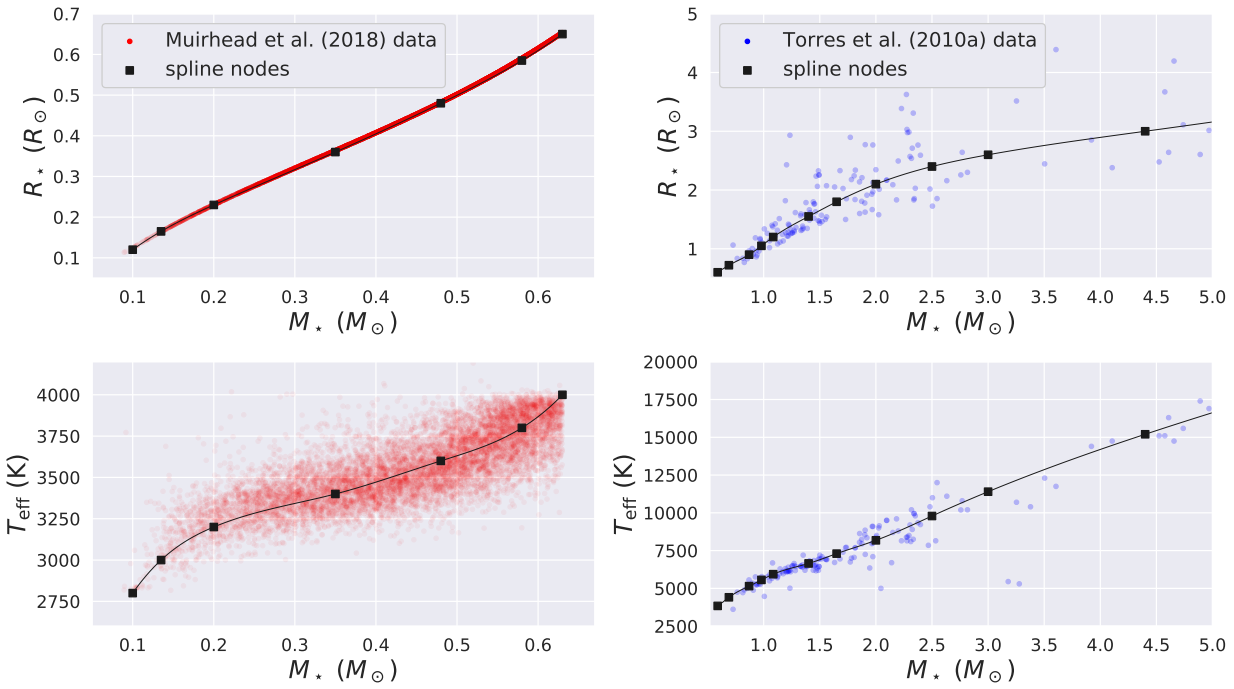

Figure 2.2: *Left:* $R_\star$ and $T_{\rm eff}$ vs $M_\star$ for stars in the *TESS* Cool dwarf Catalog. Red points are stars from the catalog, and black squares are nodes used to draw spline relations through these points. *Right:* $R_\star$ and $T_{\rm eff}$ vs $M_\star$ for stars in Torres et al. (2010). Blue points are stars from Torres et al. (2010), and black squares are nodes used to draw spline relations through these points.

pirical and semi-empirical relations between stellar properties used to populate these fields in the TIC.

For stars with $M_\star > 0.63 M_\odot$ (corresponding roughly to $T_{\rm eff} > 4000$ K), we determine stellar properties using the results from Torres et al. (2010). Using the same method discussed in Section 3 of Stassun et al. (2018b), we draw spline curves through the distribution of points in $M_\star - T_{\rm eff}$ and $M_\star - R_\star$ space. For stars with $M_\star \leq 0.63 M_\odot$, we repeat this process using a sample of stars from the specially curated *TESS* Cool dwarf Catalog (Muirhead et al. 2018). We select nodal points using the sample such that they are continuous with the curves obtained for hotter stars.

The spline curves and the samples on which they are based are shown in Figure 2.2. The result of this process is a set of relations that allows us to estimate the $R_\star$ and $T_{\rm eff}$ of a star given $M_\star$.

Probability Calculation

We employ a Bayesian framework in our procedure, and thus make use of Bayes' theorem:

$$p(S_j|D) \propto p(S_j)p(D|S_j) \tag{2.1}$$

where $p(S_j|D)$ is the posterior probability of the jth scenario S_j given the data D, $p(S_j)$ is the prior probability of scenario S_j, and $p(D|S_j)$ is the marginal likelihood of the data D given the scenario S_j (sometimes also referred to as the global likelihood, or the Bayesian evidence). Because we work with a transit model characterized by the parameter vector θ_j, we express the marginal likelihood as the marginalization of the likelihood $p(D|\theta_j, S_j)$ over θ_j:

$$p(D|S_j) = \int p(\theta_j|S_j)p(D|\theta_j, S_j)d\theta \tag{2.2}$$

where $p(\theta_j|S_j)$ is the prior distribution of the model parameters. We discuss how these quantities are calculated throughout the remainder of this section.

After calculating $p(S_j|D)$ for each scenario, we determine the relative probability of each scenario using the equation

$$\mathcal{P}_j = \frac{p(S_j|D)}{\sum_j p(S_j|D)}. \tag{2.3}$$

From here, we define two quantities that are useful for vetting and validation purposes. First, the "False Positive Probability" (FPP) is given by

$$\mathrm{FPP} = 1 - (\mathcal{P}_{\mathrm{TP}} + \mathcal{P}_{\mathrm{PTP}} + \mathcal{P}_{\mathrm{DTP}}), \tag{2.4}$$

where $\mathcal{P}_{\mathrm{TP}}$ is the probability of the transiting planet scenario, $\mathcal{P}_{\mathrm{PTP}}$ is the probability of the primary transiting planet scenario, and $\mathcal{P}_{\mathrm{DTP}}$ is the probability of the diluted transiting planet scenario (i.e., all of which involve a planet transiting the target star, see Table 2.1). This quantity represents the probability that the observed transit is due to something other than a transiting planet around the target star. Second, the "Nearby False Positive Probability" (NFPP) is given by

$$\mathrm{NFPP} = \sum(\mathcal{P}_{\mathrm{NTP}} + \mathcal{P}_{\mathrm{NEB}} + \mathcal{P}_{\mathrm{NEBx2P}}), \tag{2.5}$$

where $\mathcal{P}_{\mathrm{NTP}}$ is the probability of the nearby transiting planet scenario for a given nearby star, $\mathcal{P}_{\mathrm{NEB}}$ is the probability of the nearby eclipsing binary scenario for a given nearby star, and $\mathcal{P}_{\mathrm{NEBx2P}}$ is the probability of a nearby eclipsing binary with twice the predicted orbital period for a nearby star (i.e., all scenarios involving nearby stars, see Table 2.1). This quantity represents the probability that the observed transit originates from a resolved nearby star rather than the target star.

Scenario Priors

The scenario prior represents the prior probability of a given scenario before the data is considered. The only scenario prior we employ in our calculation is the probability of a transiting planet or eclipsing binary having the $P_{\rm orb}$ applied to the model.[7] For both transiting planets and eclipsing binaries, we assume the probability distribution of $P_{\rm orb}$ takes the form of a broken power law in the range $0.1 - 50$ days. Using these probability distributions, we calculate the prior probability of a orbital period $P'_{\rm orb}$ by integrating the probability distribution between $P'_{\rm orb} - 0.1$ and $P'_{\rm orb} + 0.1$:

$$p(P'_{\rm orb}) = \int_{P'_{\rm orb}-0.1}^{P'_{\rm orb}+0.1} p(P_{\rm orb}) dP_{\rm orb}. \tag{2.6}$$

While integrating over period is not strictly necessary for calculating this prior, we do so following convention from previous validation tools (e.g., Morton 2012).

For transiting planets we base the behavior of this distribution on studies of planet occurrence rates as a function of orbital period (e.g., Dong and Zhu 2013; Dressing and Charbonneau 2015; Howard et al. 2012; Mulders et al. 2015a, 2018; Petigura et al. 2013). We express $p(P_{\rm orb})$ as a broken power law with a break at $P_{\rm orb} = 10$ days and the form

$$p(P_{\rm orb}) \sim \begin{cases} P_{\rm orb}^{1.5} & 0.1\,{\rm days} \leq P_{\rm orb} \leq 10\,{\rm days} \\ P_{\rm orb}^{0.0} & 10\,{\rm days} < P_{\rm orb} \leq 50\,{\rm days} \end{cases} \tag{2.7}$$

(see Figure 2.3). Note that while planet occurrence is typically expressed as a non-separable function of both planet radius and $P_{\rm orb}$ (Foreman-Mackey et al. 2014; Fulton and Petigura 2018; Hsu et al. 2019; Neil and Rogers 2020), we treat the two variables as independent in our calculation procedure.

For eclipsing binaries we base the behavior of this distribution on the results of the *Kepler* Eclipsing Binary Catalog (Kirk et al. 2016), which contains the properties of thousands of objects that were classified as EBs based on their light curve morphologies. After correcting the catalog for eclipsing binaries that were not detected due to orbital misalignment, we find that $p(P_{\rm orb})$ is best expressed as a broken power law with a break at $P_{\rm orb} = 0.3$ days and the form

$$p(P_{\rm orb}) \sim \begin{cases} P_{\rm orb}^{5.0} & 0.1\,{\rm days} \leq P_{\rm orb} \leq 0.3\,{\rm days} \\ P_{\rm orb}^{0.5} & 0.3\,{\rm days} < P_{\rm orb} \leq 50\,{\rm days} \end{cases} \tag{2.8}$$

(see Figure 2.3).

It is common for validation procedures to also include priors that capture the overall planet occurrence and stellar multiplicity rate. Planet occurrence rate studies have revealed that the probability of a FGKM dwarf hosting a planet with $P_{\rm orb} < 50$ days ranges from $10 - 100\%$, decreasing as a function of increasing host star mass (e.g., Dressing and Charbonneau 2015; Fressin et al. 2013; Petigura et al. 2013). Stellar multiplicity rate studies

[7] We note that as of 8 May 2023, this prior is no longer used in the code. However, we keep the description here for the sake of completeness.

have determined that the probability of a FGKM dwarf hosting a stellar companion with $P_{\rm orb} < 50$ days ranges from $1 - 10\%$, increasing as a function of increasing host mass (Moe and Di Stefano 2017). This implies that all scenarios involving transiting planets should have a prior probability $10 - 100\times$ higher than those involving eclipsing binaries. At first, we included this prior in the algorithm. However, after testing the performance of our tool on known transiting planets and astrophysical false positives (see Section 2.4), we found that false positive scenarios were penalized too heavily, often leading the code to classify signals that are caused by false positives as planets. To avoid having TOIs erroneously classified as planets in the future, we omit these priors from our calculation procedure.

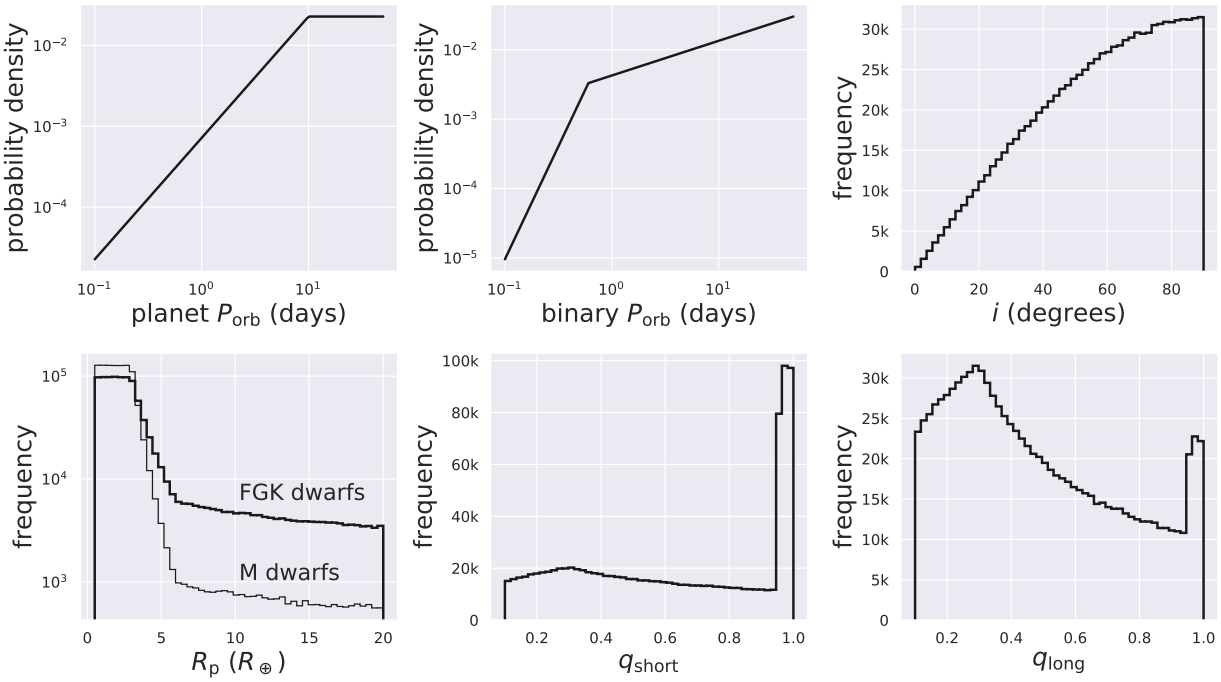

Figure 2.3: Visualizations of the distributions used to determine model priors and sample parameters in our calculations. *Top left:* The probability density function for the orbital periods of transiting planets. *Top center:* The probability density function for the orbital periods of eclipsing binaries. *Top right:* The parameter prior distribution for inclination. *Bottom left:* The parameter prior distribution for planet radius. *Bottom center:* The parameter prior distribution for short-period stellar companion mass ratio. *Bottom right:* The parameter prior distribution for long-period stellar companion mass ratio.

Parameter Prior Distributions

Every scenario we test is associated with a vector θ_j of parameters that are needed for modeling the light curves of each scenario. The parameters that compose these vectors for each scenario are shown in Table 2.1. To reflect the fact that certain values of these parameters are more common than others, each is associated with a probability distribution. In this section, we define each of these parameters and their respective probability distributions. Examples of these distributions are shown in Figure 2.3 for a sample size of 10^6.

The parameter i represents the inclination of the orbit of a transiting planet or eclipsing binary. Assuming an isotropic distribution of orbits, the distribution of inclinations takes the form

$$p(i) \sim \sin i. \tag{2.9}$$

The parameter R_p represents the radius of a transiting planet. Because this distribution is known to be dependent on host star mass, we use different distributions for M dwarfs and FGK dwarfs. The two distributions differ in the prevalence of giant planets ($R_\mathrm{p} > 6R_\oplus$), which are known to be less common around M dwarfs than they are around their more massive counterparts by a factor of ~ 10 (e.g., Dressing and Charbonneau 2013; Fressin et al. 2013; Mulders et al. 2015b; Petigura et al. 2013). We express these distributions as broken power laws with breaks at $R_\mathrm{p} = 3R_\oplus$ and $R_\mathrm{p} = 6R_\oplus$ and a range of $R_\mathrm{p} = 0.5 - 20R_\oplus$ (e.g., Mulders et al. 2015b, 2018).[8] For M dwarfs the distribution takes the form

$$p(R_\mathrm{p}) \sim \begin{cases} R_\mathrm{p}^{0.0} & 0.5R_\oplus \leq R_\mathrm{p} \leq 3R_\oplus \\ R_\mathrm{p}^{-7.0} & 3R_\oplus < R_\mathrm{p} \leq 6R_\oplus \\ R_\mathrm{p}^{-0.5} & 6R_\oplus < R_\mathrm{p} \leq 20R_\oplus \end{cases} \tag{2.10}$$

and for FGK dwarfs the distribution takes the form

$$p(R_\mathrm{p}) \sim \begin{cases} R_\mathrm{p}^{0.0} & 0.5R_\oplus \leq R_\mathrm{p} \leq 3R_\oplus \\ R_\mathrm{p}^{-4.0} & 3R_\oplus < R_\mathrm{p} \leq 6R_\oplus \\ R_\mathrm{p}^{-0.5} & 6R_\oplus < R_\mathrm{p} \leq 20R_\oplus \end{cases} . \tag{2.11}$$

The parameter q_short represents the mass ratio between the host star and a short-period stellar companion (i.e., an eclipsing binary). To calculate this distribution, we extrapolate from the results of Moe and Di Stefano (2017) for Sun-like stars. In the study, q is parameterized as a broken power law with a break at $q = 0.3$ and a range of $q = 0.1 - 1.0$. In addition, the parameterization takes into account the excess of stellar "twins" (stellar companions with $q > 0.95$) with a term $\mathcal{F}_\mathrm{twin}$ (defined as the fraction of stars with $q > 0.3$ that have $q > 0.95$) that boosts the prevalence of these stars in the probability distribution. For short-period stellar companions, the distribution takes the form

$$p(q_\mathrm{short}) \sim \begin{cases} q_\mathrm{short}^{0.3} & 0.1 \leq q \leq 0.3 \\ q_\mathrm{short}^{-5.0} & 0.3 < q \leq 1.0 \end{cases} \tag{2.12}$$

[8] Note that we do not model the gap in the radius distribution between $1.5 - 2.0R_\oplus$ (Fulton et al. 2017).

with $\mathcal{F}_{\rm twin} = 0.3$.

The parameter $q_{\rm long}$ represents the mass ratio between the target star and a long-period stellar companion (i.e., an unresolved bound companion). Again, we utilize the parameterization and extrapolate results of Moe and Di Stefano (2017) for Sun-like stars. For long-period stellar companions, the distribution takes the form

$$p(q_{\rm long}) \sim \begin{cases} q_{\rm long}^{0.3} & 0.1 \leq q \leq 0.3 \\ q_{\rm long}^{-0.95} & 0.3 < q \leq 1.0 \end{cases} \tag{2.13}$$

with $\mathcal{F}_{\rm twin} = 0.05$.

The parameter "simulated star" represents the properties of a star drawn from a population of stars simulated with TRILEGAL. To determine the properties of blended stars used in DTP, DEB, DEBx2P, BTP, BEB, and BEBx2P scenarios, we simulate a population of stars in a 0.1 deg^2 region of the sky centered at the target star. We then produce a distribution of possible foreground/background stars by removing all stars with *TESS* magnitudes brighter than the target and fainter than 21, which typically yields between $300 - 1000$ stars. When simulating an instance of these scenarios, we draw a star directly from this distribution.

Marginal Likelihoods

Because the integral in Equation 2.2 is typically impossible to solve analytically, it is common to approximate the integral by sampling $p(\theta_j|S_j)$. This is, in fact, what is done when calculating odds ratios between competing scenarios in the `PASTIS` and `VESPA` validation procedures. In this work, we calculate the marginal likelihood using Arithmetic Mean Estimation (Kass and Raftery 1995). This method allows us to calculate the marginal likelihood using Monte Carlo sampling by approximating Equation 2.2 as

$$p(D|S_j) \sim \frac{1}{N} \sum_{n=1}^{N} p(D|\theta_j^{(n)}, S_j) \tag{2.14}$$

where $\theta_j^{(n)}$ is the nth sample from the parameter prior distribution and N is the total number of samples. This is typically regarded as the simplest estimator of the marginal likelihood, but it is often avoided because it can produce a large variance in $p(D|S_j)$ if N is not sufficiently high and is relatively inefficient when integrating over a large number of parameters. We take two approaches to combat these drawbacks: (1) we chose a N high enough to produce results that are consistent between consecutive calculations (which we determine to be $N = 10^6$), and (2) we make simplifying assumptions in our transiting planet and eclipsing binary models that minimize the number of parameters we must marginalize over.

The first simplifying assumption we make is to assume that the $M_\star$, $R_\star$ and $T_{\rm eff}$ of each resolved star is known precisely. Unless the user provides these parameters, they are assumed to be equal to those listed in the TIC. In addition, any other stars added to our transit model that do not have estimates for these quantities (e.g., eclipsing binaries or

unresolved companions) are assumed to be precisely characterized based on their $M_\star$ (see Section 2.2). Because the transit models are sensitive to these parameters, this assumption saves us from having to marginalize over a distribution of target star properties.

The second simplifying assumption we make is to assume a fixed orbital period and zero eccentricity (e) in all scenarios considered, which significantly simplifies the orbital solution of the system. There is strong evidence that short-period planets are biased towards lower e (e.g., Kane et al. 2012; Kipping 2013b; Shabram et al. 2016). According to the NASA Exoplanet Archive,[9] 84% of confirmed planets with $P_{\rm orb} < 30$ days and reported eccentricities have $e < 0.2$. The same justification can be applied to short-period eclipsing binaries. Moe and Di Stefano (2017), showed that the e distribution of binary stars with $P_{\rm orb} < 10$ days goes like $e^{-0.8}$. This implies that 72% of short-period eclipsing binaries have $e < 0.2$. Because a majority of TOIs will have $P_{\rm orb} < 30$ days (due to the ~ 27 day intervals in which sectors are observed and the general requirement for at least 2 transits be observed for a system to become a planet candidate), we believe the assumption of circular orbits is justified in most cases. However, users of `TRICERATOPS` should be aware that this assumption becomes less valid as longer orbital periods are considered.

We calculate $p(D|\theta_j^{(n)}, S_j)$ as the product of two terms:

$$p(D|\theta_j^{(n)}, S_j) = p(D_{\rm tra}|\theta_j^{(n)}, S_j) \times w^{(n)} \tag{2.15}$$

where the first term is the likelihood of the transit data and $w^{(n)}$ is a weight that encapsulates our ability to rule out unresolved companions near the target star using high-resolution imaging follow-up. This weight is intended to decrease the likelihood of scenarios involving unresolved companions when stronger constraints on the existence such companions are applied.

The likelihood of the transit data is calculated using the equation

$$p(D_{\rm tra}|\theta_j^{(n)}, S_j) \propto \prod exp\left[-\frac{1}{2}\left(\frac{y_l - f(t_l|\theta_j^{(n)})}{\sigma}\right)^2\right] \tag{2.16}$$

where y_l is the flux of the lth data point, $f(t_l|\theta_j^{(n)})$ is the flux given by the model for the parameter vector $\theta_j^{(n)}$ at the time of the lth data point, and σ is the characteristic uncertainty of the flux.

For PTP, PEB, PEBx2P, STP, SEB, and SEBx2P scenarios we calculate $w^{(n)}$ using Equation 23 of Moe and Di Stefano (2017). Equation 23 of Moe and Di Stefano (2017) provides the frequency of bound stellar companions as a function of primary mass and orbital period. We calculate this quantity for the nth sample of the parameter prior distribution using the following steps: (1) determine magnitude difference between the primary and secondary star using the mass of the target and the nth draw of $q_{\rm long}$, (2) use the contrast curve obtained from high-resolution imaging to determine the angular separation beyond

[9] `https://exoplanetarchive.ipac.caltech.edu/`

which the simulated secondary would have been detected, (3) convert this angular separation to an orbital period using the parallax of the target and the masses of the target and simulated secondary, and (4) use this orbital period and Equation 23 of Moe and Di Stefano (2017) to calculate the corresponding frequency of bound stellar companions. If no high-resolution imaging data is available to fold in, the angular separation used in step (2) is assumed to be 2″.2 (Gaia Collaboration et al. 2018).

For DTP, DEB, DEBx2P, BTP, BEB, and BEBx2P scenarios we calculate $w^{(n)}$ using the results of the TRILEGAL simulation discussed in Section 2.2. Specifically, we calculate this likelihood as the frequency of unresolved foreground and background stars aligned with the target star in the sky. This calculation is performed with the following steps: (1) determine the magnitude difference between the target star and the nth drawn foreground/background star, (2) use the contrast curve obtained from high-resolution imaging to determine the angular separation beyond which the simulated foreground/background star would have been detected, (3) use this separation and the total number of simulated stars to estimate the frequency of unresolved foreground/background stars near the target. As for the previous scenarios, if no high-resolution imaging data is available to fold in, the angular separation used in step (2) is assumed to be 2″.2 (Gaia Collaboration et al. 2018).

We set the maximum value of $w^{(n)}$ for each scenario to 1. We also set $w^{(n)} = 1$ for TP, EB, EBx2P, NTP, NEB, and NEBx2P scenarios, which do not involve unresolved companions.

Light Curve Modeling

We calculate Equation 2.16 by modeling light curves using a modified version of `batman` (Kreidberg 2015). Here, we describe the steps that go into simulating the transits of each scenario.

The simplest scenario to model is the TP scenario, in which we assume that all of the flux originates from the host star. For this scenario, we use `batman` in its default form. For this scenario, as well as all other scenarios, we use quadratic limb darkening coefficients chosen based on the $T_{\rm eff}$ and $\log g$ of the host star (Claret 2018).

For all scenarios involving eclipsing binaries, we must account for the fact that the flux is split between the host star and the short-period companion. Doing so requires an estimate for the flux contributed by the eclipsing binary, which we find by determining a relation between $M_\star$ and *TESS* magnitude. We begin by querying the TIC for all stars located a distance between $99 - 101$ pc away. We then draw a spline curve through the distribution of points in the *TESS* magnitude – $M_\star$ plane, which is shown in Figure 2.4. This relation allows us to calculate the *TESS* band flux ratio between two stars given their masses and adjust the in-transit flux of the light curve accordingly.

For scenarios involving unresolved companions, we again must account for the flux dilution from the additional star. For scenarios involving a unresolved bound companion (whose mass is determined by $q_{\rm long}$), we use the spline relation shown in Figure 2.4 to determine the flux contribution of the star. For scenarios involving an unresolved foreground/background

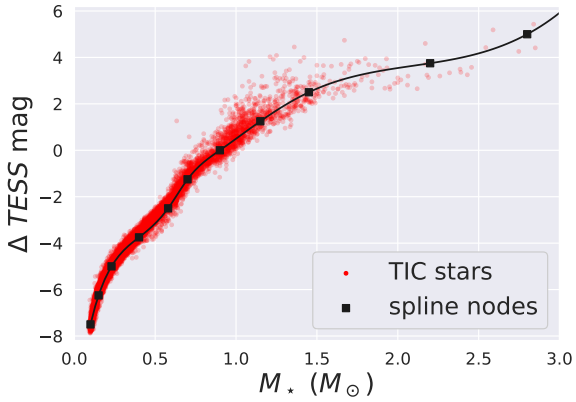

Figure 2.4: Δ *TESS* magnitude between a star of mass $M_\star$ and a 10th magnitude, $1M_\odot$ star. Red points are stars queried from the TIC located between $99 - 101$ pc away. Black squares are the nodes of the spline relation used to calculate the *TESS* mag of unresolved stars modeled in our calculations.

star, we use the *TESS* magnitude provided by TRILEGAL to determine the flux contribution of the star.

Lastly, we apply constraints to our transit models for all "EB" and "EBx2P" scenarios. For the former, we require $q_{\rm short} < 0.95$ and for the expected secondary eclipse depth to be shallower than $1.5\times$ the scatter of the *TESS* light curve flux (else the secondary eclipse would have been detected and identified as such). For the latter, we require $q_{\rm short} > 0.95$. If the nth model light curve does not satisfy these conditions, we set the likelihood of the transit to zero.

2.3 Examples

For illustrative purposes we display here each step of our calculation for two TOIs, one of which has been confirmed as a transiting planet and one of which has been ruled out as a nearby eclipsing binary.

TIC 270380593 (TOI 465.01)

We apply our algorithm on the previously-confirmed TOI 465.01 (WASP-156b; Demangeon et al. 2018), a $\sim 6R_\oplus$ planet orbiting a K dwarf with a 3.84 day orbital period. The host star, which has a *TESS* magnitude of 10.73 and is located 122 pc away, was observed with a 2-minute cadence in sector 4.

We begin by searching for all other stars within 10 pixels of the target star. This is shown in Figure 2.5, where the location of each nearby star relative to the local *TESS* pixels

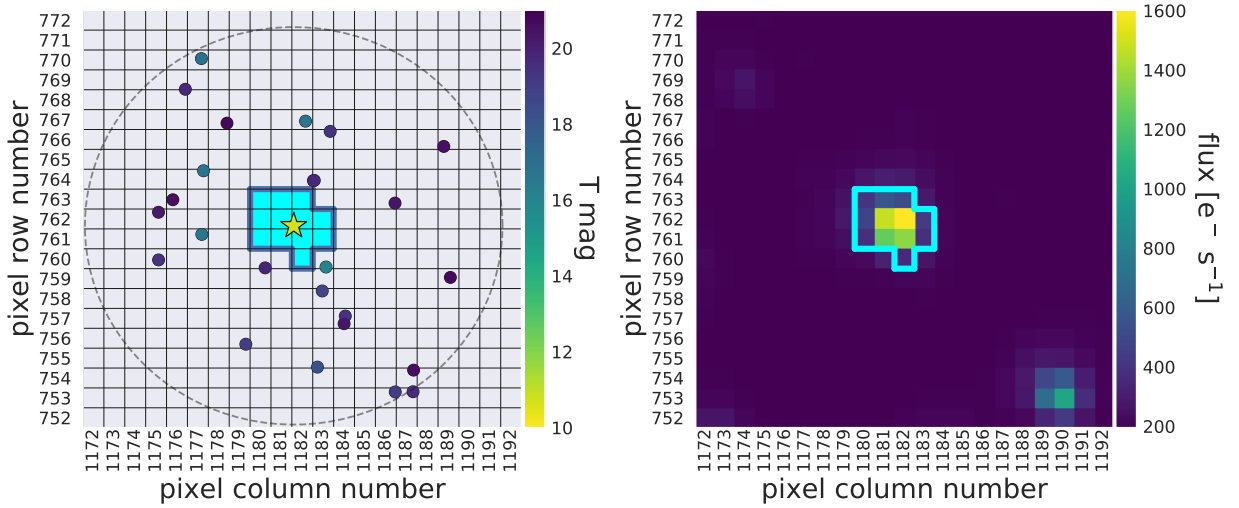

Figure 2.5: Visualization of TIC querying for TOI 465.01 (TIC 270380593). Left: All stars within 10 pixels of the target star (the limits of which are approximated by the black dashed line). The target star is located in the center pixel and is indicated by a star symbol. The aperture used to extract the light curve is highlighted in blue. Right: Time-averaged *TESS* image of the same pixels, with the same aperture overlaid.

is shown on the left and the corresponding *TESS* image is shown on the right. Next, we calculate the flux contribution of each star and determine which contribute enough flux to the aperture to produce a transit with the reported depth. In this case, the target star is the only star bright enough to host the signal. We therefore ignore NTP, NEB, and NEBx2P scenarios for the remainder of this analysis, which leaves 15 scenarios to be considered.

Next, we determine the best-fit model parameters for each of the 15 scenarios considered. The results of this step are displayed in Figure 2.6 and Table 2.2. Figure 2.6 shows the best-fit transit models for each scenario compared to the extracted *TESS* light curve. Table 2.2 shows the best-fit values for several transit model parameters. We see in both of these that the best-fitting scenario is the TP scenario.

The final step in the procedure is to calculate the relative probability of each scenario using Equation 2.3. These probabilities are shown in the right-most columns of Table 2.2. For this TOI, we find that FPP = 0.33 and NFPP = 0.0.

The above calculation was done assuming unresolved companions near the target star can be ruled out beyond 2.″2. However, if one is able to further constrain the separation beyond which an unresolved star could exist, this number can be decreased to that new separation. On 2019 July 10, we obtained adaptive optics (AO) assisted high-resolution images of this TOI with ShARCS/ShaneAO on the Shane 3-meter telescope at Lick Observatory, shown in Figure 2.7. These images were reduced using the steps outlined in Hirsch et al. (2019)

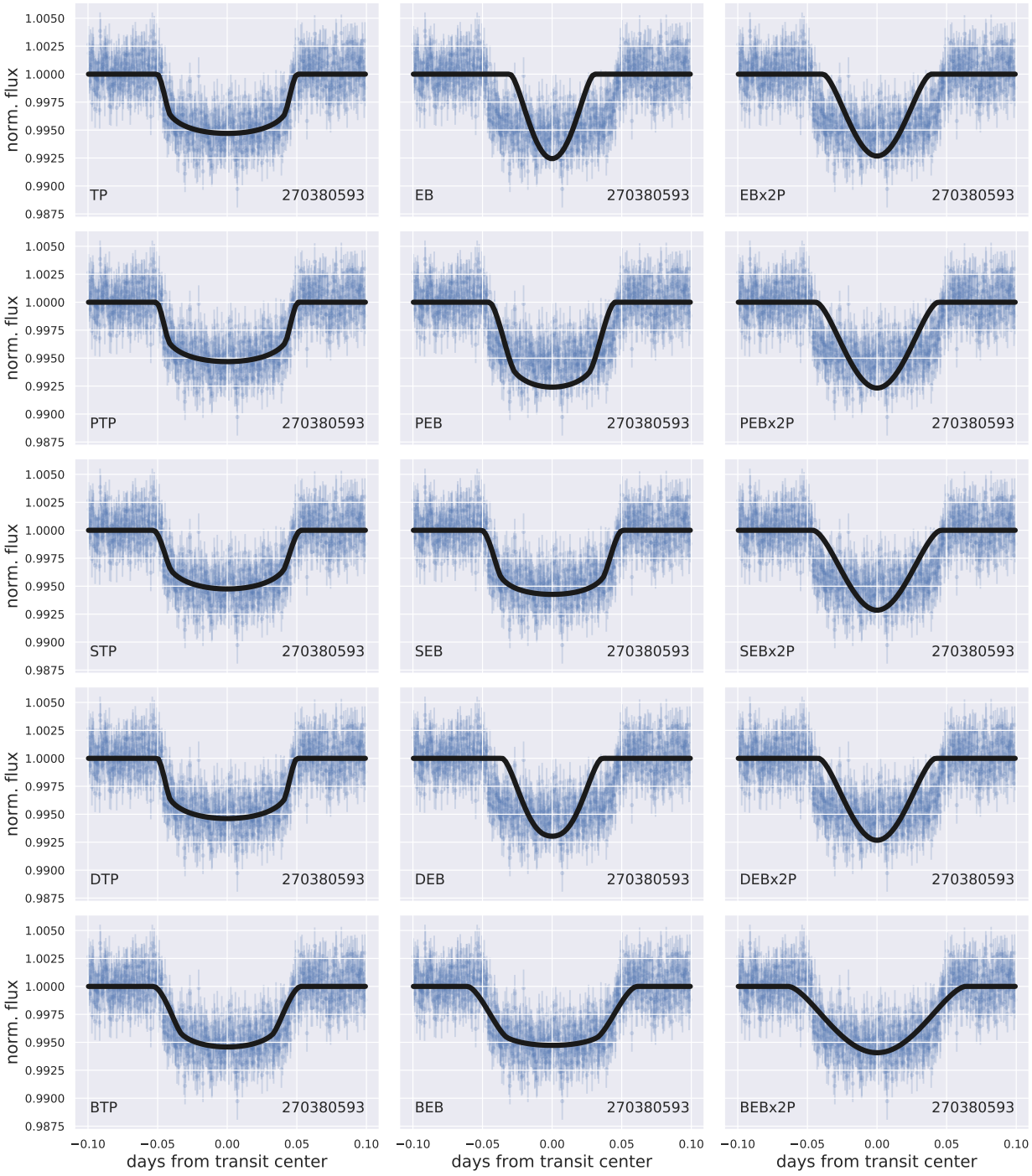

Figure 2.6: Fit of each transit scenario for TOI 465.01. The purple points are 2-minute cadence *TESS* data, while the black curves are the best-fit light curves. The scenario being fit for is in the bottom left of each panel, and the TIC ID of the star being fit for is in the bottom right of each panel.

Scenario	TIC ID	$M_\star$ ($M_\odot$)	$R_\star$ ($R_\odot$)	$P_{\rm orb}$ (days)	i (deg)	$R_{\rm p}$ ($R_\oplus$)	$R_{\rm EB}$ ($R_\odot$)	$\mathcal{P}_j$	$\mathcal{P}_j$ with AO
TP	270380593	0.81	0.85	3.84	87.3	6.27		0.39	0.61
EB	270380593	0.81	0.85	3.84	85.3		0.10	< 0.01	< 0.01
EBx2P	270380593	0.81	0.85	7.67	85.3		0.84	< 0.01	< 0.01
PTP	270380593	0.81	0.85	3.84	87.4	6.35		0.22	0.14
PEB	270380593	0.81	0.85	3.84	86.4		0.10	< 0.01	< 0.01
PEBx2P	270380593	0.81	0.85	7.67	85.4		0.83	< 0.01	< 0.01
STP	270380593	0.79	0.82	3.84	87.8	8.71		0.31	0.19
SEB	270380593	0.63	0.65	3.84	89.8		0.10	0.01	< 0.01
SEBx2P	270380593	0.48	0.49	7.67	87.3		0.49	< 0.01	< 0.01
DTP	270380593	0.81	0.85	3.84	87.5	6.26		0.06	0.06
DEB	270380593	0.81	0.85	3.84	85.7		0.10	< 0.01	< 0.01
DEBx2P	270380593	0.81	0.85	7.67	85.3		0.83	< 0.01	< 0.01
BTP	270380593	0.55	0.48	3.84	89.3	19.36		< 0.01	< 0.01
BEB	270380593	0.81	0.75	3.84	89.7		0.19	< 0.01	< 0.01
BEBx2P	270380593	0.83	1.01	7.67	85.4		0.85	< 0.01	< 0.01
TIC*	270380593	$0.81^{+0.10}_{-0.10}$	$0.85^{+0.06}_{-0.06}$						
WASP-156b**	270380593	$0.84^{+0.05}_{-0.05}$	$0.76^{+0.03}_{-0.03}$		$89.1^{+0.6}_{-0.9}$	$5.72^{+0.22}_{-0.22}$			

Table 2.2: The probability of each scenario j ($\mathcal{P}_j$) for TOI 465.01. * Host star properties from version 8 of the TIC (Stassun et al. 2018b). ** Best-fit host star and planet properties from Demangeon et al. (2018).

and Savel et al. (2020), which we refer the reader to for more information. With these observations, we produce a contrast curve (also shown in Figure 2.7) that can be folded in to the `TRICERATOPS` analysis in order to further constrain the probabilities of scenarios involving unresolved companions.

To show how this changes the results of our tool, we repeat the calculation with this constraint applied. The impact that this AO follow-up has on the probability of each scenario is shown in the right-most column of Table 2.2, which now yields FPP = 0.19.

TIC 438490744 (TOI 529.01)

We also apply our algorithm on TOI 529.01, a candidate with a 1.67 day orbital period that has been ruled out as a NEB around the nearby star TIC 438490748 (see Section 2.5 for more details). The originally proposed host star is an M dwarf with a *TESS* magnitude of 14.14 and a distance of 63 pc away. This TOI was observed with a 2-minute cadence in sector 6.

We again begin by searching for all other stars within 10 pixels of the target star, as shown in Figure 2.8. After calculating the flux contribution due to each star, it is determined that two nearby stars, TIC 438490736 and TIC 438490748, contribute enough light to the aperture for them to host the observed transit. As a result, there are 21 scenarios to be considered for this TOI.

Figure 2.9 and Table 2.3 show the best-fit transits and transit model parameters for these scenarios, respectively. According to these results, the most probable scenario is the

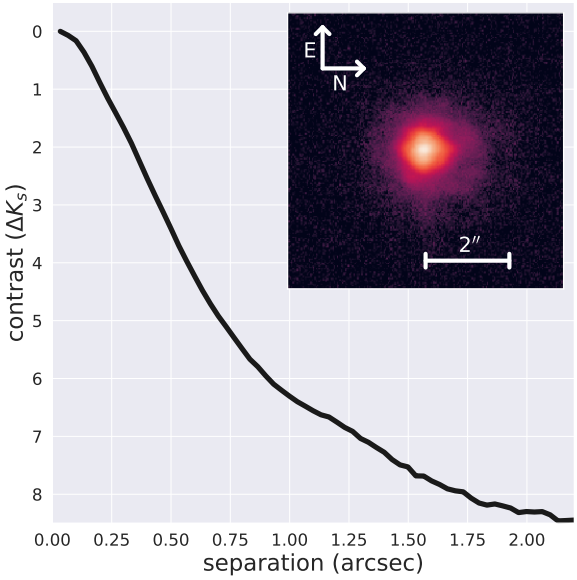

Figure 2.7: High-resolution image of TOI 465 obtained with ShARCS/ShaneAO in K_s band and corresponding contrast curve.

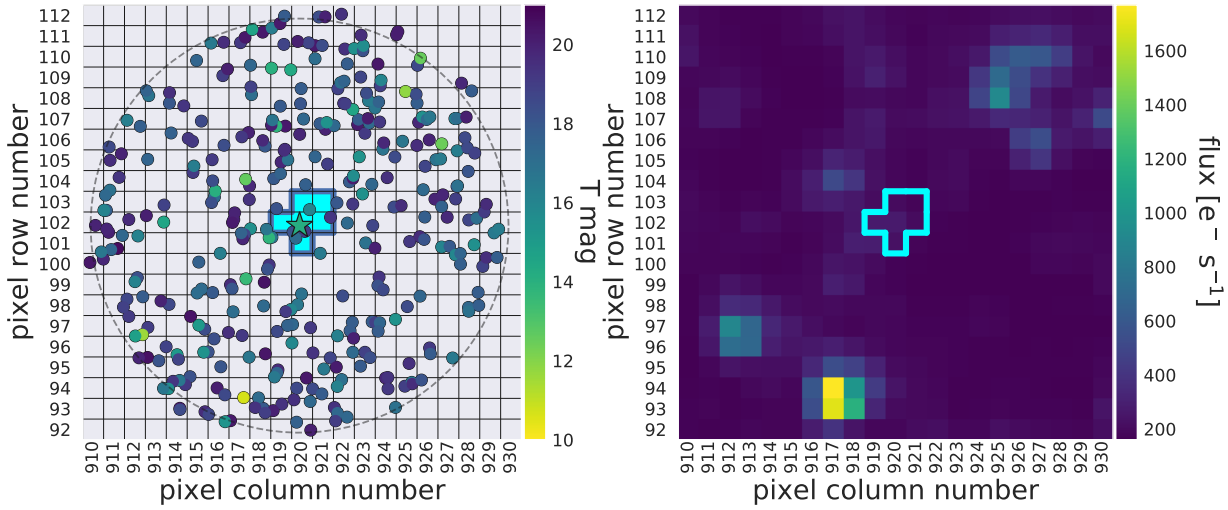

Figure 2.8: Visualization of TIC querying for TOI 529.01 (TIC 438490744). Left: All stars within 10 pixels of the target star (the limits of which are approximated by the black dashed line). The target star is located in the center pixel and is indicated by a star symbol. The aperture used to extract the light curve is highlighted in blue. Right: Time-averaged *TESS* image of the same pixels, with the same aperture overlaid.

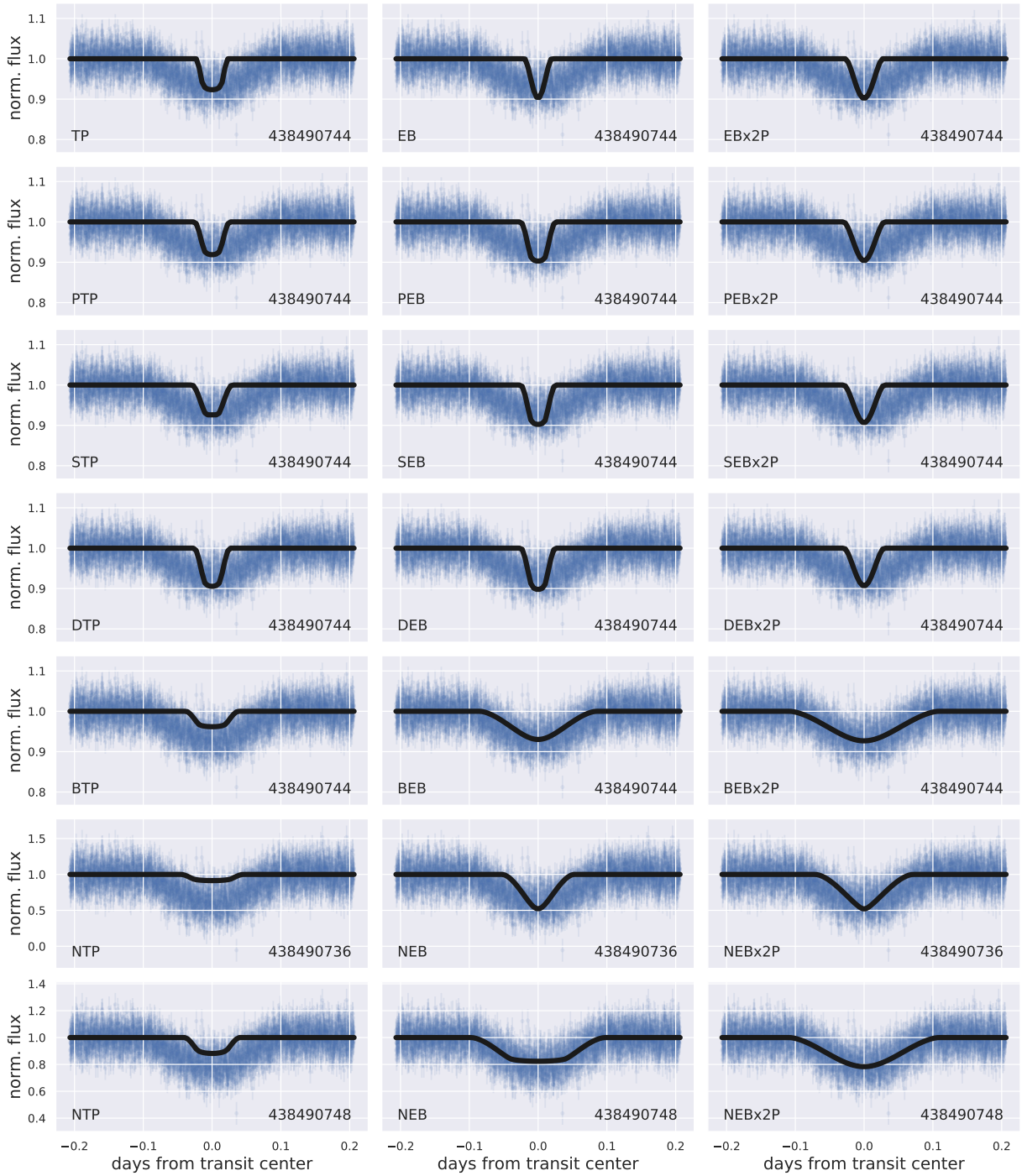

Figure 2.9: Fit of each transit scenario for TOI 529.01. The purple points are 2-minute cadence *TESS* data, while the black curves are the best-fit light curves. The scenario being fit for is in the bottom left of each panel, and the TIC ID of the star being fit for is in the bottom right of each panel.

Scenario	TIC ID	$M_\star$ ($M_\odot$)	$R_\star$ ($R_\odot$)	$P_{\rm orb}$ (days)	i (deg)	$R_{\rm p}$ ($R_\oplus$)	$R_{\rm EB}$ ($R_\odot$)	$\mathcal{P}_j$
TP	438490744	0.21	0.24	1.67	89.9	6.89		< 0.01
EB	438490744	0.21	0.24	1.67	86.6		0.10	< 0.01
EBx2P	438490744	0.21	0.24	3.33	87.3		0.24	< 0.01
PTP	438490744	0.21	0.24	1.67	90.0	8.61		< 0.01
PEB	438490744	0.21	0.24	1.67	89.5		0.10	< 0.01
PEBx2P	438490744	0.21	0.24	3.33	87.7		0.24	< 0.01
STP	438490744	0.09	0.10	1.67	89.2	19.70		< 0.01
SEB	438490744	0.18	0.22	1.67	89.7		0.10	< 0.01
SEBx2P	438490744	0.48	0.24	3.33	87.7		0.24	< 0.01
DTP	438490744	0.21	0.24	1.67	89.2	9.82		< 0.01
DEB	438490744	0.21	0.24	1.67	89.5		0.10	< 0.01
DEBx2P	438490744	0.21	0.24	3.33	87.7		0.24	< 0.01
BTP	438490744	0.51	0.45	1.67	89.8	19.92		< 0.01
BEB	438490744	1.05	1.42	1.67	89.6		1.05	< 0.01
BEBx2P	438490744	0.93	1.67	3.33	84.4		0.97	< 0.01
NTP	438490736	0.67	0.69	1.67	89.5	19.94		< 0.01
NEB	438490736	0.67	0.69	1.67	88.1		0.56	< 0.01
NEBx2P	438490736	0.67	0.69	3.33	89.5		0.69	< 0.01
NTP	438490748	0.51	0.45	1.67	89.7	19.98		< 0.01
NEB	438490748	1.12	1.75	1.67	89.8		0.76	0.06
NEBx2P	438490748	1.08	1.54	3.33	85.2		1.16	0.94
TIC*	438490744	$0.21^{+0.02}_{-0.02}$	$0.24^{+0.01}_{-0.01}$					

Table 2.3: The probability of each scenario j ($\mathcal{P}_j$) for TOI 529.01. * Host star properties from version 8 of the TIC (Stassun et al. 2018b).

NEBx2P scenario around the nearby star TIC 438490748. In fact, the preference for this scenario is so strong that this TOI has FPP > 0.99 and NFPP > 0.99.

2.4 Planet Vetting and Validation

In this section, we analyze the performance of `TRICERATOPS` by running it on several classified TOIs observed with both 2-minute cadence and 30-minute cadence observations. Using these results, we define the conditions a TOI must meet to be vetted and validated.

2-minute Cadence Data

We begin by running our code on TOIs identified in 2-minute cadence data collected by *TESS*. In the first two years of the *TESS* mission, these observations were collected for ∼200,000 nearby dwarfs stars across nearly the entire sky. These observations are processed by the *TESS* Science Processing Operations Center (SPOC) pipeline (Jenkins et al. 2016), which identifies TCEs and generates data validation reports that contain information useful for further vetting. These stars are then subjected to manual vetting by the *TESS* Science Office to compile a set of TOIs that consist of the TCEs with the best chances of being actual planets.

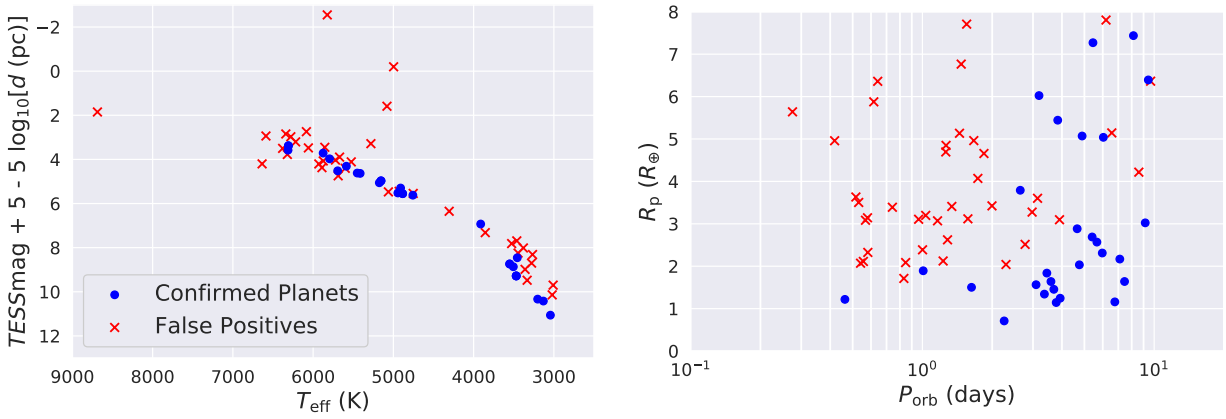

Figure 2.10: Host star (*left*) and planet (*right*) properties of confirmed planets and false positives used in our performance analysis. The sample includes systems with a diversity of host spectral types, planet orbital periods, and predicted planet radii (i.e., the best-fit radii from the TP scenario).

We use publicly available information from the *TESS* Follow-up Observation Program (TFOP) website[10] and 2-minute cadence *TESS* light curves from MAST to obtain the phase-folded light curves and apertures that we input into `TRICERATOPS` for each TOI. Because a key function of our algorithm is the identification of TOIs that are false positives around nearby stars, we use light curves extracted using simple aperture photometry instead of those processed with pre-data-conditioning step of the SPOC pipeline, which removes contamination and variability originating from nearby stars. In order to recreate the conditions under which one would use our tool on new TOIs, we only use data from the first sector in which each TOI is observed and restrict the analysis to TOIs with at least 3 transits.

In order to have a ground truth with which to compare the results of our algorithm, we restrict our sample of TOIs to those that have been designated as confirmed planets (CPs) and those that have been designated as false positives (FPs) by the TFOP. We also discard TOIs that have been designated FPs due to instrumental false alarms (which our tool does not test for), TOIs without estimates for $M_\star$, $R_\star$, and $T_{\rm eff}$ in the TIC, and TOIs for which we are unable to feasibly recover a transit with the purported orbital parameters. Lastly, we only include planets with best-fit planet radii $R_{\rm p} < 8R_\oplus$ under the TP scenario. This radius corresponds roughly to the minimum radius of a brown dwarf (e.g., Sorahana et al. 2013) and has been used as an upper limit in the size of objects that can be validated in past validation studies (e.g., Mayo et al. 2018), due to the fact that giant planets, brown dwarfs, and low-mass stars are typically indistinguishable based on radius alone. This leaves 68 TOIs in total, 28 of which are confirmed planets and 40 of which are false positives. The

[10]https://exofop.ipac.caltech.edu/tess/index.php

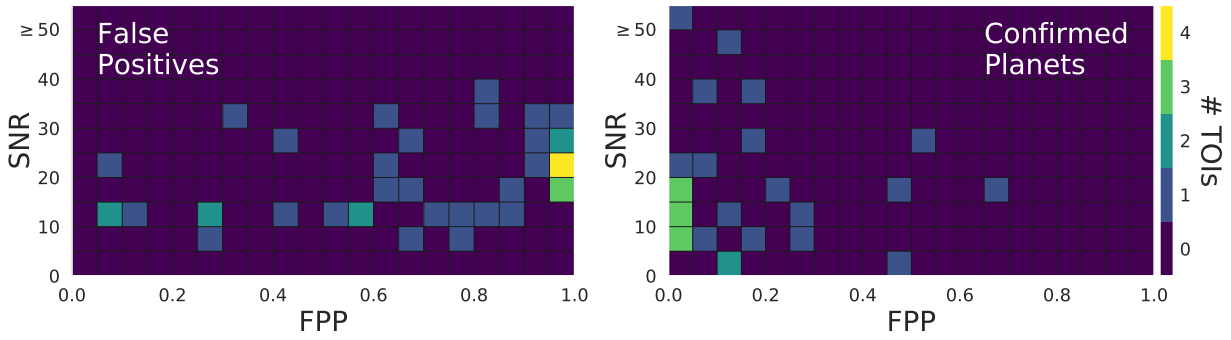

Figure 2.11: SNR vs FPP for all false positives (*left*) and confirmed planets (*right*) used in our performance analysis. Our tool performs better for TOIs with higher SNRs. `TRICERATOPS` performs best when SNR > 15.

system properties of these TOIs are displayed in Figure 2.10.

After generating light curves for these TOIs, we calculate the FPP and NFPP for each to determine the limits within which `TRICERATOPS` can be used reliably. First, we explore how our predictions depend on the signal-to-noise ratio (SNR) of the data. We define the SNR as

$$\mathrm{SNR} = \frac{\delta_{\mathrm{obs}}}{\sigma_{\mathrm{CDPP}}}\sqrt{n_{\mathrm{tra}}} \tag{2.17}$$

where δ_{obs} is the observed transit depth (i.e., not corrected for dilution from nearby stars), σ_{CDPP} is the combined differential photometric precision (CDPP; Christiansen et al. 2012) of the 2-minute cadence data, and n_{tra} is the number of observed transits. We calculate σ_{CDPP} by applying the `estimate_cdpp` method of `lightkurve` (Lightkurve Collaboration et al. 2018) over the duration of the transit. Because this quantity incorporates our confidence in the size of a transiting object and the overall density of data points in-transit, is should correlate with the ability of `TRICERATOPS` to characterize the shape of a given transit.

The results of this analysis are shown in Figure 2.11. For both CPs and FPs, `TRICERATOPS` generally has more accurate predictions when SNR is higher. Specifically, FPP alone does not appear to be a reliable predictor of TOI disposition when SNR < 15, where FPs are frequently assigned low values of FPP that would ideally be reserved for CPs.

Second, we explore how our algorithm performs when NFPP is also considered. Figure 2.12 shows the distribution of the TOIs in NFPP–FPP space for SNR < 15 (on the left) and SNR > 15 (on the right). In the figure, we differentiate TOIs that are CPs, TOIs that have been ruled out as FPs around nearby stars (nearby false positives, or NFPs), and TOIs that have been ruled out as FPs originating from the immediate vicinity of the target star (target false positives, or TFPs). The most salient feature of this figure is the region defined by NFPP $< 10^{-3}$ and FPP < 0.5 that contains nearly all of the CPs, none of the NFPs or

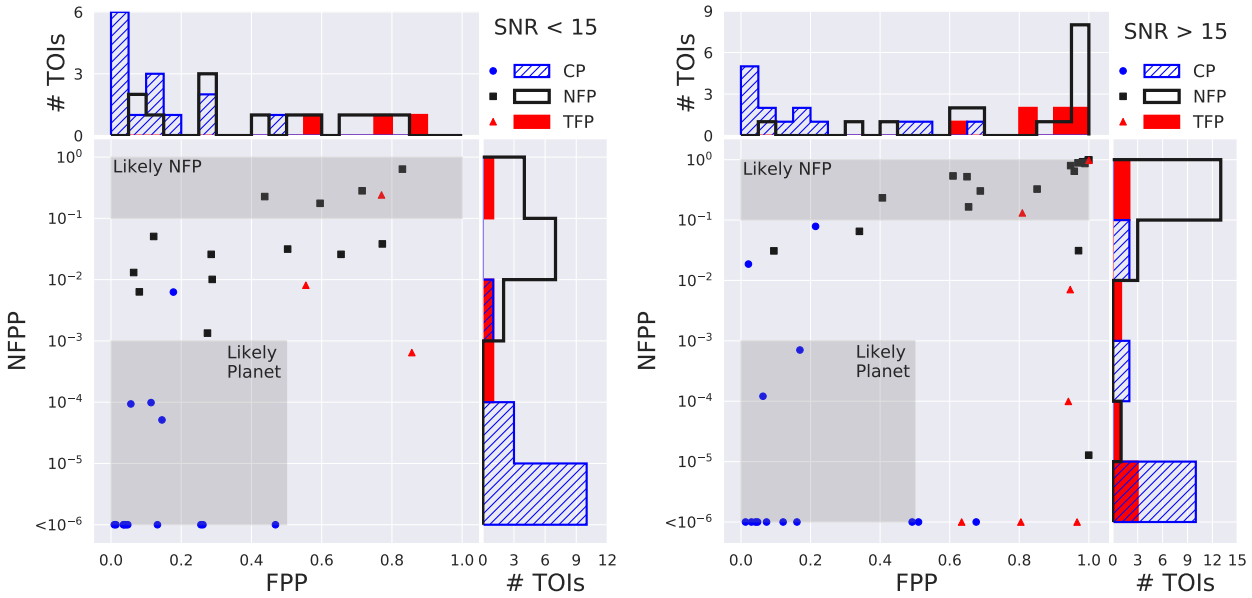

Figure 2.12: NFPP vs FPP for SNR < 15 (*left*) and SNR > 15 (*right*). We designate TOIs with NFPP $< 10^{-3}$ and FPP < 0.5 as likely planets. For TOIs with NFPP $< 10^{-3}$, and FPP ≤ 0.01, we are able to rule out FPs with a high enough confidence to consider them validated. Lastly, we are able to identify TOIs that are NFPs with high confidence when NFPP $> 10^{-1}$.

TFPs, and is independent of SNR. We designate TOIs that exist within this region as likely planets.

Another visible feature of Figure 2.12 is the pile-up of CPs in the region defined by NFPP $< 10^{-3}$ and FPP < 0.05. Because this region is representative of TOIs with the best chances of being bona fide planets, we use it as a guide in defining our criteria for validating planets. Typically, the standard for validating planets (e.g., with `VESPA`) is to achieve a FPP below 1%. We therefore define validated planets as TOIs with NFPP $< 10^{-3}$ and FPP < 0.015 (or FPP ≤ 0.01, when rounding to the nearest percent).

As a cross-check of the `TRICERATOPS` performance, we also calculate the FPPs of these TOIs in using `VESPA`. We run `VESPA` using the coordinates, stellar photometry (*TESS* mag, Bmag, Vmag, Jmag, Hmag, and Kmag), $T_{\rm eff}$, $\log g$, and parallax listed for each TOI in the TIC. We use the same transit data used in our `TRICERATOPS` runs and assume a maximum unresolved star separation of 2.″2. The FPPs obtained with `VESPA` are compared to the FPPs obtained with `TRICERATOPS` in Figure 2.13, where we see both similarities and differences between the two tools. First, TOIs that score FPP < 0.2 with `VESPA` tend to also score FPP < 0.2 with `TRICERATOPS`. For both tools, nearly all of these low FPP TOIs are confirmed planets. We also notice that, in general, `TRICERATOPS` returns higher values of FPP than

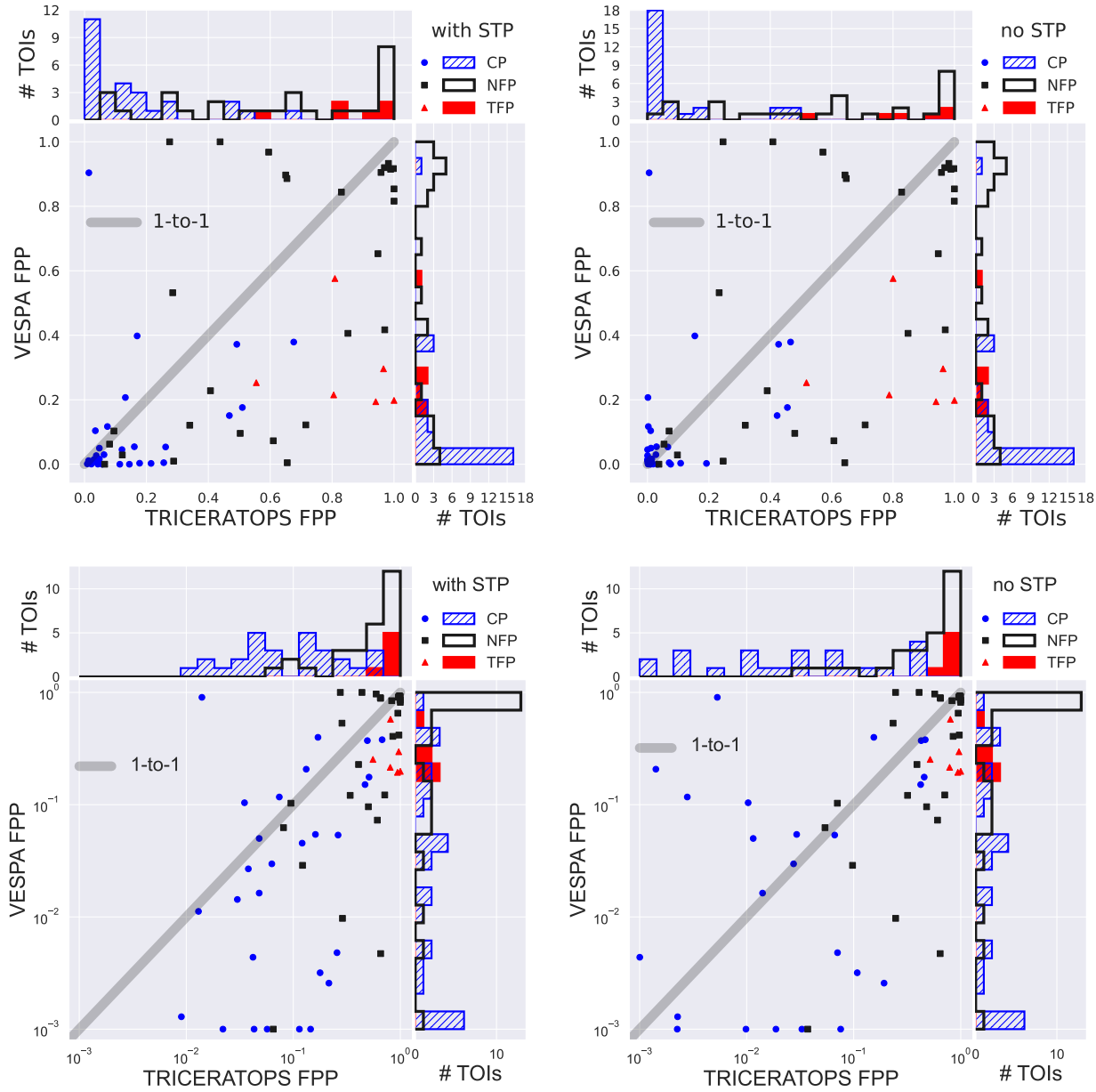

Figure 2.13: `VESPA` FPP vs `TRICERATOPS` FPP for the TOIs in Figure 2.12. *Left:* Comparison with the STP scenario included in the `TRICERATOPS` calculation. *Right:* Comparison without the STP scenario included in the `TRICERATOPS` calculation. The bottom panels are the same as the top panels, but are shown with a log scale.

`VESPA` does (i.e., most points lie below the 1-to-1 line). This is because `TRICERATOPS` tests more false positive scenarios than `VESPA` does. Specifically, `VESPA` does not test for the STP scenario or any of the nearby false positive scenarios (i.e., NTP, NEB, and NEBx2P). As a consequence, many of the FPs analyzed with `VESPA` surpass the threshold for validation (FPP < 0.01) despite not being planets. Because it accounts for additional FP scenarios, `TRICERATOPS` is more conservative, and is less likely to validate false positives. Lastly, it is clear that there are significant deviations between the results of the two tools at larger values of FPP (i.e., the points do not lie directly on the 1-to-1 line). These deviations are expected, and can simply be attributed to differences in how the two codes calculate FPP (after all, if they gave the exact same results, there would not be a need for a new tool). The most important thing is that the two tools agree in the low-FPP regime, where planets are validated, so candidates in the high-FPP regime are not of large concern.

To more closely examine the impact of including additional scenarios in `TRICERATOPS`, we repeat this comparative analysis with the STP scenario excluded from `TRICERATOPS`. These results are shown in the right-hand panels of 2.13. While the impact is small, the removal of the STP scenario leads to a general decrease in `TRICERATOPS` FPP. This is most clearly visible in the bottom panels of the figure, which show the data in log scale. Namely, we see that many planets that only achieved FPP < 0.01 with `VESPA` in the original comparison now achieve validation with both tools.

30-minute Cadence Data

One might expect our code to have a more difficult time distinguishing CPs from FPs when using data with a longer cadence, as they would yield fewer points with which to characterize the shape of the transit. To test this, we also run our code on 30-minute cadence light curves of the same TOIs. We use `eleanor` (Feinstein et al. 2019) to extract these light curves from *TESS* Full Frame Images (FFIs) within the same sectors and apertures used to obtain the 2-minute cadence light curves.[11]

In Figure 2.14, we show how SNR affects the new FPP calculations. As in the previous section, `TRICERATOPS` is able to correctly identify CPs and FPs more frequently when SNR is high, but the correlation is weaker overall. Specifically, the FPPs of CPs are less concentrated near zero here than those calculated with the 2-minute data.

In Figure 2.15, we reproduce the NFPP vs FPP analysis from the previous section using the 30-minute cadence data. We again see that most CPs are contained within a region defined by NFPP $< 10^{-3}$ and FPP < 0.5, with very few FPs also falling within this region. Specifically, the region contains 18 CPs and only 2 FPs. In addition, almost no CPs have a FPP > 0.7 (with the exception of one, which is mistaken for a nearby false positive), which implies that a high FPP is still indicative of actual FPs. We thus again designate TOIs with NFPP $< 10^{-3}$ and FPP < 0.5 as likely planets. However, unlike the results obtained

[11]More precisely, we run our code on 67 of the 68 TOIs analyzed in the previous section. We were unable to recover the FFI data for TOI 1796.01 (the TOI with the highest SNR in Figure 2.11) due to a bug in `eleanor`, which returns a error claiming that the TOI has not yet been observed upon searching for its data.

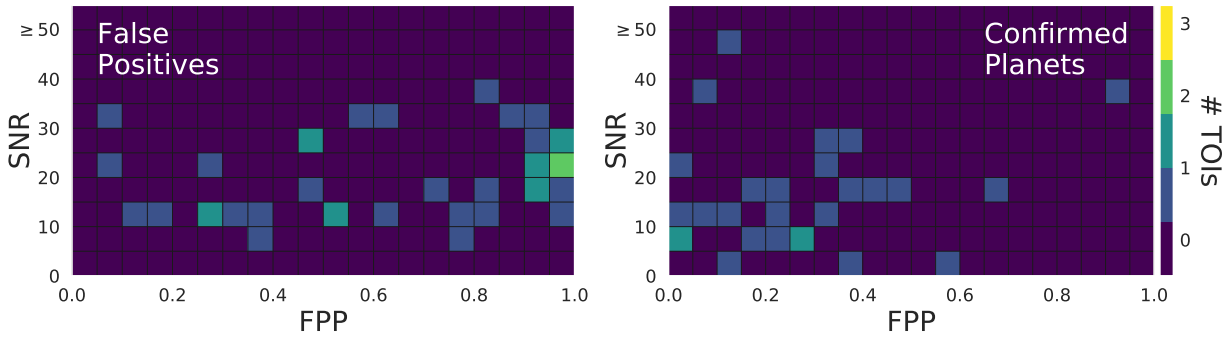

Figure 2.14: SNR vs FPP for the same false positives (*left*) and confirmed planets (*right*) shown in Figure 2.11, but calculated using light curves extracted from 30-minute cadence *TESS* data. While there still appears to be a correlation between SNR and performance, it is less clear here than in Figure 2.11.

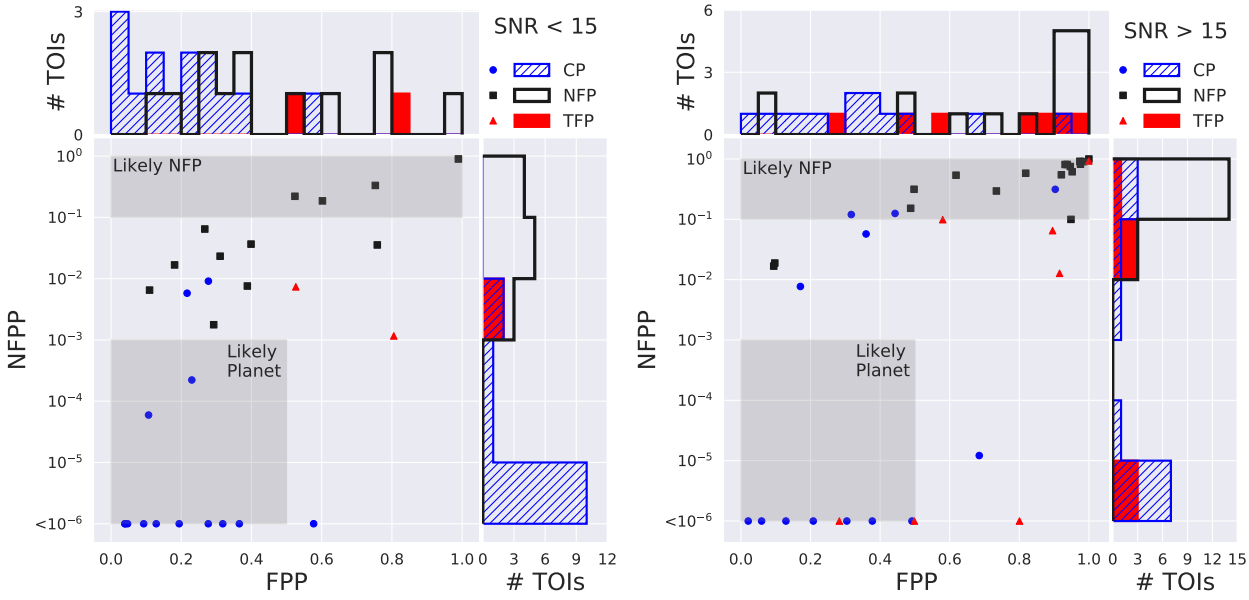

Figure 2.15: NFPP vs FPP for SNR < 15 (*left*) and SNR > 15 (*right*), but calculated using 30-minute cadence *TESS* data. While we are unable to identify a region in which we can validate TOIs, we can still designate TOIs with NFPP $< 10^{-3}$ and FPP < 0.5 as likely planets. Additionally, we are still able to identify TOIs that are NFPs with high confidence when NFPP $> 10^{-1}$.

with the 2-minute cadence data, there does not appear to be a region of parameter space in which planets can be confidently validated. Nonetheless, `TRICERATOPS` results involving long cadence *TESS* data are useful for vetting TOIs and prioritizing them for follow-up observations to further investigate the nature of the signal.

2.5 Nearby False Positive Identification

In addition to its ability to identify likely planets and validate TOIs, `TRICERATOPS` is proficient at identifying NFPs. In Figures 2.12 and 2.15, TOIs with a NFPP $> 10^{-1}$ are NFPs 85% and 82% of the time, respectively. Additionally, the region defined by NFPP $> 10^{-1}$ contains over half of the NFPs in our sample for calculations conducted using both 2-minute and 30-minute data. These results suggest that `TRICERATOPS` can be used to predict which TOIs are NFPs and to determine which nearby stars have the highest probability of hosting the observed transit. We therefore classify TOIs in this region of parameter space as likely NFPs.

As an additional step to assess the ability of our tool to identify NFPs, we compile a set of observations collected by members of *TESS* Follow-up Observing Program (TFOP)[12] Sub Group 1 (SG1) that rule out 30 TOIs as NFPs. The follow-up observations were scheduled using the `TESS Transit Finder`, which is a customized version of the `Tapir` software package (Jensen 2013). Below, we outline these observations and compare the empirical results with the NFPPs predicted by `TRICERATOPS` using 2-minute cadence data. A summary of these targets is given in Table 2.4 and details about the facilities used are given in Table 3.8.

Another method of discerning NFPs is by searching for centroid offsets in the *TESS* pixels encompassing a TOI. Often times, the true source of a NFP can be identified using the magnitude and direction of these offsets. In addition to the observations collected by TFOP SG1, we compare our `TRICERATOPS` predictions with the difference image centroiding analyses for these TOIs in their SPOC data validation reports (Twicken et al. 2018).

With these comparisons, we display that `TRICERATOPS` often yields similar results to both follow-up observations and predictions made using centroid offsets. For several of these TOIs (17/30), our tool assigns a NFPP high enough to classify them as likely NFPs. For those that do not meet this criterion, FPP and NFPP are high enough to rule out the possibility of the TOI being a planet. Lastly, in cases where there are several NFP candidates (of which there are 28), `TRICERATOPS` is frequently (10/28) able to predict which nearby star is the true host of the transit signal.

TIC 260043723 (TOI 217.01)

TFOP SG1 confirms the true host of the signal is TIC 260043722. Previous HAT South data suggested that this TOI is a NEB, which was confirmed by PEST Observatory R_C-band observations with a depth of 200 ppt. This star was also correctly identified as the

[12] https://tess.mit.edu/followup

Target TIC ID	TOI Number	TFOP SG1 Disposition	True Host TIC ID	FPP	Total NFPP	True Host NFPP	# NFP Candidates	True Host Rank
260043723	217.01	NEB	260043722	0.0806	0.0063	0.0059	2	1
279740441	273.01	NEB	279740439	0.6095	0.5377	0.2041	2	2
250386181	390.01	NEB	250386182	0.9703	0.0311	0.0311	2	1
219388773	399.01	NEB	219388775	0.2882	0.0101	0.0101	1	1
176778112	408.01	NEB	176778114	0.3405	0.0650	0.0438	2	1
20178111	467.01	NEB	20178112	0.4065	0.2332	0.1638	3	1
427352241	485.01	NEB	427352247	0.6498	0.5219	0.0693	3	2
108645766	497.01	NEB	108645800	0.8299	0.6361	-	4	-
274138511	506.01	NEB	760244235	0.1215	0.0507	0.0030	10	6
431999925	513.01	NEB	431999916	0.9819	0.9230	0.1482	8	2
438490744	529.01	NEB	438490748	1.0000	0.9938	0.9938	2	1
302895996	531.01	NEB	302895984	0.9477	0.7971	0.0509	5	3
53593457	543.01	NEB	53593470	0.9580	0.6436	-	5	-
59003115	556.01	NEB	59003118	0.2854	0.0258	0.0050	2	2
1133072	566.01	NEB	830310300	0.9687	0.8854	0.0124	9	6
146463781	636.01	NEB	146463868	0.9887	0.8640	-	3	-
432008938	643.01	NEB	432008934	0.9996	0.00001	-	2	-
54085154	662.01	NEB	54085149	0.2747	0.0013	0.0008	2	1
147660201	670.01	NPC	147660207	0.6543	0.1652	0.0868	9	1
391821647	708.01	NEB	$\sim 35''$ W	0.5955	0.1760	-	141	-
373424049	742.01	NEB	373424060	0.4377	0.2268	0.0006	31	23
271596418	868.01	NEB	271596416	0.6551	0.0259	0.0078	7	1
364107753	909.01	NEB	1310226289	0.0645	0.0131	0.0068	4	1
253990973	1061.01	NEB	253985122	0.5030	0.0315	0.0037	9	4
308034948	1206.01	NEB	unknown	0.7727	0.0383	-	108	-
274762761	1256.01	NEB	274762865	0.9981	0.9869	-	6	-
267561446	1284.01	NEB	267561450	0.7151	0.2818	0.0235	13	4
274662200	1285.01	NEB	274662220	0.6880	0.3031	0.0501	21	2
408203470	1289.01	NEB	408203452	0.8512	0.3258	0.1435	10	1
233681149	1340.01	NEB	233681148	0.0947	0.0309	0.0309	1	1

Table 2.4: TFOP SG1 false-positive identification compared to `TRICERATOPS` predictions. "Total NFPP" is the total NFPP for the TOI. "True Host NFPP" is the NFPP for only the true host of the signal. "# NFP Candidates" is the number of nearby sources bright enough to host the signal. "True Host Rank" is the rank of the true host NFPP, compared to the NFPPs of all other NFP candidates (where a rank of 1 corresponds to the highest NFPP).

host of the signal by the SPOC centroid offset analysis. `TRICERATOPS` identifies 2 nearby sources other than the target star bright enough to host the signal, one of which is TIC 260043722. The total NFPP calculated by `TRICERATOPS` is 0.0063. TIC 260043722 has a NFPP of 0.0059, making it the most probable NFP host. This NFPP is too low to classify the TOI as a likely NFP and too high to classify the TOI as a likely planet. In addition, the calculated FPP of 0.0806 is too high to classify the TOI as a validated planet.

TIC 279740441 (TOI 273.01)

TFOP SG1 confirms the true host of the signal is TIC 279740439. The signal was a nearby planet candidate (signal not on the original TOI, but still possibly planetary) based on

Observatory	Location	Aperture (m)	Pixel scale (arcsec)	FOV (arcmin)
Univ. Louisville Moore Obs. / CDK20N	Louisville, KY, US	0.51	0.54	37×37
Univ. Louisville Manner Telescope	Mt. Lemmon, AZ, US	0.61	0.39	26×26
Mt. Kent Observatory / CDK700	Toowoomba, Australia	0.7	0.4	27×27
Hazelwood Observatory	Churchill, Victoria, Australia	0.318	0.55	20×13.5
LCOGT 0.4m	(various)	0.4	0.57	29.2×19.5
LCOGT 1.0m	(various)	1.0	0.39	26.5×26.5
Fred L. Whipple Obs. / MEarth-North	Amado, AZ, USA	0.4	0.76	26×26
Tel. Carlos Sánchez / MuSCAT2	Teide Obs., Tenerife, Spain	1.52	0.44	7.4×7.4
El Sauce Observatory	Coquimbo Province, Chile	0.36	1.47	18.8×12.5
Perth Exoplanet Survey Telescope (PEST)	Perth, Australia	0.3	1.2	31×21
HATNet	(various)	0.11	14	492×492
HAT-South	(various)	0.18	3.7	492×492
TRAPPIST-South	La Silla, Chile	0.6	0.6	22×22
Steward Observatory Phillips Telescope	Mt. Lemmon, AZ, US	0.6	0.38	26×26

Table 2.5: Facilities used for TFOP SG1 followup.

observations from the TRAPPIST telescope that show a depth of 40 ppt in a custom $I + z$-band filter. Later observations with LCOGT (Brown et al. 2013) showed a V-band depth of 30 ppt on the nearby candidate; the wavelength-dependent eclipse depth indicates that it is an eclipsing binary. This star was also correctly identified as the host of the signal by the SPOC centroid offset analysis. `TRICERATOPS` identifies 2 nearby sources other than the target star bright enough to host the signal, one of which is TIC 279740439. The total NFPP calculated by `TRICERATOPS` is 0.5377. TIC 279740439 has a NFPP of 0.2041, making it the 2nd most probable NFP host. This NFPP is high enough to classify the TOI as a likely NFP. In addition, the calculated FPP of 0.6095 is too high to classify the TOI as a likely planet or validated planet.

TIC 250386181 (TOI 390.01)

TFOP SG1 confirms the true host of the signal is TIC 250386182. The TOI is a NEB, based on LCOGT observations in the PanSTARRS zs filter showing a depth of roughly 350 ppt. This star was also correctly identified as the host of the signal by the SPOC centroid offset analysis. `TRICERATOPS` identifies 2 nearby sources other than the target star bright enough to host the signal, one of which is TIC 250386182. The total NFPP calculated by `TRICERATOPS` is 0.0311. TIC 250386182 has a NFPP of 0.0311, making it the most probable NFP host. This NFPP is too low to classify the TOI as a likely NFP. However, the calculated FPP of 0.9703 is too high to classify the TOI as a likely planet or validated planet.

TIC 219388773 (TOI 399.01)

TFOP SG1 confirms the true host of the signal is TIC 219388775. The TOI is a NEB with depth of 130 ppt, based on LCOGT zs observations. This star was also correctly identified as the host of the signal by the SPOC centroid offset analysis. `TRICERATOPS` identifies 1

nearby source other than the target star bright enough to host the signal, which is TIC 219388775. The total NFPP calculated by `TRICERATOPS` is 0.0101. TIC 219388775 has a NFPP of 0.0101, making it the most probable NFP host. This NFPP is too low to classify the TOI as a likely NFP and too high to classify the TOI as a likely planet. In addition, the calculated FPP of 0.2882 is too high to classify the TOI as a validated planet.

TIC 176778112 (TOI 408.01)

TFOP SG1 confirms the true host of the signal is TIC 176778114. The TOI is a NEB with primary and secondary eclipse depths of $\sim$ 430 ppt and $\sim$ 300 ppt in LCOGT r' observations. This star was also correctly identified as the host of the signal by the SPOC centroid offset analysis. `TRICERATOPS` identifies 2 nearby sources other than the target star bright enough to host the signal, one of which is TIC 176778114. The total NFPP calculated by `TRICERATOPS` is 0.0650. TIC 176778114 has a NFPP of 0.0438, making it the most probable NFP host. This NFPP is too low to classify the TOI as a likely NFP and too high to classify the TOI as a likely planet. In addition, the calculated FPP of 0.3405 is too high to classify the TOI as a validated planet.

TIC 20178111 (TOI 467.01)

TFOP SG1 confirms the true host of the signal is TIC 20178112. The TOI is a NEB, based on PEST Observatory R_C observations that show a $\sim$ 55 ppt eclipse on TIC 20178112, which *Gaia* shows as two stars with magnitudes $G = 14.2$ and $G = 15.9$. This star was also correctly identified as the host of the signal by the SPOC centroid offset analysis. `TRICERATOPS` identifies 3 nearby sources other than the target star bright enough to host the signal, one of which is TIC 20178112. The total NFPP calculated by `TRICERATOPS` is 0.2332. TIC 20178112 has a NFPP of 0.1638, making it the most probable NFP host. This NFPP is high enough to classify the TOI as a likely NFP. In addition, the calculated FPP of 0.4065 is too high to classify the TOI as a validated planet.

TIC 427352241 (TOI 485.01)

TFOP SG1 confirms the true host of the signal is TIC 427352247. The TOI is a NEB, based on LCOGT r' observations that show a 200 ppt, V-shaped eclipse. This star was also correctly identified as the host of the signal by the SPOC centroid offset analysis. `TRICERATOPS` identifies 3 nearby sources other than the target star bright enough to host the signal, one of which is TIC 427352247. The total NFPP calculated by `TRICERATOPS` is 0.5219. TIC 427352247 has a NFPP of 0.0693, making it the 2nd most-probably NFP host. This NFPP is high enough to classify the TOI as a likely NFP. In addition, the calculated FPP of 0.6498 is too high to classify the TOI as a likely planet or validated planet.

TIC 108645766 (TOI 497.01)

TFOP SG1 confirms the true host of the signal is TIC 108645800. The TOI is a NEB, based on LCOGT r' observations with a depth of at least 100 ppt, and confirmed by archival HAT South data. This star was also correctly identified as the host of the signal by the SPOC centroid offset analysis. `TRICERATOPS` identifies 4 nearby sources other than the target star bright enough to host the signal, one of which is TIC 108645800. The total NFPP calculated by `TRICERATOPS` is 0.6361, but the NFPP around TIC 108645800 was not calculated due to unknown stellar parameters. This NFPP is high enough to classify the TOI as a likely NFP. In addition, the calculated FPP of 0.8299 is too high to classify the TOI as a likely planet or validated planet.

TIC 274138511 (TOI 506.01)

TFOP SG1 confirms the true host of the signal is TIC 760244235. The TOI is a NEB with depth of at least 200 ppt, based on LCOGT r' observations. This star was also correctly identified as the host of the signal by the SPOC centroid offset analysis. `TRICERATOPS` identifies 10 nearby sources other than the target star bright enough to host the signal, one of which is TIC 760244235. The total NFPP calculated by `TRICERATOPS` is 0.0507. TIC 760244235 has a NFPP of 0.0030, making it the 6th most probable NFP host. This NFPP is too low to classify the TOI as a likely NFP and too high to classify the TOI as a likely planet. In addition, the calculated FPP of 0.1215 is too high to classify the TOI as a validated planet.

TIC 431999925 (TOI 513.01)

TFOP SG1 confirms the true host of the signal is TIC 431999916. The TOI is a NEB with depth of at least 90 ppt, based on LCOGT i' observations. This star was also correctly identified as the host of the signal by the SPOC centroid offset analysis. `TRICERATOPS` identifies 8 nearby sources other than the target star bright enough to host the signal, one of which is TIC 431999916. The total NFPP calculated by `TRICERATOPS` is 0.9230. TIC 431999916 has a NFPP of 0.1482, making it the 2nd most probable NFP host. This NFPP is high enough to classify the TOI as a likely NFP. In addition, the calculated FPP of 0.9819 is too high to classify the TOI as a likely planet or validated planet.

TIC 438490744 (TOI 529.01)

TFOP SG1 confirms the true host of the signal is TIC 438490748. The TOI is a NEB with depth of $\sim$ 80 ppt, based on K2 and HAT-South data. TIC 438490748 (the source of the signal) is a pair of stars in *Gaia*, so the true depth may be deeper. This star was also correctly identified as the host of the signal by the SPOC centroid offset analysis. `TRICERATOPS` identifies 2 nearby sources other than the target star bright enough to host

the signal, one of which is TIC 438490748. The total NFPP calculated by `TRICERATOPS` is 0.9938. TIC 438490748 has a NFPP of 0.9938, making it the most probable NFP host. This NFPP is high enough to classify the TOI as a likely NFP. In addition, the calculated FPP of 1.0 is too high to classify the TOI as a likely planet or validated planet.

TIC 302895996 (TOI 531.01)

TFOP SG1 confirms the true host of the signal is TIC 302895984. The TOI is a NEB with a depth of 200 ppt in the I band from LCOGT observations. This star was also correctly identified as the host of the signal by the SPOC centroid offset analysis. `TRICERATOPS` identifies 5 nearby sources other than the target star bright enough to host the signal, one of which is TIC 302895984. The total NFPP calculated by `TRICERATOPS` is 0.7971. TIC 302895984 has a NFPP of 0.0509, making it the 3rd most probable NFP host. This NFPP is high enough to classify the TOI as a likely NFP. In addition, the calculated FPP of 0.9477 is too high to classify the TOI as a likely planet or validated planet.

TIC 53593457 (TOI 543.01)

TFOP SG1 confirms the true host of the signal is TIC 53593470. The TOI is a NEB with a depth of ~ 250 ppt in both g' and i' in LCOGT observations. This star was also correctly identified as the host of the signal by the SPOC centroid offset analysis. `TRICERATOPS` identifies 5 nearby sources other than the target star bright enough to host the signal, one of which is TIC 53593470. The total NFPP calculated by `TRICERATOPS` is 0.6436, but the NFPP around TIC 53593470 was not calculated due to unknown stellar parameters. This NFPP is high enough to classify the TOI as a likely NFP. In addition, the calculated FPP of 0.9580 is too high to classify the TOI as a likely planet or validated planet.

TIC 59003115 (TOI 556.01)

TFOP SG1 confirms the true host of the signal is TIC 59003118. This is K2-78b (EPIC 210400751) (Crossfield et al. 2016), which was later shown to be an NEB (Cabrera et al. 2017). This star was also correctly identified as the host of the signal by the SPOC centroid offset analysis. `TRICERATOPS` identifies 2 nearby sources other than the target star bright enough to host the signal, one of which is TIC 59003118. The total NFPP calculated by `TRICERATOPS` is 0.0258. TIC 59003118 has a NFPP of 0.0050, making it the 2nd most probable NFP host. This NFPP is too low to classify the TOI as a likely NFP and too high to classify the TOI as a likely planet. In addition, the calculated FPP of 0.2854 is too high to classify the TOI as a validated planet.

TIC 1133072 (TOI 566.01)

TFOP SG1 confirms the true host of the signal is TIC 830310300. The TOI is a NEB, based on observations from LCOGT and Mt. Kent Observatory in i', and El Sauce Observatory in R_C. The depth is at least 500 ppt in i'. In this case, the SPOC centroid offset analysis failed to identify the presence of a background source at the 3σ level of significance. `TRICERATOPS` identifies 9 nearby sources other than the target star bright enough to host the signal, one of which is TIC 830310300. The total NFPP calculated by `TRICERATOPS` is 0.8854. TIC 830310300 has a NFPP of 0.0124, making it the 6th most probable NFP host. This NFPP is high enough to classify the TOI as a likely NFP. In addition, the calculated FPP of 0.9687 is too high to classify the TOI as a likely planet or validated planet.

TIC 146463781 (TOI 636.01)

TFOP SG1 confirms the true host of the signal is TIC 146463868. The TOI is a NEB, based on LCOGT I_C-band observations with a depth of 300 ppt. This star was also correctly identified as the host of the signal by the SPOC centroid offset analysis. `TRICERATOPS` identifies 3 nearby sources other than the target star bright enough to host the signal, one of which is TIC 146463868. The total NFPP calculated by `TRICERATOPS` is 0.8640, but the NFPP around TIC 146463868 was not calculated due to unknown stellar parameters. This NFPP is high enough to classify the TOI as a likely NFP. In addition, the calculated FPP of 0.9887 is too high to classify the TOI as a likely planet or validated planet.

TIC 432008938 (TOI 643.01)

TFOP SG1 confirms the true host of the signal is TIC 432008934. The TOI is a NEB, based on the centroid offset from the SPOC S01-S09 vetting report. `TRICERATOPS` identifies 2 nearby sources other than the target star bright enough to host the signal, but neither is TIC 432008934. The total NFPP calculated by `TRICERATOPS` is $1e-5$. This NFPP is too low to classify the TOI as a likely NFP. However, the calculated FPP of 0.9996 is too high to classify the TOI as a likely planet or validated planet.

TIC 54085154 (TOI 662.01)

TFOP SG1 confirms the true host of the signal is TIC 54085149. The TOI is a NEB, based on LCOGT i' observations that show a depth of 400 ppt at two different epochs. In this case, the SPOC centroid offset analysis found a significant offset, but the offset did not point directly to the true host. `TRICERATOPS` identifies 2 nearby sources other than the target star bright enough to host the signal, one of which is TIC 54085149. The total NFPP calculated by `TRICERATOPS` is 0.0013. TIC 54085149 has a NFPP of 0.0008, making it the most probable NFP host. This NFPP is too low to classify the TOI as a likely NFP and too high to classify

the TOI as a likely planet. In addition, the calculated FPP of 0.2747 is too high to classify the TOI as a validated planet.

TIC 147660201 (TOI 670.01)

TFOP SG1 confirms the true host of the signal is TIC 147660207. This candidate was retired from SG1 as nearby planet candidate. Observations show the true source of the signal to be a ~ 4 ppt event in the nearby star TIC 147660207, which is still an active planet candidate as of this writing. The event was seen in R_C from El Sauce Observatory, and in i' from Mt. Kent and Hazelwood Observatories. This star was also correctly identified as the host of the signal by the SPOC centroid offset analysis. `TRICERATOPS` identifies 9 nearby sources other than the target star bright enough to host the signal, one of which is TIC 147660207. The total NFPP calculated by `TRICERATOPS` is 0.1652. TIC 147660207 has a NFPP of 0.0868, making it the most probable NFP host. This NFPP is high enough to classify the TOI as a likely NFP. In addition, the calculated FPP of 0.6543 is too high to classify the TOI as a likely planet or validated planet.

TIC 391821647 (TOI 708.01)

TFOP SG1 confirms the TOI is a NFP. The TOI is a NEB, based on large scatter in the image centroid from sector to sector in a very crowded field, and a possible secondary eclipse. From the SPOC S01–S09 report, this is a clear NEB $\sim 35''$ west. Although the exact source of the NEB is not clear from the SPOC centroid offset analysis, it is likely too faint, and thus the event is too deep to be planetary. `TRICERATOPS` identifies 141 nearby sources other than the target star bright enough to host the signal. The total NFPP calculated by `TRICERATOPS` is 0.1760. This NFPP is high enough to classify the TOI as a likely NFP. In addition, the calculated FPP of 0.5955 is too high to classify the TOI as a likely planet or validated planet.

TIC 373424049 (TOI 742.01)

TFOP SG1 confirms the true host of the signal is TIC 373424060. The TOI is a NEB, based on LCOGT observations that show a depth of ~ 200 ppt in the zs filter. This star was also correctly identified as the host of the signal by the SPOC centroid offset analysis. `TRICERATOPS` identifies 31 nearby sources other than the target star bright enough to host the signal, one of which is TIC 373424060. The total NFPP calculated by `TRICERATOPS` is 0.2268. TIC 373424060 has a NFPP of 0.0006, making it the 23rd most probable NFP host. This NFPP is high enough to classify the TOI as a likely NFP. In addition, the calculated FPP of 0.4377 is too high to classify the TOI as a validated planet.

TIC 271596418 (TOI 868.01)

TFOP SG1 confirms the true host of the signal is TIC 271596416. The TOI is a NEB, based on LCOGT observations that show a depth of 70–100 ppt in zs and ~ 30 ppt in i'. This star was also correctly identified as the host of the signal by the SPOC centroid offset analysis. `TRICERATOPS` identifies 7 nearby sources other than the target star bright enough to host the signal, one of which is TIC 271596416. The total NFPP calculated by `TRICERATOPS` is 0.0259. TIC 271596416 has a NFPP of 0.0078, making it the most probable NFP host. This NFPP is too low to classify the TOI as a likely NFP and too high to classify the TOI as a likely planet. In addition, the calculated FPP of 0.6551 is too high to classify the TOI as a validated planet.

TIC 364107753 (TOI 909.01)

TFOP SG1 confirms the true host of the signal is TIC 1310226289. The TOI is a NEB, based on LCOGT observations that show a depth of at least 75 ppt in zs. This star was also correctly identified as the host of the signal by the SPOC centroid offset analysis. `TRICERATOPS` identifies 4 nearby sources other than the target star bright enough to host the signal, one of which is TIC 1310226289. The total NFPP calculated by `TRICERATOPS` is 0.0131. TIC 1310226289 has a NFPP of 0.0068, making it the most probable NFP host. This NFPP is too low to classify the TOI as a likely NFP and too high to classify the TOI as a likely planet. In addition, the calculated FPP of 0.0645 is too high to classify the TOI as a validated planet.

TIC 253990973 (TOI 1061.01)

TFOP SG1 confirms the true host of the signal is TIC 253985122. The TOI is a NEB, based on PEST Observatory R_C band observations with a depth of ~ 600 ppt. In this case, the SPOC centroid offset analysis failed to identify the presence of a background source at the 3σ level of significance. `TRICERATOPS` identifies 9 nearby sources other than the target star bright enough to host the signal, one of which is TIC 253985122. The total NFPP calculated by `TRICERATOPS` is 0.0315. TIC 253985122 has a NFPP of 0.0037, making it the 4th most probable NFP host. This NFPP is too low to classify the TOI as a likely NFP and too high to classify the TOI as a likely planet. In addition, the calculated FPP of 0.5030 is too high to classify the TOI as a likely planet or validated planet.

TIC 308034948 (TOI 1206.01)

TFOP SG1 confirms the TOI is a NEB. Stellar parameters from *Gaia* and TIC indicate $R_* > 40\ R_\odot$, but the orbital period of < 1 day would place the companion's orbit inside the star if it were on target. The SPOC centroid offset suggest that the signal originates from a star to the south. `TRICERATOPS` identifies 108 nearby sources other than the target

star bright enough to host the signal. The total NFPP calculated by `TRICERATOPS` is 0.0383. This NFPP is too low to classify the TOI as a likely NFP and too high to classify the TOI as a likely planet. In addition, the calculated FPP of 0.7727 is too high to classify the TOI as a likely planet or validated planet.

TIC 274762761 (TOI 1256.01)

TFOP SG1 confirms the true host of the signal is TIC 274762865. The TOI is a NEB, based on archival MEarth-North (Irwin et al. 2015; Nutzman and Charbonneau 2008) observations that show no event on target, and eclipses at the *TESS* ephemeris in a neighboring star. SPOC difference image analysis correctly identified this star as the true host. `TRICERATOPS` identifies 6 nearby sources other than the target star bright enough to host the signal, one of which is TIC 274762865. The total NFPP calculated by `TRICERATOPS` is 0.9869, but the NFPP around TIC 274762865 was not calculated due to unknown stellar parameters. This NFPP is high enough to classify the TOI as a likely NFP. In addition, the calculated FPP of 0.9981 is too high to classify the TOI as a likely planet or validated planet.

TIC 267561446 (TOI 1284.01)

TFOP SG1 confirms the true host of the signal is TIC 267561450. The TOI is a NEB, based on observations by the University of Louisville Manner Telescope and MuSCAT2 at Teide Observatory in g', r', i', and z' that show a $\sim$ 200 ppt eclipse. This star was also correctly identified as the host of the signal by the SPOC centroid offset analysis. `TRICERATOPS` identifies 13 nearby sources other than the target star bright enough to host the signal, one of which is TIC 267561450. The total NFPP calculated by `TRICERATOPS` is 0.2818. TIC 267561450 has a NFPP of 0.0235, making it the 4th most probable NFP host. This NFPP is high enough to classify the TOI as a likely NFP. In addition, the calculated FPP of 0.7151 is too high to classify the TOI as a likely planet or validated planet.

TIC 274662200 (TOI 1285.01)

TFOP SG1 confirms the true host of the signal is TIC 274662220. The TOI is a NEB, based on observations at the University of Louisville Manner Telescope that show a depth of 150 ppt in r'. This star was also correctly identified as the host of the signal by the SPOC centroid offset analysis. `TRICERATOPS` identifies 21 nearby sources other than the target star bright enough to host the signal, one of which is TIC 274662220. The total NFPP calculated by `TRICERATOPS` is 0.3031. TIC 274662220 has a NFPP of 0.0501, making it the 2nd most probable NFP host. This NFPP is high enough to classify the TOI as a likely NFP. In addition, the calculated FPP of 0.6880 is too high to classify the TOI as a likely planet or validated planet.

TIC 408203470 (TOI 1289.01)

TFOP SG1 confirms the true host of the signal is TIC 408203452. The TOI is a NEB, based on observations in a long-pass GG495 filter at the Steward Observatory Phillips 0.6m Telescope on Mount Lemmon that show a 35 ppt eclipse. Observations at the University of Louisville Moore Observatory show a depth of 60 ppt in r'. This star was also correctly identified as the host of the signal by the SPOC centroid offset analysis. `TRICERATOPS` identifies 10 nearby sources other than the target star bright enough to host the signal, one of which is TIC 408203452. The total NFPP calculated by `TRICERATOPS` is 0.3258. TIC 408203452 has a NFPP of 0.1435, making it the most probable NFP host. This NFPP is high enough to classify the TOI as a likely NFP. In addition, the calculated FPP of 0.8512 is too high to classify the TOI as a likely planet or validated planet.

TIC 233681149 (TOI 1340.01)

TFOP SG1 confirms the true host of the signal is TIC 233681148. The TOI is a NEB, based on SPOC S14–S16 reports that show a centroid offset to the closest star SW. Single pixel photometry on the *TESS* FFIs supports this conclusion. `TRICERATOPS` identifies 1 nearby source other than the target star bright enough to host the signal, which is TIC 233681148. The total NFPP calculated by `TRICERATOPS` is 0.0309. TIC 233681148 has a NFPP of 0.0309, making it the most probable NFP host. This NFPP is too low to classify the TOI as a likely NFP and too high to classify the TOI as a likely planet. In addition, the calculated FPP of 0.0947 is too high to classify the TOI as a validated planet.

2.6 Results

We apply our code to 384 SPOC TOIs that have neither been confirmed as bona fide planets nor rejected as false positives by TFOP. We again restrict our analysis to TOIs with $R_{\rm p} < 8R_{\oplus}$, TOIs with host stars that are well characterized in the TIC, and TOIs for which we are able to recover a transit with the purported orbital parameters. However, unlike the sample used in Section 2.4, we permit TOIs with orbital periods up to 50 days and extract their light curves using data from all sectors in which they were observed. The results of these calculations are displayed in Figure 2.16 and Table 2.7.

In the top panels of Figure 2.16, we show the host star and planet properties of all TOIs color-coded by FPP. In these panels, we see that TOIs with smaller radii and longer orbital periods tend to have lower FPPs. In the center panels of the figure, we show the same data color-coded by NFPP. In these panels, we again see a propensity for TOIs with smaller radii and longer orbital periods to have lower NFPPs. Nonetheless, there are several TOIs with large radii and short orbital periods that have low NFPP values, which generally represent TOIs without nearby stars bright enough to produce their observed transits. Additionally, we see that neither FPP nor NFPP is closely tied to host spectral type.

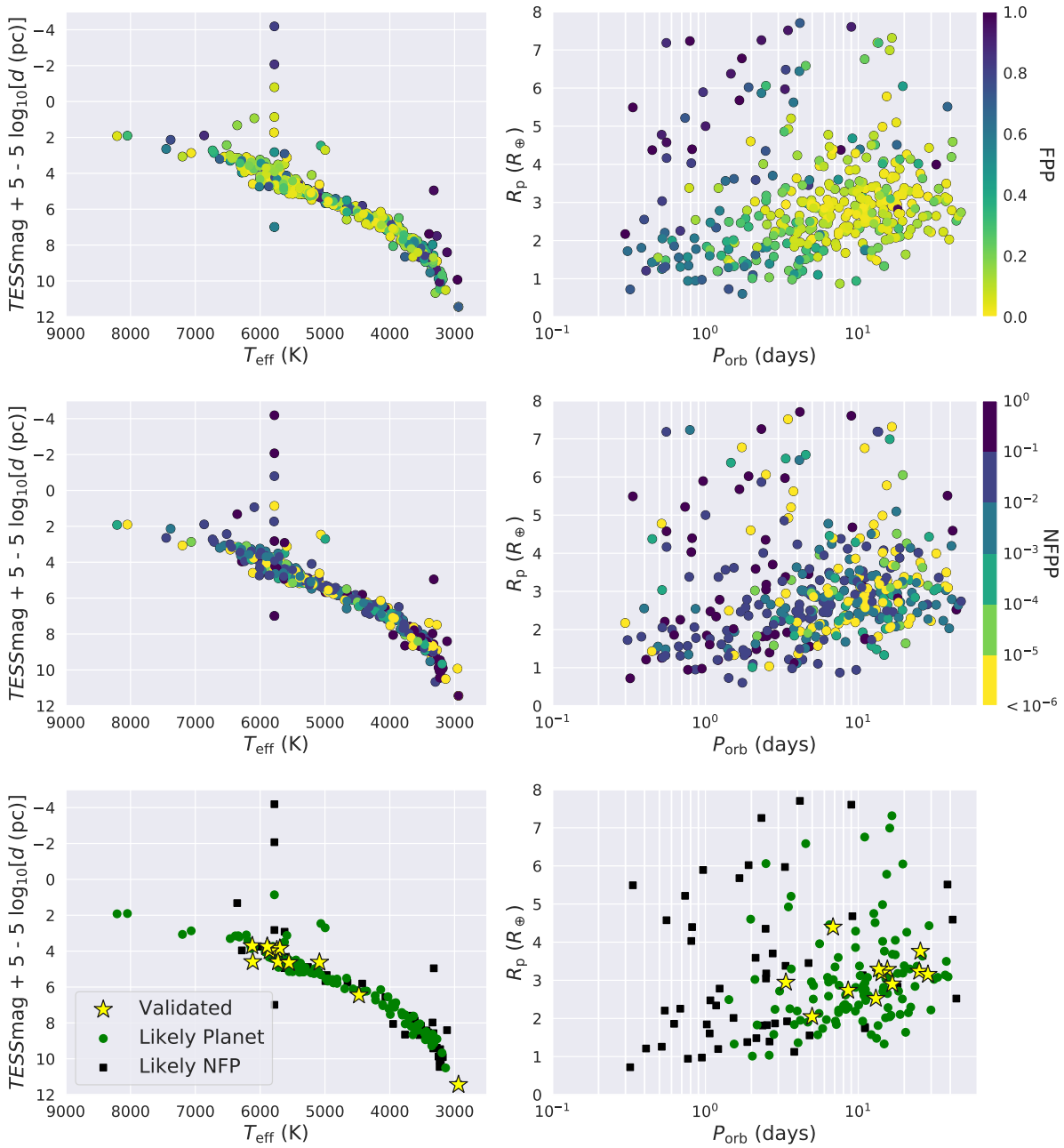

Figure 2.16: Host star properties (*left*) and planet properties (*right*) of analyzed TOI systems. In the top panels, we color each system according to its FPP. In the center panels, we color each system according to its NFPP. In the bottom panels, we distinguish TOIs that have been classified as validated planets, likely planets, and likely NFPs. In general, planets with smaller radii and longer orbital periods are more likely to be identified as planets. The vertical stack of stars at $T_{\rm eff} \sim 6000$ K are stars with unknown surface temperatures that were assigned a Solar $T_{\rm eff}$ on the TFOP website.

TOI Number	FPP	Original Validation Paper
261.01	0.0067 ± 0.0004	this work
261.02	0.0009 ± 0.0002	this work
469.01	0.0133 ± 0.0016	this work
682.01	0.0069 ± 0.0020	this work
736.01	0.0092 ± 0.0005	Crossfield et al. (2019)
836.01	0.0141 ± 0.0019	this work
1054.01	0.0115 ± 0.0008	this work
1203.01	0.0125 ± 0.0011	this work
1230.01	0.0132 ± 0.0005	this work
1233.01	0.0135 ± 0.0012	Daylan et al. (2021)
1339.02	0.0127 ± 0.0011	Badenas-Agusti et al. (2020)
1774.01	0.0133 ± 0.0010	this work

Table 2.6: Statistically validated TOIs.

In the bottom panels of Figure 2.16, we present the properties of TOIs that have been classified as validated planets, likely planets, and likely NFPs by our analysis. In total, we statistically validate 12 TOIs, identify 125 TOIs as likely planets, and identify 52 likely NFPs. Our sample of validated TOIs have host stars with a variety of spectral types and planets with radii ranging from 1–5 $R_\oplus$ and orbital periods ranging from 3–30 days. The details for all tested TOIs are given in Table 2.7.

The TOI numbers of the planet candidates statistically validated in this analysis are presented in Table 2.6. Of these, 9 are newly validated and 3 have already been empirically validated via a combination of follow-up observations. The agreement of our statistical validation and the empirical validation of these planet candidates is encouraging for the efficacy of both methods. In addition, we include the FPP calculated by `TRICERATOPS` in Table 2.6. Because FPP is expected to have some scatter across runs, we perform the calculation 20 times for each validated TOI and list the mean and standard deviation of the resulting distribution. In doing so, we affirm that our original FPP calculation that validated the planet candidate was not an outlier.

2.7 Discussion

In Figure 2.16 we present the results of `TRICERATOPS` runs for 384 TOIs, 189 of which are assigned classifications of validated planet, likely planet, or likely NFP. In this figure, a number of patterns emerge that could have broader implications for the population of planets detected by *TESS* and the *TESS* FP rate. As we noted previously, TOIs classified as validated planets or likely planets generally have smaller radii and longer orbital periods. One could interpret this as meaning planets are more common in this region of parameter

space. However, we would be remiss if we did not acknowledge that this result is in part due to our choice of $R_{\rm p}$ and $P_{\rm orb}$ priors, which prefer transiting planet scenarios in this region of parameter space. We realize that this effect could be concerning for those who wish to use `TRICERATOPS` for large-scale statistical studies of planets detected by *TESS*, especially in the case where the true underlying prior distributions are unknown, because it could bias their results to agree with previous planet occurrence rate studies. We therefore plan to add alternative prior distributions, such as a uniform prior, that the user can select when they wish their results to be free of such a bias.

To test the extent to which our results are biased by our prior distribution for $R_{\rm p}$, we reran our code on all 384 TOIs with a uniform $R_{\rm p}$ prior. Because our original $R_{\rm p}$ prior penalizes planet candidates with $R_{\rm p} > 5R_{\oplus}$, one might expect more of these planet candidates to be classified as validated planets or likely planets when the uniform prior is applied. With the uniform prior, the number of validated planet decreased from 12 to 2 (the number of which with $R_{\rm p} > 5R_{\oplus}$ increased from 0 to 1), the number of likely planets decreased from 125 to 93 (the number of which with $R_{\rm p} > 5R_{\oplus}$ increased from 8 to 9), and the number of likely NFPs increased from 52 to 93 (the number of which with $R_{\rm p} > 5R_{\oplus}$ did not change). These results show that the chance of a planet candidate being classified as a validated planet or a likely NFP is strongly dependent on the choice of $R_{\rm p}$ prior. However, as we do not see a large change in the number of classifications for TOIs with $R_{\rm p} > 5R_{\oplus}$, we cannot conclude that our original $R_{\rm p}$ prior significantly biases our results against these TOIs.

Another notable feature of Figure 2.16 is the large number of ultra-short-period planet (i.e., planets with $P_{\rm orb} < 1$ day) TOIs, of which there are 41 with $R_{\rm p} < 8R_{\oplus}$. Past studies have found that this type of planet only occurs around $< 1\%$ of stars (Adams et al. 2016; Sanchis-Ojeda et al. 2014), but the true rate could be higher if all of these candidates are actual planets. However, this interpretation is dependent on the actual false positive rate of these TOIs. The fact that `TRICERATOPS` classifies none of these USP candidates as likely planets and many as NFPs suggests that this false positive rate is high. To ensure that this prediction is not an artifact of the aforementioned $P_{\rm orb}$ prior (which is biased towards eclipsing binary scenarios in this region of parameter space), we also repeated our calculations without this prior. Upon removing the prior the number of likely planets increased from 125 to 127, while the number of validated planets and likely NFPs remained the same. The increase can be attributed to three ultra-short-period planet candidates (TOIs 460.01, 561.02, and 864.01) whose classifications were changed from likely NFP to likely planet. This small increase in the number of likely planets suggests that our results are only moderately affected by our $P_{\rm orb}$ prior, and that most ultra-short-period planet candidates are in fact false positives.

In addition to a statistical validation tool, `TRICERATOPS` can be used as a vetting tool to prioritize follow-up observations of TOIs. Consider candidates that are classified as a likely planets, but with a FPPs just above the validation threshold. Several TOIs we classify as likely planets match this description, and some (e.g., TOI 1055, Bedell et al. in prep) have been confirmed concurrently with this paper. These TOIs make would ideal targets for high-resolution imaging follow-up, because the resulting data products can be incorporated to

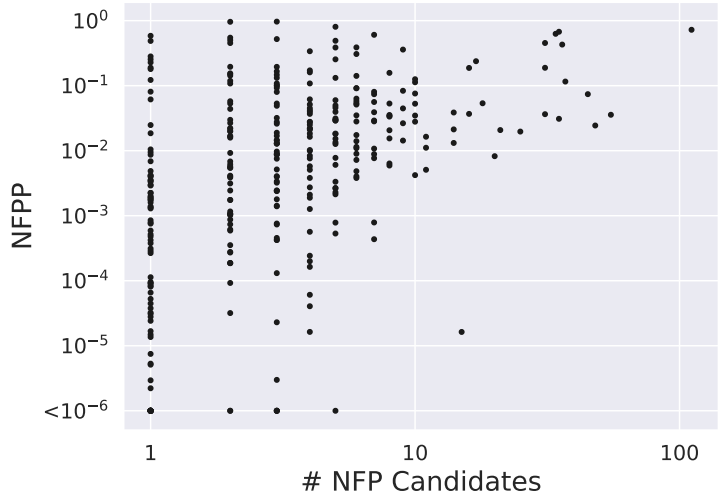

Figure 2.17: NFPP versus number of nearby stars bright enough to be an NFP for each of the 384 TOIs tested in Section 2.6. TOIs with no potential NFPs are omitted. While the average NFPP increases as the number of possible NFPs increases, `TRICERATOPS` is able to classify TOIs with any number of nearby host candidates as likely NFPs (NFPP $> 10^{-1}$).

achieve a lower FPP and validate the planet candidate. In addition, we displayed in Section 2.5 that `TRICERATOPS` is proficient at identifying NFPs, and is often able to predict which nearby star hosts the observed signal. By prioritizing nearby stars with high probabilities of hosting NFPs, observers can increase the rate of true NFP identification. Doing so would allow other members of the *TESS* follow-up community to focus on TOIs that are more likely to be bona fide planets. To display the broad applicability of this prioritization method (i.e., to show that it is not only relevant for TOIs in very crowded fields), we show in Figure 2.17 the NFPP as a function of the number of nearby stars bright enough to be NFPs for the 384 TOIs in our analysis. As one might predict, the expected NFPP increases in more crowded fields. Nonetheless, TOIs with as few as one NFP candidate can be classified as likely NFPs. In other words, `TRICERATOPS` provides information pertaining to the probability of a given TOI being a NFP beyond what can be gathered from the crowdedness of the surrounding field.

Our tool can also be combined with other validation and vetting tools to provide even more robust validation analyses. As of now, `TRICERATOPS` is the only validation tool compatible with *TESS* data that models transits from nearby contaminant stars. Seeing as identifying NFPs is one of the strengths of our tool, it can be used as the first step in such an analysis. For example, one could use `TRICERATOPS` to identify TOIs with sufficiently low NFPPs, and then use tools like `VESPA` (Morton 2015; Morton 2012) and `DAVE` (Kostov et al. 2019) to further constrain the FPP of the planet candidate around the target star. Additionally, comparing the results of several tools would allow one to build a stronger statistical argument for or against the existence of a planet.

To improve the utility of TRICERATOPS, we plan on adding features that will make the procedure more efficient and robust. First, we will add a feature that searches for in-transit centroid offsets to constrain the probabilities of NFPs. Second, we will improve our priors by expanding to more dimensions that affect planet occurrence rates, such as planet multiplicity. In this vein, it has been shown that planet candidates that are members of systems with multiple planet candidates are almost always bona fide planets (e.g., Lissauer et al. 2012). This in and of itself is strong evidence that candidate multi-planet systems with validated planets (including TOIs 736, 836, 1233, and 1339) actually host multiple transiting planets. Third, we will make our tool compatible with additional follow-up constraints, such as time-series photometry that rules out signals around nearby stars and spectroscopic observations that provide limits on eclipsing binary properties, to improve its ability to validate planet candidates. Lastly, we will add additional astrophysical scenarios to our calculation procedure, such as that involving a non-circular orbit and that involving an eclipsing binary where only the secondary eclipse is detected.

2.8 Conclusions

We present a new tool, TRICERATOPS, designed for rapid validation of *TESS* Objects of Interest. Using a Bayesian framework, this tool calculates the probabilities of various transit-producing scenarios for a given TOI in order to provide a false positive probability (FPP) and a nearby false positive probability (NFPP). Our tool is also able to fold in information from follow-up observations as additional constraints in these calculations.

We test our tool on 68 TOIs that have been designated as either confirmed planets or astrophysical false positives by members of the *TESS* Observation Follow-up Program (TFOP) based on follow-up observations. We define three classifications based on the results of this analysis. For a TOI to be validated, it must have high cadence observations, NFPP $< 10^{-3}$, and FPP < 0.015. For a TOI to be classified as a likely planet, it must have NFPP $< 10^{-3}$ and FPP < 0.5. Lastly, for a TOI to be classified as a likely nearby false positive (NFP), it must have NFPP $> 10^{-1}$. To display the proficiency of our tool in identifying NFPs, we also compare our predictions to TOIs that have been identified as actual NFPs by TFOP.

We apply our tool to 384 TOIs with 2-minute cadence observations that have not yet been classified as confirmed planets or rejected as false positives. We statistically validate 12 TOIs, classify 125 TOIs as likely planets, and classify 52 TOIs as likely NFPs.

In addition to planet validation, we recommend using TRICERATOPS to identify TOIs with high probabilities of being planets or NFPs and prioritizing these candidates as targets for further vetting via follow-up observations. When used in combination with other vetting tools, such as VESPA and DAVE, our tool can also be utilized to perform even more thorough validation analyses of planet candidates. We hope this tool will be a valuable resource in the search for planets with *TESS*.

TIC ID	TOI Number	$R_{\rm p}$ ($R_\oplus$)	$P_{\rm orb}$ (days)	SNR	FPP	NFPP	# NFP Candidates	Classification
278683844	119.01	2.13	5.54	8.3	0.04	9.25e-05	2	Likely Planet
278683844	119.02	1.93	10.69	7.0	0.06	1.88e-04	2	Likely Planet
231702397	122.01	2.51	5.08	6.6	0.06	2.79e-05	1	Likely Planet
52368076	125.03	3.38	19.98	4.0	0.04	0.00e+00	0	Likely Planet
391949880	128.01	3.06	4.94	6.9	0.10	2.76e-02	4	
263003176	130.01	2.32	14.34	4.3	0.04	4.02e-03	2	
89020549	132.01	3.02	2.11	12.4	0.03	8.12e-05	1	Likely Planet
219338557	133.01	2.37	8.20	10.5	0.05	0.00e+00	1	Likely Planet
234994474	134.01	1.49	1.40	17.3	0.11	7.62e-03	4	
62483237	139.01	2.93	11.06	13.0	0.03	0.00e+00	0	Likely Planet
425997655	174.03	1.57	12.16	1.6	0.05	5.16e-04	1	Likely Planet
425997655	174.04	1.12	3.98	1.8	0.30	4.19e-03	1	
262530407	177.01	2.24	2.85	21.9	0.08	5.91e-04	2	Likely Planet
251848941	178.01	2.87	6.56	12.1	0.04	4.11e-03	1	
251848941	178.02	3.14	10.35	12.1	0.07	1.76e-03	1	
251848941	178.03	2.43	9.96	9.9	0.07	9.49e-03	1	
207141131	179.01	2.98	4.14	21.1	0.02	0.00e+00	0	Likely Planet
76923707	181.01	6.58	4.53	38.7	0.24	1.63e-04	4	Likely Planet
183985250	193.01	7.23	0.79	35.6	0.99	1.75e-03	2	
12421862	198.01	1.64	20.43	11.6	0.13	1.48e-05	1	Likely Planet
350618622	201.02	1.74	5.85	1.9	0.45	0.00e+00	0	Likely Planet
281781375	204.01	2.52	43.83	1.1	0.27	1.66e-01	3	Likely NFP
281575427	205.01	3.03	4.25	8.8	0.09	1.42e-03	3	
55650590	206.01	5.22	0.74	6.2	0.73	1.60e-01	4	Likely NFP
314865962	208.01	2.97	22.45	4.0	0.02	2.45e-03	3	
52204645	209.01	3.02	4.38	7.1	0.07	2.73e-03	4	
141608198	210.01	7.61	9.01	7.2	0.92	1.32e-01	5	Likely NFP
206609630	212.01	5.49	0.34	54.2	1.00	5.02e-01	2	Likely NFP
234345288	213.01	2.84	23.52	10.9	0.20	4.24e-04	3	Likely Planet
167415965	214.02	0.94	9.70	2.1	0.34	7.41e-02	45	
231912935	215.01	3.63	26.30	7.9	0.23	3.18e-05	2	Likely Planet
150098860	220.01	3.53	10.70	9.2	0.10	2.81e-02	6	
316937670	221.01	1.86	0.62	8.1	0.69	1.95e-01	2	Likely NFP
326453034	223.01	4.02	14.45	3.1	0.36	0.00e+00	1	Likely Planet
160074939	230.01	7.19	13.34	12.9	0.12	1.86e-02	1	
415969908	233.01	2.60	11.67	11.3	0.06	0.00e+00	0	Likely Planet
305048087	237.01	1.57	5.43	3.3	0.08	0.00e+00	0	Likely Planet
9006668	238.01	1.61	1.27	7.2	0.35	5.77e-02	2	
101948569	240.01	3.26	19.47	11.5	0.03	9.71e-03	3	
118327550	244.01	3.60	7.40	11.4	0.50	0.00e+00	0	Likely Planet
201793781	248.01	2.85	5.99	11.5	0.02	2.44e-03	2	

179985715	249.01	2.64	6.61	9.0	0.06	1.30e-02	3	
224225541	251.01	2.96	4.94	8.1	0.02	6.57e-05	1	Likely Planet
237924601	252.01	5.00	1.00	11.9	0.93	8.02e-02	3	
322063810	253.01	1.21	3.52	11.9	0.22	2.23e-02	2	
37749396	260.01	1.81	13.47	3.7	0.20	0.00e+00	0	Likely Planet
63898957	261.01	2.95	3.36	5.8	<0.01	0.00e+00	0	Validated
63898957	261.02	2.52	13.04	1.3	<0.01	0.00e+00	0	Validated
70513361	262.01	2.75	11.15	12.9	0.06	0.00e+00	0	Likely Planet
120916706	263.01	4.58	0.56	20.7	0.97	4.88e-01	1	Likely NFP
164767175	266.01	2.72	10.77	8.9	0.03	0.00e+00	0	Likely Planet
164767175	266.02	1.97	6.19	8.3	0.05	0.00e+00	0	Likely Planet
259511357	271.01	4.35	2.48	12.1	0.73	2.54e-01	1	Likely NFP
281979481	274.01	2.21	0.54	12.1	0.67	1.41e-01	6	Likely NFP
439456714	277.01	4.23	3.99	18.6	0.14	8.09e-02	1	
244161191	278.01	2.17	0.30	21.2	1.00	0.00e+00	0	
122613513	279.01	3.08	11.49	10.9	0.05	0.00e+00	0	Likely Planet
42054565	280.01	2.87	10.18	10.0	0.06	1.39e-03	1	
38696105	281.01	4.09	5.57	12.7	0.19	5.49e-03	2	
29781292	282.02	3.03	31.32	3.6	0.23	7.36e-04	2	Likely Planet
382626661	283.01	2.08	17.62	5.8	0.05	1.76e-03	1	
220459976	285.01	2.65	32.33	3.0	0.06	1.87e-03	1	
150030205	286.01	1.51	4.51	5.9	0.22	8.38e-03	4	
150030205	286.02	2.03	39.36	6.2	0.06	2.98e-03	1	
153065527	406.01	1.48	13.17	10.2	0.02	2.66e-04	1	Likely Planet
100990000	411.01	2.19	9.57	8.3	0.05	0.00e+00	0	Likely Planet
100990000	411.02	1.36	4.04	4.6	0.23	0.00e+00	0	Likely Planet
94986319	421.01	6.99	16.07	23.2	0.10	2.77e-04	2	Likely Planet
31374837	431.02	1.55	0.49	16.1	0.14	1.60e-03	1	
44647437	435.01	6.48	3.35	12.0	0.79	5.91e-04	1	
179034327	444.01	2.95	17.96	9.0	0.01	1.06e-03	2	
153077621	454.01	2.83	18.08	23.8	0.97	9.61e-01	2	Likely NFP
89256802	457.01	2.34	1.18	24.7	0.72	1.80e-01	1	Likely NFP
64071894	458.01	3.05	17.53	5.1	0.03	1.34e-03	1	
9804616	460.01	4.78	0.52	44.5	0.92	0.00e+00	0	
4646810	461.01	2.71	14.49	5.3	0.10	0.00e+00	0	Likely Planet
420049884	462.01	2.51	4.11	6.2	0.14	4.51e-02	4	
398733009	464.01	4.40	0.82	15.4	0.99	5.85e-01	1	Likely NFP
33692729	469.01	3.29	13.63	12.7	0.01	8.32e-12	2	Validated
37770169	470.01	4.50	12.19	12.5	0.11	1.89e-03	4	
100608026	475.01	2.62	8.26	12.5	0.03	7.83e-04	5	Likely Planet
317548889	480.01	3.02	6.87	18.7	0.04	1.36e-05	1	Likely Planet
427348923	484.01	3.45	4.73	12.0	0.83	8.05e-01	5	Likely NFP
260708537	486.01	0.60	1.74	4.6	0.62	3.50e-02	6	
31852980	487.01	2.44	24.33	3.5	0.14	5.73e-03	2	

452866790	488.01	1.20	1.20	9.3	0.24	2.18e-02	2	
19025965	493.01	3.95	5.95	16.3	0.10	6.15e-02	1	
19519368	494.01	2.46	1.70	8.5	0.28	3.35e-02	8	
123702439	499.01	4.12	8.52	21.0	0.13	4.19e-02	4	
134200185	500.01	1.32	0.55	12.6	0.74	3.47e-02	10	
453211454	509.01	3.18	18.12	13.1	0.02	0.00e+00	1	Likely Planet
238086647	510.01	3.57	1.35	1.2	0.64	3.69e-02	4	
119292328	512.01	1.84	7.19	10.3	0.07	4.55e-04	3	Likely Planet
264979636	518.01	4.51	17.88	2.3	0.67	9.21e-05	1	
148479278	520.01	2.05	0.52	6.3	0.58	2.79e-02	10	
27649847	521.01	1.33	1.54	12.8	0.34	0.00e+00	0	Likely Planet
19451711	522.01	2.55	0.40	12.5	0.77	8.85e-03	7	
71512186	525.01	3.76	14.82	6.8	0.02	8.36e-05	1	Likely Planet
200593988	526.01	4.38	7.70	23.4	0.99	2.92e-02	5	
144700903	532.01	5.87	2.33	18.7	0.58	8.05e-02	7	
309791156	533.01	6.05	19.57	15.8	0.45	2.30e-05	3	Likely Planet
237751146	538.01	5.68	1.67	24.0	1.00	9.67e-01	3	Likely NFP
238004786	539.01	1.72	0.31	11.7	0.64	7.58e-02	10	
50618703	544.01	1.94	1.55	19.4	0.11	5.77e-03	4	
161477033	553.02	2.51	11.93	9.7	0.04	2.01e-03	1	
161477033	553.03	2.79	40.90	6.3	0.04	2.25e-03	1	
407966340	554.01	3.35	7.05	9.1	0.14	4.80e-04	1	Likely Planet
55488511	557.01	2.56	3.35	1.4	0.20	3.47e-03	1	
101011575	560.01	2.95	6.40	16.0	0.02	0.00e+00	1	Likely Planet
377064495	561.01	2.86	10.78	10.0	0.02	0.00e+00	0	Likely Planet
377064495	561.02	1.43	0.45	8.7	0.58	0.00e+00	0	
377064495	561.03	2.08	16.37	4.1	0.05	0.00e+00	0	Likely Planet
37575651	568.01	3.86	9.60	9.7	0.07	1.37e-17	1	Likely Planet
126733133	570.01	6.38	1.47	24.2	0.94	7.87e-04	7	
296739893	620.01	2.86	5.10	17.7	0.07	0.00e+00	1	Likely Planet
133334108	637.01	1.87	2.85	11.6	0.26	1.13e-01	10	Likely NFP
22221375	652.01	2.20	3.98	12.0	0.07	7.49e-06	1	Likely Planet
35009898	654.01	2.01	1.53	23.5	0.35	1.89e-01	1	Likely NFP
124573851	669.01	3.63	3.95	13.3	0.03	3.97e-03	3	
151825527	672.01	5.20	3.63	26.8	0.08	5.68e-07	2	Likely Planet
158588995	674.01	4.60	1.98	43.1	0.03	0.00e+00	1	Likely Planet
294395926	678.01	4.18	11.32	18.4	0.12	5.79e-02	6	
429304876	682.01	4.39	6.84	17.3	<0.01	0.00e+00	0	Validated
77156829	696.01	0.95	0.86	8.1	0.60	6.17e-02	4	
77156829	696.02	1.33	14.78	6.6	0.26	2.42e-04	4	Likely Planet
77253676	697.01	2.29	8.61	9.8	0.04	0.00e+00	0	Likely Planet
141527579	698.01	2.02	15.09	7.7	0.11	6.14e-04	2	Likely Planet
149302744	699.01	3.26	14.80	3.1	0.23	3.65e-02	31	
149302744	699.02	3.36	33.62	2.9	0.17	3.09e-02	35	

150428135	700.02	3.03	37.42	-0.3	0.16	7.21e-03	6	
150428135	700.03	2.75	9.98	4.2	0.08	4.03e-03	6	
237914496	702.01	2.25	3.57	8.8	0.25	7.56e-04	1	Likely Planet
237928815	703.01	2.37	8.67	7.1	0.06	2.24e-03	1	
237928815	703.02	2.64	45.12	1.3	0.07	2.91e-03	1	
260004324	704.01	1.12	3.81	1.9	0.48	2.38e-01	17	Likely NFP
391904697	705.01	2.74	47.02	1.8	0.16	2.51e-02	4	
396720998	709.01	3.99	32.38	25.9	1.00	0.00e+00	0	
38510224	711.01	2.32	18.38	6.7	0.30	5.44e-03	2	
150151262	712.01	2.92	9.53	10.3	0.13	1.28e-02	3	
167600516	713.01	2.23	36.00	6.4	0.07	7.54e-03	3	
167600516	713.02	1.39	1.87	3.9	0.50	2.91e-02	7	
219195044	714.01	3.46	4.32	8.4	0.19	8.73e-03	3	
219195044	714.02	3.56	10.18	5.7	0.16	5.15e-03	3	
38571020	721.01	2.72	12.29	1.9	0.17	1.27e-02	5	
38509907	722.01	3.36	15.30	4.5	0.20	4.97e-02	5	
177077336	723.01	1.30	1.42	4.0	0.59	3.96e-02	5	
34068865	731.01	0.72	0.32	10.3	0.72	1.26e-01	10	Likely NFP
36724087	732.01	0.94	0.77	16.1	0.57	2.54e-01	5	Likely NFP
36724087	732.02	1.73	12.25	17.4	0.20	3.97e-02	4	
106402532	733.01	2.01	4.89	8.3	0.09	7.67e-03	7	
181804752	736.01	2.05	4.99	27.2	<0.01	1.08e-10	1	Validated
181804752	736.02	0.97	0.95	13.3	0.71	1.47e-01	3	Likely NFP
219189765	737.01	6.78	1.73	20.9	1.00	0.00e+00	0	
310009611	740.01	3.59	2.13	13.3	0.78	7.24e-01	111	Likely NFP
359271092	741.01	0.87	7.58	6.4	0.13	1.32e-02	14	
444842193	745.01	2.47	1.08	9.1	0.53	1.89e-01	31	Likely NFP
73228647	755.01	1.97	2.54	11.0	0.20	4.47e-02	9	
73649615	756.01	2.78	1.24	14.2	0.56	3.59e-01	9	Likely NFP
130924120	757.01	3.67	17.47	11.5	0.03	5.25e-05	1	Likely Planet
165317334	761.01	3.10	10.56	13.2	0.05	2.78e-02	4	
178709444	762.01	7.51	3.47	31.6	0.94	0.00e+00	0	
178819686	763.01	3.29	5.60	5.8	0.06	1.84e-02	4	
178819686	763.02	3.40	12.28	5.7	0.04	9.95e-03	4	
219401954	765.01	2.54	0.86	7.5	0.14	1.92e-03	1	
277634430	771.01	7.26	2.33	9.0	0.95	3.07e-01	6	Likely NFP
286864983	772.01	6.76	11.02	23.9	0.23	1.84e-34	1	Likely Planet
306996324	776.01	2.28	15.66	11.6	0.04	1.31e-04	3	Likely Planet
306996324	776.02	1.68	8.24	6.6	0.05	3.38e-03	3	
334305570	777.01	7.32	16.60	18.3	0.11	0.00e+00	1	Likely Planet
374095457	779.01	3.38	0.78	24.8	0.07	1.08e-02	7	
429358906	782.01	2.04	16.05	9.4	0.12	0.00e+00	0	Likely Planet
451645081	783.01	3.09	16.23	8.0	0.29	1.63e-05	15	Likely Planet
460984940	784.01	2.14	2.80	13.4	0.22	5.37e-02	18	

374829238	785.01	4.13	18.64	12.1	0.31	2.08e-02	21	
375059587	786.01	2.45	12.67	3.9	0.15	2.11e-03	4	
350584963	787.01	1.62	2.13	2.9	0.69	2.63e-03	5	
349829627	788.01	4.46	6.49	4.1	0.08	5.32e-04	5	Likely Planet
300710077	789.01	1.10	5.45	6.7	0.44	9.17e-02	6	
278895705	795.01	3.49	8.76	3.5	0.20	5.92e-03	8	
277099925	796.01	4.03	0.81	11.5	0.81	4.29e-01	36	Likely NFP
271596225	797.01	1.32	1.80	6.1	0.62	7.40e-02	7	
271596225	797.02	1.49	4.14	3.3	0.51	5.13e-02	6	
255685030	799.01	2.11	5.54	6.6	0.20	8.72e-03	3	
179308757	800.01	5.89	0.97	7.0	0.85	6.75e-01	35	Likely NFP
177258735	801.01	1.34	0.78	3.0	0.61	6.36e-03	8	
167303382	802.01	0.98	3.69	3.2	0.24	1.43e-02	9	
41227743	804.01	1.77	1.42	4.4	0.49	1.97e-02	25	
38460940	805.01	6.44	4.12	7.1	0.59	9.24e-03	2	
33831980	806.01	4.14	21.92	8.9	0.14	1.02e-03	2	
30853470	807.01	1.81	5.27	3.2	0.38	1.75e-03	2	
30122649	808.01	2.69	9.74	12.3	0.02	3.81e-03	6	
388106759	810.01	2.66	28.30	1.9	0.17	1.14e-02	6	
125405602	821.01	3.18	13.82	11.4	0.14	0.00e+00	0	Likely Planet
158978373	823.01	7.19	13.54	9.7	0.31	1.98e-02	2	
276128561	829.01	4.86	3.29	16.4	0.28	8.35e-02	9	
350332997	832.01	6.02	1.92	18.5	0.72	1.19e-01	2	Likely NFP
405700729	835.01	3.59	4.79	18.8	0.57	1.55e-02	8	
440887364	836.01	2.73	8.59	14.1	0.01	0.00e+00	0	Validated
440887364	836.02	1.84	3.82	5.8	0.07	8.50e-04	1	Likely Planet
238898571	863.01	1.27	0.53	2.2	0.74	5.61e-02	7	
231728511	864.01	3.04	0.52	5.7	0.81	7.85e-04	1	
358460246	867.01	2.49	15.40	2.5	0.16	2.83e-02	7	
200807066	869.01	2.62	26.48	5.9	0.08	2.39e-03	3	
219229644	870.01	2.30	22.04	2.8	0.09	0.00e+00	0	Likely Planet
219344917	871.01	2.27	28.69	5.3	0.10	3.87e-03	2	
220459826	872.01	2.65	2.24	8.3	0.29	5.15e-02	4	
237920046	873.01	1.73	5.93	3.6	0.32	2.22e-02	4	
232025086	874.01	2.45	5.90	1.3	0.12	2.60e-02	3	
14165625	875.01	2.47	11.02	11.5	0.04	1.07e-03	2	
32497972	876.01	3.09	38.70	0.1	0.04	0.00e+00	0	Likely Planet
210873792	900.01	2.50	4.84	6.1	0.26	5.28e-02	10	
261257684	904.01	2.72	18.35	9.6	0.03	2.22e-06	1	Likely Planet
350153977	908.01	3.27	3.18	13.1	0.20	2.77e-02	3	
369327947	910.01	1.01	2.03	5.7	0.28	5.66e-04	4	Likely Planet
406941612	912.01	1.90	4.68	15.0	0.07	4.05e-05	4	Likely Planet
407126408	913.01	2.57	11.09	6.9	0.02	4.77e-07	3	Likely Planet
259863352	1051.01	3.30	21.70	2.0	0.09	4.21e-04	1	Likely Planet

317060587	1052.01	3.30	9.14	3.4	0.10	3.82e-03	4	
366989877	1054.01	3.28	15.51	11.1	0.01	6.64e-09	1	Validated
320004517	1055.01	4.05	17.47	12.2	0.02	0.00e+00	0	Likely Planet
421894914	1056.01	2.85	5.31	1.9	0.16	1.06e-03	2	
31553893	1058.01	3.36	11.11	4.8	0.02	1.53e-02	5	
299799658	1062.01	2.38	4.11	8.9	0.14	1.29e-03	1	
406976746	1063.01	2.35	10.07	10.5	0.03	0.00e+00	0	Likely Planet
79748331	1064.01	2.80	6.44	4.7	0.05	1.45e-02	3	
79748331	1064.02	2.95	12.23	13.9	0.04	1.29e-02	3	
327301957	1074.01	2.98	13.93	13.7	0.03	6.16e-03	2	
351601843	1075.01	2.00	0.60	11.4	0.41	5.32e-02	3	
370133522	1078.01	1.26	0.52	17.0	0.41	1.55e-01	2	Likely NFP
161032923	1080.01	2.26	3.97	8.3	0.17	1.11e-02	11	
261108236	1082.01	3.62	16.35	7.1	0.06	2.19e-02	4	
322270620	1083.01	2.48	12.96	8.4	0.10	3.22e-03	3	
383390264	1098.01	3.38	10.18	4.0	0.06	2.99e-06	3	Likely Planet
290348383	1099.01	3.49	6.44	13.3	0.07	2.48e-02	1	
409934330	1114.01	6.06	2.49	37.4	0.32	0.00e+00	0	Likely Planet
304100538	1116.01	2.34	5.01	4.5	0.16	1.64e-02	4	
29960110	1201.01	3.05	2.49	5.3	0.29	2.82e-01	1	Likely NFP
23434737	1203.01	3.76	25.49	11.0	0.01	0.00e+00	0	Validated
467666275	1204.01	1.97	1.38	4.0	0.38	3.57e-02	55	
287776397	1205.01	4.01	2.39	2.7	0.15	1.64e-02	11	
364393429	1207.01	1.39	2.63	2.1	0.51	1.16e-01	37	Likely NFP
273985865	1208.01	1.92	3.42	5.1	0.35	1.32e-01	3	Likely NFP
30037565	1209.01	4.19	40.72	1.8	0.19	8.24e-03	20	
50312495	1211.01	3.74	14.71	6.4	0.06	6.88e-03	1	
451606970	1214.01	5.51	38.36	6.8	0.67	6.28e-01	34	Likely NFP
453260209	1215.01	1.20	1.21	4.4	0.71	3.88e-01	6	Likely NFP
141527965	1216.01	1.75	4.55	3.5	0.30	4.21e-03	10	
248092710	1217.01	4.59	41.46	6.0	0.17	1.08e-01	4	Likely NFP
294781547	1218.01	2.27	13.77	4.3	0.22	5.09e-03	11	
294981566	1219.01	2.36	1.91	7.6	0.34	2.44e-02	48	
374997123	1222.01	2.32	10.19	1.4	0.23	1.27e-03	4	
382437043	1223.01	4.08	14.64	1.3	0.20	2.64e-02	9	
299798795	1224.01	1.95	4.18	4.6	0.08	0.00e+00	0	Likely Planet
150428703	1225.01	2.33	13.90	4.0	0.20	5.32e-02	8	
177115354	1226.01	2.48	3.93	6.5	0.34	3.54e-02	8	
300038935	1228.01	4.43	29.05	5.5	0.05	2.00e-04	4	Likely Planet
287156968	1230.01	3.23	25.06	11.4	0.01	0.00e+00	0	Validated
447061717	1231.01	3.37	24.25	17.3	0.03	2.46e-32	3	Likely Planet
260647166	1233.01	3.19	14.18	13.3	0.01	1.63e-05	4	Validated
260647166	1233.02	3.19	19.59	10.6	0.03	6.08e-05	4	Likely Planet
260647166	1233.03	2.45	6.20	8.6	0.02	2.14e-03	5	

260647166	1233.04	2.02	3.80	7.3	0.07	8.97e-03	6	
153951307	1238.01	2.34	3.29	14.0	0.06	3.34e-03	1	
153951307	1238.02	1.57	0.76	2.3	0.50	2.00e-02	2	
154716798	1239.01	4.75	12.64	24.0	0.11	0.00e+00	0	Likely Planet
198212955	1242.01	1.81	0.38	7.6	0.64	9.25e-02	3	
219698776	1243.01	2.97	4.66	13.7	0.48	3.14e-03	2	
219850915	1244.01	2.55	6.40	8.7	0.07	1.65e-02	2	
229781583	1245.01	2.29	4.82	12.8	0.15	1.74e-02	6	
230127302	1246.01	3.88	18.65	9.7	0.06	3.00e-02	5	
230127302	1246.02	3.00	4.31	4.3	0.07	1.81e-02	5	
230127302	1246.03	2.73	5.90	3.6	0.08	1.34e-02	5	
232540264	1247.01	3.10	15.92	14.1	0.02	3.53e-04	2	Likely Planet
232976128	1249.01	3.43	13.08	12.0	0.06	3.99e-03	1	
237222864	1255.01	3.12	10.29	13.8	0.10	5.31e-06	1	Likely Planet
355867695	1260.01	2.46	3.13	6.9	0.05	4.05e-03	3	
355867695	1260.02	2.87	7.49	5.9	0.05	8.71e-04	2	Likely Planet
406672232	1263.01	1.84	1.02	2.6	0.34	1.88e-01	16	Likely NFP
467179528	1266.01	2.60	10.90	12.3	0.02	1.68e-05	1	Likely Planet
467179528	1266.02	2.10	18.80	5.8	0.21	2.42e-05	1	Likely Planet
198241702	1269.01	2.31	4.25	6.4	0.10	1.02e-02	4	
417948359	1272.01	5.97	3.32	17.1	0.93	6.06e-01	7	Likely NFP
13499636	1275.01	2.85	11.32	6.7	0.11	4.91e-02	3	
153949511	1277.02	3.14	37.07	6.8	0.06	0.00e+00	0	Likely Planet
224297258	1279.01	2.81	9.61	14.7	0.03	0.00e+00	0	Likely Planet
232971294	1281.01	2.58	6.39	5.6	0.12	7.58e-04	3	Likely Planet
352764091	1287.01	3.30	9.60	8.4	0.09	6.06e-03	5	
269701147	1339.02	3.15	28.58	8.1	0.01	3.78e-05	1	Validated
229747848	1347.01	2.06	0.85	7.0	0.59	6.32e-02	6	
199444169	1410.01	3.38	1.22	14.1	0.13	2.91e-02	5	
116483514	1411.01	1.37	1.45	8.2	0.20	1.45e-02	3	
148782377	1415.01	4.99	14.42	11.8	0.02	0.00e+00	0	Likely Planet
158025009	1416.01	1.76	1.07	5.9	0.19	5.32e-02	2	
346418409	1423.01	3.70	2.76	25.0	0.63	5.48e-01	2	Likely NFP
418959198	1424.01	2.90	4.90	15.3	0.04	1.89e-02	3	
293954617	1430.01	2.15	7.43	10.1	0.03	5.12e-06	1	Likely Planet
138588540	1434.01	2.22	29.89	8.8	0.03	3.71e-08	1	Likely Planet
153976959	1435.01	1.31	0.69	6.4	0.55	1.69e-02	2	
154383539	1436.01	1.78	0.87	12.0	0.63	4.40e-02	2	
198356533	1437.01	2.72	18.84	4.2	0.02	1.79e-03	3	
233617847	1440.01	3.06	15.52	4.0	0.49	4.53e-01	2	Likely NFP
233951353	1441.01	2.73	22.10	4.4	0.06	2.67e-03	5	
235683377	1442.01	1.21	0.41	8.0	0.84	1.01e-01	3	Likely NFP
258514800	1444.01	1.46	0.47	3.5	0.65	9.12e-02	6	
259172391	1445.01	3.26	9.81	13.3	0.05	1.09e-02	6	

294471966	1446.01	2.45	6.32	5.2	0.12	2.13e-02	14	
343628284	1448.01	3.28	8.11	11.4	0.12	3.43e-02	8	
356158613	1449.01	4.02	24.71	10.2	0.39	3.69e-02	16	
356158613	1449.02	1.82	2.37	6.0	0.57	4.54e-01	31	Likely NFP
377293776	1450.01	1.10	2.04	3.0	0.72	2.06e-02	8	
417931607	1451.01	3.08	33.07	5.2	0.09	2.87e-04	1	Likely Planet
420112589	1452.01	1.77	11.06	2.1	0.46	3.86e-01	5	Likely NFP
198390247	1453.02	1.21	4.31	1.8	0.34	2.10e-02	4	
16920150	1459.01	4.68	9.16	12.9	0.45	1.43e-01	2	Likely NFP
188768068	1462.01	1.83	2.18	7.8	0.09	9.03e-05	1	Likely Planet
229944666	1464.01	3.08	11.33	10.6	0.18	1.83e-02	5	
237086564	1466.01	2.79	1.87	12.6	0.11	3.91e-02	7	
240968774	1467.01	2.14	5.97	9.5	0.10	4.84e-03	6	
243185500	1468.01	2.65	15.53	11.4	0.09	3.78e-04	1	Likely Planet
243185500	1468.02	1.38	1.88	7.9	0.32	1.51e-01	2	Likely NFP
284441182	1470.01	2.42	2.53	1.9	0.13	3.87e-02	14	
306263608	1471.01	4.26	20.77	6.6	0.02	3.23e-05	1	Likely Planet
306955329	1472.01	4.78	6.36	14.1	0.09	8.98e-03	3	
352413427	1473.01	2.90	5.26	5.4	0.02	2.43e-03	3	
428679607	1669.01	2.65	2.68	4.7	0.09	2.29e-03	5	
259168516	1680.01	1.55	4.80	4.8	0.30	1.08e-01	2	Likely NFP
321041369	1681.01	3.62	1.54	19.8	0.69	9.95e-02	3	
58542531	1683.01	2.72	3.06	8.1	0.06	0.00e+00	0	Likely Planet
28900646	1685.01	1.56	0.67	17.2	0.65	5.35e-02	6	
102672709	1686.01	4.24	6.70	5.7	0.04	3.33e-03	5	
103448870	1687.01	4.39	10.26	9.0	0.60	7.98e-07	3	
268334473	1691.01	3.68	16.73	12.2	0.02	0.00e+00	0	Likely Planet
288636342	1692.01	5.10	17.73	7.8	0.03	7.77e-03	5	
353475866	1693.01	1.46	1.77	4.9	0.31	4.59e-02	5	
396740648	1694.01	5.62	3.77	24.4	0.61	0.00e+00	0	
422756130	1695.01	2.22	3.13	12.1	0.23	1.40e-02	6	
470381900	1696.01	3.18	2.50	6.1	0.28	1.58e-01	8	Likely NFP
1884091865	1697.01	3.13	10.69	5.0	0.34	1.72e-01	4	Likely NFP
15863518	1713.01	4.17	0.56	22.7	0.81	5.98e-02	5	
14336130	1716.01	3.02	8.09	13.7	0.05	6.84e-03	2	
257241363	1718.01	3.96	5.59	22.6	0.02	3.10e-05	1	Likely Planet
85242435	1722.01	4.29	9.61	14.1	0.02	2.72e-04	2	Likely Planet
71431780	1723.01	3.16	13.72	9.0	0.02	7.34e-04	3	Likely Planet
81212286	1724.01	2.26	0.69	14.4	0.84	5.21e-01	3	Likely NFP
241225337	1727.01	2.58	1.83	10.7	0.33	3.13e-02	5	
285048486	1728.01	4.92	3.49	25.5	0.10	0.00e+00	1	Likely Planet
318022259	1730.01	2.58	6.22	22.7	0.03	1.69e-02	3	
318022259	1730.02	1.48	2.16	8.8	0.22	1.08e-01	3	Likely NFP
470987100	1732.01	2.66	4.12	15.0	0.06	1.59e-02	2	

159418353	1739.01	2.24	8.30	7.9	0.10	0.00e+00	0	Likely Planet
174041208	1740.01	2.51	19.43	7.6	0.05	4.23e-04	3	Likely Planet
232650365	1746.01	1.83	2.53	2.3	0.50	1.95e-01	3	Likely NFP
408636441	1759.01	3.50	37.70	10.6	0.03	2.36e-13	5	Likely Planet
420112587	1760.01	1.74	11.06	8.4	0.56	4.91e-01	5	Likely NFP
4897275	1774.01	2.90	16.71	8.0	0.01	1.13e-04	1	Validated
21535395	1776.01	1.58	2.80	7.6	0.29	9.57e-05	1	Likely Planet
29191624	1777.01	2.82	14.65	5.2	0.05	3.13e-04	1	Likely Planet
39699648	1778.01	3.43	6.52	9.9	0.07	3.54e-03	1	
160045097	1782.01	2.47	4.99	7.4	0.05	4.87e-03	1	
229938290	1783.01	0.73	1.42	0.3	0.74	3.19e-02	3	
286916251	1794.01	3.84	8.78	4.0	0.04	1.16e-03	2	
368435330	1797.01	3.30	3.65	17.4	0.03	4.46e-05	1	Likely Planet
198153540	1798.01	2.33	8.02	10.0	0.05	1.87e-04	2	Likely Planet
8967242	1799.01	1.93	7.09	8.3	0.09	2.94e-06	1	Likely Planet
119584412	1801.01	2.15	21.28	5.2	0.07	0.00e+00	0	Likely Planet
138762614	1802.01	2.46	16.80	8.4	0.08	2.67e-02	2	
144401492	1803.01	4.51	12.89	17.4	0.29	0.00e+00	0	Likely Planet
144401492	1803.02	3.08	6.29	13.9	0.02	0.00e+00	1	Likely Planet
148679712	1804.01	3.01	4.93	16.6	0.05	5.08e-03	4	
165763244	1805.01	3.23	24.07	8.8	0.03	1.40e-03	3	
166648874	1806.01	3.04	15.15	11.4	0.02	0.00e+00	0	Likely Planet
180695581	1807.01	1.48	0.55	15.3	0.28	8.66e-03	1	
390651552	1827.01	1.40	1.47	21.3	0.02	1.05e-02	1	
27194429	1831.01	7.18	0.56	12.2	0.87	2.98e-02	2	
307956397	1832.01	7.71	4.15	22.5	0.71	2.28e-01	1	Likely NFP
347332255	1835.01	2.15	5.64	11.2	0.57	0.00e+00	1	
381714186	1839.01	2.49	1.42	11.7	0.27	0.00e+00	0	Likely Planet
202426247	1860.01	1.61	1.07	4.3	0.54	3.39e-01	4	Likely NFP
390651552	1827.01	1.40	1.47	21.3	0.02	1.05e-02	1	
27194429	1831.01	7.18	0.56	12.2	0.87	2.98e-02	2	
307956397	1832.01	7.71	4.15	22.5	0.71	2.28e-01	1	Likely NFP
347332255	1835.01	2.15	5.64	11.2	0.57	0.00e+00	1	
381714186	1839.01	2.49	1.42	11.7	0.27	0.00e+00	0	Likely Planet
202426247	1860.01	1.61	1.07	4.3	0.54	3.39e-01	4	Likely NFP
188589164	2013.01	1.03	2.61	12.8	0.20	0.00e+00	0	Likely Planet
368287008	2015.01	3.38	3.35	16.4	0.26	1.23e-01	1	Likely NFP
219508169	2016.02	2.80	2.46	14.3	0.04	4.13e-03	2	
357501308	2018.01	2.22	7.44	12.2	0.02	1.86e-04	2	Likely Planet
159781361	2019.01	5.78	15.35	11.9	0.02	0.00e+00	0	Likely Planet
11996814	2022.01	4.37	0.45	25.0	0.99	4.35e-04	7	
16884216	2023.01	2.47	11.19	17.4	0.03	0.00e+00	0	Likely Planet

Table 2.7: `TRICERATOPS` predictions for undesignated TOIs.

Chapter 3

Validation of 13 Hot and Potentially Terrestrial Planets

An earlier version of this article was published as: Giacalone, S., Dressing, C. D., Hedges, C., Kostov, V. B., Collins, K. A., Jensen, E. L. N., Yahalomi, D. A., Bieryla, A., Ciardi, D. R., Howell, S. B., Lillo-Box, J., Barkaoui, K., Winters, J. G., Matthews, E., Livingston, J. H., Quinn, S. N., Safonov, B. S., Cadieux, C., Furlan, E., Crossfield, I. J. M., Mandell, A. M., Gilbert, E. A., Kruse, E., Quintana, E. V., Ricker, G. R., Seager, S., Winn, J. N., Jenkins, J. M., Duffy Adkins, B., Baker, D., Barclay, T., Barrado, D., Batalha, N. M., Belinski, A. A., Benkhaldoun, Z., Buchhave, L. A., Cacciapuoti, L., Charbonneau, D., Chontos, A., Christiansen, J. L., Cloutier, R., Collins, K. I., Conti, D. M., Cutting, N., Dixon, S., Doyon, R., El Mufti, M., Esparza-Borges, E., Essack, Z., Fukui, A., Gan, T., Gary, K., Ghachoui, M., Gillon, M., Girardin, E., Glidden, A., Gonzales, E. J., Guerra, P., Horch, E. P., Hełminiak, K. G., Howard, A. W., Huber, D., Irwin, J. M., Isopi, G., Jehin, E., Kagetani, T., Kane, S. R., Kawauchi, K., Kielkopf, J. F., Lewin, P., Luker, L., Lund, M. B., Mallia, F., Mao, S., Massey, B., Matson, R. A., Mireles, I., Mori, M., Murgas, F., Narita, N., O'Dwyer, T., Petigura, E. A., Polanski, A. S., Pozuelos, F. J., Palle, E., Parviainen, H., Plavchan, P. P., Relles, H. M., Robertson, P., Rose, M. E., Rowden, P., Roy, A., Savel, A. B., Schlieder, J. E., Schnaible, C., Schwarz, R. P., Sefako, R., Selezneva, A., Skinner, B., Stockdale, C., Strakhov, I. A., Tan, T.-G., Torres, G., Tronsgaard, R., Twicken, J. D., Vermilion, D., Waite, I. A., Walter, B., Wang, G., Ziegler, C., Zou, Y., 2022, *The Astronomical Journal*, 163, 99.

JWST will be able to probe the atmospheres and surface properties of hot, terrestrial planets via emission spectroscopy. We identify 18 potentially terrestrial planet candidates detected by the Transiting Exoplanet Survey Satellite (*TESS*) that would make ideal targets for these observations. These planet candidates cover a broad range of planet radii ($R_{\rm p} \sim 0.6-2.0R_{\oplus}$) and orbit stars of various magnitudes ($K_s = 5.78-10.78$, $V = 8.4-15.69$) and effective temperatures ($T_{\rm eff} \sim 3000-6000$K). We use ground-based observations collected through the *TESS* Follow-up Observing Program (TFOP) and two vetting tools – `DAVE` and `TRICERATOPS` – to assess the reliabilities of these candidates as planets. We validate 13 planets: TOI-206 b, TOI-500 b, TOI-544 b, TOI-833 b, TOI-1075 b, TOI-1411 b, TOI-1442 b, TOI-1693 b, TOI-1860 b, TOI-2260 b, TOI-2411 b, TOI-2427 b, and TOI-2445 b. 7 of

these planets (TOI-206 b, TOI-500 b, TOI-1075 b, TOI-1442 b, TOI-2260 b, TOI-2411 b, and TOI-2445 b) are ultra-short-period planets. TOI-1860 is the youngest (133 ± 26 Myr) Solar twin with a known planet to-date. TOI-2260 is a young (321 ± 96 Myr) G dwarf that is among the most metal-rich ([Fe/H] $= 0.22 \pm 0.06$ dex) stars to host an ultra-short-period planet. With an estimated equilibrium temperature of $\sim$ 2600 K, TOI-2260 b is also the fourth hottest known planet with $R_{\rm p} < 2\,R_{\oplus}$.

3.1 Introduction

Over the last two decades, the combination of planet radii ($R_{\rm p}$) and planet masses ($M_{\rm p}$) measured from transit and radial velocity (RV) observations have enabled the calculations of bulk densities for hundreds of exoplanets. With the help of theoretical models of the interior structures of planets (Fortney et al. 2007; Grasset et al. 2009; Seager et al. 2007; Valencia et al. 2006, 2007a,b; Zeng and Sasselov 2013; Zeng and Seager 2008; Zeng et al. 2016), the bulk densities of these planets have made it possible to identify planets with terrestrial compositions (e.g., Barros et al. 2014; Batalha et al. 2011; Carter et al. 2012; Dragomir et al. 2013; Dressing et al. 2015; Gillon et al. 2017a; Motalebi et al. 2015; Rogers 2015). As a consequence, out understanding of terrestrial planets outside of the Solar System has progressed significantly in recent years. For instance, terrestrial planets with orbital periods shorter than 30 days are now known to have maximum radii between 1.5 and 2.0 $R_{\oplus}$ (e.g., Buchhave et al. 2016; Rogers 2015).

Another notable discovery resulting from these surveys is the distinct gap in occurrence rate between planets with $R_{\rm p} < 1.5\,R_{\oplus}$ and planets with $R_{\rm p} > 2.0\,R_{\oplus}$ (Fulton and Petigura 2018; Fulton et al. 2017) (often referred to as the "radius gap"), with the former regime corresponding to planets with terrestrial compositions and the latter regime corresponding to planets with volatile-rich gaseous envelopes. This feature has important implications for the formation and evolution of short-period terrestrial planets, and several theories have predicted it or put forth an explanation for its origin. Some have proposed that the gap is a natural consequence of planets forming in gas-poor and gas-rich environments (Lee and Chiang 2016; Lee et al. 2014; Lopez and Rice 2018), while others contend that the gap is a result of atmospheric loss via photoevaporation (Jackson et al. 2012; Jin and Mordasini 2018; Jin et al. 2014; Lopez and Fortney 2013; Owen and Wu 2013, 2017), core-powered mass loss (Ginzburg et al. 2016, 2018), or planetesimal collision (Schlichting et al. 2015; Shuvalov 2009). This gap has also been found to depend on planet orbital period (Martinez et al. 2019; Van Eylen et al. 2018), stellar mass (Cloutier and Menou 2020; Fulton and Petigura 2018; Wu 2019), and system age (Berger et al. 2020; David et al. 2021), which indicates that the terrestrial planet formation mechanism responsible for the feature could vary from system to system.

More recently, attempts have been made to more closely characterize terrestrial planets by observing their thermal emission phase curves. These near- and mid-infrared observations can reveal whether a terrestrial planet is surrounded by a thin atmosphere or has an

airless surface, as only the former is expected to produce phase curves with evidence of atmospheric heat redistribution (Koll and Abbot 2016; Kreidberg and Loeb 2016; Seager and Deming 2009; Selsis et al. 2011). Using this method, Demory et al. (2016) found evidence of atmospheric circulation for 55 Cnc e and Kreidberg et al. (2019) inferred the absence of an atmosphere for LHS 3844 b. In addition, Kreidberg et al. (2019) was able to use the wavelength-dependent planet-to-star flux ratio to estimate the surface composition of LHS 3844 b, finding that it is consistent with a basaltic composition that could result from widespread volcanism.

Our ability to characterize short-period terrestrial planets will improve drastically with the launch of *JWST*, which will allow for the characterization of exoplanet atmospheres and surface properties via transmission spectrocopy, emission spectroscopy, and emission photometry (Greene et al. 2016). For most of the known terrestrial planets, detecting atmospheric absorption features in transmission spectrawould be extremely challenging (the exception being those orbiting ultra-cool dwarfs and white dwarfs; Kaltenegger et al. 2020; Lustig-Yaeger et al. 2019), but many of these planets would make excellent targets for thermal emission measurements. With these observations, one can infer the presence or lack of atmospheres surrounding short-period terrestrial planets (Koll et al. 2019; Lustig-Yaeger et al. 2019; Mansfield et al. 2019). For planets with atmospheres, relatively low-S/N emission photometry and/or spectroscopy will reveal modest information about atmospheric composition and identify suitable targets for further atmospheric characterization with future high-precision instruments. For planets without atmospheres, emission measurements will permit the characterization of the surfaces of planets, such as those hot enough for the existence of day-side lava oceans (Essack et al. 2020; Kite et al. 2016; Rouan et al. 2011; Samuel et al. 2014).

The most highly anticipated *JWST* instrument for these observations is the Mid-Infrared Instrument (MIRI), which can perform low resolution spectroscopy between 5 and 12 μm. This wavelength range contains a number of features that can be used to discern planets with atmospheres from those without atmospheres. Morley et al. (2017) and Lincowski et al. (2018) simulated emission spectra for several terrestrial exoplanets assuming various atmospheric compositions, finding a number of notable absorption features. Specifically, Earth-like and O_2-dominated outgassed atmospheres can be identified via strong H_2O absorption between 5 and 7 μm, whereas Venus-like atmospheres display prominent SO_2 absorption between 7 and 9 μm and strong CO_2 absorption above 10 μm. Lincowski et al. (2018) also modeled the case of O_2-dominated desiccated (water-poor) atmospheres, which may be particularly relevant for planets orbiting M dwarfs (Luger and Barnes 2015), finding that they are distinguishable by a lack of H_2O absorption between 5 and 7 μm and strong O_3 absorption at 9.6 μm. Zilinskas et al. (2020) modeled emission spectra of N_2-dominated atmospheres for the hot terrestrial planet 55 Cnc e, finding that C-rich atmospheres have a distinct HCN feature at 7.5 μm. Hu et al. (2012) considered the cases of hot planets with airless surfaces when simulating thermal emission spectra. These spectra are largely blackbody-like but feature notable SiO absorption between 7 and 13 μm, which could be abundant for planets close enough to their host stars for their surfaces to vaporize (Schaefer

et al. 2012). This SiO absorption is expected to vary based on the types of rocks being vaporized (e.g., basaltic vs feldspathic vs ultramafic), and can therefore reveal information about surface composition.

In anticipation of the launch of *JWST*, many have designed methods and frameworks for identifying good targets for thermal emission observations (e.g., Batalha et al. 2017; Kempton et al. 2018). Kempton et al. (2018) defined the emission spectroscopy metric (ESM), a proxy for the signal-to-noise ratio attainable for a terrestrial planet being observed with emission spectroscopy, in order to determine what planets should be prioritized for these observations, drawing the threshold above which the best targets exist at 7.5. As of 2018, only 7 confirmed terrestrial planets (GJ 1132 b, HD 219134 b, HD 219134 c, 55 Cnc e, HD 3167 b, K2-141 b, and GJ 9827 b) had met this criterion, and 3 of these (HD 219134 b, HD 219134 c, and 55 Cnc e) have host stars too bright for emission spectroscopy observations with *JWST*. If an extensive emission photometry/spectroscopy survey of short-period terrestrial planets is to be conducted, more of these planets must be discovered.

The Transiting Exoplanet Survey Satellite mission (*TESS*; Ricker et al. 2010), an ongoing survey searching for transiting planets across nearly the entire sky, has already significantly expanded the size of this sample. Since the start of the mission in mid-2018, an additional 15 planets with $R_{\rm p} < 2\,R_{\oplus}$, ESM > 7.5, and a host stars amenable to *JWST* observations have been discovered. In addition, we have identified 18 *TESS* Objects of Interest (TOIs; Guerrero et al. 2021), stars that exhibit decreases in brightness consistent with the signals caused by transiting planets, that would also meet these requirements if confirmed to host planets with terrestrial compositions. Nonetheless, because some of these TOIs could end up being astrophysical false positives (such as eclipsing binaries around nearby stars contaminating the *TESS* aperture), the community would benefit from a vetting analysis that identifies the potentially terrestrial planet candidates that have the best chances of being bona fide planets. In this paper, we scrutinize *TESS* data and follow-up observations to assess the possibility that these 18 TOIs are actual planets and argue for future characterization efforts.

In Section 3.2, we discuss our sample of 18 TOIs and describe how they were selected. In Section 3.3, we describe our vetting analysis procedure. In Section 3.4, we present follow-up observations of these TOIs that are incorporated into our analysis. In Section 3.5, we present results of our vetting analysis and validate 13 of the TOIs. In Section 4.5, we discuss the implications of our results with respect to *JWST* emission spectroscopy. Lastly, in Section 3.7, we provide concluding remarks.

3.2 Sample

The goal of this paper is to identify a sample of small, hot, and likely terrestrial planets that would be favorable targets for emission spectroscopy observations with *JWST*. We selected our sample by first identifying all TOIs with orbital periods ($P_{\rm orb}$) < 10 days and $R_{\rm p} < 2\,R_{\oplus}$, which corresponds approximately to the largest a planet can be without having a volatile-rich gaseous envelope (e.g., Buchhave et al. 2016; Rogers 2015). The $P_{\rm orb}$ of each

TOI is gathered from ExoFOP-*TESS*.[1] We estimate the $R_{\rm p}$ of each TOI using the transit depths (δ) listed on ExoFOP-*TESS* and the stellar properties in version 8.1 of the *TESS* Input Catalog (TIC; Stassun et al. 2018b).[2] Next, we removed all TOIs that have been flagged as false positives (FPs) or false alarms (FAs) on ExoFOP-*TESS* under "TFOPWG Disposition." FPs are typically caused by eclipsing binaries around stars close enough to the target star to contaminate the *TESS* aperture, while FAs are typically caused by stellar rotation or instrumental variability that produces a signal resembling a planetary transit. Because the events caused by FPs and FAs are often shallow enough to be mistaken as the transits of small planets, scrutinizing observations of small TOIs for FP and FA signatures is an important step in determining which are bona fide planets. Our procedure for further vetting TOIs that pass this condition is described in Section 3.3.

Lastly, we determined which of our planets candidates would be most amenable to thermal emission measurements with *JWST*. To do this, we calculated the emission spectroscopy metric (ESM) for each of the remaining TOIs. The ESM is a quantity introduced in Kempton et al. (2018) to serve as a proxy for the signal-to-noise ratio (S/N) one should expect to obtain when observing the emission spectrum of an exoplanet with *JWST*. More specifically, ESM is given by the equation

$$\mathrm{ESM} = 4.26 \times 10^6 \times \frac{B_{7.5}(T_{\rm day})}{B_{7.5}(T_{\rm eff})} \times \left(\frac{R_{\rm p}}{R_\star}\right)^2 \times 10^{-m_K/5} \tag{3.1}$$

where $B_{7.5}$ is Planck's function evaluated at 7.5 μm for a given temperature, $T_{\rm day}$ is the dayside temperature of the planet in Kelvin (which is assumed to be 1.1x the equilibrium temperature of the planet), $T_{\rm eff}$ is the effective temperature of the host star in Kelvin, $R_\star$ is the stellar radius, and m_K is the apparent magnitude of the host star in K band. When calculating equilibrium temperature (here and throughout the remainder of the paper), we assume zero bond albedo and full day-night heat redistribution.[3] Kempton et al. (2018) recommends that terrestrial planets with ESM $\gtrsim 7.5$ be prioritized for emission spectroscopy observations. We therefore removed TOIs with ESMs lower than this threshold. The host star and the planet properties of our final list of 18 TOIs are shown in Table 4.1.

It is worth noting that small planets are not the only good targets for *JWST* emission spectroscopy. In fact, Equation 3.1 shows that larger planets with thick atmospheres would produce an even higher signal through these observations. However, this paper focuses specifically on terrestrial planets.

[1] `https://exofop.ipac.caltech.edu/tess/index.php` – search performed on 2021-03-11.

[2] $P_{\rm orb}$ and δ are reported by either the SPOC pipeline or Quick Look Pipeline, which are discussed further below.

[3] We acknowledge that, due to these assumptions, all equilibrium temperatures discussed in this paper are only rough estimates.

TOI	K_s mag	parallax (mas)	$T_{\rm eff}$ (K)	$\log g$	$R_\star$ $(R_\odot)$	δ (ppm)	$R_{\rm p}$ $(R_\oplus)$	$P_{\rm orb}$ (days)	ESM
206.01	10.06 ± 0.02	20.92 ± 0.05	3380 ± 160	4.87 ± 0.01	0.35 ± 0.01	1540 ± 230	1.51 ± 0.12	0.736	8.7 ± 1.4
500.01	7.73 ± 0.03	21.07 ± 0.02	4450 ± 130	4.53 ± 0.10	0.75 ± 0.06	246 ± 27	1.29 ± 0.13	0.548	9.3 ± 1.2
539.01	9.23 ± 0.02	9.20 ± 0.02	4900 ± 130	4.52 ± 0.09	0.81 ± 0.05	310 ± 40	1.56 ± 0.14	0.310	8.1 ± 1.1
544.01	7.80 ± 0.02	24.29 ± 0.04	4220 ± 120	4.61 ± 0.11	0.66 ± 0.06	590 ± 6	1.76 ± 0.16	1.549	10.3 ± 0.9
731.01	5.78 ± 0.02	106.21 ± 0.03	3540 ± 160	4.78 ± 0.01	0.46 ± 0.01	242 ± 20	0.78 ± 0.04	0.322	20.4 ± 1.7
833.01	8.15 ± 0.03	23.94 ± 0.02	3920 ± 160	4.65 ± 0.01	0.60 ± 0.02	580 ± 60	1.58 ± 0.10	1.042	10.0 ± 1.2
1075.01	9.11 ± 0.02	16.24 ± 0.03	3920 ± 160	4.67 ± 0.01	0.58 ± 0.02	970 ± 90	1.97 ± 0.10	0.605	14.7 ± 1.3
1242.01	9.77 ± 0.03	9.06 ± 0.03	4250 ± 130	4.56 ± 0.11	0.71 ± 0.07	578 ± 32	1.87 ± 0.18	0.381	9.8 ± 0.9
1263.01	7.10 ± 0.02	21.45 ± 0.04	5100 ± 130	4.55 ± 0.08	0.82 ± 0.05	258 ± 32	1.43 ± 0.12	1.021	9.9 ± 1.3
1411.01	7.25 ± 0.02	30.76 ± 0.02	4180 ± 120	4.57 ± 0.11	0.69 ± 0.06	366 ± 21	1.44 ± 0.14	1.452	8.9 ± 0.9
1442.01	10.09 ± 0.02	24.26 ± 0.04	3330 ± 160	4.92 ± 0.01	0.31 ± 0.01	1350 ± 80	1.24 ± 0.05	0.409	10.3 ± 0.7
1693.01	8.33 ± 0.02	32.44 ± 0.04	3470 ± 160	4.77 ± 0.01	0.46 ± 0.01	1010 ± 120	1.60 ± 0.11	1.767	7.8 ± 1.1
1860.01	6.79 ± 0.02	21.78 ± 0.03	5670 ± 100	4.51 ± 0.07	0.93 ± 0.04	232 ± 29	1.54 ± 0.12	1.066	11.1 ± 1.5
2260.01	8.68 ± 0.02	9.85 ± 0.03	5430 ± 130	4.51 ± 0.08	0.90 ± 0.05	313 ± 35	1.73 ± 0.13	0.352	10.5 ± 1.3
2290.01	9.07 ± 0.02	17.19 ± 0.02	3860 ± 160	4.68 ± 0.01	0.57 ± 0.02	600 ± 60	1.51 ± 0.09	0.386	11.8 ± 1.2
2411.01	8.53 ± 0.02	16.77 ± 0.08	4100 ± 120	4.52 ± 0.11	0.73 ± 0.07	520 ± 50	1.81 ± 0.19	0.783	10.7 ± 1.4
2427.01	7.05 ± 0.02	35.04 ± 0.03	4070 ± 120	4.58 ± 0.11	0.68 ± 0.06	560 ± 24	1.75 ± 0.17	1.306	15.6 ± 1.6
2445.01	10.78 ± 0.02	20.56 ± 0.10	3330 ± 160	4.96 ± 0.01	0.27 ± 0.01	2400 ± 400	1.44 ± 0.12	0.371	13.0 ± 2.0

Table 3.1: TOI parameters from TICv8.1 and ExoFOP.

TOI	$R_{\rm p}$ ($R_\oplus$)	$P_{\rm orb}$ (days)	T_0 (BJD - 2457000)	b	a (AU)	$T_{\rm eq}$ (K)	ESM
206.01	1.30 ± 0.05	0.7363104 ± 0.0000003	1325.5431 ± 0.0004	0.66 ± 0.03	0.0112 ± 0.0001	910 ± 36	6.4 ± 0.5
500.01	1.16 ± 0.12	0.5481579 ± 0.0000006	1468.3917 ± 0.0006	0.58 ± 0.17	0.0128 ± 0.0011	1693 ± 105	7.3 ± 1.2
539.01	1.25 ± 0.10	0.3096071 ± 0.0000004	1354.1044 ± 0.0009	0.39 ± 0.20	0.0089 ± 0.0007	2311 ± 108	5.1 ± 0.6
544.01	2.03 ± 0.10	1.5483510 ± 0.0000015	1469.7570 ± 0.0005	0.64 ± 0.08	0.0251 ± 0.0019	1082 ± 47	13.0 ± 1.8
731.01	0.59 ± 0.02	0.3219659 ± 0.0000004	1543.4874 ± 0.0006	0.09 ± 0.07	0.0069 ± 0.0001	1416 ± 65	11.5 ± 0.6
833.01	1.27 ± 0.07	1.0418777 ± 0.0000324	1597.2560 ± 0.0010	0.31 ± 0.14	0.0171 ± 0.0003	1118 ± 49	6.5 ± 0.6
1075.01	1.72 ± 0.08	0.6047328 ± 0.0000032	1654.2511 ± 0.0008	0.18 ± 0.12	0.0118 ± 0.0001	1336 ± 56	10.9 ± 1.0
1242.01	1.65 ± 0.23	0.3814851 ± 0.0000004	1683.7103 ± 0.0004	0.40 ± 0.22	0.0097 ± 0.0010	1751 ± 110	7.7 ± 1.4
1263.01	1.36 ± 0.11	1.0213646 ± 0.0001277	1683.5569 ± 0.0018	0.37 ± 0.19	0.0185 ± 0.0014	1656 ± 75	9.2 ± 1.3
1411.01	1.36 ± 0.16	1.4520358 ± 0.0000098	1739.4762 ± 0.0014	0.32 ± 0.20	0.0230 ± 0.0026	1136 ± 59	7.6 ± 1.1
1442.01	1.17 ± 0.06	0.4090677 ± 0.0000003	1683.4523 ± 0.0003	0.33 ± 0.13	0.0071 ± 0.0002	1072 ± 54	8.9 ± 0.8
1693.01	1.41 ± 0.10	1.7666957 ± 0.0000054	1817.6827 ± 0.0014	0.30 ± 0.14	0.0226 ± 0.0004	764 ± 19	6.0 ± 0.9
1860.01	1.31 ± 0.04	1.0662107 ± 0.0000014	1683.6041 ± 0.0003	0.69 ± 0.02	0.0204 ± 0.0002	1885 ± 28	7.9 ± 0.4
2260.01	1.62 ± 0.13	0.3524728 ± 0.0000047	1928.2390 ± 0.0007	0.77 ± 0.04	0.0097 ± 0.0001	2609 ± 86	8.7 ± 0.9
2290.01	1.17 ± 0.07	0.3862224 ± 0.0000033	1764.9871 ± 0.0013	0.27 ± 0.15	0.0086 ± 0.0001	1484 ± 31	7.1 ± 0.8
2411.01	1.68 ± 0.11	0.7826942 ± 0.0000037	2116.0139 ± 0.0010	0.39 ± 0.14	0.0144 ± 0.0001	1355 ± 45	9.9 ± 1.2
2427.01	1.80 ± 0.12	1.3060011 ± 0.0000102	2169.6202 ± 0.0004	0.87 ± 0.02	0.0202 ± 0.0002	1117 ± 46	17.2 ± 2.1
2445.01	1.25 ± 0.08	0.3711281 ± 0.0000005	2144.5697 ± 0.0004	0.27 ± 0.14	0.0064 ± 0.0001	1060 ± 54	9.6 ± 1.2

Table 3.2: Best fit planet parameters.

Light Curve Generation

All of our TOIs were identified by the NASA Science Processing Operations Center (SPOC) pipeline (Jenkins et al. 2016), which analyzes data collected at a 2-minute or 20-second cadence. The SPOC pipeline identifies potential TOIs by conducting a search for transiting planet signatures using a wavelet-based, adaptive noise-compensating matched filter with the Transiting Planet Search (TPS; Jenkins 2002; Jenkins et al. 2010) algorithm. It then performs a limb-darkened transit model fit to the detected signatures (Li et al. 2019) and constructs a number of diagnostic tests to help assess the planetary nature of the detected signals (Twicken et al. 2018), which are compiled in data validation reports. The pipeline then removes the transits of each potential signature and calls TPS to detect additional transiting planet signatures, stopping when it fails to identify additional transits or reaches a limit of eight detected signatures. The SPOC pipeline generates two light curves for each TOI: light curves extracted via simple aperture photometry (SAP; Morris et al. 2020; Twicken et al. 2010), and light curves extracted via SAP with an additional presearch data conditioning step (PDCSAP; Smith et al. 2012; Stumpe et al. 2012, 2014). The PDC step aids in planet detection by removing background trends and flux contamination due to nearby bright stars, a process that is well-established in exoplanet transit surveys (Stumpe et al. 2012).

While the SPOC pipeline typically generates light curves that are sufficient for analyzing transits, it is not designed to preserve out-of-transit variation originating from the system. Because we are interested in whether our planet candidates show evidence of phase curves caused by reflected light in the *TESS* data, we take a different approach to extracting light curves that detrends the instrument systematics and stellar rotation signal while preserving transits and potential eclipses. Firstly, using the same approach as that discussed in Hedges et al. (2021), we build design matrices consisting of 1) an estimate of the *TESS* scattered light background base on the top 4 principal components of the pixels outside of the optimum pipeline aperture, estimated via Singular Value Decomposition, 2) a basis spline with a knot spacing of 0.25 days to capture stellar variability, 3) the centroids of the image in column and row dimension, 4) the single scale Cotrending Basis Vectors from the *TESS* pipeline, 5) a simple BLS transit model, at a fixed period, transit mid point, and duration, and 6) a simple eclipse model, consisting of a cosine phase curve and a simple box eclipse at phase 0.5. Using the same methods from Hedges et al. (2020), we fit these design matrices to all sectors simultaneously, fitting a single transit and a single eclipse model for all sectors, but allowing each individual sector to have unique solutions for the background, spline, centroid and CBV matrices. By taking this approach of fitting all the sectors simultaneously, we are the most sensitive to the small signal of eclipses, since all sectors are able to contribute to our eclipse measurement. Even with this rigorous approach, we detect no eclipse with a $\geq 3\sigma$ significance for the planet candidates in this paper.

Our light curve generation code does not subtract out contamination due to nearby stars, which is an important step for correctly determining the radius of a planet candidate. However, because the code uses the same apertures as the SPOC pipeline, we are able to

TOI	$T_{\rm eff}$ (K)	$\log g$	$M_\star$ ($M_\odot$)	$R_\star$ ($R_\odot$)
206	3383 ± 157	4.89 ± 0.03	0.35 ± 0.01	0.35 ± 0.01
500	4621 ± 50	4.63 ± 0.10	0.88 ± 0.25	0.75 ± 0.06
539	5031 ± 50	4.58 ± 0.10	0.91 ± 0.24	0.81 ± 0.05
544	4369 ± 100	4.73 ± 0.10	0.85 ± 0.20	0.66 ± 0.02
731	3540 ± 160	4.79 ± 0.03	0.48 ± 0.03	0.46 ± 0.01
833	3920 ± 160	4.67 ± 0.04	0.61 ± 0.03	0.60 ± 0.02
1075	3921 ± 157	4.69 ± 0.03	0.60 ± 0.02	0.58 ± 0.02
1242	4348 ± 100	4.69 ± 0.10	0.83 ± 0.31	0.68 ± 0.10
1263	5166 ± 50	4.54 ± 0.10	0.78 ± 0.20	0.82 ± 0.05
1411	4266 ± 100	4.73 ± 0.10	0.59 ± 0.23	0.66 ± 0.10
1442	3330 ± 160	4.92 ± 0.04	0.29 ± 0.02	0.31 ± 0.01
1693	3499 ± 70	4.80 ± 0.03	0.49 ± 0.03	0.46 ± 0.01
1835	5336 ± 100	4.65 ± 0.10	0.83 ± 0.03	0.79 ± 0.02
1860	5752 ± 100	4.58 ± 0.10	0.99 ± 0.03	0.94 ± 0.02
2260	5534 ± 100	4.62 ± 0.10	0.99 ± 0.04	0.94 ± 0.05
2290	3813 ± 70	4.70 ± 0.02	0.56 ± 0.01	0.57 ± 0.02
2411	4099 ± 123	4.59 ± 0.03	0.65 ± 0.02	0.68 ± 0.02
2427	4072 ± 121	4.62 ± 0.03	0.64 ± 0.02	0.65 ± 0.02
2445	3333 ± 157	4.97 ± 0.04	0.25 ± 0.01	0.27 ± 0.01

Table 3.3: Adopted stellar parameters.

remove contamination using the crowding factor (labeled as `CROWDSAP` in the PDCSAP FITS headers) for each of our targets. We perform this subtraction when fitting the photometry for the orbital and physical parameters of the planet candidates, which is further described in Section 3.2.

Adopted Stellar Parameters

We adopt stellar parameters for each of our host stars using a combination of spectrum analysis and empirical relation. The tools used to calculate stellar parameters from spectra are outlined in Section 3.4 and the empirical relations used to calculate stellar parameters are described below. Because different methods yield different parameters (e.g., some spectrum-based analysis methods only provide effective temperature and surface gravity, whereas others also provide estimates for stellar mass and radius), we take a curated approach for each of our stars. We describe this process in detail here and present the adopted parameters in Table 3.3.

When available, we use spectra to estimate $T_{\rm eff}$. Where more than one spectrum-based estimate of $T_{\rm eff}$ is available, we adopt the average of the estimates. If spectra are not available,

or if our stellar classification tools are unable to estimate parameters for a given star (which is sometimes the case for stars with $T_{\rm eff} \leq 4500$ K), we adopt the $T_{\rm eff}$ listed in the TIC.

For stars with observed with Keck/HIRES and $T_{\rm eff} > 4250$ K, we adopt the $R_\star$ estimated from the spectrum. For all other stars with $T_{\rm eff} > 4250$ K, we adopt the $R_\star$ listed in the TIC. For all stars with $T_{\rm eff} \leq 4250$ K, we estimate $R_\star$ and its uncertainties with the calibrations by Mann et al. (2015), using the 2MASS $K_{\rm S}$-band magnitudes and *Gaia* DR2 parallaxes.

For stars with observed with Keck/HIRES and $T_{\rm eff} > 4700$ K, we adopt the stellar mass ($M_\star$) estimated from the spectrum. For all other stars with observed spectra and $T_{\rm eff} > 4250$ K, we calculate $M_\star$ using the $R_\star$ listed in the TIC and the surface gravity estimated from the spectra. For all stars with $T_{\rm eff} \leq 4250$ K, we estimate $M_\star$ with the near-infrared mass-luminosity calibrations in Mann et al. (2015) and Benedict et al. (2016) (adopting the average of the two), using the 2MASS $K_{\rm S}$-band magnitudes and *Gaia* DR2 parallaxes.

For stars with observed spectra and $T_{\rm eff} > 4250$ K, we adopt the surface gravity ($\log g$) estimated from the spectra. Where more than one spectrum-based estimate of $\log g$ is available, we adopt the average of the estimates. For all other stars, $\log g$ is calculated using the values of $M_\star$ and $R_\star$ determined with the methods described above.

Transit Fits

To estimate the orbital and planetary parameters for each of our planet candidates, we fit each of our light curves with Markov chain Monte Carlo sampling using the `exoplanet` (Foreman-Mackey et al. 2021) python package. Our transit model assumed a circular orbit and was initialized with the following priors: (1) Gaussian priors for $M_\star$ and $R_\star$, (2) a Gaussian prior for the natural logarithm of $P_{\rm orb}$, (3) a Gaussian prior for the time of inferior conjunction (T_0), (4) a uniform prior for the impact parameter (b), (5) uniform priors for quadratic limb darkening coefficients (Kipping 2013a), (6) a Gaussian prior for the natural logarithm of the transit depth, and (7) a Gaussian prior for the flux zero point of the light curve. For each TOI, we ran a 10 walker ensemble for 20000 steps and ensured that convergence was achieved, then discarded the first 10000 steps as burn-in. The best-fit parameters for each planet candidate are shown in Table 3.2 and the corresponding best-fit light curve models are shown in Figure 3.1.

For most of the TOIs in this paper, these fits only included *TESS* data. However, transits of TOI-206.01, TOI-1075.01, TOI-1442.01, TOI-1693.01, TOI-2411.01, TOI-2411.01, TOI-2427.01, and TOI-2445.01 were also had observed by ground-based telescopes. For these targets, we perform joint fits including both the *TESS* data and the ground-based data. We fit for limb darkening coefficients, transit depth, and flux zero point independently for each dataset while treating $M_\star$, $R_\star$, $P_{\rm orb}$, T_0, and b as parameters that are shared between the datasets. The ground-based data is discussed in Section 3.4. In these cases, we adopt the planet radii inferred from the *TESS* data.

Using these new planet properties, we recalculate the ESM for each TOI. All TOIs except for TOI-206.01, TOI-500.01, TOI-539.01, and TOI-1693.01 retained an ESM > 7.5. In addition, we find that TOI-544.01 may have a radius slightly larger than $2R_\oplus$. Even

though these TOIs do not meet our initial selection criteria with their newly calculated properties, we keep them in our analysis.

3.3 Vetting Procedure

We examine each of the unconfirmed TOIs described in Table 4.1 using both follow-up observations and analyses with the vetting tools `dave` (Kostov et al. 2019) and `TRICERATOPS` (Giacalone and Dressing 2020; Giacalone et al. 2021). Follow-up observations are used to search for evidence of false positives outside of the *TESS* data, while `dave` and `TRICERATOPS` are used to search for false positive signatures within the *TESS* data.

We utilize three forms of follow-up observations in our vetting analysis. First, we acquired high-resolution images, such as those obtainable with adaptive optics, to search for unresolved companions (either bound or chance-aligned) near the target. These companions can dilute the *TESS* transit, leading to an underestimation in the planet radius, or can even be the sources of false positives if the companion hosts an eclipsing binary (Ciardi et al. 2015; Furlan et al. 2017; Hirsch et al. 2017; Teske et al. 2018). Second, we obtained reconnaissance spectra to search for evidence of spectroscopic binaries around the target stars. Evidence of a binary star in the form of single-line or double-line spectroscopic binaries could either indicate that the planet candidate itself is an eclipsing binary or that there is an unresolved star in the system causing us to underestimate the radius of the planet candidate. In addition, deriving stellar parameters from spectra allows us to reaffirm the photometrically-derived parameters in the TIC, which is important for a correct calculation of the planet radius and equilibrium temperature. Third, we used ground-based facilities with higher spatial resolutions than *TESS* to obtain time-series photometry of the field of stars within $2\farcm5$ from the target during the time of transit. Because it is possible for nearby stars to contaminate the *TESS* aperture, transits due to nreaby eclipsing binary stars can be mistakable as transits due to planet-size objects around the target star. These scenarios can be ruled out by either observing the transit on the target star, free of any contamination from nearby stars, or ruling out eclipsing binaries around all nearby stars bright enough to cause a false positive. These observations are further described in Section 3.4.

Next, we analyze each TOI with `dave`, which vets planet candidates at both the pixel and light curve level. At the pixel level, `dave` uses centroid offset analyses to identify evidence of false positives due to contamination from nearby stars. A similar difference image centroiding analysis is performed by the SPOC for each of its Threshold Crossing Events (TCEs; Twicken et al. 2018). For all TOIs, we cross-check with the corresponding SPOC data validation report to see if an offset is detected in the SPOC analysis. At the light curve level, `dave` searches for signatures – such as differences in odd and even transits, secondary eclipses, and non-transit variability – that are indicative of false positives (e.g., Ansdell et al. 2018; Morton 2012; Shallue and Vanderburg 2018). For these analyses, we use the SAP/PDCSAP light curves generated by the SPOC pipeline.

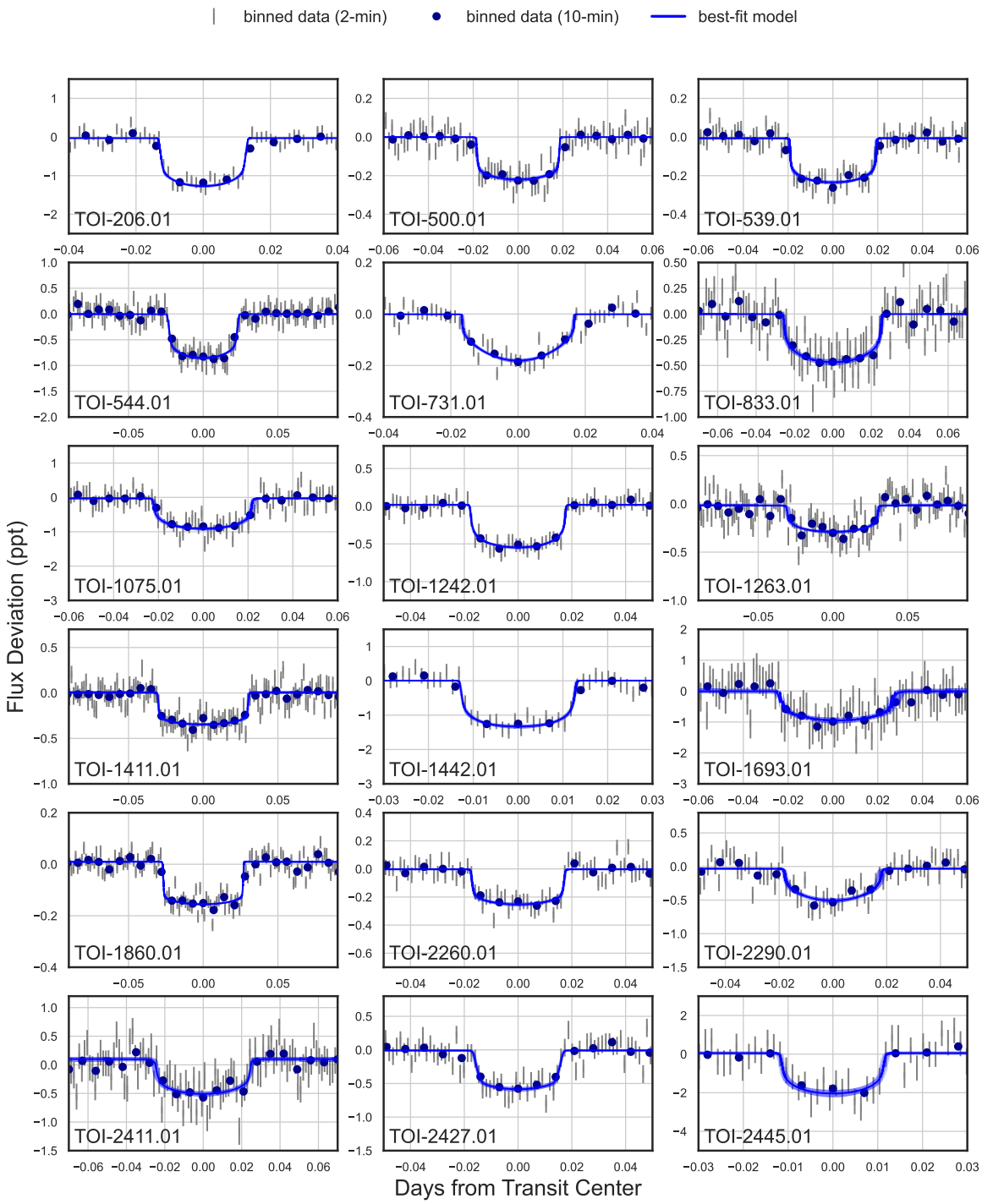

Figure 3.1: Phase-folded *TESS* data and best-fit transit models for each TOI. The parameters associated with these fits are shown in Table 3.2. The *TESS* data is purged of 5σ outliers and binned for clarity.

Lastly, we analyze each TOI using `TRICERATOPS`, which vets a planet candidate by calculating the Bayesian probability that the candidate is an astrophysical false positive. The analysis begins by querying the TIC for all stars in a 2.′5 radius around the target star and modeling the *TESS* pixel response function to determine the amount of flux contamination each contributes to the aperture. For each star that contributes enough flux to cause the observed transit, the tool simulates light curves due to transiting planets and eclipsing binaries and calculates the marginal likelihood of each transit-producing scenario. These are combined with prior probabilities to calculate the false positive probability (FPP, the total probability that the observed transit is due to something other than a transiting planet around the target star) and nearby false positive probability (NFPP, the total probability that the observed transit originated from a known nearby star) for the planet candidate. A planet candidate that achieves a sufficiently small FPP (FPP < 0.01) and NFPP (NFPP $< 10^{-3}$) can be considered validated (Giacalone et al. 2021). For this analysis, we use the same light curves generated using the methodology described in Section 3.2 (without contamination due to nearby stars removed with the `CROWDSAP` factor). Because the FPPs and NFPPs returned by `TRICERATOPS` have an intrinsic scatter, we run the tool 20 times on each TOI and report the means and standard deviations of these probabilities. Ultimately, we decide whether a planet is validated based on the results of this analysis.

`TRICERATOPS` also has the ability to fold in follow-up observations to place tighter constraints on the chances of false positive scenarios. Specifically, high-resolution images are used to constrain the area of sky around the target that unresolved companion stars can exist. Folding in this data therefore reduces the probabilities of scenarios like those involving hierarchical and background eclipsing binaries. In addition, time-series photometry allows us to remove nearby stars that have been cleared from being eclipsing binaries from the analysis. When available, we utilized this data during this step of vetting.

3.4 Follow-Up Observations

We analyze our TOIs using observations obtained by the *TESS* Follow-up Observing Program (TFOP) Working Groups.[4] The data from these observations are available for download on the ExoFOP-*TESS* website and are summarized below.

High-Resolution Imaging

We obtained high-resolution images of our TOIs using adaptive optics, speckle, and lucky imaging. In each of these observations, we search for stars with 5″ from the target star. In situations where companions were detected, we cross-checked the TIC to determine if these companions were previously known. These observations, which were obtained by members of TFOP Sub Group 3 (SG3), are summarized in Table 3.4, are displayed in Figure 3.2, and are discussed below.

[4]https://tess.mit.edu/followup

TOI	Telescope	Instrument	Filter	Image Type	Companion	Contrast (Δ mag)				
					($< 5''$)	$0\farcs1$	$0\farcs5$	$1\farcs0$	$1\farcs5$	$2\farcs0$
206	SOAR (4.1 m)	HRCam	I_c	Speckle	-	1.625	4.323	4.641	4.958	5.275
	Gemini-S (8 m)	Zorro	562 nm	Speckle	-	4.115	4.398	4.309	-	-
	Gemini-S (8 m)	Zorro	832 nm	Speckle	-	4.908	5.787	6.081	-	-
500	SOAR (4.1 m)	HRCam	I_c	Speckle	-	1.721	4.738	5.164	5.591	6.017
	Gemini-S (8 m)	Zorro	562 nm	Speckle	-	5.307	6.083	6.564	-	-
	Gemini-S (8 m)	Zorro	832 nm	Speckle	-	5.057	6.441	7.386	-	-
539	SOAR (4.1 m)	HRCam	I_c	Speckle	-	1.660	5.238	5.462	5.686	5.910
544	CAHA (2.2 m)	AstraLux	SDSSz	Lucky	-	2.614	6.015	4.053	-	-
	Shane (3 m)	ShARCS	K_s	AO	-	0.588	3.272	4.774	5.816	6.625
	Shane (3 m)	ShARCS	J	AO	-	0.842	3.223	4.713	5.940	6.872
	WIYN (3.5 m)	NESSI	562 nm	Speckle	-	1.817	4.431	4.856	-	-
	WIYN (3.5 m)	NESSI	832 nm	Speckle	-	1.646	5.025	5.933	-	-
	SOAR (4.1 m)	HRCam	I_c	Speckle	-	1.903	5.370	5.629	5.887	6.145
731	Gemini-S (8 m)	DSSI	692 nm	Speckle	-	4.721	6.998	7.872	-	-
	Gemini-S (8 m)	DSSI	880 nm	Speckle	-	4.498	6.470	6.889	-	-
833	SOAR (4.1 m)	HRCam	I_c	Speckle	-	1.922	5.068	5.285	5.503	5.720
	Gemini-S (8 m)	Zorro	562 nm	Speckle	-	4.319	4.752	4.932	-	-
	Gemini-S (8 m)	Zorro	832 nm	Speckle	-	5.162	6.805	8.119	-	-
1075	SOAR (4.1 m)	HRCam	I_c	Speckle	-	1.708	4.990	5.310	5.631	5.9518
	Gemini-S (8 m)	Zorro	562 nm	Speckle	-	4.061	4.278	4.429	-	-
	Gemini-S (8 m)	Zorro	832 nm	Speckle	-	5.009	5.653	6.126	-	-
1242	CAHA (2.2 m)	AstraLux	SDSSz	Lucky	-	2.143	4.128	4.047	3.898	-
	Shane (3 m)	ShARCS	K_s	AO	Y	0.438	2.039	3.549	4.641	5.567
	Shane (3 m)	ShARCS	J	AO	Y	0.237	1.186	2.313	3.304	4.055
	Gemini-N (8 m)	'Alopeke	562 nm	Speckle	-	3.718	3.980	4.017	-	-
	Gemini-N (8 m)	'Alopeke	832 nm	Speckle	-	4.551	6.087	6.856	-	-
1263	WIYN (3.5 m)	NESSI	562 nm	Speckle	-	1.690	3.799	4.049	-	-
	WIYN (3.5 m)	NESSI	832 nm	Speckle	-	1.679	5.066	5.533	-	-
	SOAR (4.1 m)	HRCam	I_c	Speckle	Y	1.782	4.081	4.565	5.049	5.532
	Palomar (5 m)	PHARO	Brγ	AO	Y	1.716	6.869	8.648	9.145	9.275
	Palomar (5 m)	PHARO	Hcont	AO	Y	1.986	7.769	8.965	9.618	9.685
1411	CAHA (2.2 m)	AstraLux	SDSSz	Lucky	-	2.368	4.425	4.461	4.309	
	Palomar (5 m)	PHARO	Brγ	AO	-	1.789	6.912	8.190	9.017	9.241
	Gemini-N (8 m)	'Alopeke	562 nm	Speckle	-	4.333	5.609	5.877	-	-
	Gemini-N (8 m)	'Alopeke	832 nm	Speckle	-	4.414	7.160	8.496	-	-
	Keck (10 m)	NIRC2	K_s	AO	-	3.892	7.574	8.308	8.317	8.312
1442	Gemini-N (8 m)	'Alopeke	562 nm	Speckle	-	3.644	3.867	4.060	-	-
	Gemini-N (8 m)	'Alopeke	832 nm	Speckle	-	4.703	5.622	6.118	-	-
	Keck (10 m)	NIRC2	K	AO	-	3.905	7.638	7.801	7.837	7.782
1693	Shane (3 m)	ShARCS	K_s	AO	-	0.610	2.790	4.155	5.208	6.081
	Palomar (5 m)	PHARO	Brγ	AO	-	2.751	6.982	8.411	8.847	8.916
	Gemini-N (8 m)	'Alopeke	562 nm	Speckle	-	4.380	4.803	4.958	-	-
	Gemini-N (8 m)	'Alopeke	832 nm	Speckle	-	4.979	6.440	7.443	-	-
1860	Shane (3 m)	ShARCS	Brγ	AO	-	0.592	3.287	4.598	5.096	5.669
	Palomar (5 m)	PHARO	Brγ	AO	-	2.366	6.873	8.346	8.984	9.051
	Gemini-N (8 m)	'Alopeke	562 nm	Speckle	-	4.659	5.327	5.631	-	-
	Gemini-N (8 m)	'Alopeke	832 nm	Speckle	-	4.984	7.356	8.978	-	-
2260	CAHA (2.2 m)	AstraLux	SDSSz	Lucky	-	2.456	5.399	5.666	-	-
	SAI (2.5 m)	SPP	I_c	Speckle	-	2.548	5.293	6.406	-	-
	Shane (3 m)	ShARCS	K_s	AO	-	0.564	2.740	4.142	5.139	6.027
	Shane (3 m)	ShARCS	J	AO	-	0.547	2.345	3.799	5.040	5.968
	Palomar (5 m)	PHARO	Brγ	AO	-	2.875	6.920	8.418	8.983	9.106
	Gemini-N (8 m)	'Alopeke	562 nm	Speckle	-	4.688	5.674	6.283	-	-
	Gemini-N (8 m)	'Alopeke	832 nm	Speckle	-	4.539	6.577	8.384	-	-
2290	SAI (2.5 m)	SPP	I_c	Speckle	-	1.207	5.176	6.509	-	-
	Gemini-N (8 m)	'Alopeke	562 nm	Speckle	-	3.740	4.231	4.424	-	-
	Gemini-N (8 m)	'Alopeke	832 nm	Speckle	-	4.965	6.128	7.071	-	-
	Keck (10 m)	NIRC2	K	AO	-	3.755	7.169	7.276	7.254	7.181
2411	SOAR (4.1 m)	HRCam	I_c	Speckle	-	1.844	5.776	6.031	6.286	6.541
	Palomar (5 m)	PHARO	Brγ	AO	-	2.566	7.197	8.199	8.637	8.712

	Keck (10 m)	NIRC2	Brγ	AO	-	3.906	6.505	6.552	6.476	6.483
2427	SOAR (4.1 m)	HRCam	I_c	Speckle	-	1.955	5.434	5.758	6.083	6.408
	Keck (10 m)	NIRC2	Brγ	AO	-	3.949	5.908	5.972	5.891	5.922
2445	Palomar (5 m)	PHARO	Brγ	AO	-	2.608	6.876	7.527	7.571	7.623
	Keck (10 m)	NIRC2	K	AO	-	3.955	6.939	6.904	6.912	6.895

Table 3.4: Summary of high-resolution imaging follow up.

CAHA/AstraLux

TOI-544, TOI-1238, TOI-1242, TOI-1411, TOI-1685, and TOI-2260 were observed with the high-spatial resolution imaging instrument AstraLux (Hormuth et al. 2008) mounted on the 2.2 m telescope at Calar Alto Observatory (CAHA; Almería, Spain). The instrument uses the lucky-imaging technique (Fried 1978) by combining a fast readout and a small plate scale to obtain thousands of images with exposure times below the speckle coherence time and using the Sloan Digital Sky Survey z filter (SDSSz). We observed TOI-1411 on UT 2020-01-13, TOI-1242 on UT 2020-02-26, TOI-1238 and TOI-1685 on UT 2020-08-07, and TOI-544 and TOI-2260 on UT 2021-03-23. We used the following strategy for each target: 7 000 frames of 10 ms exposure time to TOI-544, 126 500 frames of 20 ms for TOI-1238, 12 055 frames of 20 ms for TOI-1242, 98 600 frames of 10 ms for TOI-1411, 87 600 frames of 20 ms for TOI-1685, and 166 860 frames of 10 ms for TOI-2260. The number of frames and exposure time was adapted to achieve a magnitude contrast at 1″ separation that would allow us to discard chance-aligned binaries mimicking the same transit depth as the planet candidates (see Lillo-Box et al. 2012, 2014). We choose a $6'' \times 6''$ field-of-view in order to be able to reduce the individual exposure time down to the 10 ms level to improve the close-by sensitivity.

The datacubes were then reduced using the observatory pipeline (Hormuth et al. 2008). As a compromise between magnitude sensitivity and spatial resolution, we selected the 10% of the best frames according to their Strehl ratio (Strehl 1902) and then aligned and combined these images to compute a final high-spatial resolution image per target. We computed the 5σ sensitivity curves for each of the images by using our own developed `astrasens` package[5] with the procedure described in Lillo-Box et al. (2014). We found no stellar companions within these computed sensitivity limits.

SAI/SPP

TOI-2260 and TOI-2290 were observed on UT 2021-02-02 and 2020-10-28, respectively, with the SPeckle Polarimeter (SPP; Safonov et al. 2017) on the 2.5 m telescope at the Caucasian Observatory of Sternberg Astronomical Institute (SAI) of Lomonosov Moscow State University. SPP uses an Electron Multiplying CCD Andor iXon 897 as a detector. The atmospheric dispersion compensator allowed for observations of these relatively faint targets through the wide-band I_c filter. Power spectra were estimated from 4000 frames with 30 ms exposures.

[5] `https://github.com/jlillo/astrasens`

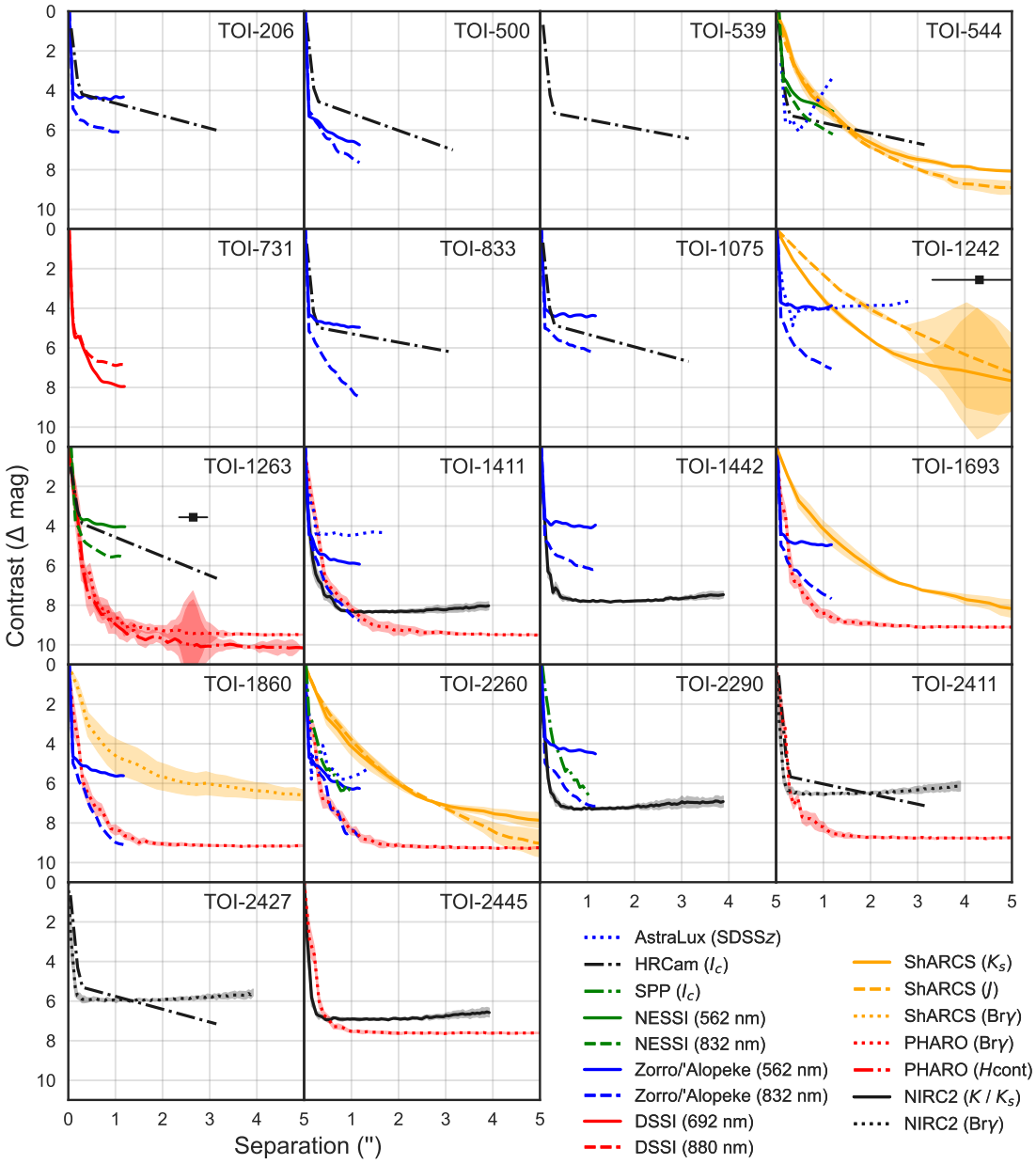

Figure 3.2: Contrast curves extracted from the high-resolution follow up summarized in Table 3.4, which allows us to rule out companions at a given separation above a certain Δ mag. Curves without shading (i.e., those from lucky and speckle imaging) were constructing by taking the 5σ upper limits of the contrasts in circular annuli around the target star. Curves with shading (i.e., those from adaptive optics imaging) were constructed by taking the mean and root-mean-square error of the contrasts in circular annuli around the target star. TOI-1242 and TOI-1263 have $< 5''$ companions, which are both known stars in the TIC. The *TESS* band Δ mags and separations of these companions are indicated by black squares. These curves are folded into the `TRICERATOPS` analysis described in Section 3.3.

The detector has a pixel scale of 20.6 mas/pixel. We did not detect any stellar companions in our observations. The 5σ sensitivity curves are presented in Figure 3.2.

WIYN/NESSI

We observed TOI-544 and TOI-1263 on UT 2019-10-12 and 2019-11-16, respectively, with the NN-Explore Exoplanet Stellar Speckle Imager (NESSI; Scott and Howell 2018; Scott et al. 2018) mounted on the 3.5 m WIYN telescope at Kitt Peak. High-speed electron-multiplying CCDs were used to capture image sequences simultaneously in two passbands at 562 and 832 nm. Data were acquired and reduced following Howell et al. (2011), yielding the 5σ contrast curves shown in Figure 3.2. No secondary sources were detected within the reconstructed $4.6'' \times 4.6''$ images.

SOAR/HRCam

We utilize speckle interferometric observations of TOI-206, TOI-500, TOI-539, TOI-544, TOI-833, TOI-1075, TOI-1263, TOI-1835, TOI-2411, and TOI-1427 taken with HRCam mounted on the 4.1m Southern Astrophysical Research (SOAR) telescope. These observations and their related analyses are outlined in Ziegler et al. (2020) and Ziegler et al. (2021). We refer the reader to those papers for more information.

Shane/ShARCS

We observed TOI-544, TOI-1242, TOI-1693, TOI-1835, TOI-1860, TOI-2260 using the ShARCS camera on the Shane 3 m telescope at Lick Observatory (Gavel et al. 2014; Kupke et al. 2012) on UT 2019-09-13, 2021-03-05, 2020-12-02, 2020-12-02, 2020-12-02, and 2021-03-29, respectively. Observations were taken using the Shane adaptive optics (AO) system in natural guide star mode. We collected our observations using a 4-point dither pattern with a separation of $4''$ between each dither position. For TOI-544, TOI-1242, and TOI-2260 we obtained observations with the K_s filter ($\lambda_o = 2.150; \Delta\lambda = 0.320\mu$m) and the J filter ($\lambda_o = 1.238; \Delta\lambda = 0.271\mu$m). For TOI-1242, we detected a $\sim 4\farcs3$ companion in both filters. For TOI-1693 we obtained observations with only the K_s filter. For TOI-1835 and TOI-1860 we obtained observations with only the narrow-band Brγ filter ($\lambda_o = 2.167; \Delta\lambda = 0.020\mu$m). See Savel et al. (2020) for a detailed description of the observing strategy and reduction procedure.

Palomar/PHARO

The Palomar Observatory observations of TOI-1263, TOI-1693, TOI-1860, TOI-1411, TOI-2260, TOI-2411, and TOI-2445 were made with the PHARO instrument (Hayward et al. 2001) behind the natural guide star AO system P3K (Dekany et al. 2013) on UT 2019-06-13, 2021-09-19, 2021-06-21, 2020-01-08, 2021-03-03, 2021-08-23, and 2021-09-20, respectively, in a standard 5-point quincunx dither pattern with steps of $5''$. Each dither position was

observed three times, offset in position from each other by 0.″5, for a total of 15 frames. The camera was in the narrow-angle mode with a full field of view of $\sim 25''$ and a pixel scale of approximately $0.025''$ per pixel. Observations were made in the narrow-band Brγ filter ($\lambda_o = 2.1686; \Delta\lambda = 0.0326\mu$m) for the three targets. TOI-1263, which was detected to have a $\sim 2.''6$ companion, was also observed in the Hcont ($\lambda_o = 1.668; \Delta\lambda = 0.018\mu$m) filter to enable a color-based determination of the bounded-ness (Lund and Ciardi 2020).

The AO data were processed and analyzed with a custom set of IDL tools. The science frames were flat-fielded and sky-subtracted. The flat fields were generated from a median average of dark subtracted flats taken on-sky. The flats were normalized such that the median value of the flats is unity. The sky frames were generated from the median average of the 15 dithered science frames; each science image was then sky-subtracted and flat-fielded. The reduced science frames were combined into a single combined image using a intra-pixel interpolation that conserves flux, shifts the individual dithered frames by the appropriate fractional pixels, and median-coadds the frames. The final resolution of the combined dither was determined from the full-width half-maximum of the point spread function which was typically $0.1''$.

Gemini-N/'Alopeke, Gemini-S/Zorro, and Gemini-S/DSSI

For TOI-206, TOI-500, TOI-833, TOI-1075, TOI-1242, TOI-1411, TOI-1442, TOI-1634, TOI-1693, TOI-1835, TOI-1860, TOI-2260, and TOI-2290, speckle interferometric observations were performed using 'Alopeke and Zorro, dual-channel high-resolution imaging instruments mounted on the Gemini 8-m North and South telescope, respectively (Scott and Howell 2018).[6] Those observations were obtained on UT 2020-12-26, 2020-03-16, 2020-01-12, 2019-09-12, 2020-02-17, 2020-06-07, 2020-06-07, 2020-12-02, 2020-02-18, 2020-06-10, 2020-06-08, 2021-06-24, and 2021-06-24 respectively.

Many thousands of 60 ms images were collected on two EMCCDs, each preceded by a narrow-band filter to minimize atmospheric dispersion. The full set of observations taken in 562 nm and 832 nm were then combined in Fourier space to produce their power spectrum and autocorrelation functions. From these, interferometric fringes were detected if a companion star was present within our $\sim 1.''2$ field of view, with an inner angle at the diffraction limit of the Gemini telescope. The data reduction pipeline produces final data products that include 5σ contrast curves and reconstructed images (Horch et al. 1996; Horch et al. 2012; Howell et al. 2011). The contrast curves at both 562 nm and 832 nm sample the spatial region near the target star from approximately 1 au to 50-100 au (depending on the distance to the target star) yielding contrast levels of 5-8 magnitudes.

For TOI-731, speckle interferometric observations were performed using the Differential Speckle Survey Instrument (DSSI; Horch et al. 2009), a dual-channel, high-resolution imager that allows simultaneous observations with filters centered at 692 nm and 880 nm. DSSI can

[6] `https://www.gemini.edu/instrumentation/current-instruments/alopeke-zorro/`

resolve binaries down to 20 mas. The observations were obtained on UT 2018-03-30 when DSSI was mounted on the Gemini-South 8-m telescope as a visiting instrument.

Keck/NIRC2

TOI-1411, TOI-1442, TOI-2290, TOI-2411, TOI-2427, and TOI-2445 were observed with the NIRC2 instrument on Keck-II behind the natural guide star AO system on UT 2020-09-09, 2020-05-28, 2021-08-28, 2021-08-28, 2021-08-24, and 2021-08-28 respectively. The observations were made in the standard 3-point dither pattern that is used with NIRC2 to avoid the left lower quadrant of the detector which is typically noisier than the other three quadrants. The dither pattern step size was 3″ and was repeated twice times offset from each other by 0.5″ for a total of 9 dithered observations. The observations for TOI-1411 were made in the K_s filter ($\lambda_o = 2.146; \Delta\lambda = 0.311\mu$m) and TOI-1442 were made in the K ($\lambda_o = 2.196; \Delta\lambda = 0.336\mu$m) filter. The camera was in the narrow-angle mode with a full field of view of $\sim 10''$ and a pixel scale of approximately 0.099442″ per pixel. The Keck AO observations revealed no additional stellar companions to within a resolution $\sim 0.05''$ FWHM. The data were processed and analyzed with the same software suite used for the Palomar PHARO observations.

Reconnaissance Spectroscopy

We obtained reconnaissance spectra of several of our TOIs to search for evidence of false positives and characterize the target stars. These spectra were obtained by members of TFOP Sub Group 2 (SG2). The observations and the stellar parameters extracted from the acquired spectra are summarized in Table 3.5. Further details on the observations and the analyses performed to search for false positive signatures and characterize the stars are provided below.

FLWO/TRES and NOT/FIES

We obtained reconnaissance spectra of TOI-544, TOI-1242, TOI-1263, TOI-1411, TOI-1693, TOI-1835, TOI-2290, TOI-2411, and TOI-2427 using the Tillinghast Reflector Echelle Spectrograph (TRES; Szentgyorgyi and Furész 2007) on the 1.5 m Tillinghast Reflector at the Fred L. Whipple Observatory (FLWO) on Mt. Hopkins, AZ. We also obtained reconnaissance spectra of TOI-1263, TOI-1835, and TOI-1860 using the high-resolution FIbre-fed Echelle Spectrograph (FIES; Telting et al. 2014) at the 2.56 m Nordic Optical Telescope (NOT) on La Palma, Spain. We analyzed the TRES and FIES spectra in order to rule out spectroscopic binaries and to confirm that the assumed luminosity classes were correct.

The TRES and FIES reconnaissance spectroscopic observations were analyzed using the Stellar Parameter Classification tool (SPC; Buchhave et al. 2012). In brief, SPC uses a correlation analysis of the observed spectra against a library of synthetic spectra calculated using Kurucz model atmospheres (Kurucz 1993a). SPC fits for the $T_{\rm eff}$, $\log g$, [M/H], and

TOI	Telescope	Instrument	$N_{\rm obs}$	$T_{\rm eff}$ (K)	$\log g$	$M_\star$ ($M_\odot$)	$R_\star$ ($R_\oplus$)	[Fe/H]	[M/H]	$v \sin i$ (km/s)
500	SMARTS (1.5 m)	CHIRON	2	4621 ± 50	4.63 ± 0.10	-	-	-	-0.22 ± 0.10	2.00 ± 0.50
539	SMARTS (1.5 m)	CHIRON	2	5031 ± 50	4.58 ± 0.10	-	-	-	-0.14 ± 0.10	3.30 ± 0.50
544	SMARTS (1.5 m)	CHIRON	4	-	-	-	-	-	-	-
	FLWO (1.5 m)	TRES	2	4369 ± 100	4.73 ± 0.10	-	-	-	-0.42 ± 0.08	1.80 ± 0.50
731	SMARTS (1.5 m)	CHIRON	2	-	-	-	-	-	-	-
833	SMARTS (1.5 m)	CHIRON	2	-	-	-	-	-	-	-
1075	SMARTS (1.5 m)	CHIRON	1	-	-	-	-	-	-	-
1242	FLWO (1.5 m)	TRES	2	4437 ± 100	4.69 ± 0.10	-	-	-	-0.13 ± 0.08	3.60 ± 0.50
	Keck (10 m)	HIRES	2	4259 ± 70	-	-	0.68 ± 0.10	0.00 ± 0.09	-	-
1263	FLWO (1.5 m)	TRES	1	5160 ± 50	4.58 ± 0.10	-	-	-	0.04 ± 0.08	2.10 ± 0.50
	NOT (2.56 m)	FIES	4	5172 ± 50	4.50 ± 0.10	-	-	-	0.00 ± 0.08	0.60 ± 0.50
1411	FLWO (1.5 m)	TRES	2	4352 ± 100	4.73 ± 0.10	-	-	-	-0.37 ± 0.08	2.00 ± 0.50
	Keck (10 m)	HIRES	2	4180 ± 70	-	-	0.66 ± 0.10	0.10 ± 0.09	-	-
1693	FLWO (1.5 m)	TRES	2	-	-	-	-	-	-	-
	Keck (10 m)	HIRES	1	3466 ± 70	-	-	0.44 ± 0.10	0.03 ± 0.09	-	-
1860	NOT (2.56 m)	FIES	1	5780 ± 50	4.54 ± 0.10	-	-	-	-0.09 ± 0.08	11.10 ± 0.50
	Keck (10 m)	HIRES	1	5724 ± 100	4.61 ± 0.10	0.99 ± 0.03	0.94 ± 0.02	0.04 ± 0.06	-	10.37 ± 1.00
2260	Keck (10 m)	HIRES	1	5534 ± 100	4.62 ± 0.10	0.99 ± 0.04	0.94 ± 0.05	0.22 ± 0.06	-	5.05 ± 1.00
2290	FLWO (1.5 m)	TRES	2	-	-	-	-	-	-	-
	Keck (10 m)	HIRES	1	3813 ± 70	-	-	0.57 ± 0.10	-0.03 ± 0.09	-	-
2411	SMARTS (1.5 m)	CHIRON	3	-	-	-	-	-	-	-
	FLWO (1.5 m)	TRES	2	-	-	-	-	-	-	-
2427	SMARTS (1.5 m)	CHIRON	2	-	-	-	-	-	-	-
	FLWO (1.5 m)	TRES	2	-	-	-	-	-	-	-

Table 3.5: Summary of reconnaissance spectroscopy follow up and derived stellar parameters. Spectrum-derived parameters for each TOI. Entries that list no stellar parameters correspond to stars too cool to have parameters extracted using data collected with the specified instrument.

projected rotational velocity ($v \sin i$) that give the highest peak correlation value using a multi-dimensional fit. We ran SPC with priors from the Yonsei-Yale isochrones on the fit (Yi et al. 2001). The library of calculated spectra used by SPC covers the following ranges: 3500 K $< T_{\rm eff} <$ 9750 K, 0.0 $< \log g <$ 5.0 (cgs), $-2.5 < [m/H] < +0.5$, and 0 km s^{-1} $< v sin\, i <$ 200 km s^{-1} (Buchhave et al. 2012). SPC is optimized for slow-rotating Solar type stars. Because it was not designed to classify cool stars ($T_{\rm eff} \lesssim 4000$ K), for TOI-544, TOI-1693, TOI-2290, TOI-2411, and TOI-2427 we used empirical relations in order to estimate the stellar parameters (see Section 3.2 for more info).

SMARTS/CHIRON

We obtained reconnaissance spectra of TOI-500, TOI-539, TOI-544, TOI-731, TOI-833, TOI-1075, TOI-2411, and TOI-2427 using the CHIRON spectrograph on the 1.5 m SMARTS telescope, located at Cerro Tololo Inter-American Observatory (CTIO), Chile (Tokovinin et al. 2013). The spectra were analyzed using a machine learning procedure based on $\sim 10,000$ TRES spectra classified by SPC and interpolated via a gradient boosting regressor that provides estimates of $T_{\rm eff}$, $\log g$, [M/H], and $v \sin i$. These classifications therefore suffer the same limitations as SPC for the coolest stars, so we estimate parameters for TOI-544, TOI-731, TOI-833, TOI-1075, TOI-2411, and TOI-2427 using the same empirical relations described in Section 3.2. The spectra for all four TOIs have cross-correlation profiles indicative of a single star and no significant RV variations.

Keck/HIRES

We obtained reconnaissance spectra of TOI-1242, TOI-1411, TOI-1693, TOI-1835, TOI-1860, TOI-2260, and TOI-2290 using the High Resolution Echelle Spectrometer (HIRES) (Vogt et al. 1994) mounted on the Keck-I 10 m telescope on Maunakea. Our HIRES spectra were analyzed to rule out double-lined spectroscopic binaries and confirm that the stars are not giants. To do the former, we used ReaMatch (Kolbl et al. 2015), which can identify double-line spectroscopic binaries with contamination ratios as small as 1%, to constrain the presence of unresolved binary stars near each TOI. To do the latter, we classified each star using SpecMatch Synthetic (Petigura 2015) and SpecMatch Empirical (Yee et al. 2017). SpecMatch Synthetic classifies stars by searching a multi-dimensional grid of synthetic spectra for that which best matches the observed spectrum. SpecMatch Empirical works similarly, but instead compares the observed spectrum to a library of spectra of well-characterized stars. The former provides estimates for $T_{\rm eff}$, $\log g$, $M_\star$, $R_\star$, [Fe/H], and $v \sin i$, while the latter provides estimates for $T_{\rm eff}$, $R_\star$, and [Fe/H]. Because SpecMatch Empirical outperforms SpecMatch Synthetic for cooler stars, we adopt the SpecMatch Empirical results for stars that SpecMatch Empirical determines to have $T_{\rm eff} < 4700$ K and we adopt the SpecMatch Synthetic results for stars that SpecMatch Empirical determines to have $T_{\rm eff} > 4700$ K.

In addition, we estimated the activity levels of targets observed with HIRES by calculating their $\log R'_{\rm HK}$ values (Linsky et al. 1979). In general, stars with higher $\log R'_{\rm HK}$ values are

TOI	[C/H]	[N/H]	[O/H]	[Na/H]	[Mg/H]	[Al/H]	[Si/H]	[Ca/H]	[Ti/H]	[V/H]	[Cr/H]	[Mn/H]	[Fe/H]	[Ni/H]	[Y/H]
1860	0.04	-0.05	0.15	-0.05	-0.03	-0.06	0.00	0.14	0.09	0.09	0.09	0.02	0.09	-0.02	0.17
2260	0.01	-0.03	0.07	0.02	0.01	0.02	0.08	0.20	0.08	0.08	0.16	0.12	0.16	0.07	0.26
Error	0.07	0.09	0.09	0.07	0.04	0.08	0.06	0.07	0.05	0.07	0.05	0.07	0.05	0.05	0.09

Table 3.6: Elemental abundances derived with `KeckSpec`. The bottom row contains the systematic uncertainty for each abundance.

younger and more active. Rotationally modulated starspots on active stars introduce more scatter in RV observations, making planet mass measurement more difficult (Hillenbrand et al. 2015). This quantity is therefore useful for planning future planet characterization efforts.

Lastly, we measured fifteen elemental abundances for three stars (TOI-1835, TOI-1860, and TOI-2260) using the `KeckSpec` algorithm (Rice and Brewer 2020) on our high-S/N HIRES spectra. This algorithm is able to reliably measure abundances for stars with $T_{\rm eff} > 4700$ K. The spectra were reduced, extracted, and calibrated following the standard approach of the California Planet Search consortium (Howard et al. 2010). We then interpolated the spectra onto the wavelength grid required for `KeckSpec` before feeding them to the algorithm. The resulting abundances are shown in Table 3.6. Because elemental abundances are believed to influence the compositions of planet interior and atmospheres (e.g., Bond et al. 2010; Konopacky et al. 2013; Moriarty et al. 2014), the quantities may be useful when characterizing these planets and their systems in the future.

Time-Series Photometry

To determine whether or not the signal observed by *TESS* is on the presumed target star and to help eliminate false positives from blends, we compile a set of observations collected by members of TFOP Sub Group 1 (SG1). These follow-up observations were scheduled using the `TESS Transit Finder`, which is a customized version of the Tapir software package (Jensen 2013). A summary of these observations is given in Table **??** and details about the facilities used are given in Table 3.8.

We search for transits around the target stars in our observations using the Bayesian Information (Schwarz 1978), considering a transit detected if a transit model is preferred over a flat line. For several of our TOIs, transits were verified on-target using these observations. These cases are further described below. We incorporate this data into the transit fits described in Section 3.2 to obtain tighter constraints on the ephemerides of the planet candidates.

LCO 1.0 m / Sinistro

We observed full transits of TOI-206.01, TOI-1075.01, TOI-1442.01, TOI-1693.01, TOI-2411.01, and TOI-2427.01 using the Sinistro cameras on the Las Cumbres Observatory (LCO) 1.0 m telescopes. Images were calibrated by the standard LCOGT BANZAI pipeline (McCully et al. 2018) and the photometric data were extracted using the AstroImageJ (AIJ) software package (Collins et al. 2017).

Transit of TOI-206.01 were observed with a i' filter on UT 2018-11-23, 2018-12-01, and 2018-12-09 and were found to have a depth of $\sim 1.0 - 1.5$ ppt. Transit of TOI-1075.01 were observed with a z_s filter on UT 2019-08-26, 2019-09-23, 2019-09-24, and 2019-09-26 and were found to have a depth of $\sim 0.5 - 1.0$ ppt. Transit of TOI-1442.01 were observed with a i' filter on UT 2020-08-14, 2020-09-26, and 2020-10-21 and were found to have a depth of

$\sim 1.0-2.0$ ppt. Transits of TOI-1693.01 were observed with a z_s filter on UT 2020-02-14 and 2020-10-11 and were found to have a depth of $\sim 0.5-1.0$ ppt. Transits of TOI-2441.01 were observed with a i' filter on UT 2021-07-10, 2021-07-25, 2021-08-27, 2021-08-29, 2021-08-30, and 2021-09-09 and were found to have a depth of $\sim 0.25-0.75$ ppt. Transits of TOI-2427.01 were observed with a z_s filter on UT 2021-08-14 and 2021-08-17 and were found to have a depth of $\sim 0.25-0.75$ ppt. The data for each of these TOIs can be seen in Figures 3.3 – 3.9.

MEarth-South

We observed full transits of TOI-1075.01 on UT 2019-09-22 and 2019-09-28 using the MEarth-South telescope array at the Cerro Tololo Inter-American Observatory (Irwin et al. 2015; Nutzman and Charbonneau 2008). The observations were collected with a RG715 filter and were found to have a transit depth of $\sim 0.5-1.0$ ppt. The data can be seen in Figure 3.4.

OMM 1.6 m / PESTO

We observed a full transit of TOI-1442.01 on UT 2020-02-09 using the PESTO camera installed at the 1.6 m Observatoire du Mont-Mégantic (OMM), Canada. PESTO is equipped with a 1024×1024 EMCCD detector with a scale of $0\farcs466$ per pixel, providing a field of view (FOV) of $7\farcm95\times7\farcm95$. The observations were collected with a i' filter and with a 30 s exposure time. Image calibrations, including bias subtraction and flat field correction, and differential aperture photometry were performed with `AstroImageJ` (Collins et al. 2017). The events were observed with a i' filter and were found to have a transit depth of ~ 1 ppt. The data can be seen in Figure 3.5.

TRAPPIST-South

We observed two full transits of TOI-2445.01 using the TRAPPIST-South telescope (Barkaoui et al. 2018; Gillon et al. 2011; Jehin et al. 2011) on UT 2021-01-08 and 2021-02-14. TRAPPIST-South is a 60-cm robotic telescope installed at La Silla observatory in Chile since 2010, and it is equipped with a thermo-electrically 2Kx2K FLI ProLine PL3041-BB CCD camera with a FOV of 22'x22' and a pixel scale of 0.65". Data calibration and photometric measurements were performed using the *PROSE*[7] pipeline (Garcia et al. 2022). Both events were observed in the $I+z$ filter and were found to have a transit depth of ~ 2.5 ppt. The data can be seen in Figure 3.10.

NAOJ 188 cm / MuSCAT, TCS / MuSCAT2, and LCO 2.0 m / MuSCAT 3

We observed transits of TOI-1442.01, TOI-1693.01, and TOI-2445.01 using the MuSCAT, MuSCAT2, and MuSCAT3 instruments (Narita et al. 2015, 2019, 2020), which collect simultaneous observations using several filters. We observed full transits of TOI-1442.01 on

[7] `https://github.com/lgrcia/prose`

UT 2021-05-21, 2021-06-06, and 2021-06-17 using MuSCAT3 on the LCO 2.0 m telescope at Haleakala Observatory. Observations were collected with g', r', i', and z_s filters and measured a transit depth of $\sim 1.0-2.0$ ppt. We observed a full transit TOI-1693.01 on UT 2020-09-18 using MuSCAT2 on the Telescopio Carlos Sánchez (TCS) at Teide Observatory. Observations were collected with g', i', and z_s filters and measured a transit depth of $\sim 0.5-1.0$ ppt. We observed a full transit of TOI-2445.01 on UT 2021-02-07 using MuSCAT on the National Astronomical Observatory of Japan (NAOJ) 188 cm telescope. Observations were collected with g', r', and z_s filters and measured a transit depth of $\sim 1.0-5.0$ ppt. These data can be seen in Figure 3.5, Figure 3.6, and Figure 3.10.

TOI	TIC ID	Telescope	Date (UT)	Filter(s)
206.01	55650590	LCO 1.0 m	2018-11-19	r'
		SLR2	2018-11-22	V
		LCO 1.0 m	2018-11-23	i'
		CKD700	2018-11-30	r'
		LCO 1.0 m	2018-12-01	$r'i'$
		LCO 1.0 m	2018-12-02	i'
		LCO 1.0 m	2018-12-06	r'
		LCO 1.0 m	2018-12-09	i'
500.01	134200185	LCO 1.0 m	2019-03-15	r'
		TRAPPIST-S.	2019-03-24	B
		LCO 0.4 m	2019-03-30	i'
		PEST	2019-03-30	R_c
		LCO 1.0 m	2019-05-02	z_s
539.01	238004786	PEST	2019-03-29	R_c
		MKO CDK700	2019-03-31	r'
		LCO 1.0 m	2019-04-06	i'
		LCO 1.0 m	2019-04-08	z_s
		LCO 1.0 m	2019-04-17	i'
544.01	50618703	LCO 1.0 m	2019-09-20	z_s
		TCS	2019-10-13	$g'r'i'$
731.01	34068865	LCO 1.0 m	2019-06-10	V
		MKO CDK700	2019-06-11	i'
		PEST	2020-01-05	R_c
		LCO 1.0 m	2020-05-12	z_s
833.01	362249359	LCO 1.0 m	2020-03-28	z_s
		LCO 1.0 m	2020-05-14	z_s
		MKO CDK700	2020-05-15	i'
1075.01	351601843	LCO 1.0 m	2019-08-25	z_s
		LCO 1.0 m	2019-08-26	z_s
		MEarth-S	2019-09-22	RG715
		LCO 1.0 m	2019-09-23	z_s

		LCO 1.0 m	2019-09-24	z_s
		LCO 1.0 m	2019-09-26	z_s
		MEarth-S	2019-09-28	RG715
1242.01	198212955	TCS	2020-01-27	$g'r'i'z_s$
		TCS	2020-02-01	$g'r'i'z_s$
		TCS	2020-02-09	$g'r'i'z_s$
		ULMT	2020-05-18	i'
		TCS	2020-06-09	$g'r'i'z_s$
1263.01	406672232	LCO 1.0 m	2020-06-15	z_s
		LCO 1.0 m	2020-07-28	z_s
1411.01	116483514	LCO 1.0 m	2020-02-28	i'
		DSW CDK500	2020-04-16	r'
		TCS	2020-04-21	$g'r'i'z_s$
		LCO 1.0 m	2020-04-29	r'
		ULMT	2020-05-02	i'
		TCS	2020-05-10	$g'r'i'z_s$
1442.01	235683377	OMM 1.6 m	2020-02-09	i'
		LCO 1.0 m	2020-08-14	i'
		LCO 1.0 m	2020-08-30	I_c
		LCO 1.0 m	2020-09-26	i'
		LCO 2.0 m	2021-05-21	$g'r'i'z_s$
		LCO 2.0 m	2021-06-06	$g'r'i'z_s$
		LCO 2.0 m	2021-06-17	$g'r'i'z_s$
1693.01	353475866	LCO 1.0 m	2020-02-14	z_s
		LCO 1.0 m	2020-10-11	z_s
		TCS	2020-09-18	$g'i'z_s$
1860.01	202426247	Adams	2020-06-06	I_c
		TCS	2020-07-20	$g'r'i'z_s$
2260.01	232568235	TRAPPIST-N	2020-09-28	z'
		Adams	2021-06-26	I_c
2290.01	321688498	LCO 1.0 m	2020-10-15	i'
2411.01	10837041	MKO CDK700	2021-01-13	i'
		LCO 1.0 m	2021-06-19	r'
		LCO 1.0 m	2021-07-10	i'
		LCO 1.0 m	2021-07-25	i'
		LCO 1.0 m	2021-08-27	i'
		LCO 1.0 m	2021-08-29	i'
		LCO 1.0 m	2021-08-30	i'
		LCO 1.0 m	2021-09-09	i'
2427.01	142937186	PEST	2021-01-12	R_c
		LCO 1.0 m	2021-01-30	z_s

		LCO 1.0 m	2021-02-22	z_s
		LCO 1.0 m	2021-08-14	z_s
		LCO 1.0 m	2021-08-17	z_s
2445.01	439867639	MLO	2021-01-10	I_c
		TRAPPIST-S	2021-01-08	$I + z$
		TRAPPIST-S	2021-01-14	$I + z$
		NAOJ 188 cm	2021-02-07	$g'r'z_s$

Table 3.7: Summary of time-series photometry follow up.

3.5 Results

Below, we provide a brief summary about each of the planet candidates analyzed in this paper. We begin with details about the target stars, including their brightnesses, distances, and the *TESS* sectors in which they were observed. In addition, we analyze the available data of each star to search for activity indicators and signs of system youth. Specifically, we apply a Lomb-Scargle periodogram to each individual sector of *TESS* photometry to constrain the level of starspot variability. We consider the detection of photometric variability to be significant if the maximum peak calculated by the peroidogram across all sectors is > 0.5. When available, we also consider the spectrum-derived $v \sin i$ and $\log R'_{\rm HK}$.

Next, we present information gleaned from each step of our vetting process. We also summarize this information in Table 3.9. For TFOP SG3 high-resolution imaging observations, we refer to the TOI as "clear" if no stars were resolved within the detection limits stated in Figure 3.2. For TFOP SG2 reconnaissance spectroscopy observations, we refer to the TOI as "clear" if the target star is confirmed to be on the main sequence and no evidence of a spectroscopic binary was detected. For TFOP SG1 time-series photometry observations, we identify all stars from *Gaia* DR2 within 2.′5 of the target star that are bright enough to cause the *TESS* transit detection based on the observed transit depth, the angular distance from the target star, and the difference in magnitude from the target star. For convenience we refer to these as "neighbor stars" in the discussion below, and we describe them as "cleared" if our photometric follow-up observations show that they have no transit-like events of the depth that would be necessary to reproduce the *TESS* event when blended with the central star.

At the end of each subsection, we decide whether the TOI is validated based on the results of the `TRICERATOPS` analysis. To forecast the potential to measure the masses of the planet candidates via precise RVs, we also estimate the semi-amplitude ($K_{\rm RV}$) and planet mass ($M_{\rm p}$) of each using the probabilistic planet mass-radius relation given in Chen and Kipping (2017) and the adopted stellar masses listed in Table 3.3. However, we stress that these estimates are merely illustrative, and should not be quoted as the actual masses and semi-amplitudes.

Observatory	Telescope/Instrument	Aperture (m)	Pixel scale (arcsec)	FOV (arcmin)
Austin College Adams Observatory (Adams)	-	0.61	0.38	26×26
Cerro Tololo Inter-American Observatory	MEarth-South	0.4	0.84	29×29
Deep Sky West Remote Observatory (DSW)	DSW CDK500	0.5	1.09	37×37
Las Cumbres Observatory (LCO)	LCO 0.4 m / SBIG-6303	0.4	0.57	29.2×19.5
Las Cumbres Observatory (LCO)	LCO 1.0 m / Sinistro	1.0	0.39	26.5×26.5
Haleakala Observatory	LCO 2.0 m / MuSCAT3	2.0	0.27	9.1×9.1
Maury Lewin Astronomical Observatory (MLO)	-	0.36	0.84	23×17
Mt. Kent Observatory (MKO)	MKO CDK700	0.7	0.4	27×27
Observatoire du Mont-Mégantic (OMM)	OMM 1.6 m / PESTO	1.6	0.47	7.95×7.95
National Astronomical Observatory of Japan (NAOJ)	NAOJ 188 cm / MuSCAT	1.88	0.36	6.1×6.1
Oukaïmeden Observatory	TRAPPIST-North	0.6	0.64	22×22
South African Astronomical Observatory	SLR2	0.5	0.37	12×12
Teide Observatory	Telescopio Carlos Sánchez (TCS) / MuSCAT2	1.52	0.44	7.4×7.4
La Silla Observatory	TRAPPIST-South	0.6	0.64	22×22
Mt. Lemmon Observatory	Univ. of Louisville Manner Telescope (ULMT)	0.61	0.39	26×26
-	Perth Exoplanet Survey Telescope (PEST)	0.3	1.2	31×21

Table 3.8: Facilities used for TFOP SG1 follow up.

TOI	High-resolution Imaging	Recon Spectroscopy	Time-series Photometry	`dave` Results	FPP	NFPP	Validated
206.01	Clear	No data	Verified on-target	Potential secondary eclipse	< 0.01	< 0.001	Y
500.01	Clear	Clear	All neighbors cleared	Clear but unreliable centroid analysis	< 0.01	< 0.001	Y
539.01	Clear	Clear	1 neighbor not cleared	Clear but unreliable centroid analysis	> 0.01	< 0.001	N
544.01	Clear	Clear	2 neighbors not cleared	Clear	< 0.01	< 0.001	Y
731.01	Clear	Clear	1 neighbor not cleared	Clear but unreliable centroid analysis	> 0.01	< 0.001	N
833.01	Clear	Clear	1 neighbor not cleared	Potential centroid offset	< 0.01	< 0.001	Y
1075.01	Clear	Clear	Verified on-target	Clear	< 0.01	< 0.001	Y
1242.01	$4''.3$ companion detected	Clear	1 neighbor not cleared	Potential centroid offset	< 0.01	> 0.001	N
1263.01	$2''.6$ companion detected	Clear	2 neighbors not cleared	Different odd-even transit depths	> 0.01	> 0.001	N
1411.01	Clear	Clear	All neighbors cleared	Clear	< 0.01	< 0.001	Y
1442.01	Clear	No data	Verified on-target	Clear but unreliable centroid analysis	< 0.01	< 0.001	Y
1693.01	Clear	Clear	Verified on-target	Clear	< 0.01	< 0.001	Y
1860.01	Clear	Clear	1 neighbor not cleared	No results	< 0.01	< 0.001	Y
2260.01	Clear	Clear	All neighbors cleared	Clear	< 0.01	< 0.001	Y
2290.01	Clear	Clear	All neighbors cleared	Potential centroid offset	> 0.01	< 0.001	N
2411.01	Clear	Clear	Verified on-target	No results	< 0.01	< 0.001	Y
2427.01	Clear	Clear	Verified on-target	Potential centroid offset	< 0.01	< 0.001	Y
2445.01	Clear	No data	Verified on-target	Clear but unreliable centroid analysis	< 0.01	< 0.001	Y

Table 3.9: Vetting results.

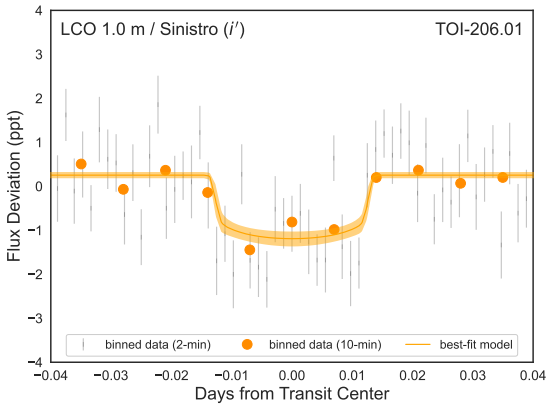

Figure 3.3: Phase-folded ground-based data and best-fit model of the transit of TOI-206.01. The data is detrended with a linear model and 3σ outliers are removed.

TOI-206.01

TOI-206.01 is a $1.30 \pm 0.05\,R_\oplus$ planet candidate with a 0.74 day orbital period orbiting a M dwarf (TIC 55650590) that is 47.7 pc away and has a V magnitude of 14.94. A Lomb-Scargle periodogram of the photometry from each *TESS* sector finds a maximum peak of 0.04, indicating that the star is quiet. TOI-206 has been observed in 26 *TESS* sectors (1–13 and 27–39).

Follow-up observations have found no evidence of this TOI being a false positive, although no spectroscopic observations have been collected. Time-series photometric follow-up has made several detections of the transit of TOI-206.01 on TIC 55650590 (shown in Figure 3.3).

The `dave` analysis of this TOI detects a potential secondary eclipse in the *TESS* light curve, which could indicate that the transit is due to an eclipsing binary. Because follow-up observations do not detect a companion star that could dilute the radius of the transiting object and because the transit was detected on-target, this eclipsing binary would need to have a grazing transit. The morphology of the transit shown in Figure 3.1 is inconsistent with that of a grazing eclipsing binary, meaning the feature detected in the *TESS* photometry is unlikely to be an actual secondary eclipse. The SPOC data validation report for this TOI reports no significant centroid offset.

The `TRICERATOPS` analysis of this TOI finds FPP $= (2.02 \pm 1.48) \times 10^{-5}$. Because all neighboring stars have been cleared, `TRICERATOPS` finds NFPP $= 0.0$. This FPP is sufficiently low to consider the planet validated. We hereafter refer to this planet as TOI-206 b.

We estimate the semi-amplitude of the RV signal for this planet to be $K_{\rm RV} = 3.1^{+2.0}_{-1.0}$ m/s, corresponding to $M_{\rm p} = 2.2^{+1.4}_{-0.7}\,M_\oplus$.

TOI-500.01

TOI-500.01 is a $1.16 \pm 0.12\,R_\oplus$ planet candidate with a 0.55 day orbital period orbiting a K dwarf (TIC 134200185) that is 47.4 pc away and has a V magnitude of 10.54. A Lomb-Scargle periodogram of the photometry from each *TESS* sector finds a maximum peak of 0.007, indicating that the star is quiet. This is corroborated by the low $v \sin i$ extracted from our CHIRON spectra. TOI-500 has been observed in 6 *TESS* sectors (6–8 and 33–35).

Follow-up observations have found no evidence of this TOI being a false positive. Time-series photometric follow-up of this TOI has cleared all neighboring stars as origins of the transit, but has not yet detected the 0.23 ppt event seen in the *TESS* data around the target star.

`dave` finds no strong indicators that the candidate is a false positive. We note, though, that the photocenter offset analysis performed by `dave` suffers from low S/N and poor quality in most of the per-transit difference images. As a result, there is large scatter in the measured photocenters for each individual transit, making it difficult for `dave` to detect a significant photocenter offset. The spoc data validation report, however, does detect significant centroid offsets in sectors 8, 34, and 35. No offsets were detected in sectors 7 or 33 by SPOC, and no data validation report was generated by the SPOC pipeline for sector 6. Given that all neighboring stars have been cleared from being nearby eclipsing binaries, these offsets are unlikely to be caused by a false positive originating from a nearby star.

The `TRICERATOPS` analysis of this TOI finds FPP $= (7.12 \pm 1.13) \times 10^{-3}$. Because all neighboring stars have been cleared, `TRICERATOPS` finds NFPP $= 0.0$. This FPP is sufficiently low to consider the planet validated. We hereafter refer to this planet as TOI-500 b.

We estimate the semi-amplitude of the RV signal for this planet to be $K_{\rm RV} = 1.4^{+1.1}_{-0.7}$ m/s, corresponding to $M_{\rm p} = 1.6^{+1.3}_{-0.7}\,M_\oplus$.

TOI-539.01

TOI-539.01 is a $1.25 \pm 0.10\,R_\oplus$ planet candidate with a 0.31 day orbital period orbiting a K dwarf (TIC 238004786) that is 108.4 pc away and has a V magnitude of 11.73. A Lomb-Scargle periodogram of the photometry from each *TESS* sector finds a maximum peak of 0.07, indicating that the star is quiet. This is corroborated by the low $v \sin i$ extracted from our CHIRON spectrum. TOI-539 has been observed in 11 *TESS* sectors (2, 6, 8, 9, 12, 29, 32–35, and 39).

Follow-up observations have found no evidence of this TOI being a false positive. Time-series photometric follow-up of this TOI has cleared all neighboring stars as origins of the transit except for TIC 767067264, which is $7\farcs2$ west and 7.9 magnitudes fainter in the *Gaia* $G_{\rm Rp}$ band. This nearby star appears not to show an event of the necessary depth but is not cleared at high confidence. The 0.31 ppt event seen in the *TESS* data has not been detected around the target star.

The `dave` analysis of this TOI finds no strong indicators that the candidate is a false positive. However, like TOI-500 b, the per-transit difference images used by `dave` have very

low SNR and the measured photocenters are unreliable. The SPOC data validation report for this TOI reports no significant centroid offset.

The `TRICERATOPS` analysis of this TOI finds FPP = $(3.98 \pm 0.03) \times 10^{-2}$ and NFPP = $(7.76 \pm 0.26) \times 10^{-22}$. This $> 1\%$ FPP comes from the scenario that the TOI is a blended eclipsing binary. While this NFPP indicates that this TOI is unlikely to originate from the nearby star TIC 767067264, the FPP is too high to validate the planet candidate.

Assuming this is a real planet, we estimate the semi-amplitude of its RV signal to be $K_{\rm RV} = 1.9^{+1.6}_{-0.7}$ m/s, corresponding to $M_{\rm p} = 1.9^{+1.6}_{-0.7}\,M_\oplus$.

TOI-544.01

TOI-544.01 is a $2.03 \pm 0.10\,R_\oplus$ planet candidate with a 1.55 day orbital period orbiting a K dwarf (TIC 50618703) that is 41.1 pc away and has a V magnitude of 10.78. A Lomb-Scargle periodogram of the photometry from each *TESS* sector finds a maximum peak of 0.25, indicating that the star is quiet. This is corroborated by the low $v \sin i$ extracted from our TRES spectrum. TOI-544 has been observed in 2 *TESS* sectors (6 and 32).

Follow-up observations have found no evidence of this TOI being a false positive. Time-series photometric follow-up of this TOI has cleared all neighboring stars as origins of the transit except for TIC 713009339 (located $5\farcs26$ south-southeast and 9.5 magnitudes fainter in the *TESS* band) and TIC 50618707 (located $9\farcs18$ east-southeast and 6.9 magnitudes fainter in the *TESS* band). TIC 713009339 is too faint to be the source of an astrophysical false positive, but TIC 50618707 is not. We would like to note that the former of these nearby stars was detected by *Gaia* but not by 2MASS, while the latter was detected by 2MASS but not by *Gaia*. The parallaxes and proper motions of these two stars are unknown, so it is possible that they are the same star observed at two different epochs. If this were the case, the star would have been within the $\sim 10'' \times 10''$ field of view of the Shane/ShARCS observations obtained on UT 2019-09-13, which reach contrasts of > 8 mags in the K_s and J bands. However, no stars other than TIC 50618703 were detected in these observations. If this star (or stars, if they are indeed different sources) are really there, it (or they) would be far too faint to host eclipsing binaries mistakable for the TOI-544.01 transit. Regardless, we consider these two nearby stars in the remaining vetting steps for the sake of completeness.

The `dave` analysis of this TOI finds no strong indicators that the candidate is a false positive. The SPOC data validation report for this TOI reports no significant centroid offset.

The `TRICERATOPS` analysis of this TOI finds FPP = $(8.25 \pm 0.91) \times 10^{-3}$ and NFPP = $(1.67 \pm 0.16) \times 10^{-16}$. This FPP and NFPP are sufficiently low to consider the planet validated. We hereafter refer to this planet as TOI-544 b.

We estimate the semi-amplitude of the RV signal for this planet to be $K_{\rm RV} = 3.2^{+2.4}_{-1.4}$ m/s, corresponding to $M_{\rm p} = 5.0^{+4.0}_{-2.0}\,M_\oplus$.

TOI-731.01

TOI-731.01 is a $0.59 \pm 0.02\,R_\oplus$ planet candidate with a 0.32 day orbital period orbiting a high-proper-motion ($\mu_\alpha = -462.5$ mas/yr, $\mu_\delta = -582.8$ mas/yr) M dwarf (TIC 34068865) that is 9.4 pc away and has a V magnitude of 10.15. A Lomb-Scargle periodogram of the photometry from each *TESS* sector finds a maximum peak of 0.07, indicating that the star is quiet. TOI-731 has been observed in 3 *TESS* sectors (9, 35, and 36).

Follow-up observations have found no evidence of this TOI being a false positive. Time-series photometric follow-up of this TOI has cleared all neighboring stars as transit sources except for TIC 34068883, which is 6.2 magnitudes fainter in *Gaia* $G_{\rm Rp}$ and was 6.″4 southwest at epoch 2020.361.[8] However, this follow-up has not detected the 0.24 ppt transit around the target star that is seen in the *TESS* data.

The `dave` analysis of this TOI finds no strong indicators that the candidate is a false positive. Compared to TOI-500, the SNR of the per-transit difference images used by `dave` is even lower and the measured centroids are unreliable. The SPOC data validation report for this TOI reports no significant centroid offset.

The `TRICERATOPS` analysis of this TOI finds FPP $= (1.89 \pm 0.46) \times 10^{-2}$ and NFPP $= (9.21 \pm 1.48) \times 10^{-26}$. This $> 1\%$ FPP comes from the scenario that the TOI is a blended eclipsing binary. This FPP is too high to consider the planet candidate validated.

Assuming this is a real planet, we estimate the semi-amplitude of the RV signal to be $K_{\rm RV} = 0.22^{+0.11}_{-0.07}$ m/s, corresponding to $M_{\rm p} = 0.15^{+0.07}_{-0.04}\,M_\oplus$.

TOI-833.01

TOI-833.01 is a $1.27 \pm 0.07\,R_\oplus$ planet candidate with a 1.04 day orbital period orbiting a K dwarf (TIC 362249359) that is 41.7 pc away and has a V magnitude of 11.72. A Lomb-Scargle periodogram of the photometry from each *TESS* sector finds a maximum peak of 0.20, indicating that the star is quiet. TOI-833 has been observed in 5 *TESS* sectors (9, 10, 11, 36, and 37).

Follow-up observations have found no evidence of this TOI being a false positive. Time-series photometric follow-up of this TOI has made tentative detections of a ∼0.8–0.9 ppt transit on two different occasions. The field around this TOI is crowded and it is not clear if the event is on target or due to blending with TIC 847323367 (located 3.″1 north and 7.9 magnitudes fainter in the *TESS* band).

The `dave` analysis of this TOI detects a potential centroid offset to the north-east, but found no other indicators that this TOI is a false positive. The SPOC data validation report for this TOI reports no significant centroid offset.

[8] This separation is continuing to decrease and will lead to a weak microlensing event with a closest approach of 510 mas in December 2028 (Bramich and Nielsen 2018). The event will not produce a brightening of more than 0.4 mmag, but is predicted to produce an astrometric shift of 1 mas, possibly detectable by a future astrometric mission.

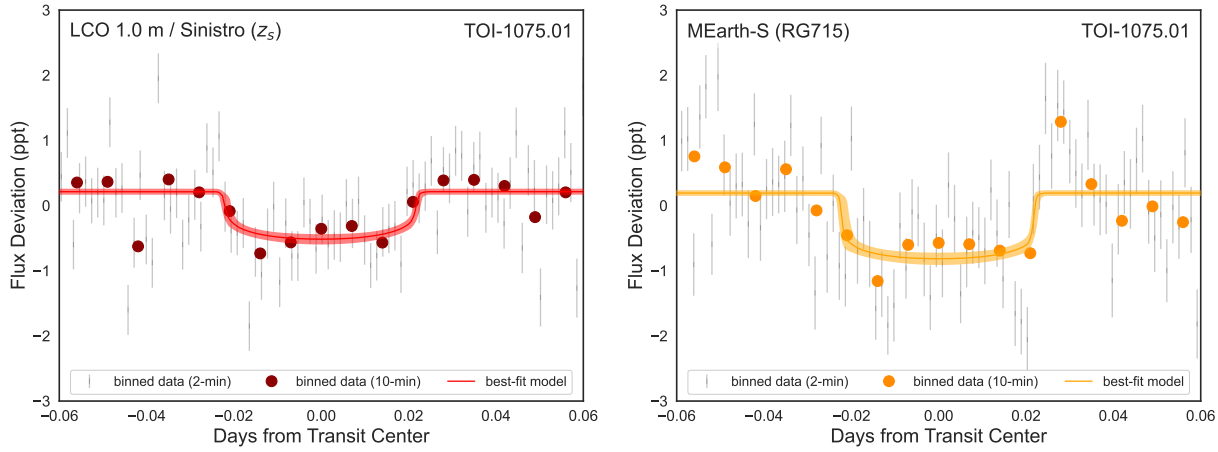

Figure 3.4: Phase-folded ground-based data and best-fit model of the transit of TOI-1075.01. The data is detrended with a linear model and 3σ outliers are removed.

The `TRICERATOPS` analysis of this TOI finds FPP $= (2.32 \pm 0.23) \times 10^{-4}$ and NFPP $= (3.89 \pm 0.11) \times 10^{-10}$. This FPP and NFPP are sufficiently low to consider the planet validated. We hereafter refer to this planet as TOI-833 b. We estimate the semi-amplitude of the RV signal for this planet to be $K_{\rm RV} = 1.8^{+1.3}_{-0.5}$ m/s, corresponding to $M_{\rm p} = 2.0^{+1.5}_{-0.6}\,M_\oplus$.

TOI-1075.01

TOI-1075.01 is a $1.72 \pm 0.08\,R_\oplus$ planet candidate with a 0.60 day orbital period orbiting a K dwarf (TIC 351601843) that is 61.5 pc away and has a V magnitude of 12.62. A Lomb-Scargle periodogram of the photometry from each *TESS* sector finds a maximum peak of 0.02, indicating that the star is quiet. TOI-1075 has been observed in 2 *TESS* sectors (13 and 27).

Follow-up observations have found no evidence of this TOI being a false positive. Time-series photometric follow-up has has made several detections of the transit of TOI-1075.01 on TIC 351601843 (shown in Figure 3.4).

The `dave` analysis of this TOI found no strong indicators that the candidate is a false positive. The SPOC data validation report for this TOI reports no significant centroid offset.

The `TRICERATOPS` analysis of this TOI finds FPP $= (1.01 \pm 0.16) \times 10^{-3}$. Because TIC 351601843 has been verified as the host of the transit, `TRICERATOPS` finds NFPP $= 0.0$. This FPP is sufficiently low to consider the planet validated. We hereafter refer to this planet as TOI-1075 b.

We estimate the semi-amplitude of the RV signal for this planet to be $K_{\rm RV} = 4.3^{+2.9}_{-1.5}$ m/s, corresponding to $M_{\rm p} = 4.0^{+2.7}_{-1.4}\,M_\oplus$.

TOI-1242.01

TOI-1242.01 is a $1.65 \pm 0.23\,R_\oplus$ planet candidate with a 0.38 day orbital period orbiting a K dwarf (TIC 198212955) that is 110 pc away and has a V magnitude of 12.78. A Lomb-Scargle periodogram of the photometry from each *TESS* sector finds a maximum peak of 0.03, indicating that the star is quiet. This is corroborated by the low $v \sin i$ extracted from our TRES spectrum. TOI-1242 has been observed in 15 *TESS* sectors (14–26, 40, and 41) and is scheduled to be re-observed in another 8 sectors (48–55) between 2022-01-28 and 2022-09-01.

High-resolution imaging of this star detects TIC 198212956, a previously known star that is 4.″3 north and 2.6 magnitudes fainter in the *TESS* band, but finds no other unresolved stars within detection limits. TIC 198212956 is almost certainly bound to TIC 198212955 due to their similar parallaxes and proper motions as reported by *Gaia* DR2. Spectroscopic observations confirm that the star is on the main sequence and rule out obvious spectroscopic binaries. Time-series photometric follow-up of this TOI has cleared all neighboring stars as origins of the transit except for TIC 198212956. The 0.6 ppt event seen in the *TESS* data has not been detected around the target star or its companion.

The `dave` analysis of this TOI detects a potential centroid offset to the north-east, but finds no other indicators that this TOI is a false positive. The SPOC data validation report for this TOI reports no significant centroid offset.

The `TRICERATOPS` analysis of this TOI find FPP $= (3.36 \pm 0.17) \times 10^{-2}$ and NFPP $= (2.92 \pm 0.16) \times 10^{-2}$. These $> 1\%$ FPP and NFPP are driven by the uncertainty over whether or not the transit originates from the target star or TIC 198212956. This FPP and NFPP are too high to consider this planet candidate validated.

Assuming this is a real planet around TIC 198212955, we estimate the semi-amplitude of the RV signal to be $K_{\rm RV} = 3.7^{+3.0}_{-1.7}$ m/s, corresponding to $M_{\rm p} = 3.7^{+2.9}_{-1.5}\,M_\oplus$.

TOI-1263.01

TOI-1263.01 is a $1.36 \pm 0.16\,R_\oplus$ planet candidate with a 1.02 day orbital period orbiting a K dwarf (TIC 406672232) that is 46.6 pc away and has a V magnitude of 9.36. A Lomb-Scargle periodogram of the photometry from each *TESS* sector finds a maximum peak of 0.12, indicating that the star is quiet. This is corroborated by the low $v \sin i$ extracted from our TRES and FIES spectra. TOI-1263 has been observed in 3 *TESS* sectors (14, 15, and 41) and is scheduled to be re-observed in another sector (55) between 2022-08-05 and 2022-09-01.

High-resolution imaging of this star detects TIC 1943945558, a previously known star that is 2.″6 south-east and 3.6 magnitudes fainter in the *TESS* band, but finds no other unresolved stars within detection limits. TIC 1943945558 is almost certainly bound to TIC 406672232 due to their similar parallaxes and proper motions as reported by *Gaia* DR2. Multiple spectroscopic observations confirm that the star is on the main sequence and rule out obvious spectroscopic binaries. Time-series photometric follow-up of this TOI has cleared

all neighboring stars as origins of the transit except for TIC 1943945558 and TIC 1943945562, which is 9.″1 north-east and 7.4 magnitudes fainter in the *TESS* band. The 0.26 ppt event seen in the *TESS* data has not been detected around the target star.

The `dave` analysis of this TOI detects a potential difference between the even and odd primary transits, which could be indicative of a false positive in the form of an eclipsing binary. `dave` did not report any other false positive indicators for this TOI. The SPOC data validation report for this TOI reports no significant centroid offset.

The `TRICERATOPS` analysis of this TOI find FPP = $(1.12 \pm 0.05) \times 10^{-2}$ and NFPP = $(1.04 \pm 0.05) \times 10^{-2}$. These $> 1\%$ FPP and NFPP are driven by the uncertainty over whether or not the transit originates from the target star or TIC 1943945562. This FPP and NFPP are too high to consider this planet candidate validated.

Assuming this is a real planet around TIC 406672232, we estimate the semi-amplitude of the RV signal to be $K_{\rm RV} = 1.8^{+1.3}_{-0.7}$ m/s, corresponding to $M_{\rm p} = 2.4^{+1.7}_{-0.8}\,M_\oplus$.

TOI-1411.01

TOI-1411.01 is a $1.36 \pm 0.16\,R_\oplus$ planet candidate with a 1.45 day orbital period orbiting a K dwarf (TIC 116483514) that is 32.5 pc away and has a V magnitude of 10.51. A Lomb-Scargle periodogram of the photometry from each *TESS* sector finds a maximum peak of 0.02, indicating that the star is quiet. This is corroborated by the $\log R'_{\rm HK}$ of -4.7252 extracted from our HIRES spectrum and the low $v \sin i$ extracted from our TRES spectrum. TOI-1411 has been observed in 3 *TESS* sectors (16, 23, and 24) and is scheduled to be re-observed in another 2 sectors (50 and 51) between 2022-03-26 and 2022-05-18.

Follow-up observations have found no evidence of this TOI being a false positive. Time-series photometric follow-up of this TOI has cleared all neighboring stars as origins of the transit. Of note to this TOI is TIC 1101969798, a periodic variable with a semiamplitude of 0.1 mag and a period of 0.107 day, that is located 90″ to the north-east.

The `dave` analysis of this TOI finds no strong indicators that the candidate is a false positive. The SPOC data validation report for this TOI reports no significant centroid offset.

The `TRICERATOPS` analysis of this TOI finds FPP = $(1.18 \pm 0.68) \times 10^{-4}$. Because all neighboring stars have been cleared, `TRICERATOPS` finds NFPP = 0.0. This FPP is sufficiently low to consider the planet validated. We hereafter refer to this planet as TOI-1411 b.

We estimate the semi-amplitude of the RV signal for this planet to be $K_{\rm RV} = 2.0^{+1.7}_{-1.0}$ m/s, corresponding to $M_{\rm p} = 2.5^{+2.0}_{-1.1}\,M_\oplus$. Vermilion et al (in prep), which detects the radial velocity signal of this planet, reports a $K_{\rm RV}$ 5σ upper limit of 4.26 m/s (or a mass of $5.66\,M_\oplus$), consistent with our estimate and with a terrestrial composition.

TOI-1442.01

TOI-1442.01 is a $1.17 \pm 0.06\,R_\oplus$ planet candidate with a 0.41 day orbital period orbiting a M dwarf (TIC 235683377) that is 41.2 pc away and has a V magnitude of 15.39. A Lomb-

Scargle periodogram of the photometry from each *TESS* sector finds a maximum peak of 0.02, indicating that the star is quiet. TOI-1442 has been observed in 15 *TESS* sectors (14–26, 40, and 41) and is scheduled to be re-observed in another 9 sectors (47–55) between 2021-12-30 and 2022-09-01.

Follow-up observations have found no evidence of this TOI being a false positive, although no spectroscopic observations of this TOI have been collected. Time-series photometric follow-up has made several detections of the transit of TOI-1442.01 on TIC 235683377 (shown in Figure 3.5).

The `dave` analysis of this TOI finds no strong indicators that the candidate is a false positive. However, the SNR of the per-transit difference images used by `dave` is very low and the measured centroids are unreliable. The SPOC data validation report for this TOI reports no significant centroid offset.

The `TRICERATOPS` analysis of this TOI finds FPP = $(7.00 \pm 4.11) \times 10^{-6}$. Because the transit has been verified on-target, `TRICERATOPS` finds NFPP = 0.0. This FPP is sufficiently low to consider the planet validated. We hereafter refer to this planet as TOI-1442 b.

We estimate the semi-amplitude of the RV signal for this planet to be $K_{\rm RV} = 3.2^{+2.2}_{-1.0}$ m/s, corresponding to $M_{\rm p} = 1.6^{+1.1}_{-0.5}\,M_\oplus$.

TOI-1693.01

TOI-1693.01 is a $1.42 \pm 0.10\,R_\oplus$ planet candidate with a 1.77 day orbital period orbiting a M dwarf (TIC 353475866) that is 30.8 pc away and has a V magnitude of 12.96. A Lomb-Scargle periodogram of the photometry from each *TESS* sector finds a maximum peak of 0.01, indicating that the star is quiet. This is corroborated by the $\log R'_{\rm HK}$ of -5.2169 extracted from our HIRES spectrum. TOI-1693 has been observed in 4 *TESS* sectors (19 and 43–45).

Follow-up observations have found no evidence of this TOI being a false positive. Time-series photometric follow-up has made several detections of the transit of TOI-1693.01 on TIC 353475866 (shown in Figure 3.6).[9]

The `dave` analysis of this TOI finds no strong indicators that the candidate is a false positive. The SPOC data validation report for this TOI reports no significant centroid offset.

The `TRICERATOPS` analysis of this TOI finds FPP = $(1.47 \pm 0.13) \times 10^{-3}$. Because the transit has been verified on-target, `TRICERATOPS` finds NFPP = 0.0. This FPP is sufficiently low to consider the planet validated. We hereafter refer to this planet as TOI-1693 b.

We estimate the semi-amplitude of the RV signal for this planet to be $K_{\rm RV} = 2.4^{+1.9}_{-0.8}$ m/s, corresponding to $M_{\rm p} = 2.8^{+2.2}_{-1.0}\,M_\oplus$.

[9]Those observations are blended with TIC 723362263, which is 3.″75 south-west and 8.3 magnitudes fainter in the *TESS* band, which is marginally too faint to have caused the *TESS* detection.

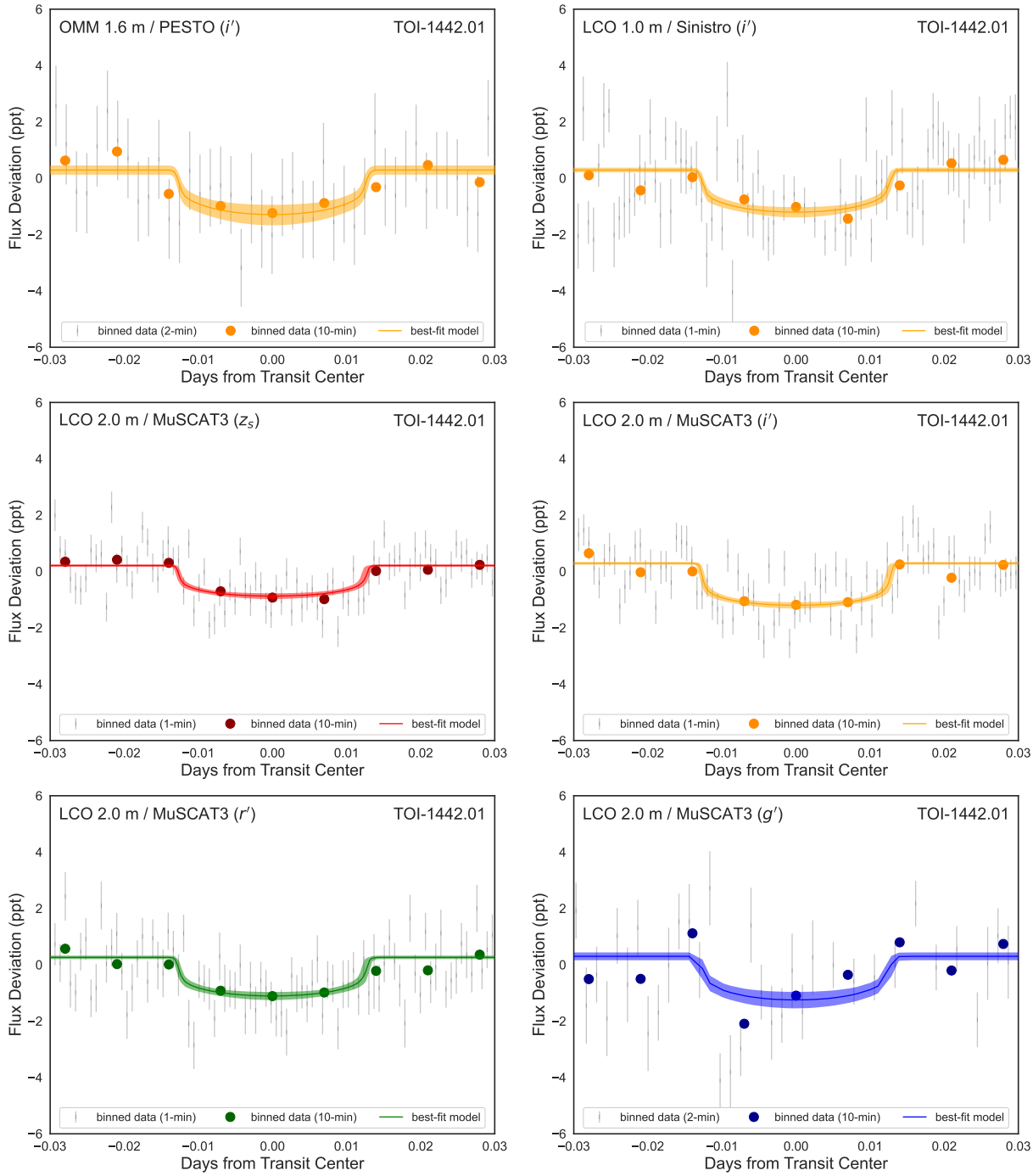

Figure 3.5: Phase-folded ground-based data and best-fit model of the transit of TOI-1442.01. The data is detrended with a linear model and 3σ outliers are removed.

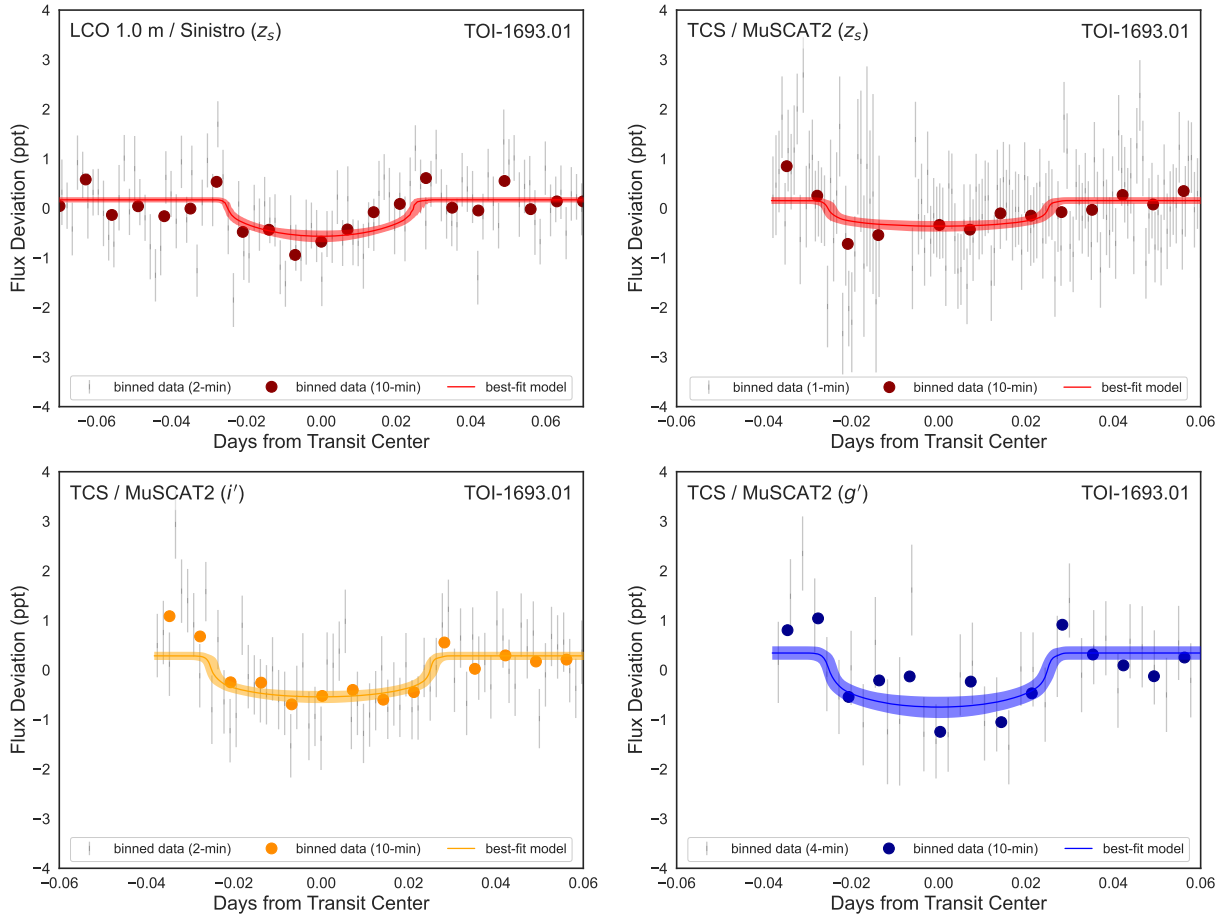

Figure 3.6: Phase-folded ground-based data and best-fit model of the transit of TOI-1693.01. The data is detrended with a linear model and 3σ outliers are removed.

TOI-1860.01

TOI-1860.01 is a $1.31 \pm 0.04\,R_\oplus$ planet candidate with a 1.07 day orbital period orbiting a G dwarf (TIC 202426247) that is 45.9 pc away and has a V magnitude of 8.4. A Lomb-Scargle periodogram of the photometry from each *TESS* sector finds a maximum peak of 0.83, indicating strong activity and a young host star. We also estimate a $\log R'_{\rm HK}$ of -4.2524 from our HIRES spectrum, which indicates that the star is young and active. TOI-1860 has been observed in 7 *TESS* sectors (14–16, 21–23, and 41) and is scheduled to be re-observed in another 3 sectors (48–50) between 2022-01-28 and 2022-04-22.

Because this is an active star, we can use the *TESS* light curve to derive its rotation period. In Figure 3.7, we display the results of a Lomb-Scargle periodogram applied to each sector separately, which gives a rotation period of 4.43 ± 0.06 days. Using the relation

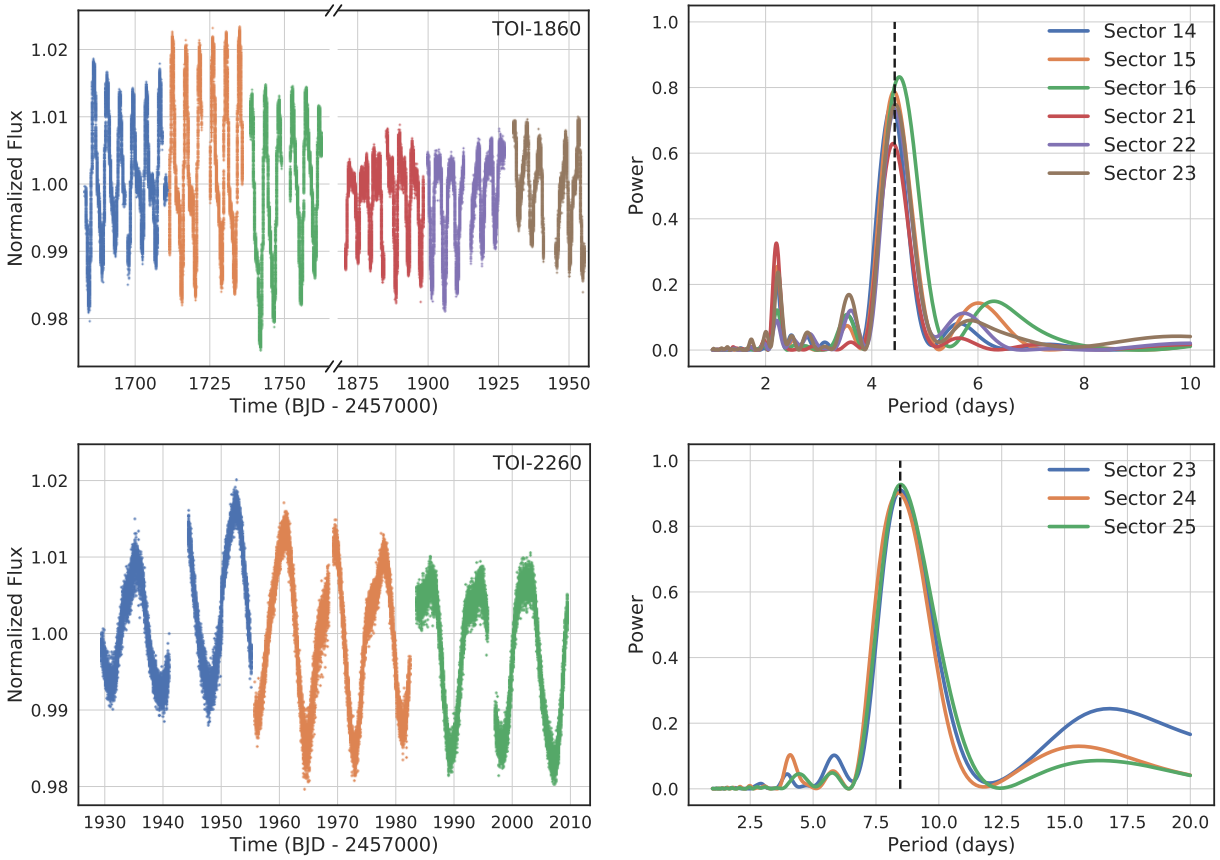

Figure 3.7: *TESS* light curves and Lomb-Scargle periodograms for TOI-1860 (top) and TOI-2260 (bottom). To estimate the rotation period of a star, we use the periodogram to calculate the peak period for each sector separately. Our estimate is then given by the mean and standard deviation of these rotation periods. For TOI-1860 and TOI-2260, we estimate a rotation period of 4.43 ± 0.04 days and 8.45 ± 0.06 days, respectively. These periods are indicated with vertical dashed lines in the right-hand panels.

defined in Barnes (2007), we estimate the age of the star to be 133 ± 26 Myr. Lastly, we use BANYAN Σ (Gagné et al. 2018) to determine the probability that the star is a member of a nearby young association. This analysis returns a 99.9% probability that TOI-1860 is a field star.

Another interesting aspect of TOI-1860 is that it has stellar parameters and a metallicity very similar to that of the Sun, and qualifies as a Solar twin according to most definitions (Cayrel de Strobel 1996; Ramırez et al. 2014). For Solar twins, there is known to be a strong correlation between [Y/Mg] and stellar age (Nissen 2015; Tucci Maia et al. 2016). Because we obtained elemental abundances for this star using `KeckSpec` (see Table 3.6), we are able

to conduct an independent check of the age of this system. Using the relation provided in Tucci Maia et al. (2016) and [Y/Mg] = 0.196 ± 0.090, we estimate an age upper limit 1.93 Gyr, which is consistent with our estimation based on gyrochronology.

Follow-up observations have found no evidence of this TOI being a false positive. Time-series photometric follow-up of this TOI has cleared all neighboring stars as origins of the transit except for TIC 1102367690, which is 5.″5 west and 5.8 magnitudes fainter in the *TESS* band. The 0.23 ppt event seen in the *TESS* data has not been detected around the target star.

`dave` was unable to perform a vetting analysis of this TOI, due to a failure of its transit model to fit the *TESS* data. The SPOC data validation report for this TOI reports no significant centroid offset.

The `TRICERATOPS` analysis of this TOI find FPP = $(1.97 \pm 0.45) \times 10^{-4}$ and NFPP = $(9.68 \pm 2.23) \times 10^{-6}$. This FPP and NFPP are sufficiently low to consider the planet validated. We hereafter refer to this planet as TOI-1860 b.

We estimate the semi-amplitude of the RV signal for this planet to be $K_{\rm RV} = 1.4^{+0.8}_{-0.4}$ m/s, corresponding to $M_{\rm p} = 2.2^{+1.3}_{-0.7}\,M_\oplus$.

TOI-2260.01

TOI-2260.01 is a $1.62 \pm 0.13\,R_\oplus$ planet candidate with a 0.35 day orbital period orbiting a G dwarf (TIC 232568235) that is 101.3 pc away and has a V magnitude of 10.47. A Lomb-Scargle periodogram of the photometry from each *TESS* sector finds a maximum peak of 0.93, indicating strong activity and a young host star. We also estimate a $\log R'_{\rm HK}$ of -4.438 from our HIRES spectrum, which indicates that the star is young and active. TOI-2260 has been observed in 3 *TESS* sectors (23–25) and is scheduled to be re-observed in another 3 sectors (50–52) between 2022-03-26 and 2022-06-13.

Because this is an active star, we can use the *TESS* light curve to derive its rotation period. In Figure 3.7, we display the results of a Lomb-Scargle periodogram applied to each sector separately, which gives a rotation period of 8.45 ± 0.03 days. Using the relation defined in Barnes (2007), we estimate the age of the star to be 321 ± 96 Myr. Lastly, we use BANYAN Σ (Gagné et al. 2018) to determine the probability that the star is a member of a nearby young association. This analysis returns a 99.9% probability that TOI-2260 is a field star.

Follow-up observations have found no evidence of this TOI being a false positive. Time-series photometric follow-up of this TOI has cleared all neighboring stars as origins of the transit.

The `dave` analysis of this TOI finds no strong indicators that the candidate is a false positive. The SPOC data validation report for this TOI reports a significant centroid offset in sector 24, but has not conducted centroid offset analyses for sectors 23 and 25. However, given that all neighboring stars have been cleared from being nearby eclipsing binaries, this offset is unlikely to be caused by a false positive coming from a nearby star.

The `TRICERATOPS` analysis of this TOI finds FPP = $(5.26 \pm 0.50) \times 10^{-3}$. Because all neighboring stars have been cleared, `TRICERATOPS` finds NFPP = 0.0. This FPP is sufficiently low to consider the planet validated. We hereafter refer to this planet as TOI-2260 b.

We estimate the semi-amplitude of the RV signal for this planet to be $K_{\rm RV} = 3.0^{+2.2}_{-1.1}$ m/s, corresponding to $M_{\rm p} = 3.5^{+2.5}_{-1.3}\,M_\oplus$.

TOI-2290.01

TOI-2290.01 is a $1.17 \pm 0.07\,R_\oplus$ planet candidate with a 0.39 day orbital period orbiting a K dwarf (TIC 321688498) that is 58.1 pc away and has a V magnitude of 12.64. A Lomb-Scargle periodogram of the photometry from each *TESS* sector finds a maximum peak of 0.03, indicating that the star is quiet. However, the $\log R'_{\rm HK}$ of -4.459 extracted from our HIRES spectrum suggests that the star may actually be quite active. TOI-2290 has been observed in 4 *TESS* sectors (17, 18, 24, and 25).

Follow-up observations have found no evidence of this TOI being a false positive. Time-series photometric follow-up of this TOI has cleared all neighboring stars as origins of the transit.

The `dave` analysis of this TOI finds a potential centroid offset, but finds no other significant false positive indicators. No data validation reports have been generated by the SPOC pipeline for this TOI.

The `TRICERATOPS` analysis of this TOI finds FPP = $(4.92 \pm 0.11) \times 10^{-1}$. Because all neighboring stars have been cleared, `TRICERATOPS` finds NFPP = 0.0. The reason for this $> 1\%$ FPP comes from the scenario that the TOI is a blended eclipsing binary. This FPP is too high to consider the planet validated.

Assuming this is a real planet, we estimate the semi-amplitude of the RV signal to be $K_{\rm RV} = 2.1^{+1.7}_{-0.7}$ m/s, corresponding to $M_{\rm p} = 1.6^{+1.4}_{-0.6}\,M_\oplus$.

TOI-2411.01

TOI-2411.01 is a $1.68 \pm 0.11\,R_\oplus$ planet candidate with a 0.78 day orbital period orbiting a K dwarf (TIC 10837041) that is 59.5 pc away and has a V magnitude of 11.27. A Lomb-Scargle periodogram of the photometry from each *TESS* sector finds a maximum peak of 0.002, indicating that the star is quiet. TOI-2411 has been observed in 2 *TESS* sectors (3 and 30).

Follow-up observations have found no evidence of this TOI being a false positive. Time-series photometric follow-up has made several detections of the transit of TOI-2411.01 on TIC 10837041 (shown in Figure 3.8).

`dave` is unable to analyze this TOI due to the very low S/N of the data. The SPOC data validation report for this TOI reports no significant centroid offset or any other false positive indicators.

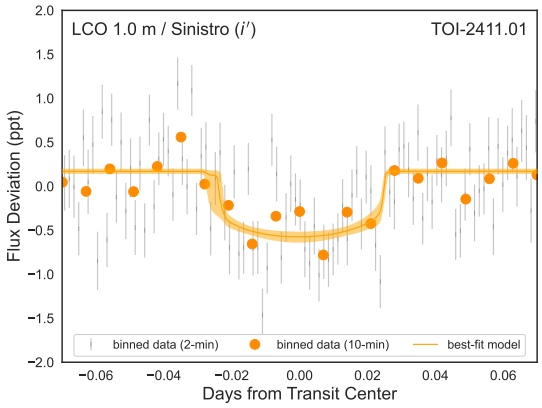

Figure 3.8: Phase-folded ground-based data and best-fit model of the transit of TOI-2411.01. The data is detrended with a linear model and 3σ outliers are removed.

The `TRICERATOPS` analysis of this TOI find FPP $= (1.17 \pm 0.05) \times 10^{-3}$. Because transits have been verified on-target, `TRICERATOPS` finds NFPP $= 0.0$. This FPP is sufficiently low to consider the planet validated. We hereafter refer to this planet as TOI-2411 b.

We estimate the semi-amplitude of the RV signal for this planet to be $K_{\rm RV} = 3.6^{+2.5}_{-1.3}$ m/s, corresponding to $M_{\rm p} = 3.9^{+2.8}_{-1.4}\,M_\oplus$.

TOI-2427.01

TOI-2427.01 is a $1.80 \pm 0.12\,R_\oplus$ planet candidate with a 1.31 day orbital period orbiting a K dwarf (TIC 142937186) that is 28.5 pc away and has a V magnitude of 10.30. A Lomb-Scargle periodogram of the photometry from each *TESS* sector finds a maximum peak of 0.05, indicating that the star is quiet. TOI-2427 has been observed in 1 *TESS* sector (31).

Follow-up observations have found no evidence of this TOI being a false positive. Time-series photometric follow-up has made several detections of the transit of TOI-2427.01 on TIC 142937186 (shown in Figure 3.9).

The `dave` analysis of this TOI finds a potential centroid offset, but finds no other indicators that this TOI is a false positive. The SPOC data validation report for this TOI also reports a significant centroid offset. However, given that all neighboring stars have been cleared from being nearby eclipsing binaries, this offset is unlikely to be caused by a false positive originating from a nearby star.

The `TRICERATOPS` analysis of this TOI finds FPP $= (7.35 \pm 2.72) \times 10^{-3}$. Because transits have been verified on-target, `TRICERATOPS` finds NFPP $= 0.0$. This FPP is sufficiently low to consider the planet validated. We hereafter refer to this planet TOI-2427 b.

We estimate the semi-amplitude of the RV signal for this planet to be $K_{\rm RV} = 3.2^{+2.4}_{-1.2}$ m/s, corresponding to $M_{\rm p} = 4.1^{+3.1}_{-1.5}\,M_\oplus$.

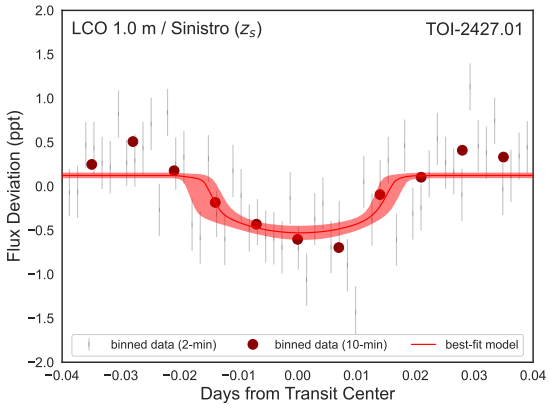

Figure 3.9: Phase-folded ground-based data and best-fit model of the transit of TOI-2427.01. The data is detrended with a linear model and 3σ outliers are removed.

TOI-2445.01

TOI-2445.01 is a $1.25 \pm 0.08\,R_\oplus$ planet candidate with a 0.37 day orbital period orbiting a M dwarf (TIC 439867639) that is 48.6 pc away and has a V magnitude of 15.69. A Lomb-Scargle periodogram of the photometry from each *TESS* sector finds a maximum peak of 0.04, indicating that the star is quiet. TOI-2445 has been observed in 2 *TESS* sectors (4 and 31).

Follow-up observations have found no evidence of this TOI being a false positive, although no spectroscopic observations of this TOI have been collected. Time-series photometric follow-up has made several detections of the transit of TOI-2445.01 on TIC 439867639 (shown in Figure 3.10).

The `dave` analysis of this TOI finds no strong indicators that the candidate is a false positive. However, like TOI-739, the SNR of the per-transit difference images used by `dave` is very low and the measured centroids are unreliable. No data validation reports have been generated by the SPOC pipeline for this TOI.

The `TRICERATOPS` analysis of this TOI finds FPP $= (1.88 \pm 0.45) \times 10^{-4}$. Because transits have been verified on-target, `TRICERATOPS` finds NFPP $= 0.0$. This FPP is sufficiently low to consider the planet validated. We hereby refer to this planet as TOI-2445 b.

We estimate the semi-amplitude of the RV signal for this planet to be $K_{\rm RV} = 4.5^{+2.8}_{-1.7}$ m/s, corresponding to $M_{\rm p} = 2.0^{+1.2}_{-0.7}\,M_\oplus$.

3.6 Discussion

In Section 3.5, we scrutinized the available data of 18 potentially terrestrial *TESS* planet candidates that display promise as subjects of emission spectroscopy observations with *JWST*.

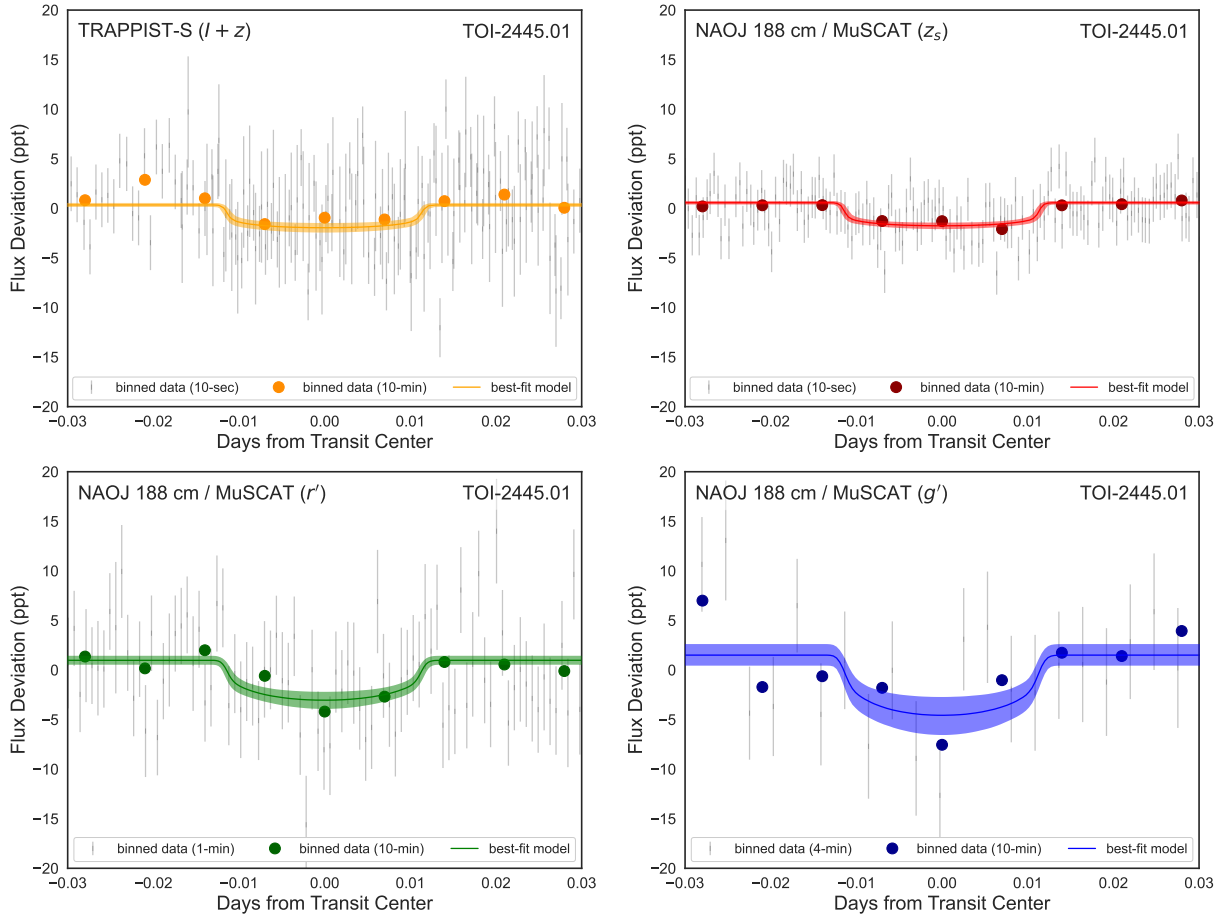

Figure 3.10: Phase-folded ground-based data and best-fit model of the transit of TOI-2445.01. The data is detrended with a linear model and 3σ outliers are removed.

Of these, 13 were validated. In Figure 3.11, we show how our targets are distributed in the planet radius – orbital period plane and the planet equilibrium temperature – stellar effective temperature planet, with all other known planets with $R_{\rm p} < 2\,R_{\oplus}$ included for reference.

The planet candidates and planets analyzed in this paper cover a wide region of parameter space that will allow for studies of hot, potentially terrestrial planets across different environments. For instance, many of the planets validated in this paper are among the hottest known planets with $R_{\rm p} < 2\,R_{\oplus}$. For stars with $T_{\rm eff} < 3500$ K, TOI-1442 b and TOI-206 b rank fifth and sixth hottest planet, respectively, with $T_{\rm eq} = 1072 \pm 54$ K and $T_{\rm eq} = 910 \pm 36$ K, only being surpassed by GJ 1252 b ($T_{\rm eq} \sim 1089$ K; Shporer et al. 2020), K2-137 b ($T_{\rm eq} \sim 1608$ K; Smith et al. 2018), TOI-1634 b ($T_{\rm eq} \sim 1608$ K; Cloutier et al. 2021), and TOI-1685 b ($T_{\rm eq} \sim 1066$ K; Bluhm et al. 2021). For stars with $3500 < T_{\rm eff} < 4000$ K, TOI-1075 b and TOI-833 b are the first and second hottest planets, respectively, with $T_{\rm eq} = 1336 \pm 56$ K

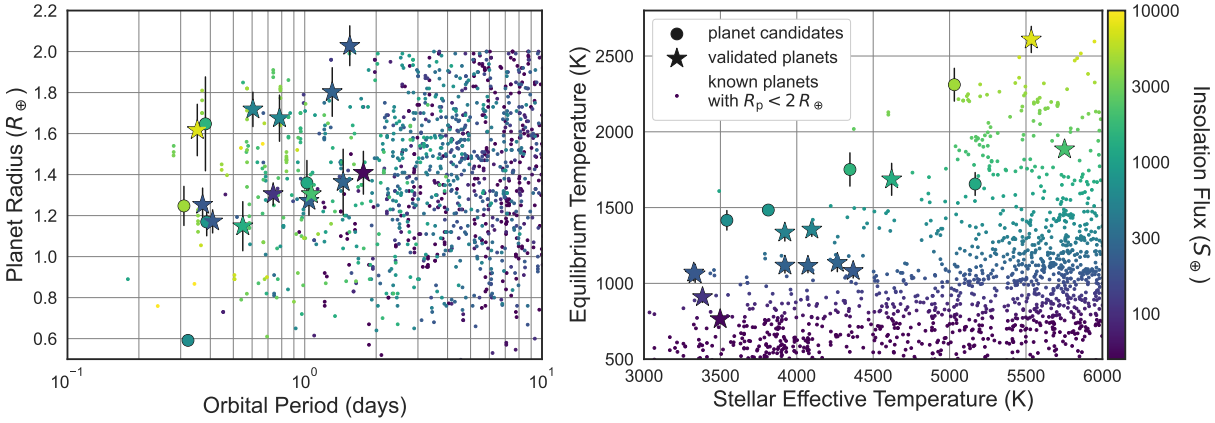

Figure 3.11: Left: Planet radii and orbital periods of all planet candidates (circles) and validated planets (stars) in this paper, along with all known planets with $R_p < 2\,R_\oplus$ (points). Right: Planet equilibrium temperatures and host star effective temperatures for the same planet candidates, validated planets, and known planets. Color indicates insolation flux. Data for known planets was obtained though the NASA Exoplanet Archive.

and $T_{eq} = 1118 \pm 49$ K, but would be superseded by TOI-2290.01 if found to be a bona fide planet. Lastly, TOI-2260 b is the fourth hottest known planet of this size to orbit any star, with $T_{eq} = 2609 \pm 86$ K, only being surpassed by KOI-55 b ($T_{eq} \sim 8000$ K; Charpinet et al. 2011), KOI-55 c ($T_{eq} \sim 7000$ K; Charpinet et al. 2011), and Kepler-1340 b ($T_{eq} \sim 2860$ K; Morton et al. 2016). All of these planets will be valuable for studying the evolution of planets with high equilibrium temperatures, which is a key parameter in core-powered atmospheric mass loss models for small planets (Ginzburg et al. 2016, 2018).

Of our 13 validated planets, 7 (TOI-206 b, TOI-500 b, TOI-1075 b, TOI-1442 b, TOI-2260 b, TOI-2411 b, and TOI-2445 b) are ultra-short-period planets, which are named for their < 1 day orbital periods (e.g., Batalha et al. 2011; Léger et al. 2009; Sanchis-Ojeda et al. 2013). One interesting case is that of TOI-2260 b, whose star we determine to have a metallicity of [Fe/H] $= 0.22 \pm 0.06$ dex. While an ultra-short-period planet orbiting such a metal-rich star is not unheard of, other planets of this type tend to orbit stars with lower metallicities (Winn et al. 2017). Specifically, according to the NASA Exoplanet Archive,[10] fewer than 10% of ultra-short-period planets orbit stars with metallicities greater than 0.2 dex. Further characterization of these planets could be helpful for understanding how these planets form around stars of different metal contents.

For TOI-1860 b and TOI-2260 b, we were able to use the *TESS* light curves of their host stars to estimate their ages, which we found to be 133 ± 26 and 321 ± 96 Myr, respectively. These ages make the planets some of the youngest known transiting planets to-date. In

[10] `https://exoplanetarchive.ipac.caltech.edu/`

addition to the recently validated TOI-1807 b, a $\sim 1.82\,R_\oplus$ planet that was found to have an age of 180 ± 40 by Hedges et al. (2021), these planets will be important case studies for determining how terrestrial planets evolve in hot environments. Specifically, they will allow us to test two competing theories behind the existence and behavior of the radius gap. Photoevaporative atmospheric mass-loss (Jackson et al. 2012; Jin and Mordasini 2018; Jin et al. 2014; Lopez and Fortney 2013; Owen and Wu 2013, 2017) predicts small planets to be stripped of their atmospheres within the first $\sim$ 100 Myr of the system lifetime, when the host star is still active enough to produce the high-energy photons responsible for atmospheric escape (Jackson et al. 2012; Ribas et al. 2005). Conversely, core-powered atmospheric mass loss is predicted to occur over a steadier $\sim$ 1 Gyr timescale (Gupta and Schlichting 2019). Some studies have explored this distinction by examining how the occurrence rate gap evolves over Gyr timescales (Berger et al. 2020; David et al. 2021; Sandoval et al. 2021). By characterizing these planets further, either by measuring their masses or observing their emission spectra with *JWST*, we will be able to determine to what extent these planets have experienced atmospheric mass loss over their short lives. Observations that support the lack of an atmosphere around these planets would provide evidence for the former, while observations that support the existence of atmospheres would provide evidence for the latter.

As was mentioned in Section 3.5, TOI-1860 is also a Solar twin. With an age of 133 ± 26 Myr, this star is the youngest Solar twin with a transiting planet discovered yet. Future studies of this system could shed light on the formation and evolution of planets around Sun-like stars.

The last notable feature of the targets included in this paper is that they span a wide range of stellar spectral types. It is believed that the radius at which short-period planets transition from having volatile-rich atmospheres to having terrestrial-like or negligible atmospheres depends on the mass of the host star. Specifically, Fulton and Petigura (2018) found evidence that this transition radius increases with increasing stellar mass. In other words, a $1.6\,R_\oplus$ planet has a higher probability of having a volatile-rich atmosphere when orbiting a K dwarf than it does when orbiting a G dwarf. Because our sample spans from low-mass M-dwarfs to Sun-like stars, acquiring emission spectroscopy observations of our targets would allow for a direct test of this hypothesis.

To explore how the *TESS* mission has thus far increased the number of potentially terrestrial planets amendable to emission spectroscopy observations, we compile a list of all terrestrial planets with ESM > 7.5 that were confirmed (i.e., have had their masses measured with precise radial velocities) or validated (i.e., have had their planetary natures certified using methods that do not involve a mass measurement) prior to the writing of this paper. Table 3.10 shows these planets, including L 168-9 b (Astudillo-Defru et al. 2020), LHS 3844 b (Vanderspek et al. 2019), HD 213885 b (Espinoza et al. 2020), HR 858 c (Vanderburg et al. 2019), HIP 26013 b (Osborn et al. 2021), GJ 1132 b (Berta-Thompson et al. 2015; Bonfils et al. 2018), LTT 3780 b (Cloutier et al. 2020a), HIP 73427 b (Teske et al. 2021), GJ 1252 b (Shporer et al. 2020), HIP 70705 b (Deeg et al. in prep), HD 158259 b (Hara et al. 2020), HD 219134 b (Motalebi et al. 2015), HD 219134 c (Gillon et al. 2017b), 55 Cnc e (Bourrier et al. 2018; McArthur et al. 2004; Winn et al. 2011), TOI-1634 b (Cloutier et al. 2021; Hirano et al.

TOI	Alt Name	K_s mag	$T_{\rm eff}$ (K)	$P_{\rm orb}$ (days)	$R_{\rm p}$ $(R_\oplus)$	$M_{\rm p}$ $(M_\oplus)$	$T_{\rm eq}$ (K)	ESM
134.01	L 168-9 b	7.082 ± 0.031	3800 ± 70	1.401500 ± 0.000180	1.39 ± 0.09	4.60 ± 0.56	981 ± 27	9.9 ± 1.4
136.01	LHS 3844 b	9.145 ± 0.023	3036 ± 77	0.462929 ± 0.000002	1.30 ± 0.02	-	805 ± 27	28.8 ± 1.8
141.01	HD 213885 b	6.419 ± 0.024	5978 ± 50	1.008035 ± 0.000020	1.75 ± 0.05	8.83 ± 0.66	2131 ± 21	14.1 ± 0.8
396.01	HR 858 c	5.149 ± 0.020	6201 ± 50	5.972930 ± 0.000600	1.94 ± 0.07	-	1317 ± 16	9.7 ± 0.7
431.02	HIP 26013 b	6.723 ± 0.021	4850 ± 75	0.490047 ± 0.000010	1.28 ± 0.04	3.07 ± 0.35	1888 ± 50	16.0 ± 1.2
667.01	GJ 1132 b	8.322 ± 0.027	3270 ± 140	1.628931 ± 0.000027	1.13 ± 0.06	1.66 ± 0.23	584 ± 30	9.5 ± 1.4
732.01	LTT 3780 b	8.204 ± 0.021	3331 ± 157	0.768448 ± 0.000054	1.33 ± 0.07	2.62 ± 0.47	892 ± 44	13.4 ± 1.6
836.02	HIP 73427 b	6.804 ± 0.018	4250 ± 120	3.816514 ± 0.000757	1.81 ± 0.27	5.76 ± 1.14	834 ± 47	8.7 ± 2.7
1078.01	GJ 1252 b	7.915 ± 0.023	3458 ± 140	0.518235 ± 0.000006	1.19 ± 0.07	2.09 ± 0.56	1089 ± 53	16.3 ± 2.2
1416.01	HIP 70705 b	7.708 ± 0.024	4884 ± 70	1.069763 ± 0.000005	1.73 ± 0.05	5.00 ± 1.10	1514 ± 24	11.0 ± 0.7
1462.01	HD 158259 b*	4.965 ± 0.023	5801 ± 157	2.178000 ± 0.000100	1.25 ± 0.10	2.22 ± 0.42	1673 ± 76	8.4 ± 1.5
1469.01	HD 219134 b	3.261 ± 0.304	4699 ± 16	3.093500 ± 0.000300	1.60 ± 0.06	4.74 ± 0.19	1014 ± 8	37 ± 6
1469.02	HD 219134 c	3.261 ± 0.304	4699 ± 16	6.764580 ± 0.000330	1.51 ± 0.05	4.36 ± 0.22	782 ± 6	18.3 ± 2.9
1773.01	55 Cnc e	4.015 ± 0.036	5172 ± 18	0.736547 ± 0.000001	1.88 ± 0.03	7.99 ± 0.33	1947 ± 13	69.9 ± 2.7
1634.01	TOI-1634 b	8.600 ± 0.014	3550 ± 69	0.989343 ± 0.000015	1.79 ± 0.08	4.91 ± 0.69	923 ± 23	13.9 ± 1.3
1685.01	TOI-1685 b	8.758 ± 0.020	3434 ± 51	0.6691403 ± 0.000002	1.70 ± 0.07	3.78 ± 0.63	1066 ± 24	13.8 ± 1.2
1807.01	HIP 65469 b**	7.568 ± 9.995	4757 ± 50	0.549372 ± 0.000007	1.82 ± 0.05	-	1730 ± 28	22.6 ± 1.4
1827.01	GJ 486 b	6.362 ± 0.018	3340 ± 54	1.467119 ± 0.000031	1.31 ± 0.07	2.82 ± 0.12	700 ± 17	21.5 ± 2.4
2431.01	HIP 11707 b***	7.554 ± 0.023	4079 ± 126	0.224200 ± 0.000020	1.62 ± 0.21	-	2048 ± 125	29 ± 8
-	HD 3167 b	7.066 ± 0.020	5261 ± 60	0.959641 ± 0.000012	1.70 ± 0.17	5.02 ± 0.38	1746 ± 46	14.0 ± 2.9
-	K2-141 b	8.401 ± 0.023	4599 ± 79	0.280324 ± 0.000002	1.51 ± 0.05	5.08 ± 0.41	2115 ± 48	15.0 ± 1.1
-	GJ 9827 b	7.193 ± 0.024	4340 ± 47	1.208982 ± 0.000007	1.58 ± 0.03	4.91 ± 0.49	1183 ± 15	14.9 ± 0.6

Table 3.10: Confirmed and validated planets with $R_{\rm p} < 2\,R_\oplus$ and ESM > 7.5. * Planet radius was calculated using the transit depth listed on ExoFOP-TESS, $\delta = 90 \pm 7$ ppm. ** The large uncertainty in the K_s mag is reported by 2MASS; the 2MASS J and H mag are 8.103 ± 0.023 and 7.605 ± 0.018, respectively. *** Entries for this row are taken from TICv8 and ExoFOP-TESS, as the authors of this paper were unable to share exact figures at the time of writing; he mass of the transiting object has been measured and is consistent with that of a planet (via personal communication).

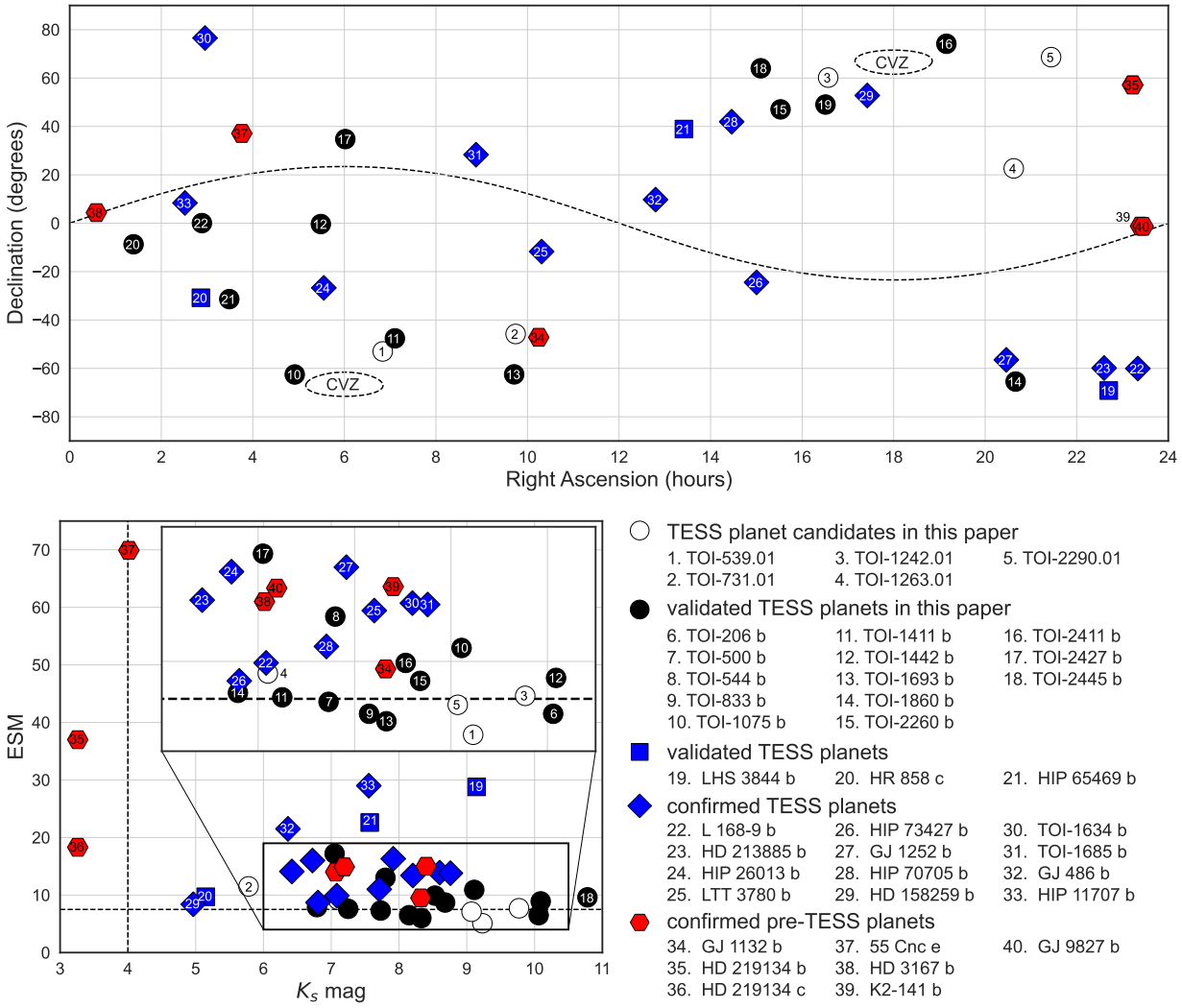

Figure 3.12: Top: Coordinates of the *TESS* planet candidates in this paper (white circles), validated *TESS* planets in this paper (black circles), validated *TESS* planets (blue squares), confirmed *TESS* planets (blue diamonds), and confirmed pre-*TESS* planets (red hexagons). The ecliptic plane and ecliptic poles (i.e., the *JWST* continuous viewing zones) are shown as dashed black lines. Bottom: Emission spectroscopy metric verses apparent K_s magnitude for each planet candidate and planet. The dashed lines indicate the minimum values a target should have to be observed with *JWST*.

2021), TOI-1685 b (Bluhm et al. 2021), HIP 65469 b (Hedges et al. 2021), GJ 486 b (Trifonov et al. 2021), HIP 11707 b (Malavolta et al. in prep), HD 3167 b (Christiansen et al. 2017; Vanderburg et al. 2016), K2-141 b (Malavolta et al. 2018), and GJ 9827 b (Niraula et al. 2017; Rice et al. 2019; Rodriguez et al. 2018). Of these, 7 were discovered and confirmed prior to the *TESS* mission, 12 were discovered by *TESS* and subsequently confirmed, and 3 were discovered by *TESS* and subsequently validated. Going by these numbers, *TESS* has increased the number of potential *JWST* emission spectroscopy targets from 7 to 22. If we include the planets validated in this paper, this count increases to 35 – a five-fold increase in the size of the sample available prior to *TESS*.

Another aspect one must consider when planning for *JWST* observations of these targets is their locations in the sky. *JWST* operates in an ecliptic coordinate framework that makes the telescope capable of observing targets within 5° of the north and south ecliptic poles (regions dubbed the "continuous viewing zones," or CVZs) at any time of the year and all other regions of the sky twice per year over time intervals that vary with ecliptic longitude. In other words, targets at or near the ecliptic poles will be observable for longer periods of time than targets near the ecliptic plane. In the top panel of Figure 3.12, we show the position of each planet candidate and confirmed/validated planet in our sample. Though no targets lie within the CVZs, several targets (e.g., TOI-206, TOI-500, TOI-539, TOI-1242, TOI-1442, HD 158259) are only a short distance away. While most of the systems in our sample would make excellent targets for these observations, those close to the CVZs would allow for more flexibility when planning observations.

Lastly, in addition to ESM, there are other properties of these systems that must be considered when planning for *JWST* observations. For instance, a star that is too bright in the passband could saturate the instrument in the minimum number of groups (2) required for a *JWST* observation.[11] A vast majority of terrestrial planet emission spectroscopy observations will be conducted using MIRI LRS, a low-resolution spectrograph with a wavelength range of $5 - 12\,\mu$m. `PandExo` (Batalha et al. 2017, 2019), a tool created to calculate the optimal exposure times for exoplanetary *JWST* observations, estimates the brightest star one can observe with MIRI LRS without saturating to have $K \sim 4$. All of the planet candidates discussed in Section 3.5 meet this criterion, and all but three previously confirmed/validated planets (HD 219134 b, HD 219134 c, and 55 Cnc e) meet this criterion. This indicates that nearly all planets in our sample will be observable with this instrument. The location of each planet candidate and confirmed/validated planet in ESM – K mag space is shown in the bottom panel of Figure 3.12.

3.7 Conclusions

We vet 18 hot *TESS* planet candidates that are potentially terrestrial ($R_\mathrm{p} < 2\,R_\oplus$) and would make good targets for emission spectroscopy observations with *JWST* (ESM $\gtrsim 7.5$) using

[11] A "group" is *JWST* terminology for the number of consecutively read frames with no resets.

several follow-up observations from the *TESS* Follow-up Observing Program and analyses performed with `dave` and `TRICERATOPS`. Of these 18, 13 were validated.

The 13 validated planets exist in a diverse set of environments that will allow for differential studies of small planets in and around the $1.5 - 2.0\,R_\oplus$ radius gap. Some key takeaways about these validated planets are as follows:

- 7 of the validated planets (TOI-206 b, TOI-500 b, TOI-1075 b, TOI-1442 b, TOI-2260 b, TOI-2411 b, and TOI-2445 b) are ultra-short-period planets.
- TOI-1860 b is a $1.34\,R_\oplus$ planet orbiting a young (133 ± 26 Myr) Solar twin. This is the youngest planetary system discovered around a Solar twin to-date.
- TOI-2260 b is a $1.68\,R_\oplus$ ultra-short-period planet orbiting a young (321 ± 96 Myr) late G dwarf. With a stellar metallicity of [Fe/H] $= 0.22 \pm 0.06$ dex, this star ranks among the most metal-rich to host an ultra-short-period planet. TOI-2260 b has a $T_{\rm eq}$ of 2609 ± 86 K and is the fourth hottest planet with $R_{\rm p} < 2\,R_\oplus$ discovered to-date.

Lastly, we assemble a list of all other previously discovered transiting planets that met our selection criteria for being ideal *JWST* emission spectroscopy targets. We discuss the prospects of using *JWST* to observe each of these known planets, along with the planet candidates and validated planets discussed in this paper.

Chapter 4

HD 56414 b: A Warm Neptune Transiting an A-type Star

An earlier version of this article was published as: Giacalone, S., Dressing, C. D., García Muñoz, A., Hooton, M. J., Stassun, K. G., Quinn, S. N., Zhou, G., Ziegler, C., Vanderspek, R., Latham, D. W., Seager, S., Winn, J. N., Jenkins, J. M., Briceño, C., Huang, C. X., Rodriguez, D. R., Shporer, A., Mann, A. W., Watanabe, D., Wohler, B., 2022, *The Astrophysical Journal Letters*, 935, L10.

We report the discovery in *TESS* data and validation of HD 56414 b (a.k.a. TOI-1228 b), a Neptune-size ($R_{\rm p} = 3.71 \pm 0.20\,R_{\oplus}$) planet with a 29-day orbital period transiting a young (Age = 420 ± 140 Myr) A-type star in the *TESS* southern continuous viewing zone. HD 56414 is one of the hottest stars ($T_{\rm eff} = 8500 \pm 150$ K) to host a known sub-Jovian planet. HD 56414 b lies on the boundary of the hot Neptune desert in planet radius – bolometric insolation flux space, suggesting that the planet may be experiencing mass loss. To explore this, we apply a photoevaporation model that incorporates the high near ultraviolet continuum emission of A-type stars. We find that the planet can retain most of its atmosphere over the typical 1-Gyr main sequence lifetime of an A-type star if its mass is $\geq 8\,M_{\oplus}$. Our model also predicts that close-in Neptune-size planets with masses $< 14\,M_{\oplus}$ are susceptible to total atmospheric stripping over 1 Gyr, hinting that the hot Neptune desert, which has been previously observed around FGKM-type stars, likely extends to A-type stars.

4.1 Introduction

Over 99% of planets have been discovered around FGKM dwarfs, main-sequence stars with effective temperatures under ~ 7500 K (Habets and Heintze 1981). Consequently, relatively little is known about planets orbiting hotter and more massive stars, which differ from cooler stars in multiple ways that could affect orbiting planets. For instance, A-type stars are often fully radiative, which could impede their abilities to dissipate tides excited by close-in planets, leading to slower orbital evolution due to tidal interactions relative to planets orbiting cooler stars with convective layers (e.g., Winn et al. 2010). Another consequence of being fully

radiative is reduced X-ray and extreme ultraviolet (XUV) emission, believed to be the main driver of atmospheric mass loss for close-in planets around FGKM-type stars (Lammer et al. 2003), which suggests that planets around these stars are less likely to lose their atmospheres. Conversely, it has also been predicted that, due to their high effective temperatures and luminosities, A-type stars can drive atmospheric mass loss of close-in planets even more rapidly than cooler stars (e.g., García Muñoz and Schneider 2019). Lastly, because A-type stars have shorter main sequence lifetimes than cooler stars, their planets tend to be younger, and perhaps less evolved.

In general, planets are more difficult to detect around A-type stars than around cooler stars. First, a planet of a given size orbiting a larger star produces a shallower transit. Second, rapid rotational speeds and pulsation-driven jitter complicate mass measurements of planets orbiting A stars (e.g., Galland et al. 2005; Griffin et al. 2000). In addition, A-type stars are intrinsically rarer than cooler stars (by a factor of ~ 100; van Leeuwen 2007), which reduces the sample around which we can search for these planets.

Nonetheless, several studies have constrained the occurrence rate of giant planets around these hot stars. Johnson et al. (2010) calculated the frequency of planets more massive than Jupiter with orbital separations < 2.5 AU by collecting radial velocities (RVs) of main sequence FGKM stars as well as somewhat more massive stars stars that may have evolved off the main sequence (and consequently have slower rotation rates). They found that giant planets generally become more common as stellar mass increases. Zhou et al. (2019b) measured the occurrence rate of transiting hot Jupiters around A-type stars and found no statistically significant difference compared to FG-type stars. Lastly, Nielsen et al. (2019) measured the occurrence of directly imaged giant planets with orbital separations between 3 and 100 AU and also found a strong correlation between occurrence rate and stellar mass.

While these studies provided valuable insight into the population of giant planets around A-type stars, the population of smaller and less massive planets is largely unexplored: only three planets smaller than Jupiter (hereafter referred to as "sub-Jovian") have been confirmed around these hot stars: Kepler-1115 b (Morton et al. 2016), Kepler-462 b (Morton et al. 2016), and Kepler-462 c (Masuda and Tamayo 2020). A larger sample is required to investigate the properties and frequency of the smaller and less massive planets orbiting A-type stars. In this paper, we add another planet to this sample: the warm Neptune HD 56414 b.

This paper is structured as follows. In Section 4.2, we present the observations used in our analysis. In Section 4.3 we characterize the planet and star. In Section 4.4 we validate the planet. Lastly, in Section 4.5, we address the significance of the newly discovered planet and conclude.

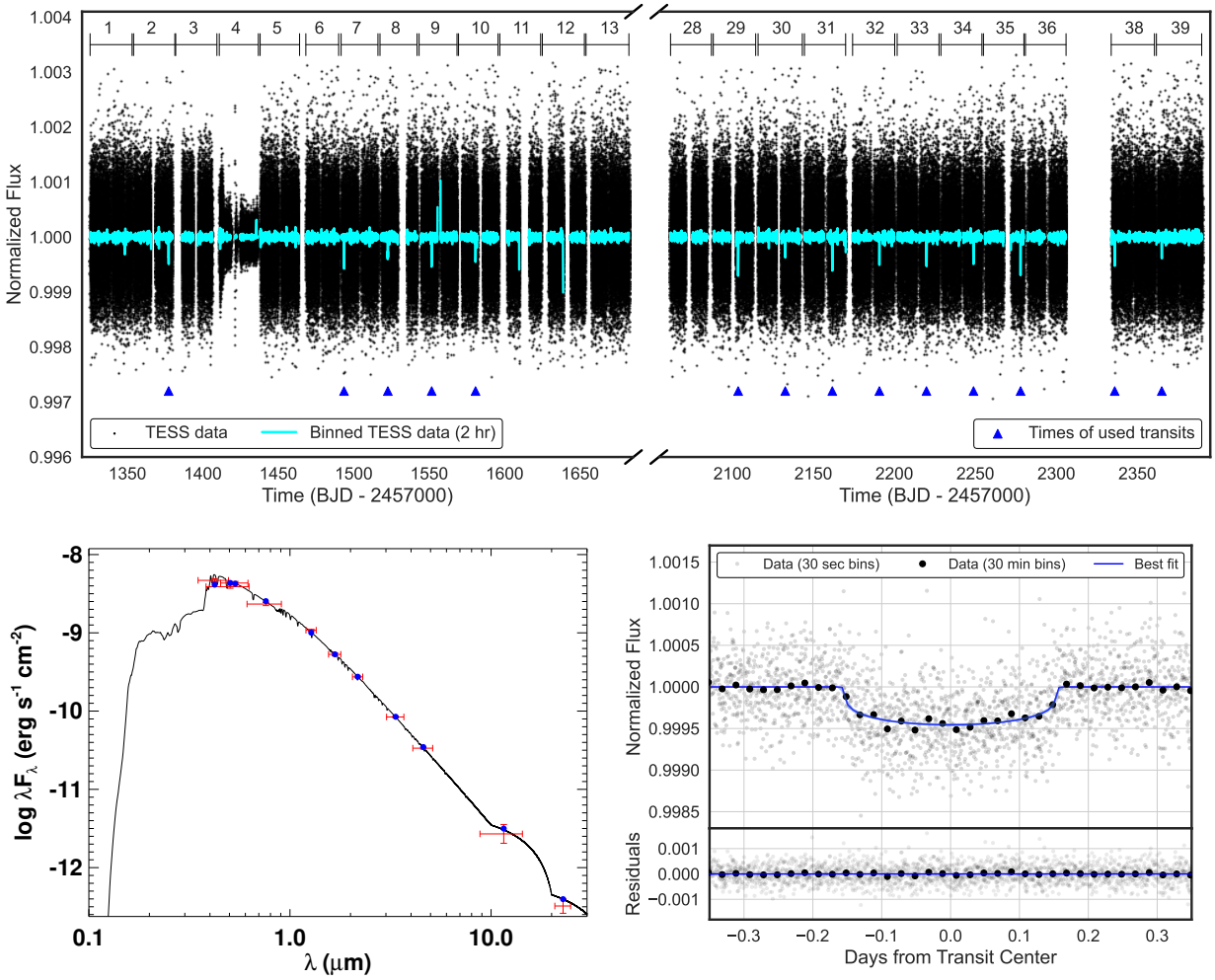

Figure 4.1: *Top*: *TESS* lightcurve produced by the SPOC pipeline after flattening and outlier removal. Blue triangles show the times of transits used for fitting. The sectors are indicated at the top of the panel. Sector 4 was removed from the light curve analysis (see Section 4.2). *Bottom left*: SED fit of HD 56414. Blue points indicate broadband photometry measurements and the black curve indicates the best-fit stellar model with $T_{\rm eff} = 8500 \pm 150$ K. *Bottom right*: Phase-folded *TESS* data centered on the transit with residual variability removed with a Gaussian Process model. The data is binned with bin widths of 30 seconds (gray points) and 30 minutes (black points). The blue line is the best-fit transit model.

4.2 Observations

TESS Photometry

HD 56414 (a.k.a. TOI-1228 or TIC 300038935) was observed by *TESS* for a total of 24 sectors between 2018 July 18 and 2021 June 24. During sectors 1–13, the target was observed with a cadence of 2 minutes. During sectors 28–36 and 38–39, the target was observed with cadences of both 2 minutes and 20 seconds. A transiting planet candidate, denoted TOI-1228.01, was identified in this data by the NASA Science Processing Operations Center (SPOC; Jenkins et al. 2016) pipeline on 2019 August 26. The data and related analyses are available for download on the Mikulski Archive for Space Telescopes (MAST). The SPOC pipeline produces two light curves: a light curve produced using simple aperture photometry (SAP) and a light curve produced using simple aperture photometry plus a pre-search data conditioning step (PDCSAP; Stumpe et al. 2014). We utilized the latter for our analysis.

The PDCSAP process retains intrinsic stellar variability, which could influence interpretation of the data by introducing correlated noise. Specifically, stars in the temperature regime of HD 56414 are often δ Scuti variables, which can pulsate at periods under a day with amplitudes of a few ppt. While we found no evidence of periodic pulsations, we noticed some aperiodic variability of a few ppt that is likely residual background or instrumental noise. We removed long-term variability by fitting the data to a cubic basis spline with a knot distance of 1 day, linearly interpolating over the 7.6 hour-long transits to remove low frequency trends without altering the transit shape. Next, we removed short-term out-of-transit variability by clipping out the transits and fitting the light curve to a cubic basis spline with a knot distance of 0.1 day. We ensured that this process did not affect the morphologies of the transits by comparing each pre-flattening transit with its post-flattening counterpart. The transits of the planet candidate were identified using the orbital period ($P_{\rm orb}$) and time of first transit center (T_0) reported by the SPOC. Lastly, we removed outliers more than 5σ from the median flux. The resulting light curve is shown in Figure 4.1.

Next, we inspected each transit and removed those with only partial coverage and those with poor data quality. Because our flattening procedure requires both pre- and post-transit baselines to properly normalize each transit, it had difficulty recovering the depths of partially detected transits. Consequently, partial transits that were significantly deeper than expected occurred near 1609.774 TBJD (where TBJD = BJD - 2457000) and 1638.824 TBJD due to gaps in data coverage. We also removed a transit that occurred at 1348.326 TBJD during sector 1, which took place following an incorrectly configured fine pointing calibration after a spacecraft momentum dump,[1] and all data from sector 4, during which a row of anomalously low pixels, caused by a smear correction applied to adjust for a saturated star located elsewhere on the CCD, passed directly through HD 56414. Our final dataset included 14 transits during 24 *TESS* sectors (see Figure 4.1).

[1]See sector 1 data release notes: `https://heasarc.gsfc.nasa.gov/docs/tess/cycle1_drn.html`

SMARTS/CHIRON Spectroscopy

We obtained reconnaissance spectra of HD 56414 on 2019 October 21, 2021 September 26, and 2022 January 13 using the CHIRON spectrograph on the 1.5 m SMARTS telescope, located at Cerro Tololo Inter-American Observatory (CTIO), Chile (Tokovinin et al. 2013). The three spectra yielded signal-to-noise ratios per resolution element of 36.6, 71.5, and 117.5, respectively, at 550 nm. Because stellar properties can be difficult to extract from spectra of hot, rapidly-rotating stars, we primarily used these spectra to determine the line-of-sight rotational velocity of the star. To do so, we obtained a line profile from each spectrum via a least-squares deconvolution (Donati et al. 1997) between the observation and a synthetic non-rotating spectral template generated from the ALTAS-9 model atmospheres (Castelli and Kurucz 2003). We then modeled the resulting line profile via a line broadening kernel that incorporates the effects of rotational, instrumental, and macroturbulent broadening. This calculation yielded $v \sin i_\star = 59.4 \pm 3.0\,\mathrm{km\,s^{-1}}$. We also use the spectra to rule out false-positive-producing scenarios, which we discuss further in Section 4.4.

SOAR/HRCam Speckle Imaging

We obtained I-band Speckle interferometric observations of HD 56414 on 2019 March 17 with HRCam mounted on the 4.1 m Southern Astrophysical Research (SOAR) telescope, located at Perro Pachón, Chile. These observations and their related analyses are outlined in Ziegler et al. (2020, 2021), to which we direct the reader for more information. The observations achieved a contrast of 5.2 magnitudes at $1''$. The speckle auto-correlation function, which covers a field of view of $3'' \times 3''$, and corresponding contrast curve are shown in Figure 4.2. We use these observations to constrain the possibility of false-positive-producing scenarios, which we discuss further in Section 4.4.

4.3 Data Analysis

Adopted Stellar Parameters

Our adopted stellar parameters were obtained using a number of sources and methods (see Table 1). We adopted the stellar right ascension (α), declination (δ), proper motion in right ascension (μ_α), proper motion in declination (μ_δ), and parallax (π) from *Gaia* eDR3 (Gaia Collaboration et al. 2021).

Next, we used the broadband spectral energy distribution (SED) and *Gaia* eDR3 parallax of the star to determine the bolometric flux ($F_{\rm bol}$), effective temperature ($T_{\rm eff}$), and radius ($R_\star$) of the star (following the procedures described in Stassun and Torres 2016; Stassun et al. 2017, 2018a). We obtained $G_{\rm BP}$ and $G_{\rm RP}$ from *Gaia* eDR3, our B and V magnitudes from APASS (Henden et al. 2016), our J, H, and K_s magnitudes from 2MASS (Skrutskie et al. 2006), and our $W1-W4$ magnitudes from ALLWISE (Cutri et al. 2014). We constrained interstellar extinction (A_V) using the analysis by Kounkel and Covey (2019) and stellar

metallicity ([Fe/H]) based on the designation of HD 56414 as a metallic-line star by Houk and Cowley (1975). We fit the Kurucz stellar atmospheric models (Kurucz 1993b), resulting in a reduced χ^2 of 1.7 (see Figure 4.1). We calculated the luminosity of the star ($L_\star$) directly using $F_{\rm bol}$ together with the *Gaia* distance, and stellar mass ($M_\star$) using the empirical relations presented in Torres et al. (2010). All of our derived properties are consistent with those quoted in version 8.2 of the *TESS* Input Catalog (Stassun et al. 2019).

Lastly, we extracted the $v \sin i_\star$ and macroturbulent velocity ($v_{\rm mac}$) from the CHIRON spectra (Section 4.2). Using this $v \sin i_\star$ and the $R_\star$ calculated above, we calculated $P_{\rm rot}/\sin i$ (where $P_{\rm rot}$ is the stellar rotation period). The rotation rate of the star is not informative of the stellar age because the star is hotter than the Kraft break. However, we assign an age of 420 ± 140 Myr based on its Theia 797 membership assigned in Kounkel and Covey (2019), which identified stellar strings and calculated their ages using a combination of machine learning analysis and isochrone fitting with a typical uncertainty of 0.15 dex.

Planet Model Fit

We fit the *TESS* photometry to a transit model using `exoplanet` (Foreman-Mackey et al. 2021). The transit model was initialized with a quadratic limb darkening law (with coefficients $u_{\star,0}$ and $u_{\star,1}$) and the following priors: (1) Gaussian priors for $M_\star$, $R_\star$, $T_{\rm eff}$, K_s magnitude, T_0, the logarithm of $P_{\rm orb}$, the logarithm of the transit depth, and the flux zero point of the light curve (2) a uniform prior on the transit impact parameter (b), and (3) a prior on eccentricity (e) based on Kipping (2013b). In addition, we included a Gaussian Process model with a simple harmonic oscillator kernel to account for residual variability in the light curve.[2] We ran a 10 walker ensemble with 20,000 steps and discarded the first 10,000 steps as burn-in. The best-fit phase-folded model is shown in Figure 4.1.

As shown in Table 1, we fit for the following physical and orbital parameters: T_0, $P_{\rm orb}$, the transit duration $T_{\rm dur}$, the planet radius ($R_{\rm p}$), b, the orbital inclination (i), the orbital semi-major axis (a), e, $u_{\star,0}$, and $u_{\star,1}$. In addition, we estimated the planet equilibrium temperature assuming zero bond albedo and full day-night heat redistribution ($T_{\rm eq}$) and the planet emission spectroscopy and transmission spectroscopy metrics (ESM and TSM) assuming a circular orbit.[3] The best-fit model is a planet with $R_{\rm p} = 3.71 \pm 0.20\,R_\oplus$ on a 29.04992 ± 0.00021 day orbit with $e < 0.68$ (3σ).

Based on the rapid rotational rate of HD 56414, we might expect to see an asymmetrical transit profile due to gravity darkening, which can be modelled to independently measure the true spin-orbit angle (Ψ; Barnes 2009). To test this, we also fit the *TESS* light curve to a gravity-darkened model following Hooton et al. (2022) in which we additionally fit for the stellar inclination ($i_\star$) and sky-projected stellar obliquity (λ). We fixed the stellar polar

[2]Although, we note that models with and without the Gaussian Process model did not yield significantly different results.

[3]ESM and TSM are quantities defined by Kempton et al. (2018) that indicate the suitability of the planet to emission and transmission spectroscopy. For TSM, we estimated the planet mass using the mass–radius relation defined in Chen and Kipping (2017) for Neptunian worlds.

Parameter	Value	Source
Identifiers		
HD	56414	
TOI	1228	
TIC	300038935	
2MASS	J07112249−6850006	
Gaia DR2	5268547016621360768	
Astrometry & Position		
α	07:11:22.48	*Gaia* eDR3
δ	-68:50:00.03	*Gaia* eDR3
μ_α (mas yr^{-1})	-0.735 ± 0.019	*Gaia* eDR3
μ_δ (mas yr^{-1})	35.120 ± 0.015	*Gaia* eDR3
π (mas)	3.735 ± 0.013	*Gaia* eDR3
Distance (pc)	267.74 ± 1.07	From parallax
Photometry		
G_{BP}	9.2908 ± 0.0006	*Gaia* eDR3
G_{RP}	9.0508 ± 0.0006	*Gaia* eDR3
B	9.390 ± 0.002	APASS
V	9.22 ± 0.03	APASS
J	8.89 ± 0.03	2MASS
H	8.85 ± 0.05	2MASS
K_s	8.82 ± 0.02	2MASS
$W1$	8.78 ± 0.02	ALLWISE
$W2$	8.80 ± 0.02	ALLWISE
$W3$	8.82 ± 0.02	ALLWISE
$W4$	9.1 ± 0.2	ALLWISE
Stellar Physical Properties		
$M_\star$ ($M_\odot$)	1.89 ± 0.11	This paper
$R_\star$ ($R_\odot$)	1.751 ± 0.065	This paper
T_{eff} (K)	8500 ± 150	This paper
$L_\star$ ($L_\odot$)	14.39 ± 0.34	This paper
$[Fe/H]$ (dex)	$0.0^{+0.3}_{-0.0}$	Houk and Cowley (1975)
A_V (mag)	0.22 ± 0.03	Kounkel and Covey (2019)
$v \sin i_\star$ (km s^{-1})	59.4 ± 3.0	This paper
v_{mac} (km s^{-1})	3.2 ± 1.0	This paper
F_{bol} (erg cm^{-2} s^{-1})	$(6.44 \pm 0.15) \times 10^{-9}$	This paper
$P_{rot}/\sin i_\star$ (days)	1.49 ± 0.09	This paper
Age (Myr)	420 ± 140	This paper
Best-Fit Planet Model Parameters		
T_0 (BJD)	2458348.324 ± 0.005	This paper
P_{orb} (days)	29.04992 ± 0.00021	This paper
T_{dur} (hours)*	7.58 ± 0.14	This paper
R_p ($R_\oplus$)	3.71 ± 0.20	This paper
b	0.34 ± 0.19	This paper
i ($^\circ$)	89.3 ± 0.4	This paper
a (AU)	0.229 ± 0.004	This paper
e	$< 0.68\,(3\sigma)$	This paper
$u_{\star,0}$	0.54 ± 0.27	This paper
$u_{\star,1}$	0.19 ± 0.37	This paper
T_{eq} (K)**	1133 ± 30	This paper
ESM	1.9 ± 0.2	This paper
TSM***	30.0 ± 1.7	This paper

Table 4.1: Adopted stellar and planet parameters. * Calculated as the total transit duration, T_{14}. ** Calculated assuming zero Bond albedo and full day-night heat redistribution. *** Planet mass estimated using the mass–radius relation defined in Chen and Kipping (2017).

temperature, stellar equatorial radius, and $v \sin i_\star$ to the median values in Table 1, and fixed the gravity darkening coefficient β according to Claret (2017). In addition, we derived $P_{\rm rot}$, Ψ, and the stellar oblateness. The parameters shared between the gravity-darkened and non-gravity-darkened fits agreed well, while the gravity-darkened-specific model parameters were only weakly constrained. We constrained the stellar inclination to $i_\star > 19°$ at the 3σ level, which rules out configurations with the rotation axis pointing towards the observer. This result is intuitive, as $P_{\rm rot}$ would need to be very short to explain the spectroscopically inferred $v \sin i_\star$ for small $i_\star$. Values of $i_\star$ between 45° and 90° were equally likely, resulting in $P_{\rm rot} = 1.33^{+0.23}_{-0.45}$ days. For λ and Ψ, all angles are plausible, although polar orbits are slightly preferred. Better constraints on these angles may be obtainable with future transit observations. In addition, λ could be obtained independently via the Rossiter-McLaughlin effect (e.g., Collier Cameron et al. 2010), although this would be difficult to accomplish given the shallow transit depth.

4.4 Planet Validation

Follow-up Observations

We utilized the ground-based follow-up observations described in Section 4.2 to search for evidence of unresolved stellar-mass companions that would imply that TOI-1228.01 is a false positive (FP). We began by using our spectra to search for single-lined and double-lined spectroscopic binaries. The two high-S/N spectra were collected at 2483.8406 and 2592.6828 TBJD, which correspond to orbital phases of 0.09 and 0.84 using the orbital parameters in Table 1. These observations yielded RVs of 0.79 ± 0.73 km/s and 1.35 ± 0.73 km/s, respectively. At these orbital phases, a $0.1\,M_\odot$ stellar companion on a circular 29-day orbit would produce a $\Delta RV > 6$ km/s. These observations therefore rule out the possibility that the transit-like event is caused by a stellar-mass companion. This was corroborated by a search for double-lined spectroscopic binaries, which produced no evidence of excess stellar lines.

We searched for evidence of longer period stellar companions using our speckle interferometric observations. Our observations rule out companion stars with $\Delta I < 1$ at orbital separations $> 0.1''$ and $\Delta I < 4.5$ at orbital separations $> 0.2''$, indicating that stellar-mass companions with brightnesses comparable to HD 56414 are unlikely to be present beyond 25 AU.

Nonetheless, these observations alone are not sufficient to validate TOI-1228.01 because some FP scenarios can evade detection by these methods. For instance, FPs can occur when the transit originates from a nearby source that is known, but is unresolved in the *TESS* data. To illustrate, Figure 4.2 shows that several additional stars lie near the aperture used to extract the light curve. We investigated these FP scenarios via the following statistical analyses.

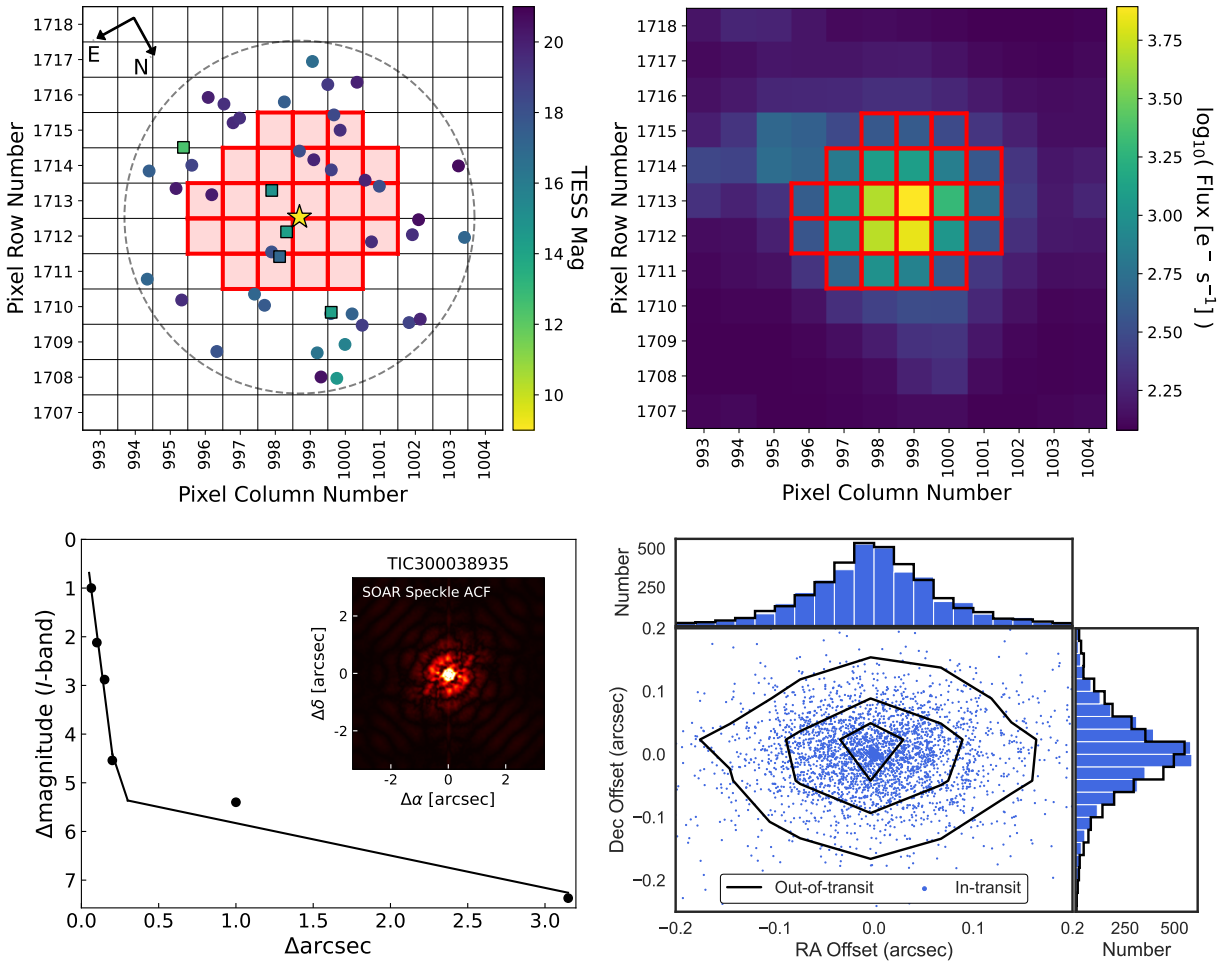

Figure 4.2: Visualizations of the vetting measures described in Section 4.4. *Top-left*: Objects within 100″ of HD 56414 (indicated by the yellow star). The SPOC aperture is shown in red, squares are nearby sources bright enough to be FP-inducing nearby eclisping binaries, and circles are nearby sources too faint to be FP-inducing nearby eclipsing binaries. *Top-right*: Corresponding *TESS* image, with the same aperture overlaid. *Bottom-left*: Speckle imaging image and contrast curve of HD 56414, which detects no companions within detection limits. *Bottom-right*: Results of centroid offset analysis with `vetting`. HD 56414 is at the origin. Solid black lines are 1σ, 2σ, and 3σ contours formed from 3,629 randomly sampled out-of-transit data points. Blue points are centroids for each in-transit data point. The difference between the two resulting distributions is not statistically significant.

Centroid Offset Analysis

FPs due to signals originating from nearby sources often cause offsets between in-transit and out-of-transit centroids, the photocenters of the target star in the *TESS* images (e.g., Bryson et al. 2013; Twicken et al. 2018). We searched for centroid offsets in the *TESS* data using the open-source tool `vetting` (Hedges 2021), which calculates a p-value for each *TESS* sector indicating whether or not an offset has been detected. For each sector in which a transit occurred, we obtained a p-value > 0.05, indicating no significant centroid offset. On average the in-transit centroids agree well with the out-of-transit centroids (see Figure 4.2), providing strong evidence that the signal observed by *TESS* originates from HD 56414.

Statistical Validation

`TRICERATOPS` (Giacalone et al. 2021) is a Bayesian tool that can be used to validate *TESS* planet candidates by calculating a FP probability (FPP; the overall probability that the signal originates from something other than a planet transiting the target star) and a nearby FP probability (NFPP; the probability that the the signal originates from a known nearby source that is listed in the TIC), where the criteria for validation are FPP < 0.015 and NFPP $< 10^{-3}$. Folding in the speckle imaging data for an added constraint on the presence of unresolved FP-inducing stars, we ran `TRICERATOPS` 50 times and calculated the mean and standard deviation of the FPP and NFPP.[4] We obtained FPP $= 0.004 \pm 0.006$ and NFPP $= (1.6 \pm 3.5) \times 10^{-7}$, which are sufficient for validation.[5] Hereafter, we refer to TOI-1228.01 as HD 56414 b.

4.5 Discussion and Conclusions

HD 56414 b is a $3.71 \pm 0.20\,R_\oplus$ planet orbiting a 420 ± 140 Myr old A-type star on a 29 day orbital period. In Figure 4.3, we compared HD 56414 b to all other confirmed transiting planets and confirmed transiting planets orbiting A-type stars. HD 56414 b is one of only 16 confirmed transiting planets orbiting an A-type star (which we define as any star with $7500\,\mathrm{K} \leq T_\mathrm{eff} \leq 10500\,\mathrm{K}$)[6] and one of only four confirmed sub-Jovian planets orbiting an A-type star. The other three sub-Jovian planets known to orbit A-type stars are Kepler-1115 b ($R_\mathrm{p} = 1.7\,R_\oplus$, $P_\mathrm{orb} = 23.6$ days), Kepler-462 b ($R_\mathrm{p} = 3.0\,R_\oplus$, $P_\mathrm{orb} = 84.7$ days), and Kepler-462 c ($R_\mathrm{p} = 4.0\,R_\oplus$, $P_\mathrm{orb} = 207.6$ days).[7]

[4]Multiple runs are necessary because the probability calculation is not deterministic.

[5]This FPP is dominated by the scenario in which an unresolved stellar companion hosts a transiting planet of a different size.

[6]The upper limit is chosen to include KELT-9b (Gaudi et al. 2017).

[7]The spectral type of Kepler-462 is disputed, as some have estimated its T_eff to be under 7500 K (e.g., Berger et al. 2018).

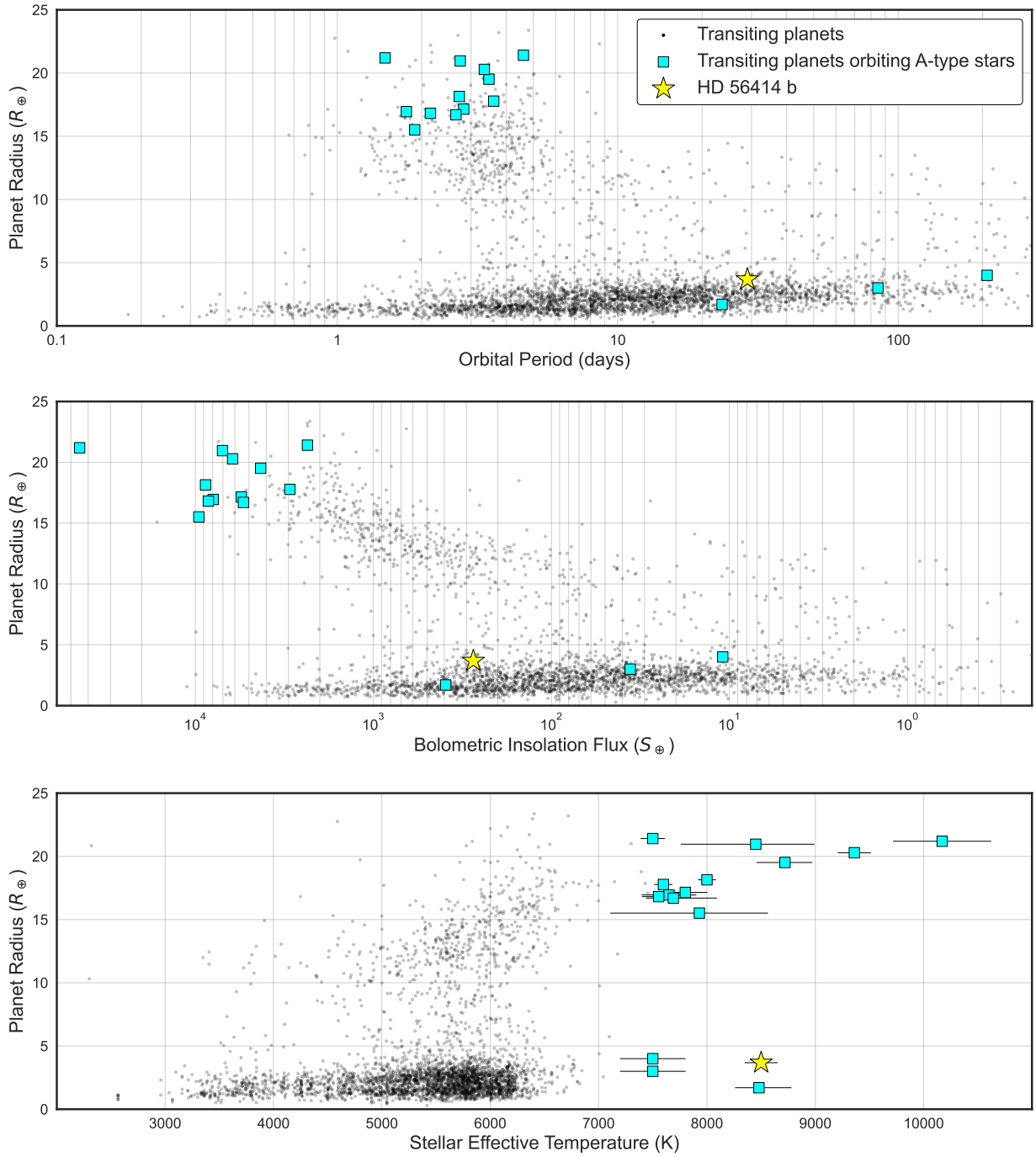

Figure 4.3: Confirmed transiting planets (cyan squares for A-type host stars; black dots for other host stars), and HD 56414 b (yellow star) in different parameter spaces. Data acquired from the NASA Exoplanet Archive.

HD 56414 b is one of only 32 transiting planets orbiting a star with a well-constrained age ($\mathrm{Age}/\sigma_{\mathrm{Age}} \geq 3$) that is < 1 Gyr (hereafter referred to as "young").[8] More specifically, this planet is one of 16 young transiting planets smaller than $4\,R_\oplus$. Among these smaller planets, HD 56414 b is one of only 5 with $P_{\mathrm{orb}} > 20$ days. Further investigation of this system could therefore provide insight into the formation and early evolution of small, long-period planets. In addition, HD 56414 is the hottest and most massive young star with a known transiting planet, making it a valuable asset for understanding how these processes depend on stellar temperature and mass.

HD 56414 b shares several characteristics with Kepler-1115 b: the two planets orbit stars with similar effective temperatures ($T_{\mathrm{eff}} \sim 8500$ K) and have similar orbital periods, leading to comparable bolometric insolation fluxes (S_{bol}). Figure 4.3 shows these two planets near what is conventionally referred to as the hot Neptune desert, a region of parameter space at short orbital periods (or, in this case, high S_{bol}) that exhibits a dearth of planets with sizes of roughly $3 - 10\,R_\oplus$ (Mazeh et al. 2016). The fact that these are the two shortest period planets orbiting A-type stars, despite the bias that planets with shorter orbital periods are more likely to transit and are easier to detect, may indicate that sub-Jovian planets with $P_{\mathrm{orb}} < 20$ days are intrinsically rare around these hot stars.

Some have proposed that the hot Neptune desert is a product of photoevaporation, the process by which planets are stripped of their atmospheres due to stellar emission of XUV ($\lambda < 912$ Å) photons (e.g., Lopez and Fortney 2013; Owen and Lai 2018; Owen and Wu 2013). García Muñoz and Schneider (2019) showed that photoevaporation could be even more efficient at stripping planets of their atmospheres around A-type stars due to high stellar continuum emission beyond the Balmer limit ($\lambda < 3646$ Å) in the near ultraviolet. To determine if a close-in Neptune-size planet could survive around such a hot star, we applied the same model for HD 56414 b. We used a PHOENIX LTE spectrum with $T_{\mathrm{eff}} = 8600$ K, $\log g = 4.0$, and [Fe/H] $= 0.0$ (Husser et al. 2013) and assumed an XUV flux of 3.6 erg cm^{-2} s^{-1} at 1 AU. This XUV flux is the same as that assumed in García Muñoz and Schneider (2019) for KELT-9 b, which is probably similar to HD 56414 because both stars are in a temperature regime where it is unlikely for a stellar corona to be present. Nonetheless, we found that our results are not strongly sensitive to the choice of XUV flux because the mass loss rate is dominated by photons in the near ultraviolet. Because the mass of HD 56414 b is unknown, we estimated the range of possible masses of the planets using multiple mass–radius relations defined by other studies. Using the relation defined in Chen and Kipping (2017), we generated a distribution of masses centered just below $14\,M_\oplus$ with 1σ lower and upper limits of $8\,M_\oplus$ and $24\,M_\oplus$, respectively. These results broadly agree with the corresponding relation defined in Otegi et al. (2020), which estimates a mass of $13.8 \pm 3.7\,M_\oplus$. To account for this range of possible masses, we ran the model on planets with masses of $M_{\mathrm{p}} = 8\,M_\oplus$, $14\,M_\oplus$, and $24\,M_\oplus$ on circular orbits with separations between 0.06 AU (corresponding to $P_{\mathrm{orb}} = 3.9$ days) and 0.229 AU (the best-fit semi-major axis). The resulting mass loss rates over a 1 Gyr timescale are shown in Figure 4.4.

[8] According to the NASA Exoplanet Archive, accessed 2022 May 18.

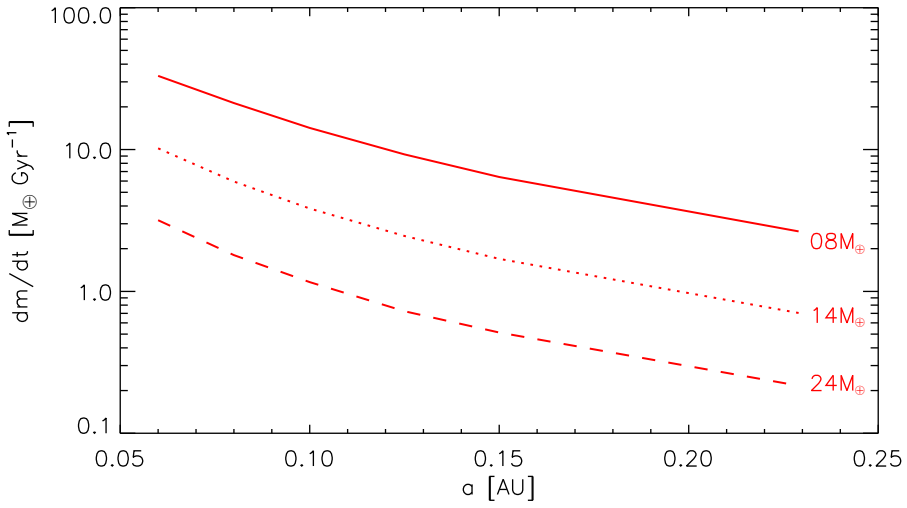

Figure 4.4: Simulated atmospheric mass loss rates as a function of orbital separation for planets with the same size as HD 56414 b orbiting a star identical to HD 56414. Each line represents a planet of a different mass. Assuming a core-to-envelope mass fraction of $\sim 10\%$, planets at 0.229 AU with $M_{\rm p} = 8\,M_{\oplus}$ can lose over a third of their atmospheric mass over the typical 1-Gyr lifetime of an A-type star. Closer in planets with $M_{\rm p} < 14\,M_{\oplus}$ are susceptible to losing all of their atmospheres over this timescale.

If we assume a core-to-envelope mass fraction of $\sim 10\%$, our results suggest that HD 56414 b could lose an over a third of its atmospheric mass over 1 Gyr if $M_{\rm p} = 8\,M_{\oplus}$. In addition, closer in planets with $M_{\rm p} < 14\,M_{\oplus}$ are susceptible to losing nearly all of their atmospheric mass. These results imply that, unless they typically more massive than $14\,M_{\oplus}$, Neptune-size planets within 0.1 AU of A-type stars are rare due to rapid stripping of their atmospheres. Consequently, if we assume that Neptune-size planets can acquire these close-in orbits via in situ formation or disk migration (e.g., Lee and Chiang 2017), we might expect to see a pile-up of remnant Neptunian cores at short orbital periods (Lecavelier des Etangs et al. 2004).

It may be possible to deepen our understanding of HD 56414 b by obtaining additional observations. As discussed in Section 4.3, the line-of-sight stellar obliquity can be revealed with additional transit or Rossiter-McLaughlin observations. Also, if the planet is actively undergoing atmospheric escape, it may be possible to detect at the Lyman-α (e.g., Vidal-Madjar et al. 2003), Hα (e.g., Yan and Henning 2018), or HeI 10830 Å lines (e.g., Spake et al. 2018). It is also possible to study this planet via emission and transmission spectroscopy with *JWST* or other facilities. We quantified these prospects by calculating the ESM and TSM for the planet, which Kempton et al. (2018) recommend be above 7.5 and 90, respectively,

for planets of similar sizes.[9] We calculated relatively low values of 1.9 ± 0.2 and 30.0 ± 1.4, respectively, owing to the small planet-to-star radius ratio of HD 56414 b. Nonetheless, the brightness of HD 56414 and its proximity to the southern *JWST* continuous viewing zone makes it a significantly better target than Kepler-1115 ($V = 11.98$, $K_s = 11.51$) and Kepler-462 ($V = 11.63$, $K_s = 10.85$). Given that HD 56414 b occupies a sparsely populated region of parameter space, it makes a compelling target for a follow-up campaign to characterize its atmosphere.

[9]Technically, Kempton et al. (2018) only calculated a recommended minimum ESM for planets with $R_{\rm p} < 1.5\,R_{\oplus}$, but we quote that number in the absence of a recommendation for larger planets.

Chapter 5

The Frequency of Small Close-In Planets Around A-type Stars

The transit method of exoplanet detection provides a window into the demographics of short-period planets of nearly all sizes, enabling a better understanding of how these planets form and evolve. The *Kepler* mission revealed the occurrence rates of these planets, but largely limited its search to stars similar to the Sun. As a result, the population of planets orbiting relatively massive and hot A-type stars is poorly understood. In this chapter, I use data from the Transiting Exoplanet Survey Satellite to calculate the occurrence rate of small planets orbiting close to A-type stars for the first time. I show that these planets are likely much rarer than they are around cooler stars, supporting results from earlier studies that found small planets to be come less common with increasing stellar mass and enriching our view of the processes that dictate planet formation and evolution.

5.1 Introduction

The *Kepler* mission (Borucki et al. 2010) enabled calculations of the occurrence rate of planets of all sizes orbiting close to FGKM-type stars (e.g., Dressing and Charbonneau 2013; Howard et al. 2012; Kunimoto and Matthews 2020). Because the primary goal of the *Kepler* mission was to calculate the occurrence rate of Earth-like planets orbiting Sun-like stars, stars that are larger, more massive, and hotter were largely ignored. Radial velocity surveys, which are also sensitive to close-in planets, also generally avoid A-type stars due to their rapid rotation rates, which greatly limit radial velocity precision and inhibit detection of orbiting planets (Galland et al. 2005; Griffin et al. 2000). As a consequence, our understanding of short-period planet demographics has historically been limited to late-type stars.

With the launch of the Transiting Exoplanet Survey Satellite (*TESS*; Ricker et al. 2010), the prospects of expanding our understanding of close-in planet demographics to early-type stars improved drastically. Because it observes stars indiscriminately across nearly the entire sky, *TESS* provides the opportunity to search for planets around stars previously inaccessible,

such as main-sequence A-type stars. For instance, Zhou et al. (2019b) and Beleznay and Kunimoto (2022) used *TESS* to provide a first glimpse at the occurrence rate of hot Jupiters orbiting these hot stars and found tentative evidence for an increased rarity of these planets with increasing stellar mass. However, to this day, the landscape of smaller planets around A-type stars is completely unexplored.

The occurrence rate of small ($R_{\rm p} < 8\,R_{\oplus}$) close-in ($P_{\rm orb} < 10$ days) planets orbiting A-type stars can reveal novel information about how planets form and evolve around stars of different masses. It is known that more massive stars have higher levels of dust mass in their protoplanetary disks (Ansdell et al. 2016), providing more material with which to build planets. It has been posited that this increased dust mass is responsible for the relatively high occurrence rate of long-period giant planets compared to Sun-like stars (Nielsen et al. 2019). More massive stars are also known to have disks that deplete in gas at a higher rate than less massive stars (Ribas et al. 2015). Thus, planets orbiting A-type stars likely have relatively little time to migrate towards their host stars via disk migration, a process that relies on the presence of gas in the disk.

After the dispersal of the protoplanetary disk, planets orbiting close to A-type stars are subjected to different environments than those orbiting cooler stars. Unlike low-mass stars, which have convective outer layers, A-type stars have primarily radiative interiors. It has been inferred that these radiative layers are less efficient at dissipating tides excited by short-period planets (e.g., Winn et al. 2010), potentially leading to slower tide-induced orbital evolutions relative to cooler stars. A-type stars are also distinct from cooler stars due to their high levels of near-ultraviolet continuum emission, which are thought to drive efficient photoevaporation of planet atmospheres over the entire main-sequence lifetime of the star (Garcia et al. 2022). Cooler stars emit relatively little in the near-ultraviolet, and are believed to photoevaporate atmospheres only during their youths, when they emit high levels of X-ray and extreme-ultraviolet radiation (e.g., Jackson et al. 2012; Lammer et al. 2003; Murray-Clay et al. 2009). While the impact of photoevaporation on the landscape of short-period planets around cool stars is fairly well understood (e.g., Lopez and Fortney 2013; Owen and Lai 2018), the role this mechanism plays on the population of planets orbiting hot stars is currently unknown.

To gain a better understanding of how planets form and evolve around stars hotter and more massive than the Sun, I perform a calculation of the occurrence rate of small short-period planets orbiting A-type stars using *TESS*. This calculation provides the first ever window into the population of planets smaller than Jupiter around these hot stars, providing new insight into the demographics of small planets throughout the galaxy.

This chapter is organized as follows. In Section 5.2, I present results of a follow-up observation campaign to vet small planet candidates orbiting A-type stars detected by *TESS*. In Section 5.3, I discuss the selection of the the sample used to constrain the occurrence rate of small close-in planets orbiting A-type stars. In Section 5.4, I outline the process for calculating the occurrence rate of these planets and present preliminary results. In Section 5.5, I discuss the implications of the calculated occurrence rate limits. In Section 5.6, I outline the remaining steps that must be completed for the final occurrence rate calculation.

TOI Number	Candidate $P_{\rm orb}$ (days)	Candidate $R_{\rm p}$ ($R_\oplus$)	Target TIC ID	Target $T_{\rm eff}$ (K)	Target $M_\star$ ($M_\odot$)	Nearby Source TIC ID
998.01	0.941	4.529	54390047	8322 ± 131	2.05 ± 0.31	750574654
1360.01	0.709	5.189	330468175	8999 ± 297	2.27 ± 0.32	330468086
1497.01	0.816	3.691	371673488	8911 ± 721	2.25 ± 0.38	389035190
1522.01	2.980	4.922	367102581	9024 ± 335	2.28 ± 0.33	387270530
1570.01	1.746	5.628	285674856	8348 ± 155	2.06 ± 0.31	285674862
2059.01	3.754	4.672	403308915	8398 ± 145	2.08 ± 0.31	403308925
2448.01	9.018	3.712	2231721005	9671 ± 189	2.47 ± 0.33	231721006
3380.01	2.009	7.755	176148945	8516 ± 150	-	176148949
4268.01	0.813	4.380	341272282	8265 ± 150	-	341272277
5429.01	4.232	7.889	5800958	8064 ± 171	1.96 ± 0.30	5800965

Table 5.1: Summary of planet candidate follow-up observing program. From left to right, the columns show: the *TESS* Object of Interest (TOI) number of the planet candidate, the orbital period of the planet candidate from ExoFOP, the predicted radius of the planet candidate from ExoFOP, the ID number of the target A-type star from the *TESS* Input Catalogue (TIC), the effective temperature of the target A-type star from the TIC, the mass of the target A-type star from the TIC, and the TIC ID of the nearby star that actually hosts the transit-like event detected by *TESS*. The masses of TIC 176148945 and TIC 341272282 are unknown.

Lastly, in Section 5.7, I provide brief concluding remarks.

5.2 Preliminary Vetting of Planet Candidates

In anticipation of the occurrence rate calculation described in the following sections, I vetted planet candidates reported by the *TESS* Science Office on the Exoplanet Follow-up Observing Program (ExoFOP) website. I began by identifying planet candidates with $R_{\rm p} < 8\,R_\oplus$ and $P_{\rm orb} < 10$ days around stars with $7500\,{\rm K} < T_{\rm eff} < 10000\,{\rm K}$. Next, I proposed for time with the 1 m Nickel Telescope at Lick Observatory and the robotic 1 m telescopes of the Las Cumbres Observatory Global Telescope Network (LCOGT) to acquire observations of these stars. The goal of this program was to identify eclipsing binary stars located near the purported planet host star by observing stars within and near the TESS target aperture over windows during which the transits detected by *TESS* were predicted to occur. These small-aperture ground-based telescopes are able to achieve significantly higher spatial resolutions than the *TESS* cameras, which have relatively low resolutions of approximately $20'' \times 20''$, allowing for the discernment of stars that are blended with the target star in *TESS* images. Nearby blended stars that have eclipsing stellar-mass companions can produce signals similar to what would be produced by a planet transiting purported planet host star (see 1). These forms of astrophysical false positives, which are referred to as "nearby eclipsing binaries"

(NEBs), are the most common type of false positive in *TESS* data. The identification of these scenarios is therefore vital for the accurate calculation of the planet occurrence rate for A-type stars.

The follow-up program identified 10 NEBs near A-type stars with planet candidates. The results of the program are summarized in Table 5.1. The data from the program, along with the analogous *TESS* data, are presented in Figures 5.1-5.10. The frequency of NEBs detected by this program suggests that TOIs associated with A-type stars have a high false positive rate. However, a more quantitative analysis is needed to claim this robustly. In the following sections, I present my procedure for calculating the occurrence rate of small stars around A-type stars and reveal preliminary results.

5.3 Sample Selection

The first step in calculating the occurrence rate of planets around a set of stars is to define the sample of stars around which to search for planets. In this study, I focus on main-sequence A-type stars. In practice, boundaries are typically drawn based on other stellar properties. For example, Mulders et al. (2015a) defined bins distinguishing stars of different stellar spectral types using $T_{\rm eff}$. More recently, Zhou et al. (2019b) defined A-type stars as those with $1.4\,M_\odot < M_\star < 2.3\,M_\odot$ and identified those likely to be on the main sequence based on their location on the *Gaia* Color-Magnitude Diagram.

I define my sample by identifying stars with the following properties according to version 8.2 of the *TESS* Input Catalogue (TIC; Stassun et al. 2019):

- The star must have an effective temperature within the range $7500\,{\rm K} \leq T_{\rm eff} \leq 10000\,{\rm K}$
- The star must have an estimated mass
- The star must have a radius such that $R_\star \leq 2.5\,R_\odot$
- The star must have a *TESS* magnitude such that $T \leq 10$
- The star must have data products from the MIT Quick Look Pipeline (QLP) available on the Mikulski Archive for Space Telescopes (MAST)

The limit on $T_{\rm eff}$ is meant to ensure that the stars are A-type stars. The limits on $M_\star$ and $R_\star$ ensures that the stars are on the main sequence and also removes particularly large stars that for which it is difficult to detect the transits of small planets. The limit on T removes particularly faint stars, for which *TESS* has a worse photometric precision and a lower sensitivity to planets. The QLP requirement is needed because the QLP-processed light curves are used in the occurrence rate calculation, which I describe further in the next section. The final sample is shown in Figure 5.11 and consists of 20,562 stars.

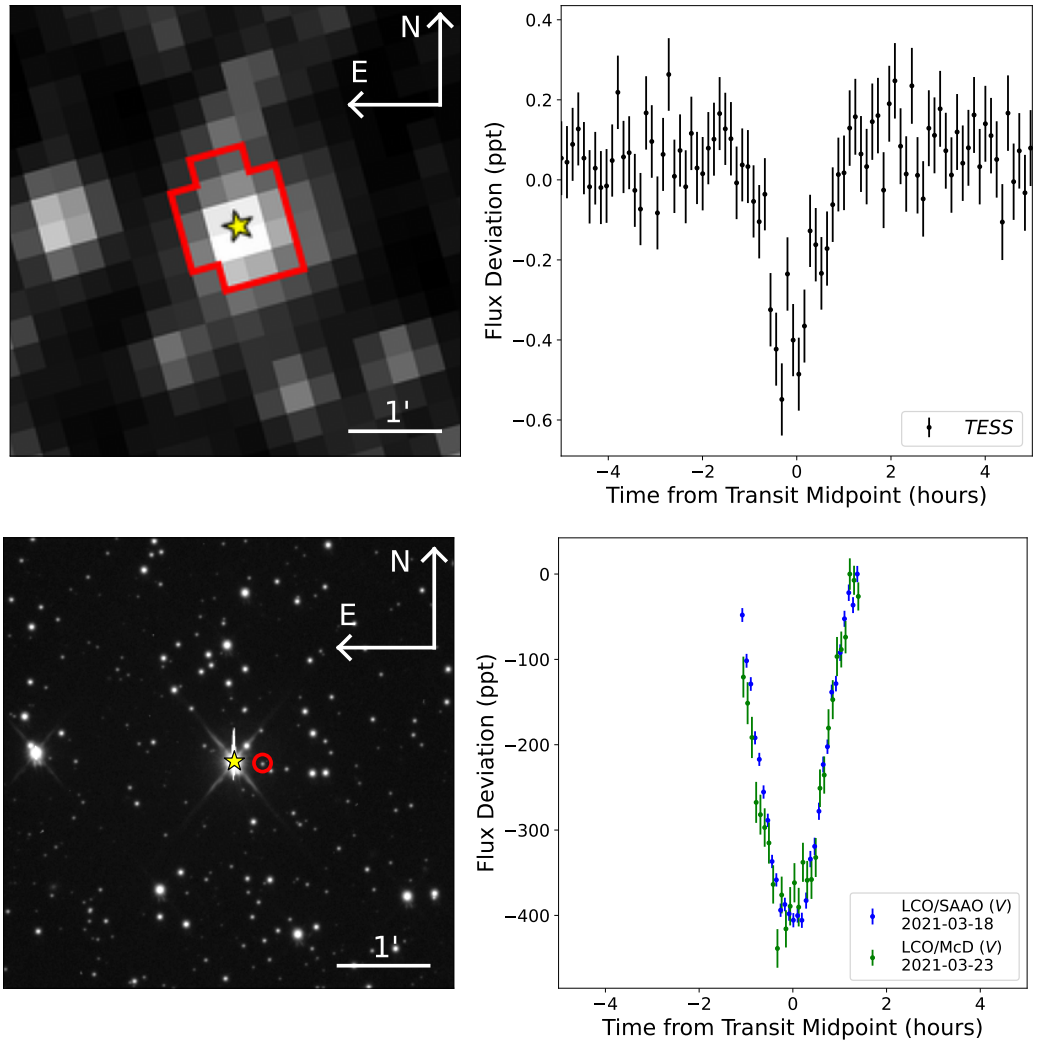

Figure 5.1: *Top left*: *TESS* image of TOI-998. The location of the target A-type star with the planet candidate is marked by a yellow star at the center of the image. The red outline indicates the aperture used to extract the *TESS* photometry. *Top right*: Extracted *TESS* light curve of TOI-998. The data is phase folded, binned, and zoomed in to the transit of the planet candidate. *Bottom left*: Image of TOI-998 collected with a 1 m LCOGT telescope. The scale and orientation of the image are the same as the *TESS* image. The target A-type star is marked by a yellow star at the center. The red circle indicates a nearby source that was searched for transit-like events. *Bottom right*: Light curves extracted from the circled nearby star. The LCOGT observations, which were taken from McDonald Observatory and the South African Astronomical Observatory on two separate nights, reveal a deep stellar eclipse with the same orbital period, transit duration, and transit timing as those predicted by *TESS*, demonstrating that TOI-998.01 is an astrophysical false positive.

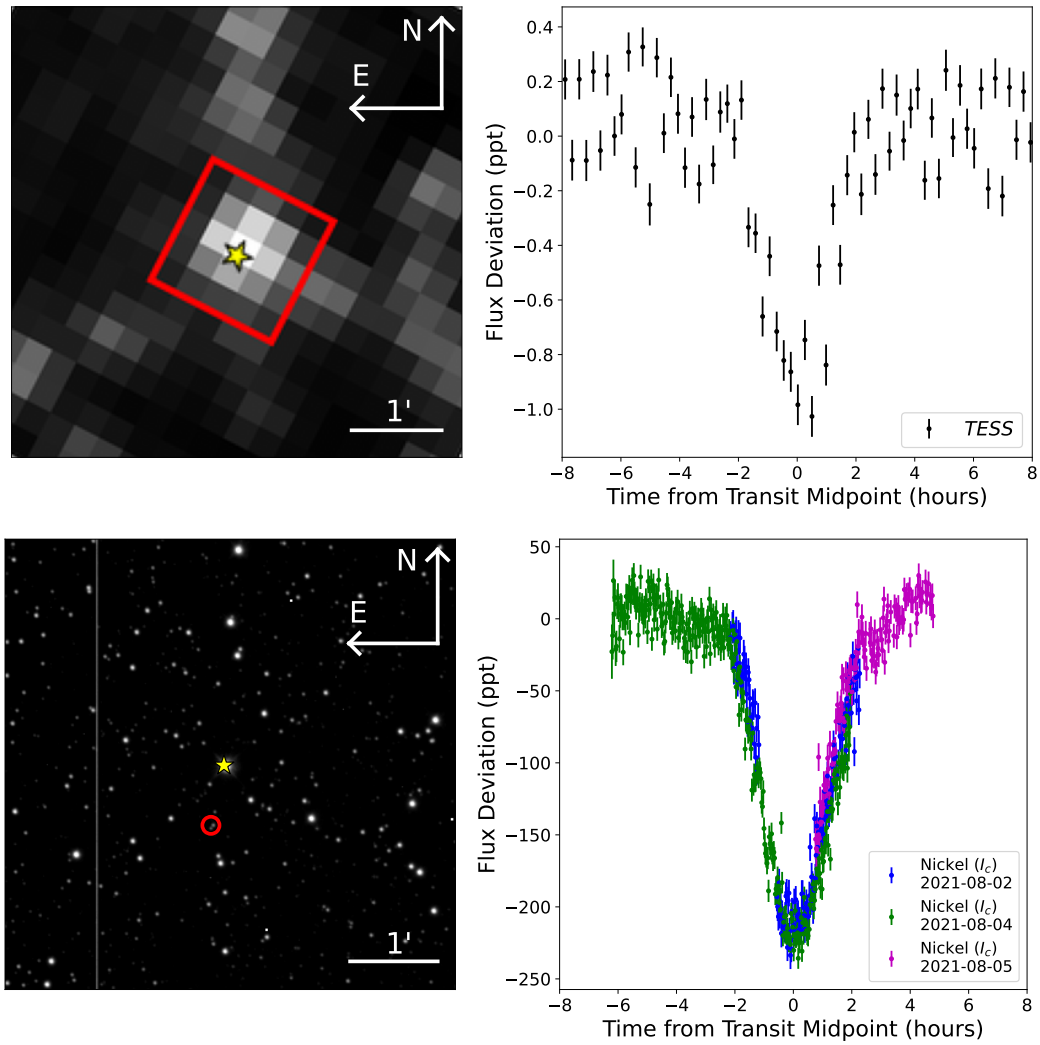

Figure 5.2: The same as Figure 5.1, but for TOI-1360, the location of which is marked with the yellow star located at the center of each image. *TESS* observations are shown on the top and observations obtained with the 1 m Nickel telescope are shown on the bottom. The Nickel observations, which were collected on three separate nights, reveal a pair of eclipsing binary stars with the same orbital period, transit duration, and transit timing as the planet candidate around the nearby source circled in red, demonstrating that TOI-1360.01 is an astrophysical false positive.

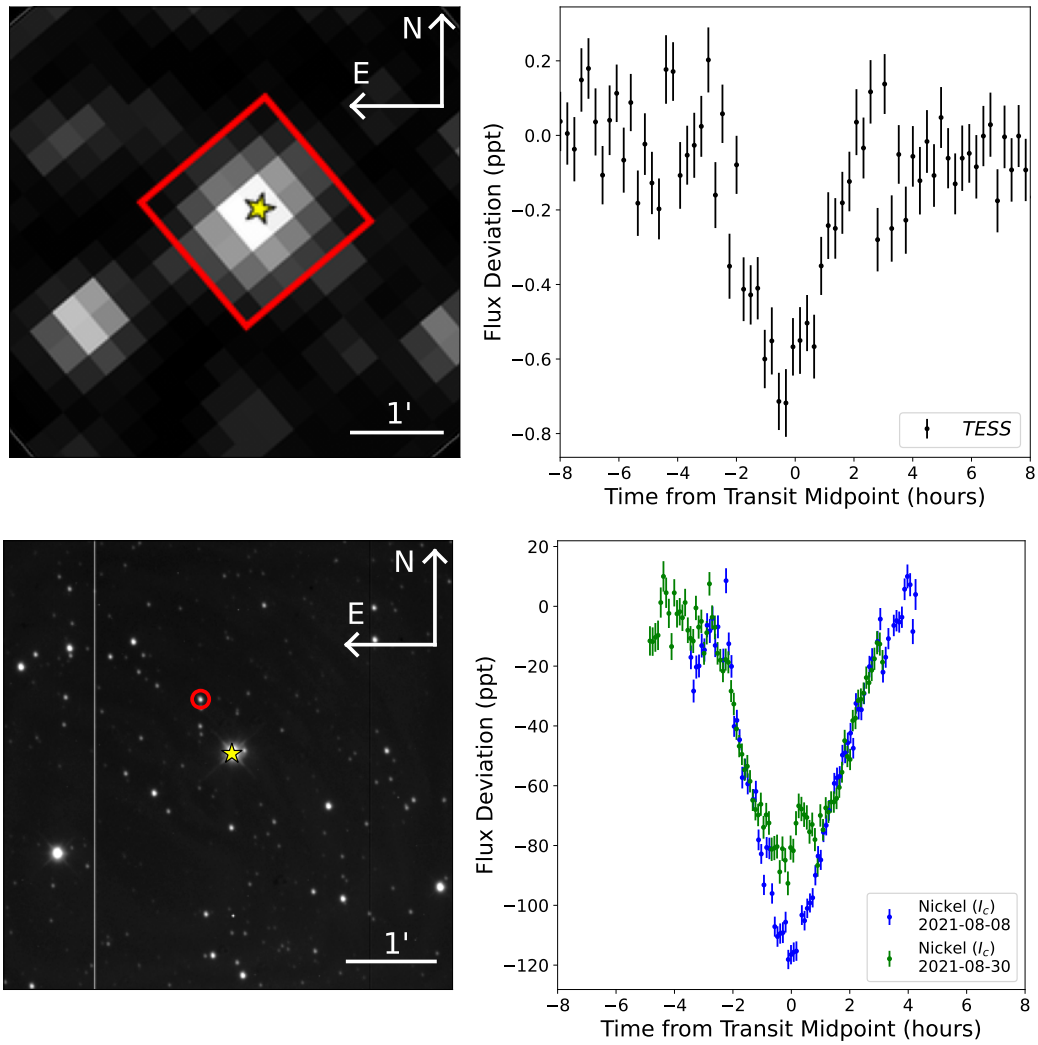

Figure 5.3: The same as Figure 5.1, but for TOI-1497, the location of which is marked with the yellow star located at the center of each image. *TESS* observations are shown on the top and observations obtained with the 1 m Nickel telescope are shown on the bottom. The Nickel observations, which were collected on two separate nights, reveal a pair of eclipsing binary stars with the same orbital period, transit duration, and transit timing as the planet candidate around the nearby source circled in red, demonstrating that TOI-1497.01 is an astrophysical false positive.

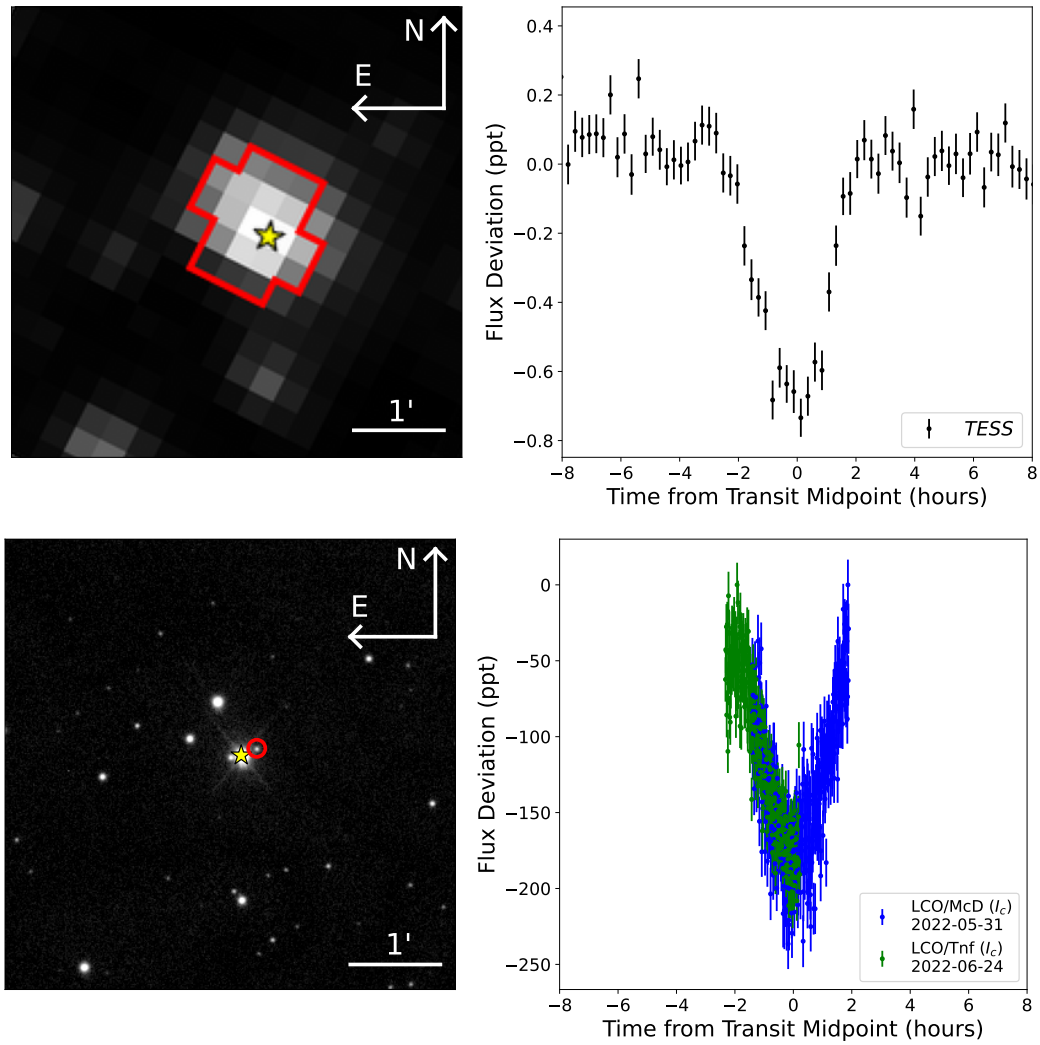

Figure 5.4: The same as Figure 5.1, but for TOI-1522, the location of which is marked with the yellow star located at the center of each image. *TESS* observations are shown on the top and observations obtained with 1 m LCOGT telescopes are shown on the bottom. The LCOGT observations, which were collected from McDonald Observatory and Teide Observatory on two separate nights, reveal a pair of eclipsing binary stars with the same orbital period, transit duration, and transit timing as the planet candidate around the nearby source circled in red, demonstrating that TOI-1522.01 is an astrophysical false positive.

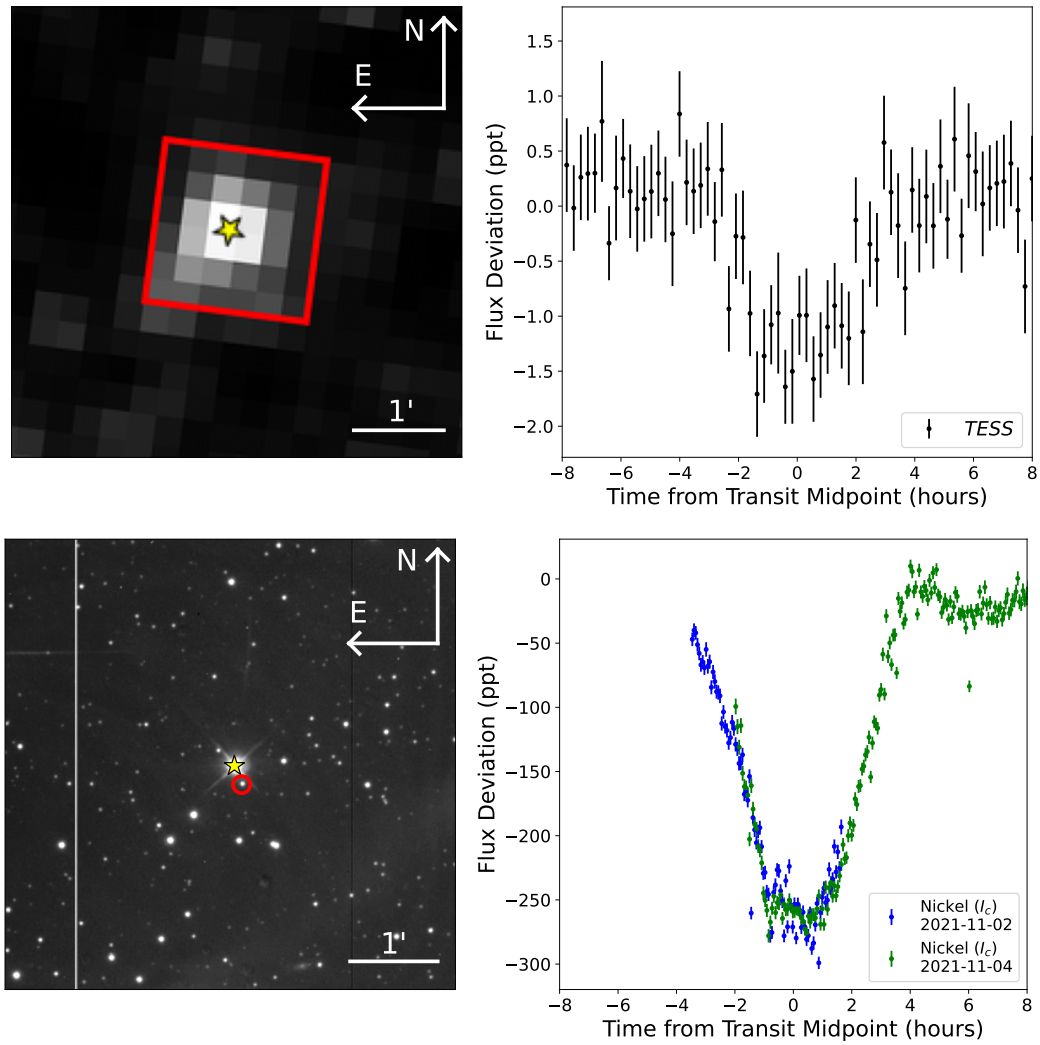

Figure 5.5: The same as Figure 5.1, but for TOI-1570, the location of which is marked with the yellow star located at the center of each image. *TESS* observations are shown on the top and observations obtained with 1 m Nickel telescopes are shown on the bottom. The Nickel observations, which were collected on two separate nights, reveal a pair of eclipsing binary stars with the same orbital period, transit duration, and transit timing as the planet candidate around the nearby source circled in red, demonstrating that TOI-1570.01 is an astrophysical false positive.

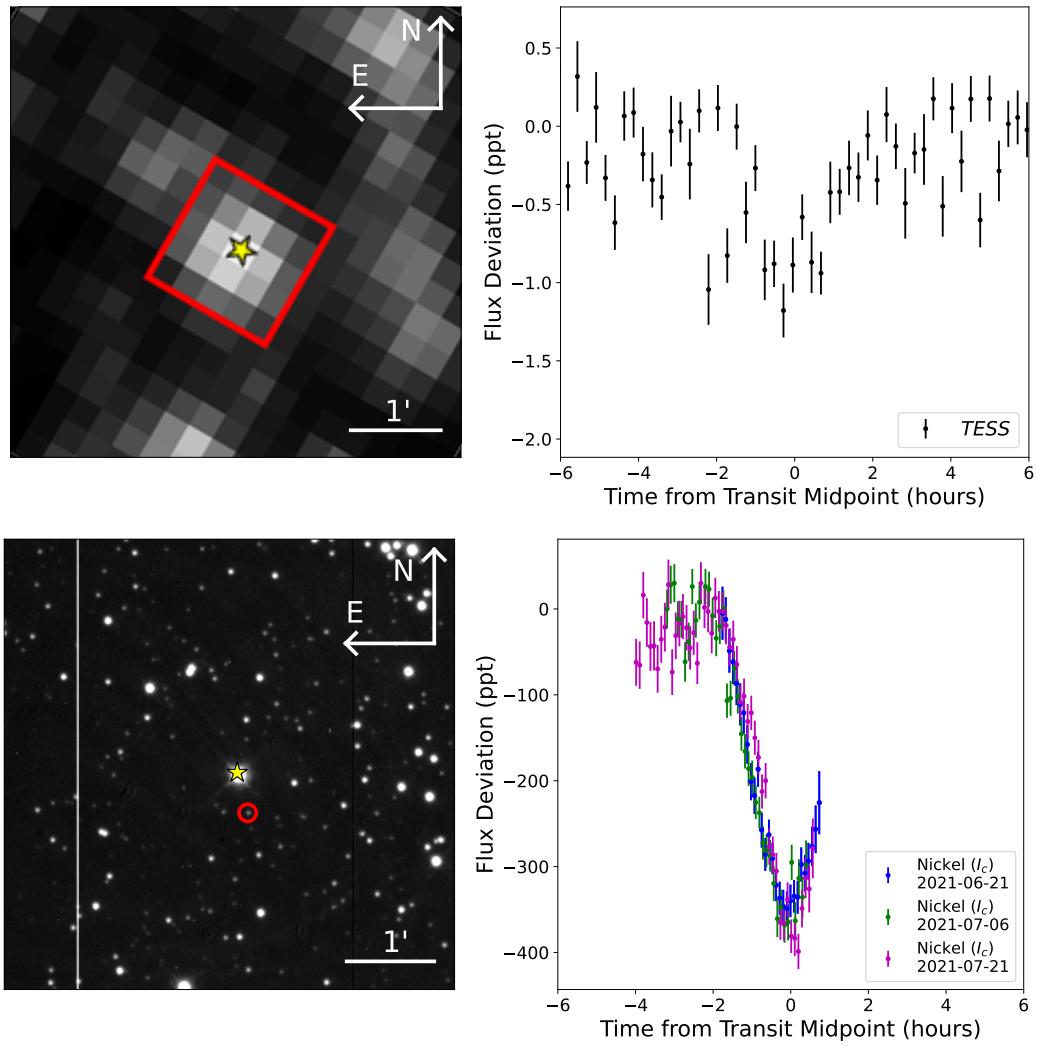

Figure 5.6: The same as Figure 5.1, but for TOI-2059, the location of which is marked with the yellow star located at the center of each image. *TESS* observations are shown on the top and observations obtained with 1 m Nickel telescopes are shown on the bottom. The Nickel observations, which were collected on three separate nights, reveal a pair of eclipsing binary stars with the same orbital period, transit duration, and transit timing as the planet candidate around the nearby source circled in red, demonstrating that TOI-2059.01 is an astrophysical false positive.

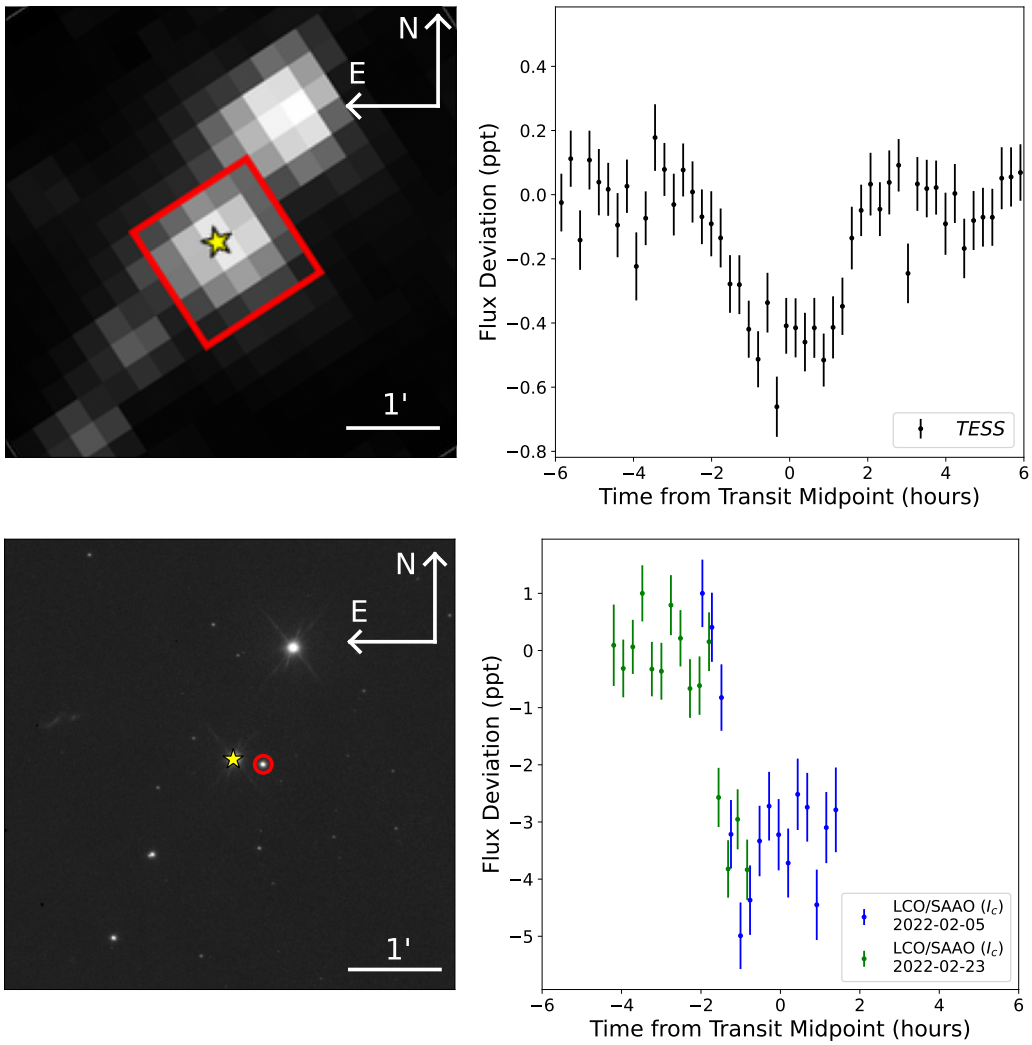

Figure 5.7: The same as Figure 5.1, but for TOI-2448, the location of which is marked with the yellow star located at the center of each image. *TESS* observations are shown on the top and observations obtained with 1 m LCOGT telescopes are shown on the bottom. The LCOGT observations, which were collected from the South African Astronomical Observatory on two separate nights, reveal a transiting planet with the same orbital period, transit duration, and transit timing as the planet candidate around the nearby source circled in red, demonstrating that TOI-2448.01 is an astrophysical false positive.

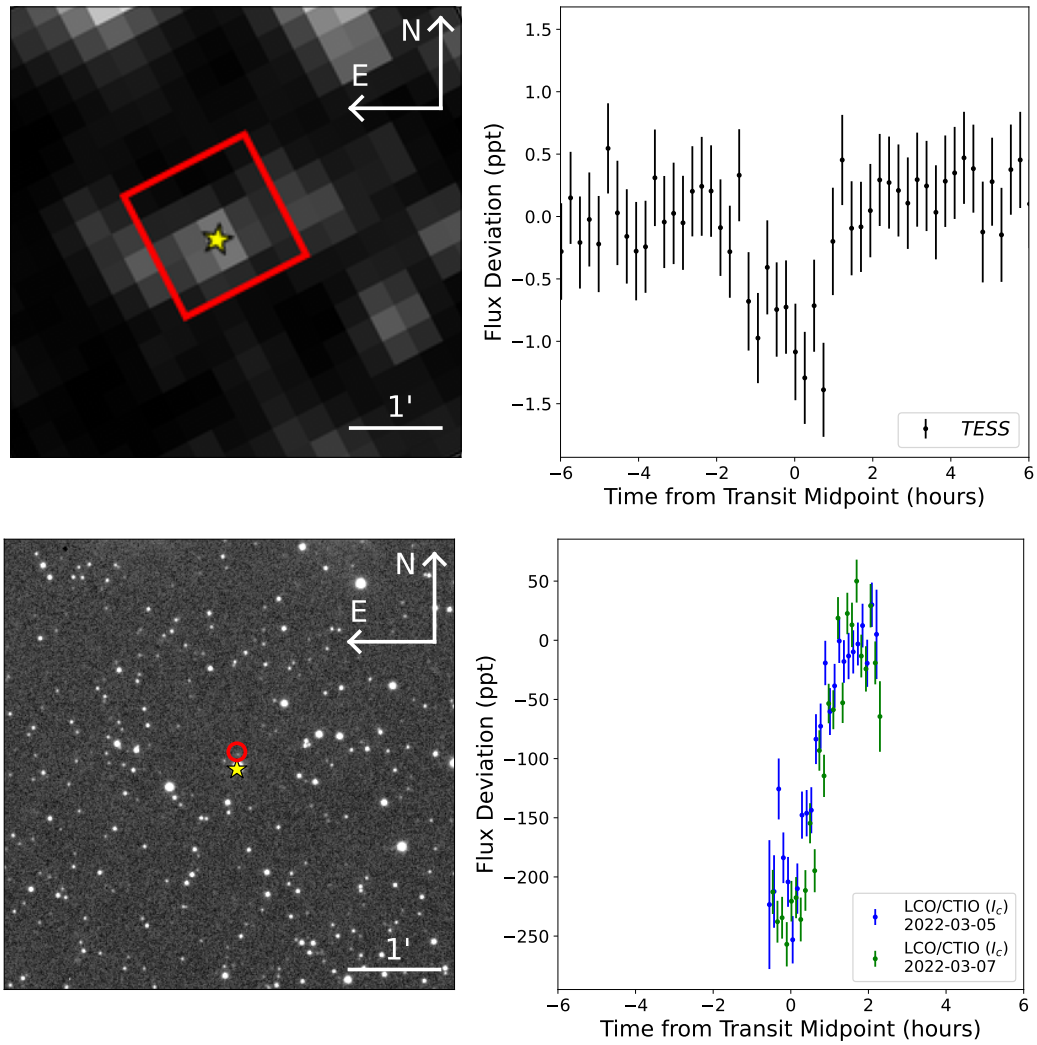

Figure 5.8: The same as Figure 5.1, but for TOI-3380, the location of which is marked with the yellow star located at the center of each image. *TESS* observations are shown on the top and observations obtained with 1 m LCOGT telescopes are shown on the bottom. The LCOGT observations, which were collected from Cerro Tololo Inter-American Observatory on two separate nights, reveal a transiting planet with the same orbital period, transit duration, and transit timing as the planet candidate around the nearby source circled in red, demonstrating that TOI-3380.01 is an astrophysical false positive.

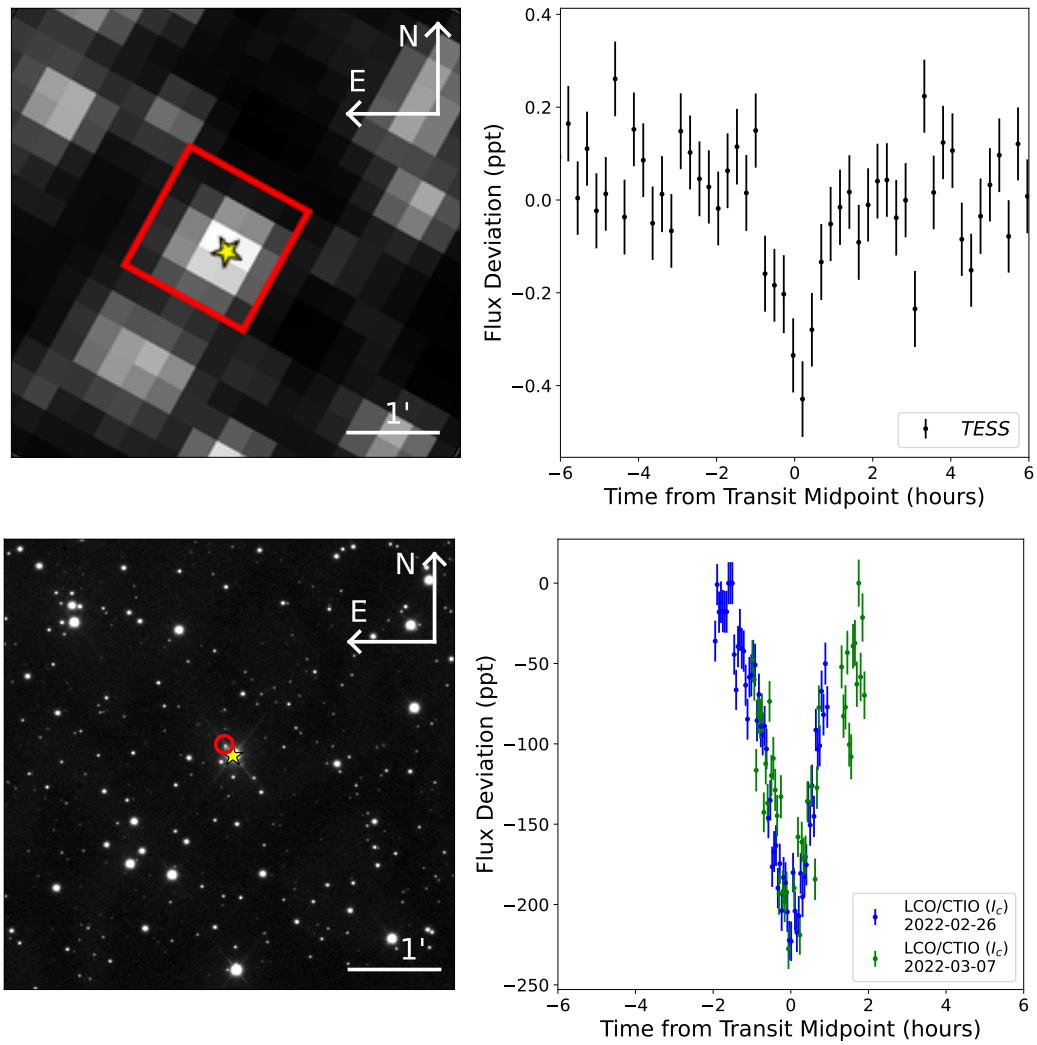

Figure 5.9: The same as Figure 5.1, but for TOI-4268, the location of which is marked with the yellow star located at the center of each image. *TESS* observations are shown on the top and observations obtained with 1 m LCOGT telescopes are shown on the bottom. The LCOGT observations, which were collected from Cerro Tololo Inter-American Observatory on two separate nights, reveal a transiting planet with the same orbital period, transit duration, and transit timing as the planet candidate around the nearby source circled in red, demonstrating that TOI-4268.01 is an astrophysical false positive.

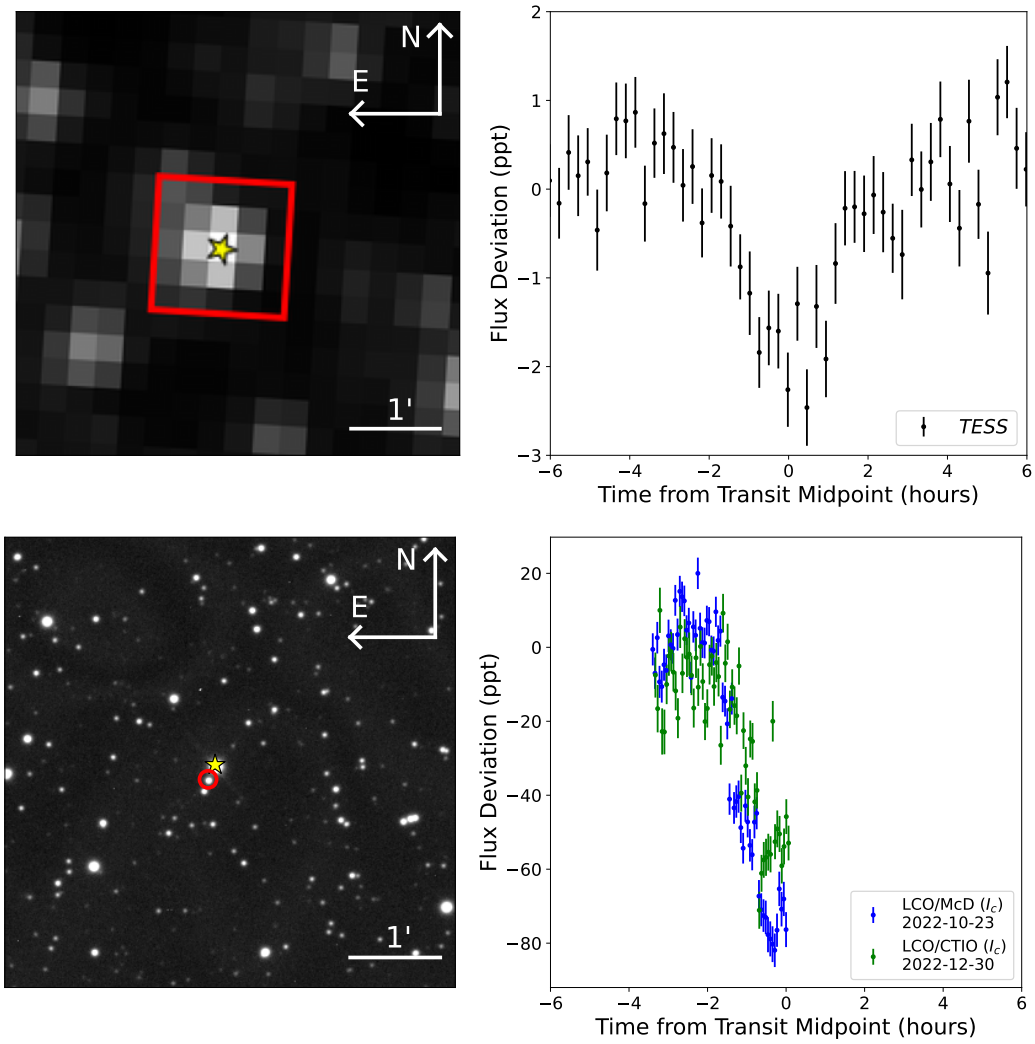

Figure 5.10: The same as Figure 5.1, but for TOI-5429, the location of which is marked with the yellow star located at the center of each image. *TESS* observations are shown on the top and observations obtained with 1 m LCOGT telescopes are shown on the bottom. The LCOGT observations, which were collected from McDonald Observatory and Cerro Tololo Inter-American Observatory on two separate nights, reveal a transiting planet with the same orbital period, transit duration, and transit timing as the planet candidate around the nearby source circled in red, demonstrating that TOI-5429.01 is an astrophysical false positive.

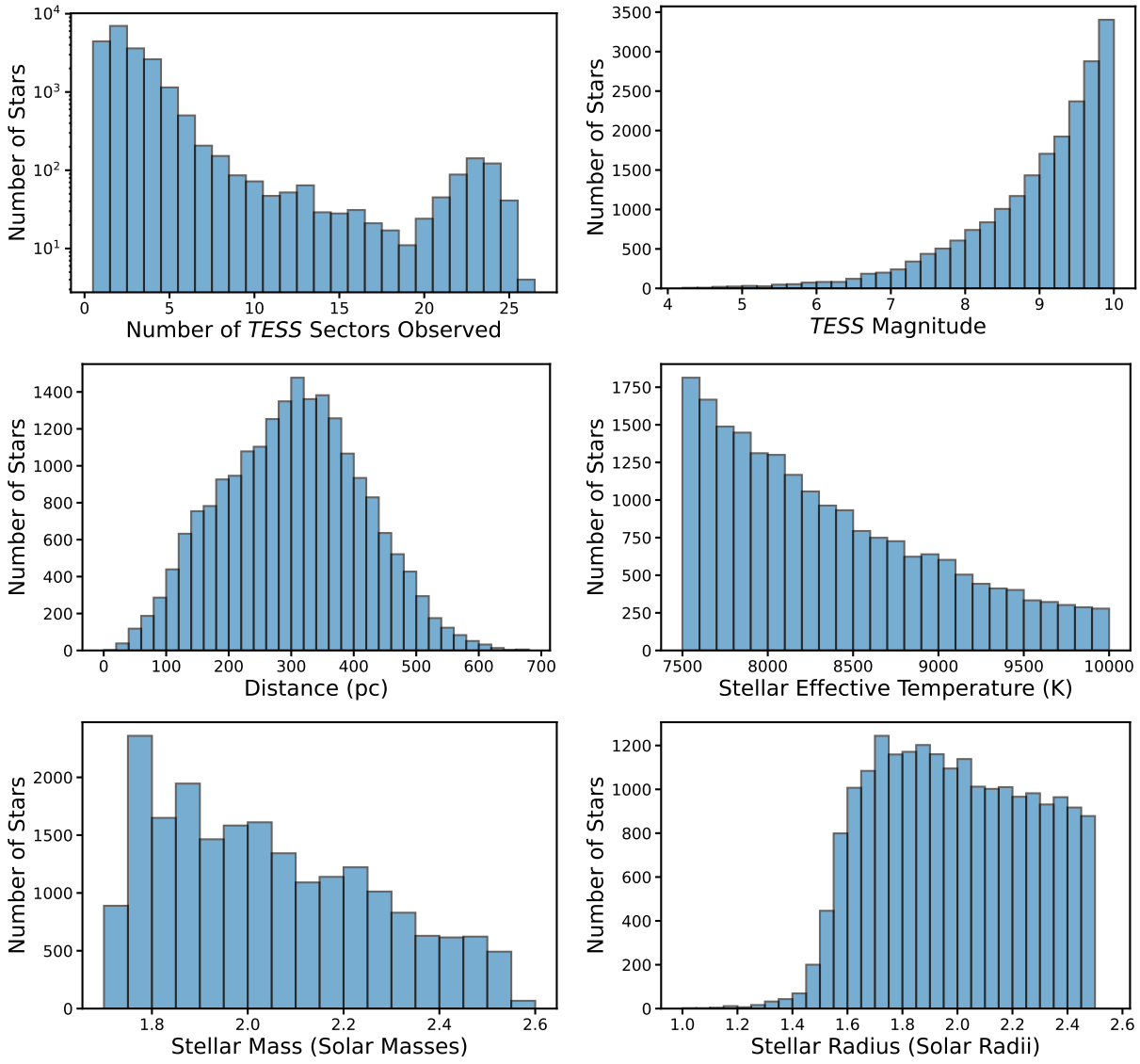

Figure 5.11: Properties of the 20,652 A-type stars that are used in the occurrence rate calculation in this chapter. In the top left panel, note that each *TESS* sector is approximately 27 days long.

5.4 Occurrence Rate Calculation

In this section, I describe the procedure for calculating the occurrence rate of close-in planets around A-type stars. In general, an occurrence rate calculation consists of four steps: (1) identifying planet candidates using a transit detection pipeline, (2) evaluating the reliability of each detected transit-like event to determine if any are false alarms or false positives, (3) quantifying the search completeness of the pipeline through injection-recovery tests, and (4) combining the information gleaned from three previous steps to determine the true frequency of planets around the sample of stars. I outline the procedure for steps (1) and (3) in detail below. Due to time constraints, step (2) could not be completed before the submission deadline of this thesis. In Section 5.6, I summarize the remaining work that will be completed in the following months. Nonetheless, I leverage a few assumptions about the pipeline to present preliminary results for step (4).

Transit Detection Pipeline

For a given star, I begin the transit search by downloading the QLP light curve file using the `Lightkurve` Python package (Lightkurve Collaboration et al. 2018). I record the "raw" flux provided by the QLP, rather than that which has been flattened using a spline-fitting procedure, and mask out all data flagged as having poor quality. I use the raw flux, rather than the spline-flattened flux provided by the QLP, for the purpose of calculating the pipeline sensitivity. Any light curve flattening procedure has the potential to remove or distort embedded transits. The impact this has on the ability of the pipeline to detect planets can only be quantified if artificial transits are injected into raw light curves before the flattening is performed (see the subsection titled "Pipeline Completeness"). I therefore apply a custom light curve flattening routine on the raw data.

The custom flattening routine is performed using the `wōtan` Python package (Hippke et al. 2019). I first separate the light curve into segments by identifying gaps > 0.5 days in length. I then discard segments < 3 days long. I flatten each segment using the "robust penalized pspline" algorithm, which fits the data to a spline curve through iterative sigma-clipping. In each iteration, data points that are $> 3\sigma$ outliers are removed, and the iterations continue until no outliers remain or until 10 iterations occur. The algorithm calculates the optimal number of knots per segment using Ridge regression (i.e., the L2 regularization method), in which the data is fit using a cost function that penalizes solutions in which a greater number of knots are used in order to combat overfitting. The minimum distance between knots is set to 0.5 days to prevent the algorithm from impacting transits in the data, which will always have durations under 12 hours for orbital periods under 10 days. Lastly, I remove 0.25 days of data from the edges of each segment, due to the flattening procedure struggling to fit the data properly near the start and end of each segment.

Next, I perform a search for periodic transit-like events using the box least-squares algorithm (BLS; Kovács et al. 2002), as implemented in `Lightkurve`. The BLS searches for events using a grid of 100,000 orbital periods between 0.5 days and 10 days that are uni-

formly separated in frequency space. I also enforce a maximum possible box width at each orbital period based on the expected transit duration given the star, assuming a circular orbit. Using the periodogram generated by the BLS, I calculate the signal detection efficiency (SDE) for each tested orbital period using the equation 6 of Kovács et al. (2002) and record all periods with SDE ≥ 10.

Beginning with the orbital period with the highest SDE, I perform a test to determine which of the identified periodic events have morphologies consistent with planetary transits.. Kunimoto et al. (2023) noted a high rate of false alarms in *TESS* data at orbital periods under ~ 1 day, likely as a result of scattered light from the rotation of the Earth, stellar variability, and blended light from nearby contact eclipsing binaries. In order to prevent these sinusoid-like false alarms from being identified as planet candidates by the pipeline, I perform a test similar to the SWEET (Sine Wave Evaluation Event Test) utilized by Thompson et al. (2018) for the *Kepler* data set. First, I phase-fold the light curve using the orbital period and center the event using the best-fit transit epoch returned by the BLS. I then fit the phase-folded data to two models using a simple grid-based optimization approach. The first model is a sinusoid model with three free parameters: amplitude, period, and phase. The second model is a transit model, as implemented by the `batman` Python package (Kreidberg 2015), with two free parameters: planet radius and orbital inclination. For the transit model, the stellar parameters are fixed to those listed in the TIC and quadratic limb darkening coefficients are selected based on $T_{\rm eff}$ and $\log g$ using the values provided in Claret (2017). Using the best-fit parameters, I calculate the Bayesian Information Criterion (BIC) for each model using a Gaussian likelihood function. Lastly, I calculate the difference between the two as $\Delta\text{BIC} = \text{BIC}_{\text{sinusoid}} - \text{BIC}_{\text{transit}}$. I consider a detected event sufficiently more transit-like than sinusoid-like if $\Delta\text{BIC} \geq 50$.

If the event with SDE ≥ 10 also has $\Delta\text{BIC} \geq 50$, it is considered a valid detection and is designated a threshold-crossing event (TCE). The transit search algorithm is terminated once a single TCE is identified for the star. If the event does not meet the ΔBIC requirement, all periods within 2% of the tested period and its harmonics are eliminated from the list of recorded high-SDE periods. The sinusoid test is then repeated for all other recorded orbital periods in descending order of SDE until either a TCE is identified or periods with SDE ≥ 10 are exhausted.

Pipeline Completeness

Properly calculating the occurrence rate of planets around the defined sample of stars requires knowledge of the completeness of the transit detection pipeline. Completeness accounts for two factors: the probability of the pipeline detecting a planet that is transiting (also known as the pipeline sensitivity) and the geometric probability of a planet being in an orientation such that it transits along our line of sight. I outline the procedure for calculating these probabilities here.

The pipeline sensitivity is determined using injection-recovery tests. These tests involve injecting artificial transit signals into real data and quantifying the ability of the pipeline

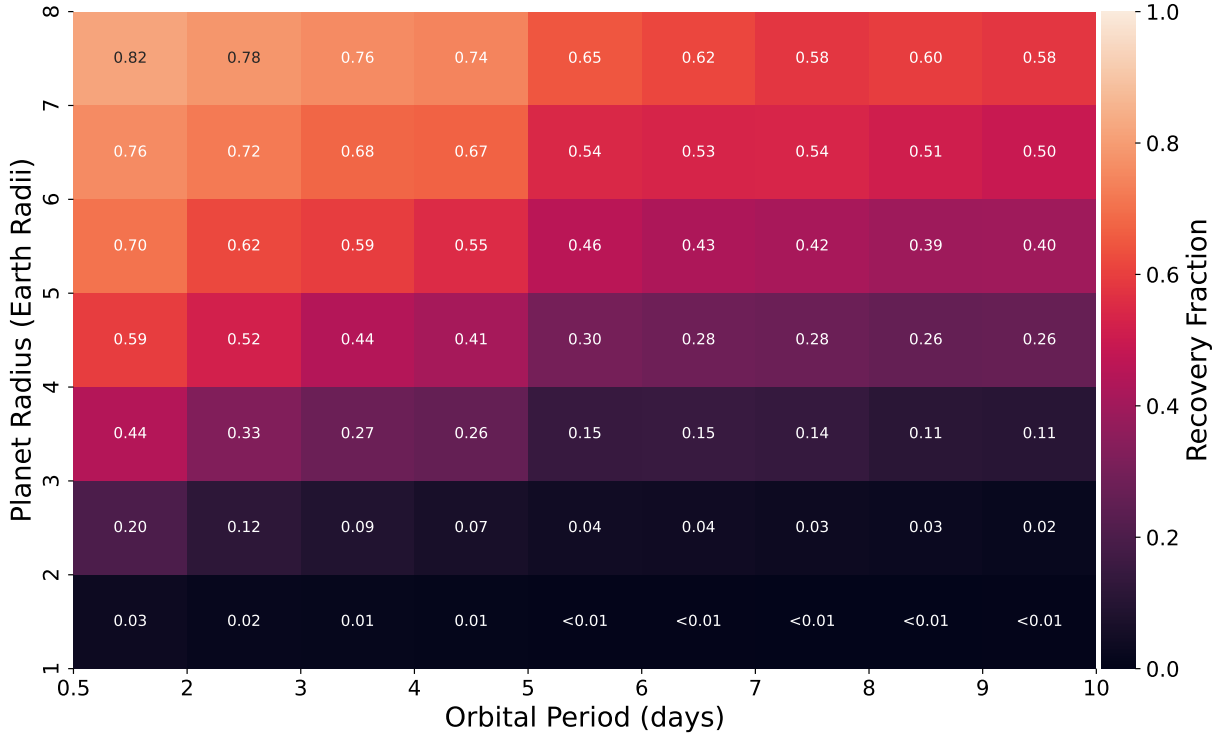

Figure 5.12: Pipeline sensitivity to small close-in planets around the sample of A-type stars described in Section 5.3. The color of each grid cell indicates the recovery fraction from injection-recovery tests. The recovery fraction is also indicated numerically within each cell. Larger planets with shorter orbital periods are more easily detectable than smaller planets with longer orbital periods. Non-monotonicity is the result of sparse sampling in the injection-recovery tests. As is discussed in Section 5.6, these tests will be expanded in the future in order to create a smoother sensitivity map.

to detect them. Because the true properties of the injected signals are known, I am able to determine how much more difficult it becomes to detect planets that are smaller and have longer orbital periods. Following the precedent established by previous occurrence rate studies (e.g., Dressing and Charbonneau 2015; Gan et al. 2023; Zhou et al. 2019b), I calculate pipeline sensitivity with the following steps. The results of this pipeline sensitivity calculation are shown in Figure 5.12.

1. I randomly select 1000 stars (without replacement) from the sample of 20,562 A-type stars defined previously and download their raw QLP light curves. These stars are the basis of the transit-recovery tests. For each star i, I simulate 100 instances of transiting systems.

2. For each instance j, I draw $R_{\rm p}$ and $P_{\rm orb}$ from uniform distributions linearly spaced over the intervals ($1\,R_\oplus$, $8\,R_\oplus$) and (0.5 days, 10 days), respectively. The midpoint time of the first transit (T_0) is randomly selected between the starting time of the light curve ($t_{\rm min}$) and $t_{\rm min} + P_{\rm orb}$. The impact parameter ($b$) of the simulated planet is drawn from from a uniform distribution over the interval [0, 0.9]. The quadratic limb-darkening coefficients of the star are determined based on the $T_{\rm eff}$ and $\log g$ of the star using the values reported by Claret (2017), assuming Solar metallicity. Transits are then injected into the raw light curves using `batman` (Kreidberg 2015), with the data supersampled to account for the different cadences used in different *TESS* sectors.

3. For each instance, I run the transit detection pipeline described previously. I consider an injected planet to be detected if the pipeline calculates an SDE ≥ 10 and determines the period of the injected planet to a precision better than ± 0.1 day. I also accept cases where the most likely $P_{\rm orb}$ determined by the BLS is half or twice the true $P_{\rm orb}$ of the injected planet, again with a precision better than ± 0.1 day. Lastly, I determine if the injected planet passes the spacecraft systematics test of the vetting procedure. If the planet is detected and passes this test, I consider it recovered and set $r_{i,j} = 1$. Otherwise, I set $r_{i,j} = 0$.

4. After all instances are run, I generate a sensitivity map for the star by defining a grid in $R_{\rm p}$ and $P_{\rm orb}$. I calculate the fraction of recovered planets in a given grid cell using the equation

$$p_{{\rm det},i} = \sum_{j \in J} r_{i,j} \Big/ \sum_{j \in J} 1 \tag{5.1}$$

   where J is the set of instances that fall within the cell.

5. Once the injection-recovery tests are run for all 1000 stars, I calculate the pipeline sensitivity per grid cell for the entire stellar sample ($\langle p_{\rm det} \rangle$) by averaging the sensitivity maps of all 1000 stars.

The full pipeline completeness is determined by also taking into account the geometric transit probability, which, for a given star i and injection instance j, can be approximated as

$$p_{{\rm geo},i,j} \approx \frac{R_{\star,i}}{a_{i,j}} = R_{\star,i} \left(\frac{G M_{\star,i} P_{{\rm orb},j}^2}{4\pi^2} \right)^{-1/3}, \tag{5.2}$$

which assumes all circular orbits and assumes that the radii and masses of the planets are negligible compared to those of their stars. I take this factor into account by treating it as a weight in Equation 5.3, such that the completeness for a given star (C_i) in a given grid cell is given by the equation

$$C_i = \sum_{j \in J} r_{i,j} p_{{\rm geo},i,j} \Big/ \sum_{j \in J} 1. \tag{5.3}$$

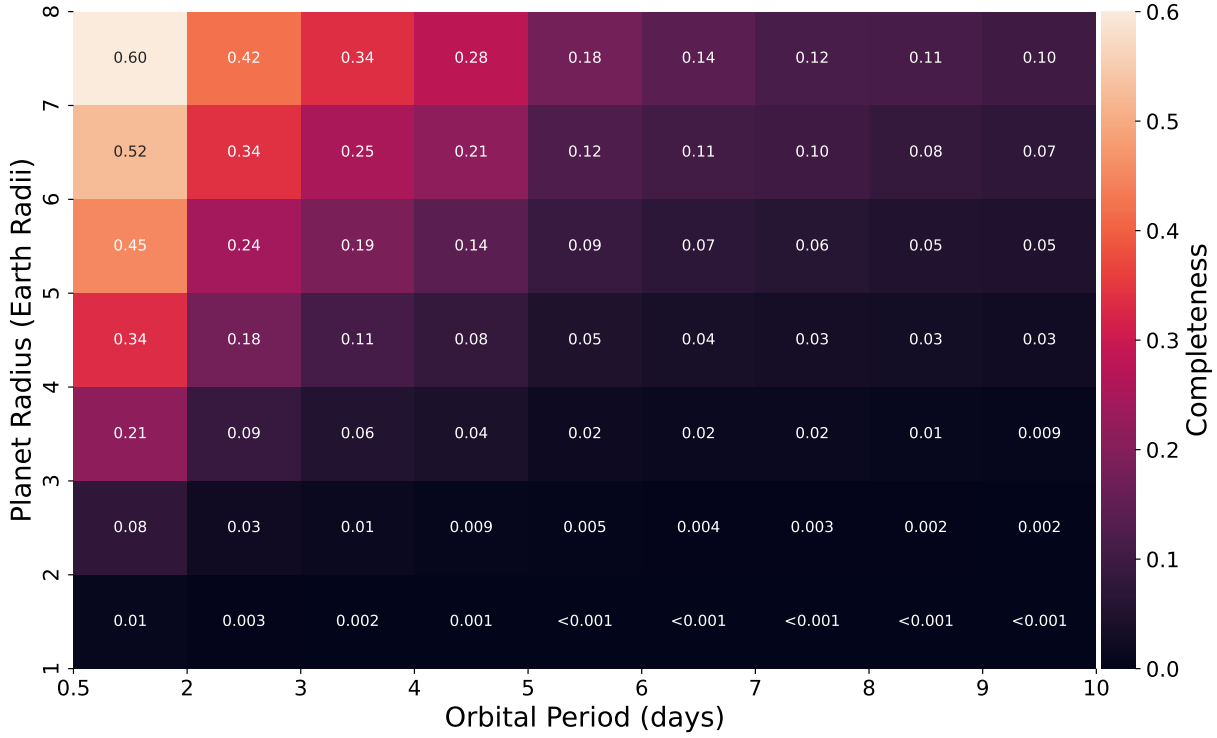

Figure 5.13: Completeness of the transit detection pipeline to planets of various sizes and orbital periods around the sample of A-type stars described in Section 5.3. The pipeline completeness considers both the pipeline sensitivity and the geometric probability of a given planet transiting. The format of this figure is the same as Figure 5.12. Non-monotonicity is the result of sparse sampling in the injection-recovery tests. As is discussed in Section 5.6, these tests will be expanded in the future in order to create a smoother sensitivity map.

Lastly, the completeness per grid cell for the entire stellar sample ($\langle C \rangle$) is found by averaging the completeness maps of all 1000 stars included in the sensitivity calculation. The results of this completeness calculation are shown in Figure 5.13.

Preliminary Results

As is mentioned in the beginning of this section, a proper calculation of the close-in planet occurrence rate for A-type stars requires vetting the TCEs identified by the transit detection pipeline to determine which should be classified as false alarms or false positives. I outline the process for doing so in Section 5.6. Here, I calculate preliminary occurrence rates by assuming that the pipeline will discover exactly the same set of planet candidates as the *TESS* mission. To identify these planet candidates, I query the ExoFOP website for planet candidates with

TOI	$P_{\rm orb}$ (days)	$R_{\rm p}$ ($R_\oplus$)	$T_{\rm eff}$ (K)	$M_\star$ ($M_\odot$)	$R_\star$ ($R_\odot$)	T mag	Disp.	Detected
742.01	0.963	2.728	8688	2.120	1.687	8.633	FP	Y
957.01	0.832	2.647	8897	2.241	1.820	8.957	FP	Y
998.01	0.941	4.529	8322	2.050	2.350	9.695	FP	Y
1037.01	1.201	3.740	9158	2.320	1.742	9.021	FP	Y
1132.01	1.551	3.482	7851	1.882	1.820	9.229	FP	Y
1354.01	1.429	6.963	9224	2.338	1.650	8.788	FP	Y
1387.01	0.784	3.896	7842	1.921	1.720	8.959	FP	Y
1497.01	0.816	3.691	8911	2.245	1.850	9.957	FP	Y
1507.01	0.467	7.778	7951	2.014	1.770	8.417	FP	N
1522.01	2.980	4.922	9024	2.279	1.890	9.396	FP	Y
1570.01	1.746	5.628	8348	2.060	1.800	9.488	FP	N
2115.01	3.694	3.023	8153	1.990	2.110	8.293	FP	Y
4180.01	1.595	4.322	7511	1.750	1.921	8.294	APC	N
4386.01	2.013	5.885	8127	1.980	1.751	9.769	PC	Y
5387.01	2.804	1.273	7531	1.740	1.520	8.199	PC	N
6260.01	2.390	2.328	7707	1.812	1.960	7.117	PC	N

Table 5.2: Predicted planet properties for planet candidates reported on ExoFOP and respective stellar properties as reported in the TIC. "Disp" indicates the disposition of the candidate as reported by TFOP, where PC = active planet candidate, APC = ambiguous planet candidate, and FP = false positive. The right-most column indicates whether or not the transit-like event was detected by the pipeline described above. Value uncertainties are excluded for ease of interpretation.

$P_{\rm orb} < 10$ day and $R_{\rm p} < 8\,R_\oplus$ orbiting stars with the properties specified in Section 5.3. I report the planetary and stellar properties of the identified systems in Table 5.2. I also report the disposition of each according to the *TESS* Follow-up Observing Program (TFOP), where PC denotes active planet candidates, APC denotes planet candidates that are ambiguous in nature, and FP denotes false positives. Lastly, to confirm that my pipeline is sensitive to those TOIs, I run my transit transit detection pipeline on the TESS photometry of each of the stars listed in Table 5.2.

A majority of the candidates in Table 5.2 were detected and classified as TCEs by my pipeline, and most of those that were detected have already been classified as false positives by TFOP (some of which are discussed in Section 5.2). The only active planet candidate detected by my pipeline is TOI-4386.01. However, a subsequent analysis with `TRICERATOPS` (Giacalone et al. 2021) reveals that the planet candidate TOI-4386.01 has a $> 99\%$ probability of being a false positive, so I consider it as such for the purpose of this calculation. Ultimately, analyses of all TCEs detected by the pipeline determined them to be false positives, meaning only an upper limit on planet occurrence rate can be calculated.

I calculate the occurrence rate using the procedure outlined in Zhou et al. (2019b) and

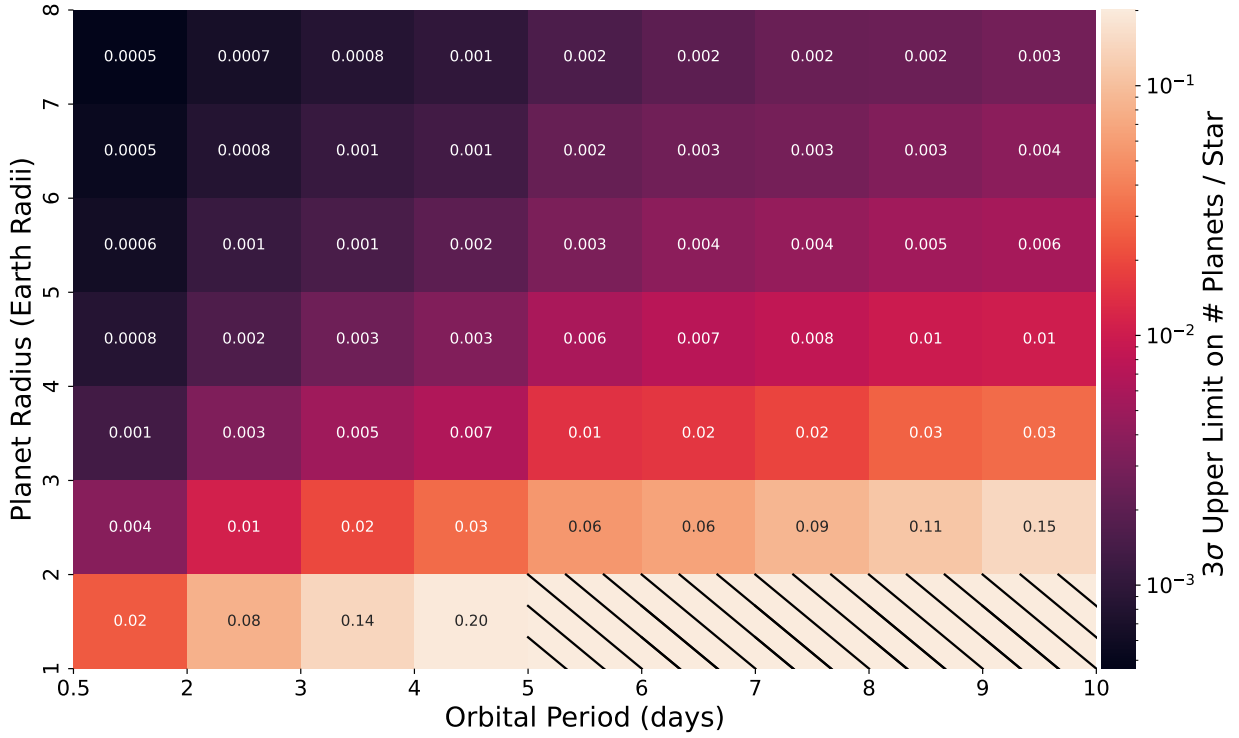

Figure 5.14: Calculated 3σ upper limits on the occurrence rates of planets orbiting A-type stars, as a function of both planet radius and orbital period. The format of this figure is the same as Figure 5.12. Regions that are hashed out have upper limits ranging from 0.2 to 1.0 planets per star and are considered incomplete. Non-monotonicity is the result of sparse sampling in the injection-recovery tests. As is discussed in Section 5.6, these tests will be expanded in the future in order to create a smoother sensitivity map.

Gan et al. (2023). The effective number of stars searched for planets in a given grid cell, after correcting for search completeness, is calculated with the equation

$$n_{\rm trial} = n_\star \langle C \rangle, \tag{5.4}$$

where $n_\star = 20,562$ is the total number of stars in the sample. I also define the number of observed planets in a given grid cell as

$$n_{\rm obs} = \sum_{i=1}^{n_{\rm p}} (1 - f_{{\rm FP},i}), \tag{5.5}$$

where $n_{\rm p}$ is the total number of planet candidates in the cell and $f_{{\rm FP},i}$ is the false positive rate, which is set to 0 for known false positives and to 1 for confirmed planets. Finally, the

occurrence rate in a given grid cell is given by

$$f_{\rm cell} = n_{\rm obs}/n_{\rm trial}. \tag{5.6}$$

Because all TCEs detected in my sample are actually false positives, the above formulation is not directly applicable. Rather than calculating the true occurrence rate, I can calculate the upper limit on the occurrence rate by assuming that the probability of detecting X planets in a given grid cell follows a binomial distribution:

$$P(n_{\rm trial}, X, f_{\rm cell}) = N f_{\rm cell}^{X}(1 - f_{\rm cell})^{n_{\rm trial}-X}, \tag{5.7}$$

where

$$N = \frac{\Gamma(n_{\rm trial}+1)}{\Gamma(X+1)\Gamma(n_{\rm trial}-X+1)}. \tag{5.8}$$

Thus, for a null detection in a given grid cell, the upper limit on planet occurrence rate to a confidence interval CI is calculated with

$$\int_0^{f_{\rm cell,upper}} (n_{\rm trial}+1) P(n_{\rm trial}, 0, f_{\rm cell}) df_{\rm cell} = CI, \tag{5.9}$$

which is solved to find

$$f_{\rm cell,upper} = 1 - (1 - CI)^{1/(n_{\rm trial}+1)}. \tag{5.10}$$

A map of 3σ ($CI = 0.997$) upper limits on the occurrence rates of planets with different sizes and orbital periods can be found in Figure 5.14.

For ease of comparison with previous occurrence rate studies, I divide planets into three size regimes: sub-Saturns ($4\,R_\oplus < R_{\rm p} < 8\,R_\oplus$), sub-Neptunes ($2\,R_\oplus < R_{\rm p} < 4\,R_\oplus$), and super-Earths ($1\,R_\oplus < R_{\rm p} < 2\,R_\oplus$). Integrated over the full range of orbital periods tested, my pipeline provides a completeness of 0.14 for sub-Saturns, 0.025 for sub-Neptunes, and 0.001 for super-Earths. Thus, at $P_{\rm orb} < 10$ days, I obtain 3σ (2σ) upper limits of 1.6 (0.8) sub-Saturns per 1000 A-type stars, 7.6 (3.9) sub-Neptunes per 1000 A-type stars, and 96 (50.7) super-Earths per 1000 A-type stars. I compare these numbers to estimates for cooler stars in the following section.

5.5 Discussion

To explore how the close-in planet occurrence rate for A-type stars differ from occurrence rates for cooler stars, I compare the results to those gleaned from *Kepler* data in Mulders et al. (2015a). That study separated the stellar sample into four spectral types based on $T_{\rm eff}$ – M ($2400 - 3700$ K), K ($3700 - 5200$ K), G ($5200 - 6000$ K), and F ($6000 - 7500$ K) dwarfs – and calculated planet occurrence rates for a wide range of $R_{\rm p}$ and $P_{\rm orb}$. In their analysis, Mulders et al. (2015b) found compelling evidence that the occurrence rates of planets with $R_{\rm p} < R_\oplus$ is lower for planets with earlier spectral types, and presented some evidence for a

similar trend in the occurrence rate of larger planets. These findings are broadly consistent with other studies conducted with the *Kepler* data set (e.g., Dressing and Charbonneau 2013; Hardegree-Ullman et al. 2019; Howard et al. 2012; Kunimoto and Matthews 2020).

The findings from Mulders et al. (2015b) compared to the results from this chapter are shown in Figure 5.15. I find strong evidence that the close-in sub-Saturn occurrence rate is lower for A-type stars than it is for FGK-type stars. I also find evidence that the close-in sub-Neptune occurrence rate is lower for A-type stars than all stars with lower $T_{\rm eff}$, lending support to the claim that the sub-Neptune occurrence rate decreases around progressively early stellar spectral types. Due to a low completeness for close-in super-Earths, I was only able to obtain loose constraints on their occurrence rate for A-type stars, but the results at least rule out the possibility of these rocky worlds being more common around A-type stars than cooler stars.

The finding that small close-in planets become rarer around hotter stars echoes recent studies of hot Jupiters, which have found tentative evidence that giant close-in planets follow a similar trend (Beleznay and Kunimoto 2022; Zhou et al. 2019b). This finding has important implications for planet formation and evolution, as it implies that planets have a more difficult time forming in-situ, migrating inwards, or surviving over long timescales when orbiting hotter stars.

The ability for close-in planets to form in-situ is predominately dictated by the dust sublimation radius ($a_{\rm sub}$), which represents the smallest distance from the star that solid planet-building material can exist due to stellar irradiation (e.g., Flock et al. 2019). In the simplest terms, $a_{\rm sub} \propto \sqrt{L_{\rm PMS}}$, where $L_{\rm PMS}$ is the pre-main-sequence stellar luminosity. For A-type stars, $L_{\rm PMS}$ is approximately an order of magnitude higher than for G-type stars (Hayashi 1961), meaning that $a_{\rm sub}$ is approximately 3$\times$ greater. Assuming young Solar-mass stars have $a_{\rm sub} \approx 0.04$ AU (Pinte et al. 2008), the average A-type star would have $a_{\rm sub} \approx 0.12$ AU, which corresponds roughly to an orbital period of 10 days for a star with $M_\star = 2\,M_\odot$. Thus, mitigated in-situ formation provides a plausible explanation for the dearth of close-in planets around hot stars.

Small planets have been detected around A-type stars at orbital periods longer than 10 days (e.g., Chapter 4; Giacalone et al. 2022), indicating that they are able form around hot stars with some non-zero efficiency. Assuming all small planets around A-type stars form beyond 10 days, their low occurrence rate at shorter orbital periods may be the result of inhibited migration through the protoplanetary disk. Mulders et al. (2015b) and Lee and Chiang (2017) showed that, for FGKM-type stars, the truncation of the disk by the stellar magnetosphere at the star-disk co-rotation radius can explain the decrease in the sub-Neptune occurrence rate with decreasing orbital period within 10 days. Lee and Chiang (2017) predicted that disks around A-type stars truncate at shorter orbital periods due to more rapid stellar rotation rates, leading to a sub-Neptune occurrence rate that is constant with period between 1 and 10 days. Unfortunately, the lack of detected sub-Neptunes around A-type stars means that this prediction cannot be tested. Disk lifetime may also play a role in the dearth of close-in small planets around A-type stars. Ribas et al. (2005) showed that the gas in disks around more massive stars dissipates on relatively short timescales. Depending

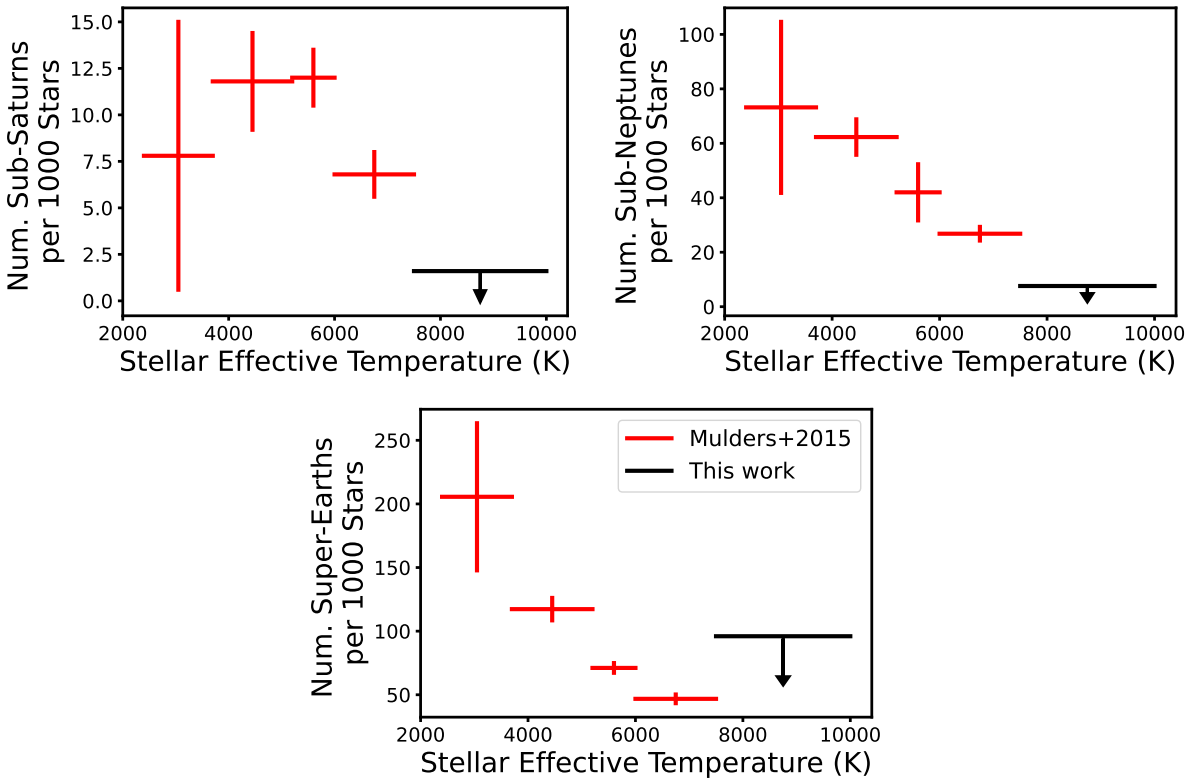

Figure 5.15: The occurrence rates of sub-Saturns, sub-Neptunes, and super-Earths with $P_{\rm orb} < 10$ days from Mulders et al. (2015a) for FGKM-type stars compared to the results from the calculation for A-type stars in this chapter. The results from the new calculation, which are 3σ upper limits, strongly suggest that the occurrence rates of close-in sub-Saturns and sub-Neptunes decrease when moving to earlier stellar spectral types. Only loose constraints are obtained for close-in super-Earths around A-type stars, which I find to be as common or less common around A-type stars than stars with later spectral types.

on the time required for small planets to form and undergo disk migration, planets around hot stars may simply lack the time required to reach close-in orbits. This would be especially true if planets preferentially form near or beyond the ice line (e.g., Kennedy and Kenyon 2008), which is located at larger orbital separations for hotter stars.

Lastly, atmospheric photoevaporation may explain some aspects of the low occurrence rate of small close-in planets. Using the model from Garcia et al. (2022), Chapter 4 (Giacalone et al. 2022) showed that the high levels of near-ultraviolet radiation from an A-type star can strip a close-in Neptune-size planets of its atmospheres on a timescale of hundreds of Myrs. This process is expected to be most efficient for sub-Saturns, due to their low surface gravities (Owen and Lai 2018), likely leaving behind cores smaller than $2\,R_\oplus$ that cannot

be detected easily in *TESS* data. However, photoevaporation can less easily explain the observed dearth of sub-Neptunes, which are much less susceptible to atmospheric stripping.

5.6 Remaining Work

The results presented in this chapter provide compelling evidence for a dearth of small close-in planets around A-type stars relative to cooler stars, but it is important to emphasize that these results are preliminary. There are a small number of steps that will be executed after the submission of this thesis in order to obtain the final set of results from this study. Here, I outline this remaining work.

Vetting of Threshold Crossing Events

In Section 5.4, I describe the algorithm used to identify TCEs, periodic events in *TESS* data with morphologies consistent with transits. In my calculation of occurrence rate, I make the approximation that this algorithm only detects TCEs that were previously labeled as planet candidates by the *TESS* Science Office . This approximation is likely close to reality, as my pipeline does not differ from the *TESS* QLP in any extraordinary way. However, a complete calculation of occurrence rate requires additional steps.

The transit detection pipeline must be run on the entire stellar sample in order to compile a complete list of TCEs, which will undoubtedly be longer than the list of planet candidates in Table 5.2. This list will contain a number of TCEs that are caused by instrumental systematics, astrophysical false positives, and large transiting companions with radii that exceed the planet sizes explored in this study. In addition to utilizing follow-up observations and analyses with tools like `TRICERATOPS`, I will implement a number of automated vetting steps to separate these TCEs from true planet candidates.

There are two categories of TCEs that result from instrumental systematics. The first, which is noted by Kunimoto et al. (2023), appears at aliases of the 13.7-day *TESS* orbital period. *TESS* transmits data at the periapse of its orbit, during which it stops collecting data and turns to face the Earth. The data immediately preceding or following these data gaps often contain scattered light that is difficult to remove via detrending, sometimes leaving artificial periodic signals that are detected by the transit detection algorithm. The second category arises from periodic *TESS* momentum dumps, which remove angular momentum from the spacecraft reaction wheels by firing thrusters. These dumps, which occur with different periodicities in different *TESS* sectors, sometimes lead to small shifts in the positions of stars in the *TESS* cameras and affect the amount of light contributing to the aperture (e.g., Vanderburg et al. 2019). These temporary fluctuations in flux can lead to transit-like signals in the light curves. In the final calculation, I will implement measures to detect these artificial signals and rule them out as instrumental false alarms.

The most common form of astrophysical false positive in *TESS* data is the nearby eclipsing binary, the scenario where a nearby pair of faint eclipsing binary stars are mistaken for a

transiting planet around another star with which they are unresolved in the *TESS* data (see Section 5.2). While these false positives are sometimes difficult to discern without follow-up observations, clear instances can be identified using centroid offset analyses, such as the difference imaging technique (Bryson et al. 2013). In short, these methods identify nearby eclipsing binaries by subtracting in-transit images from out-of-transit images to locate the true origin of a given transit-like signal in the *TESS* pixels. The more distant the source of a transit-like event from the target star, the larger the shift in the centroid of the light will be. This metric has been used to reliably identify likely false positives in both *Kepler* and *TESS* data (e.g., Bryson et al. 2013; Gan et al. 2023; Kostov et al. 2019). I will implement steps to detect centroid offsets in my final occurrence rate calculation in order to rule out clear false positives.

Lastly, large transiting planets, brown dwarfs, and stellar-mass companions can be removed from the list of TCEs by fitting the *TESS* light curves to transit models, such as those available in the `exoplanet` Python package. These fits will allow be to identify these scenarios in an automated way by providing estimates of the radius and impact parameter of the transiting object. Because my occurrence rate analysis is only concerned with small planets, I will reject TCEs with $R_{\rm p} > 8\,R_{\oplus}$ or with likely grazing transits $b > 0.9$.

Improving the Pipeline Sensitivity Map

When calculating the sensitivity of the transit detection pipeline in Section 5.4, I used a total of 100,000 artificial planet signals injected into the raw *TESS* light curves. While this number is large enough to provide preliminary constraints on occurrence rate, a much larger number will be utilized in the final calculation. Typically, more than 1,000,000 injections are used in these calculations (e.g., Dressing and Charbonneau 2013; Gan et al. 2023; Howard et al. 2012), which is sufficient to smooth out noise and provide monotonicity in sensitivity as a function of $R_{\rm p}$ and $P_{\rm orb}$. Nonetheless, these improvements will not impact the occurrence rate limits reported here in a qualitative way.

Expanding the Sample Size

In Section 5.3, I defined the sample used in this occurrence rate study with the motivation of selecting A-type stars that are the easiest to detect planets around (i.e., the brightest and smallest of them). In truth, the sample can likely be expanded by using a different set of stellar selection criteria. The ability to detect a transiting planet around a star is dependent on the apparent magnitude of the star (which determines the photometric precision), the size of the star (which controls the transit depth), and the length of the observational baseline (planets are easier to detect if more transits are observed). Because of this, there are likely additional stars observed by *TESS* that are appropriate to include in the stellar sample. For instance, A-type stars larger than $2.5\,R_{\odot}$ could be included if they are relatively bright or have been observed in a large number of *TESS* sectors, and A-type stars that are fainter than $T = 10$ could be included if they are relatively small or have been observed in a large

number of *TESS* sectors. This relationship has been nicely characterized for *Kepler* data using the Multi-Event Statistic (MES; Christiansen et al. 2012). In the final calculation of occurrence rate, I will expand the stellar sample size using the MES, likely providing even stronger upper limits.

5.7 Conclusions

Early transit and radial velocity surveys have painted a detailed picture of the demographics of planets around stars like the Sun and cooler (i.e., FGKM-type stars). However, the landscape of close-in planets orbiting relatively hot and massive stars has been left largely unexplored. Using data from *TESS*, I provide constraints on the occurrence rate of small ($R_{\rm p} < 8\,R_{\oplus}$) close-in ($P_{\rm orb} < 10$ days) planets orbiting A-type stars for the first time.

Using a sample of over 20,000 bright A-type stars, I search for transiting planets using a custom transit detection pipeline. Ultimately, no planets were detected, suggesting that small planets with orbital periods under 10 days are rare around these hot stars. To quantify this, I use injection-recovery tests in order to characterize the search completeness of my pipeline. With this analysis, I obtain the following preliminary upper limits on planet occurrence rate:

- Sub-Saturns ($4\,R_{\oplus} < R_{\rm p} < 8\,R_{\oplus}$) with $P_{\rm orb} < 10$ days have an occurrence rate of < 1.6 planets per 1000 A-type stars, at 3σ confidence. Based on occurrence rate calculations for FGKM-type stars, this indicates that these planets are rarer around A-type stars than their cooler counterparts.

- Sub-Neptunes ($2\,R_{\oplus} < R_{\rm p} < 4\,R_{\oplus}$) with $P_{\rm orb} < 10$ days have an occurrence rate of < 7.6 planets per 1000 A-type stars, at 3σ confidence. Based on occurrence rate calculations for FGKM-type stars, this indicates that these planets are rarer around A-type stars than their cooler counterparts.

- Super-Earths ($1\,R_{\oplus} < R_{\rm p} < 2\,R_{\oplus}$) with $P_{\rm orb} < 10$ days have an occurrence rate of < 96 planets per 1000 A-type stars, at 3σ confidence. Based on occurrence rate calculations for FGKM-type stars, this suggests that these planets are rarer around A-type stars than they are around KM-type stars, and are as common or less common around A-type stars than they are around FG-type stars.

These findings are consistent with earlier results that found planets with $R_{\rm p} < 4\,R_{\oplus}$ to become increasingly rare around progressively hotter main-sequence stars (e.g., Mulders et al. 2015a). This is most likely due to a combination of larger dust sublimation radii for hotter stars, which prevents rocky cores from forming in-situ very close to the star, and an increased rate of gas dissipation in protoplanetary disks around hotter stars, which results in less time for planets to migrate inwards. The decrease in sub-Saturn occurrence rate around hotter stars is a novel result, and indicates that these planets are either unable to form or migrate to close in orbits (similar to the sub-Neptunes and super-Earths) or are rapidly

stripped of their atmospheres due to efficient photoevaporation driven by near-ultraviolet continuum emission from their hot host stars.

Lastly, I outline the final steps needed to complete the occurrence rate calculation, which includes establishing a procedure for vetting candidates detected by the transit detection pipeline in a systematic way. I also list improvements that will be made to the calculation in the future, which will result in even stronger limits on the planet occurrence rates.

Chapter 6

Future Work

Since the discovery of the first exoplanet, the field of exoplanetary science has an experienced explosive growth that shows no signs of slowing. In addition to current efforts, a number of new missions and instruments will come online over the next several decades that will continue to revolutionize our understanding of planets throughout the Galaxy.

At the time of the writing of this thesis (Spring 2023), *TESS* is approaching its sixth year of data collection and is expected to continue to collect data until the end of its second extended mission in October 2024. With a highly stable orbit and enough fuel to sustain several more years of operation (Ricker et al. 2010), there is a strong possibility of *TESS* surviving into the 2030s. As *TESS* continues to collect data, it will become more sensitive to small planets orbiting bright stars, planets of all sizes orbiting faint stars, and planets with orbital periods greater than 10 days. As such, *TESS* will continue to enable novel studies of close-in transiting planets for years to come.

A larger *TESS* data set will provide the opportunity to conduct more robust occurrence rate calculations that access regions of stellar parameter space that are currently poorly understood. For instance, additional monitoring of A-type stars will provide greater sensitivity to planets smaller than Neptune, as well as longer period planets, orbiting these hot stars. Repeating the calculation in Chapter 5 after the conclusion of the mission will provide even greater constraints on planet formation and evolution models around early-type stars. Another exciting prospect with continued *TESS* extended missions is the opportunity to study planets orbiting ultracool dwarfs. The *Kepler* mission allowed for the calculation of planet occurrence rates for early-type M dwarfs, but the population of planets orbiting stars of even lower mass is still poorly understood (Dressing and Charbonneau 2013, 2015; Mulders et al. 2015a,b). Because the stars with the lowest masses also have the lowest luminosities, and therefore tend to be much fainter in the *TESS* passband, a longer baseline of observation is required to detect the transits of orbiting planets. Further extended *TESS* missions will make the detection of these planets more feasible. Lastly, *TESS* has provided the unprecedented ability to search for transiting planets around both very young stars (Age $<$ 500 Myr; e.g., Hedges et al. 2021; Newton et al. 2019) and stars that have evolved off of the main sequence (e.g., Grunblatt et al. 2022; Saunders et al. 2022). As novel occurrence rate studies aiming

to examine these populations of planets take shape, validation tools like `TRICERATOPS` will play an important role in determining the reliability of planet candidates in their respective samples (e.g., Fernandes et al. 2022).

The emergence of new ground-based instruments with which to study exoplanets will greatly complement discoveries made in *TESS* data. For instance, the newly commissioned Keck Planet Finder (KPF) spectrograph on the 10 m Keck-I telescope will enable mass measurements for planets with radial velocity amplitudes under 1 m/s and planets orbiting stars fainter than $V = 12$ (Gibson et al. 2018). In addition, KPF will be a powerful tool for measuring the obliquities of stars with transiting planets, or the angles between the stellar spin axes and the planet orbital axes, by leveraging the Rossiter-McLaughlin effect (McLaughlin 1924; Rossiter 1924). Previous studies have found that stellar obliquities provide a window into the dynamical histories of planetary systems. For instance, it is known that the obliquities of stars with hot Jupiters depend on the effective temperature of the star, where stars cooler than the Kraft break ($T_{\rm eff} = 6250\,{\rm K}$; Kraft 1967) tend to have spins aligned with the orbital axes of their planets and stars hotter than the Kraft break often have spins that are misaligned with the orbital axes of their planets (Albrecht et al. 2022; Winn et al. 2010). Some interpret this to mean that hot Jupiters arrive at their close-in orbits via high-eccentricity tidal migration, the process by which the orbit of a wide-separation giant planet is excited into a high eccentricity and inclination and subsequently shrinks due to tidal interactions with the host star near periastron, rather than in-situ formation or migration through a protoplanetary disk (Rice et al. 2022).

Another interesting prospect enabled by the *TESS* mission is the possibility of studying the obliquity distribution of stars with close-in transiting brown dwarfs. Brown dwarfs are known to be rare at short orbital separations (e.g., Kraus et al. 2008), but *TESS* has significantly increased the sample size, especially around bright and hot stars (e.g., Benni et al. 2021; Psaridi et al. 2022). Preliminary obliquity measurements hint that brown dwarfs tend to have orbits that are aligned with the spin axes of their host stars, even when those stars are hotter than the Kraft break (Zhou et al. 2019a), indicating that these massive substellar objects may arrive at short orbital periods via different mechanisms from hot Jupiters. As a National Science Foundation Astronomy and Astrophysics Postdoctoral Fellow, I will use KPF to investigate this correlation by measuring the stellar obliquities of hot stars with newly-discovered short-period ($P_{\rm orb} < 10$ days) brown dwarfs, as well as stars of all temperatures with tidally detached ($P_{\rm orb} > 10$ days) brown dwarfs. These observations will complement recent direct imaging studies that compare the spin-orbit alignments of stars and wide-separation giant planets with those of stars and wide-separation brown dwarfs. These observations have provided evidence that the two classes of objects have distinct eccentricity and stellar obliquity distributions (Bowler et al. 2020, 2023), bolstering the hypothesis that they have different formation pathways. This research will also provide a more holistic picture of how close-in planets form and evolve around early-type stars, supplementing the results of Chapter 5.

In Chapter 3, I presented 13 newly validated small ($R_{\rm p} < 2\,R_\oplus$) planets that would make ideal targets for thermal emission observations with *JWST*. Planets of this radius are

especially interested because they bound the radius at which planets go from being terrestrial to having volatile-rich envelopes (Rogers 2015). By observing the thermal phase curves of a small planet either photometrically or spectroscopically, it is possible to infer the presence of an atmosphere (e.g., Mansfield et al. 2019), testing the ability of these planets to accrete and retain or outgas atmospheres. With capabilities in the near- and mid-infrared, *JWST* is the perfect facility for detecting this thermal emission. Recently, MIRI observations of the temperate terrestrial planet TRAPPIST-1 b (Gillon et al. 2017a) found that the planet likely lacks a substantial atmosphere, hinting that Earth-like planets around cool stars may frequently be bare (Greene et al. 2023). However, a larger sample is required to determine if this is true for all planets of this class. In the future, I will propose for *JWST* time to obtain similar observations for the planets validated in Chapter 3.

JWST also provides the ability to search for and study outgassed atmospheres around particularly hot terrestrial planets. Rocky planets with dayside temperatures greater than $\sim$ 800 K are expected to be molten (giving them the colloquial name "lava words"), producing outgassed silicate atmospheres with strong emission features in the mid infrared (Schaefer et al. 2012; Zilinskas et al. 2022). The compositions of the surface melt and outgassed atmospheres are theorized to very with equilibrium temperature, which may lead to detectable differences for close-in terrestrial planets that experience different levels of stellar irradiation. Kite et al. (2016) explored these potential differences by comparing the rate of surface-interior recycling to the expected outgassing rate for lava worlds of different surface temperatures. The study found that the surfaces of planets with daysides hotter than $\sim$ 2400 vaporize faster than their surface pools can be replenished with their interior reservoirs, leading to a compositionally evolved surfaces and the accumulation of relatively high-pressure dayside atmospheres. This surface evolution may also result in a high-albedo surface than can detected via thermal phase curve observations. TOI-2260 b, which was validated in Chapter 3, is one of the hottest terrestrial planets known to date and orbits a relatively bright star, making it one of the best targets for testing this theory.

Beyond *TESS* and *JWST*, multiple space-based missions will deliver exoplanet-related data within the next decade. The fourth data release from the *Gaia* mission (Gaia Collaboration et al. 2016), which is expected to be published during or after 2025, will contain the astrometric orbits for potentially tens of thousands of giant planets and brown dwarfs with orbital separations between 1 and 10 AU (Perryman et al. 2014). Using this sample, we can uncover the distribution of the spin-orbit alignments between stars and their substellar companions at intermediate separations that are currently inaccessible via the transit and direct imaging methods. For non-transiting companions, stellar obliquity can be determined if the rotation period and of the star is known (e.g., from *TESS*), the $v \sin i$ has been measured spectroscopically, and the *Gaia* astrometry places tight constraints on the orbital inclination of the companion. It has also been predicted that dozens of these long-period companions will be transiting (Perryman et al. 2014), allowing for the measurement of sky-projected stellar obliquity via the Rossiter-McLaughlin effect, assuming the ephemerides of the companions can be sufficiently refined with follow-up radial velocity and transit observations.

Transiting long-period gas giants detected by *Gaia* will also be enticing targets for trans-

mission spectroscopy observations to probe their atmospheric compositions. Most giant planets with transmission spectroscopy observations (e.g., with the *Hubble Space Telescope*; Sing et al. 2016) have short-period orbits, which biases the sample of giant planets with characterized atmospheres towards high equilibrium temperatures. Because planets with longer orbital periods are less likely to transit, very few temperate giant planets with characterized atmospheres exist (Alam et al. 2022). Transiting giant planets detected by *Gaia* provide an opportunity to increase this number substantially.

These transiting giant planets are also interesting from the perspective of exomoons (e.g., Harada et al. 2023). Many of the planets and brown dwarfs detected by *Gaia* will fall within the habitable zones of their systems, raising the unique opportunity to search for evidence of terrestrial satellites in orbit around them. While a moon would likely be too small to detect via transit, the presence of optically thick rings can be inferred by measuring an anomalously large planet radius or detecting a transit when the astrometrically determined inclination of the planet predicts no transit at all (Akinsanmi et al. 2020; Piro and Vissapragada 2020). Transmission spectroscopy observations can provide evidence of rings as well (Alam et al. 2022). The frequent detection of rings would indicate that moons commonly form around gas giants in the habitable zone. A future high-photometric-precision and long-baseline transit mission may be able to infer the presence of these moons by way of transit duration variations (Kipping 2009). Alternatively, as adaptive optics and coronographic capabilities improve, we many be able to directly image these planets and detect their moons via radial velocity monitoring (Vanderburg and Rodriguez 2021; Vanderburg et al. 2018).

The *Nancy Grace Roman Space Telescope*, which is scheduled to launch in 2027, will enable multiple new developments in exoplanet science (Spergel et al. 2015). The Galactic Bulge Time Domain Survey is expected to detect over 1000 exoplanets, including Earth-mass planets in the habitable zone, via gravitational microlensing (Penny et al. 2019). This will likely enable the most precise measurement of the occurrence rate of Earth-size planets on wide-separation orbits to date. In addition, the survey will detect tens of thousands of transiting hot Jupiters, allowing for differential studies to determine how the occurrence rates of these planets depend on the region of the galaxy in which they form (Montet et al. 2017). Lastly, the mission will test new space-based coronagraphic technologies that will aid in the development of future direct imaging missions.

In 2026 and 2029, the European Space Agency will launch the *PLATO* and *ARIEL* missions, respectively. *PLATO* will continue the legacy of *Kepler* and *TESS* by searching for transiting planets across a wide area of the sky and further enabling demographics studies of close-in planets (Rauer et al. 2014). *PLATO* will be particular useful for probing the occurrence rates planets orbiting A-type stars at longer orbital periods than those currently accessible with *TESS*, due to having a longer observational baseline per star. *ARIEL* will study the atmospheres of nearly 1000 exoplanets via transmission and emission spectroscopy in order to compile a statistical catalog of atmospheric compositions (Tinetti et al. 2016).

The 2020 NASA Decadal Survey on Astronomy and Astrophysics has placed exoplanet science at the focal point for future missions, with the identification and characterization of Earth-like planets outside of the solar system as one of the main scientific priorities for the

coming decades. In particular, the future NASA IR/O/UV flagship mission, now dubbed the *Habitable Worlds Observatory*, will direct image exoplanets in the habitable zones of Sun-like stars. In addition to potentially directly imaging the first true Earth analogue, the mission will enable myriad of other scientific studies that advance our understanding of how planets form and evolve. The work presented in this thesis helps lay the foundation for this mission and others like it.

Bibliography

Adams, Elisabeth R. et al. (2016). "Ultra-short-period Planets in K2 SuPerPiG Results for Campaigns 0-5". In: *The Astronomical Journal* 152, 47.

Akinsanmi, B. et al. (2020). "Can planetary rings explain the extremely low density of HIP 41378 f?" In: *Astronomy & Astrophysics* 635, L8.

Alam, Munazza K. et al. (2022). "The First Near-infrared Transmission Spectrum of HIP 41378 f, A Low-mass Temperate Jovian World in a Multiplanet System". In: *The Astrophysical Journal Letters* 927, L5.

Albrecht, Simon H. et al. (2022). "Stellar Obliquities in Exoplanetary Systems". In: *Publications of the Astronomical Society of the Pacific* 134, 082001.

Alonso, Roi et al. (2004). "TrES-1: The Transiting Planet of a Bright K0 V Star". In: *The Astrophysical Journal Letters* 613, pp. L153–L156.

Alsubai, K. A. et al. (2013). "The Qatar Exoplanet Survey". In: *Acta Astronomica* 63, pp. 465–480.

Ansdell, M. et al. (2016). "ALMA Survey of Lupus Protoplanetary Disks. I. Dust and Gas Masses". In: *The Astrophysical Journal* 828, 46.

Ansdell, Megan et al. (2018). "Scientific Domain Knowledge Improves Exoplanet Transit Classification with Deep Learning". In: *The Astrophysical Journal Letters* 869, L7.

Astudillo-Defru, N. et al. (2020). "A hot terrestrial planet orbiting the bright M dwarf L 168-9 unveiled by TESS". In: *Astronomy & Astrophysics* 636, A58.

Auvergne, M. et al. (2009). "The CoRoT satellite in flight: description and performance". In: *Astronomy & Astrophysics* 506, pp. 411–424.

Badenas-Agusti, Mariona et al. (2020). "HD 191939: Three Sub-Neptunes Transiting a Sun-like Star Only 54 pc Away". In: *The Astronomical Journal* 160, 113.

Bakos, G. et al. (2004). "Wide-Field Millimagnitude Photometry with the HAT: A Tool for Extrasolar Planet Detection". In: *Publications of the Astronomical Society of the Pacific* 116, pp. 266–277.

Bakos, G. Á. et al. (2013). "HATSouth: A Global Network of Fully Automated Identical Wide-Field Telescopes". In: *Publications of the Astronomical Society of the Pacific* 125, p. 154.

Barkaoui, K. et al. (2018). "VizieR Online Data Catalog: WASP-161b, WASP-163b and WASP-170b (Barkaoui+, 2019)". In: *VizieR Online Data Catalog* J/AJ/157/43.

Barnes, Jason W. (2009). "Transit Lightcurves of Extrasolar Planets Orbiting Rapidly Rotating Stars". In: *The Astrophysical Journal* 705, pp. 683–692.

Barnes, Sydney A. (2007). "Ages for Illustrative Field Stars Using Gyrochronology: Viability, Limitations, and Errors". In: *The Astrophysical Journal* 669, pp. 1167–1189.

Barros, S. C. C. et al. (2014). "Revisiting the transits of CoRoT-7b at a lower activity level". In: *Astronomy & Astrophysics* 569, A74.

Batalha, Natalie M. et al. (2011). "Kepler's First Rocky Planet: Kepler-10b". In: *The Astrophysical Journal* 729, 27.

Batalha, Natasha E. et al. (2017). "PandExo: A Community Tool for Transiting Exoplanet Science with JWST & HST". In: *Publications of the Astronomical Society of the Pacific* 129, p. 064501.

— (2019). *PandExo: Instrument simulations for exoplanet observation planning*. Astrophysics Source Code Library, record ascl:1906.016.

Beleznay, Maya and M. Kunimoto (2022). "Exploring the dependence of hot Jupiter occurrence rates on stellar mass with TESS". In: *Monthly Notices of the Royal Astronomical Society* 516, pp. 75–83.

Benedict, G. F. et al. (2016). "The Solar Neighborhood. XXXVII: The Mass-Luminosity Relation for Main-sequence M Dwarfs". In: *The Astronomical Journal* 152, 141.

Benni, P. et al. (2021). "Discovery of a young low-mass brown dwarf transiting a fast-rotating F-type star by the Galactic Plane eXoplanet (GPX) survey". In: *Monthly Notices of the Royal Astronomical Society* 505, pp. 4956–4967.

Berger, Travis A. et al. (2018). "Revised Radii of Kepler Stars and Planets Using Gaia Data Release 2". In: *The Astrophysical Journal* 866, 99.

Berger, Travis A. et al. (2020). "The Gaia-Kepler Stellar Properties Catalog. II. Planet Radius Demographics as a Function of Stellar Mass and Age". In: *The Astronomical Journal* 160, 108.

Berta-Thompson, Zachory K. et al. (2015). "A rocky planet transiting a nearby low-mass star". In: *Nature* 527, pp. 204–207.

Bluhm, P. et al. (2021). "An ultra-short-period transiting super-Earth orbiting the M3 dwarf TOI-1685". In: *Astronomy & Astrophysics* 650, A78.

Bond, Jade C. et al. (2010). "The Compositional Diversity of Extrasolar Terrestrial Planets. I. In Situ Simulations". In: *The Astrophysical Journal* 715, pp. 1050–1070.

Bonfils, X. et al. (2018). "Radial velocity follow-up of GJ1132 with HARPS. A precise mass for planet b and the discovery of a second planet". In: *Astronomy & Astrophysics* 618, A142.

Borucki, William J. et al. (2010). "Kepler Planet-Detection Mission: Introduction and First Results". In: *Science* 327, 5968.

Bourrier, V. et al. (2018). "The 55 Cancri system reassessed". In: *Astronomy & Astrophysics* 619, A1.

Bowler, Brendan P. et al. (2020). "Population-level Eccentricity Distributions of Imaged Exoplanets and Brown Dwarf Companions: Dynamical Evidence for Distinct Formation Channels". In: *The Astronomical Journal* 159, 63.

Bowler, Brendan P. et al. (2023). "Rotation Periods, Inclinations, and Obliquities of Cool Stars Hosting Directly Imaged Substellar Companions: Spin-Orbit Misalignments Are Common". In: *The Astronomical Journal* 165, 164.

Bramich, D. M. and M. B. Nielsen (2018). "An Almanac of Predicted Microlensing Events for the 21st Century". In: *Acta Astronomica* 68, pp. 183–203.

Brown, T. M. et al. (2013). "Las Cumbres Observatory Global Telescope Network". In: *Publications of the Astronomical Society of the Pacific* 125, p. 1031.

Bryson, S. et al. (2020). "A Probabilistic Approach to Kepler Completeness and Reliability for Exoplanet Occurrence Rates". In: *The Astronomical Journal* 159, 279.

Bryson, Stephen T. et al. (2013). "Identification of Background False Positives from Kepler Data". In: *Publications of the Astronomical Society of the Pacific* 125, p. 889.

Buchhave, Lars A. et al. (2012). "An abundance of small exoplanets around stars with a wide range of metallicities". In: *Nature* 486, pp. 375–377.

Buchhave, Lars A. et al. (2016). "A 1.9 Earth Radius Rocky Planet and the Discovery of a Non-transiting Planet in the Kepler-20 System". In: *The Astronomical Journal* 152, 160.

Burke, Christopher J. et al. (2015). "Terrestrial Planet Occurrence Rates for the Kepler GK Dwarf Sample". In: *The Astrophysical Journal* 809, 8.

Cabrera, J. et al. (2017). "Disproving the validated planets K2-78b, K2-82b, and K2-92b. The importance of independently confirming planetary candidates". In: *Astronomy & Astrophysics* 606, A75.

Carter, Joshua A. et al. (2012). "Kepler-36: A Pair of Planets with Neighboring Orbits and Dissimilar Densities". In: *Science* 337, p. 556.

Castelli, F. and R. L. Kurucz (2003). "New Grids of ATLAS9 Model Atmospheres". In: ed. by N. Piskunov et al. Vol. 210. A20.

Catanzarite, Joseph H (2015). *Autovetter Planet Candidate Catalog for Q1-Q17 Data Release 24*.

Cayrel de Strobel, G. (1996). "Stars resembling the Sun". In: *The Astronomy and Astrophysics Review* 7, pp. 243–288.

Charbonneau, David et al. (2000). "Detection of Planetary Transits Across a Sun-like Star". In: *The Astrophsyical Journal Letters* 529, pp. L45–L48.

Charpinet, S. et al. (2011). "A compact system of small planets around a former red-giant star". In: *Nature* 480, pp. 496–499.

Chen, Jingjing and David Kipping (2017). "Probabilistic Forecasting of the Masses and Radii of Other Worlds". In: *The Astrophysical Journal* 834, 17.

Christiansen, Jessie L. et al. (2012). "The Derivation, Properties, and Value of KeplerCombined Differential Photometric Precision". In: *Publications of the Astronomical Society of the Pacific* 124, p. 1279.

Christiansen, Jessie L. et al. (2017). "Three's Company: An Additional Non-transiting Super-Earth in the Bright HD 3167 System, and Masses for All Three Planets". In: *The Astronomical Journal* 154, 122.

Ciardi, David R. et al. (2015). "Understanding the Effects of Stellar Multiplicity on the Derived Planet Radii from Transit Surveys: Implications for Kepler, K2, and TESS". In: *The Astrophysical Journal* 805, 16.

Claret, A. (2017). "Limb and gravity-darkening coefficients for the TESS satellite at several metallicities, surface gravities, and microturbulent velocities". In: *Astronomy & Astrophysics* 600, A30.

Claret, Antonio (2018). "A new method to compute limb-darkening coefficients for stellar atmosphere models with spherical symmetry: the space missions TESS, Kepler, CoRoT, and MOST". In: *Astronomy & Astrophysics* 618, A20.

Cloutier, Ryan (2019). "The Independent Discovery of Planet Candidates around Low-mass Stars and Astrophysical False Positives from the First Two TESS Sectors". In: *The Astronomical Journal* 158, 81.

Cloutier, Ryan and Kristen Menou (2020). "Evolution of the Radius Valley around Low-mass Stars from Kepler and K2". In: *The Astronomical Journal* 159, 211.

Cloutier, Ryan et al. (2020a). "A Pair of TESS Planets Spanning the Radius Valley around the Nearby Mid-M Dwarf LTT 3780". In: *The Astronomical Journal* 160, 3.

Cloutier, Ryan et al. (2020b). "TOI-1235 b: A Keystone Super-Earth for Testing Radius Valley Emergence Models around Early M Dwarfs". In: *The Astronomical Journal* 160, 22.

Cloutier, Ryan et al. (2021). "TOI-1634 b: An Ultra-short-period Keystone Planet Sitting inside the M-dwarf Radius Valley". In: *The Astronomical Journal* 162, 79.

Collier Cameron, A. et al. (2010). "Line-profile tomography of exoplanet transits - II. A gas-giant planet transiting a rapidly rotating A5 star". In: *Monthly Notices of the Royal Astronomical Society* 407, pp. 507–514.

Collins, Karen A. et al. (2017). "AstroImageJ: Image Processing and Photometric Extraction for Ultra-precise Astronomical Light Curves". In: *The Astronomical Journal* 153, 77.

Coughlin, Jeffrey L. et al. (2014). "Contamination in the Kepler Field. Identification of 685 KOIs as False Positives via Ephemeris Matching Based on Q1-Q12 Data". In: *The Astronomical Journal* 147, 119.

Crossfield, Ian J. M. et al. (2016). "197 Candidates and 104 Validated Planets in K2First Five Fields". In: *The Astrophysical Journal Supplement Series* 226, 7.

Crossfield, Ian J. M. et al. (2019). "A Super-Earth and Sub-Neptune Transiting the Late-type M Dwarf LP 791-18". In: *The Astrophysical Journal Letters* 883, L16.

Cutri, R. M. et al. (2014). "VizieR Online Data Catalog: AllWISE Data Release (Cutri+ 2013)". In: *VizieR Online Data Catalog* II/328.

Dai, Fei et al. (2020). "The TESS-Keck Survey. III. A Stellar Obliquity Measurement of TOI-1726 c". In: *The Astronomical Journal* 160, 193.

Dai, Fei et al. (2021). "TKS X: Confirmation of TOI-1444b and a Comparative Analysis of the Ultra-short-period Planets with Hot Neptunes". In: *The Astronomical Journal* 162, 62.

Dalba, Paul A. et al. (2020). "The TESS-Keck Survey. I. A Warm Sub-Saturn-mass Planet and a Caution about Stray Light in TESS Cameras". In: *The Astronomical Journal* 159, 241.

Dalba, Paul A. et al. (2022). "The TESS-Keck Survey. VIII. Confirmation of a Transiting Giant Planet on an Eccentric 261 Day Orbit with the Automated Planet Finder Telescope". In: *The Astronomical Journal* 163, 61.

David, Trevor J. et al. (2021). "Evolution of the Exoplanet Size Distribution: Forming Large Super-Earths Over Billions of Years". In: *The Astronomical Journal* 161, 265.

Daylan, Tansu et al. (2021). "TESS Discovery of a Super-Earth and Three Sub-Neptunes Hosted by the Bright, Sun-like Star HD 108236". In: *The Astronomical Journal* 161, 85.

de Leon, J. P. et al. (2021). "37 new validated planets in overlapping K2 campaigns". In: *Monthly Notices of the Royal Astronomical Society* 508, pp. 195–218.

Dekany, Richard et al. (2013). "PALM-3000: Exoplanet Adaptive Optics for the 5 m Hale Telescope". In: *The Astrophysical Journal* 776, 130.

Demangeon, O. D. S. et al. (2018). "The discovery of WASP-151b, WASP-153b, WASP-156b: Insights on giant planet migration and the upper boundary of the Neptunian desert". In: *Astronomy & Astrophysics* 610, A63.

Demory, B. -O. et al. (2011). "Detection of a transit of the super-Earth 55 Cancri e with warm Spitzer". In: *Astronomy & Astrophysics* 533, A114.

Demory, B. -O. et al. (2020). "A super-Earth and a sub-Neptune orbiting the bright, quiet M3 dwarf TOI-1266". In: *Astronomy & Astrophysics* 642, A49.

Demory, Brice-Olivier et al. (2016). "A map of the large day-night temperature gradient of a super-Earth exoplanet". In: *Nature* 532, pp. 207–209.

Dıaz, R. F. et al. (2014). "PASTIS: Bayesian extrasolar planet validation - I. General framework, models, and performance". In: *Monthly Notices of the Royal Astronomical Society* 441, pp. 983–1004.

Donati, J. -F. et al. (1997). "Spectropolarimetric observations of active stars". In: *Monthly Notices of the Royal Astronomical Society* 291, pp. 658–682.

Dong, Jiayin et al. (2022). "NEID Rossiter-McLaughlin Measurement of TOI-1268b: A Young Warm Saturn Aligned with Its Cool Host Star". In: *The Astrophysical Journal Letters* 926, L7.

Dong, Subo and Zhaohuan Zhu (2013). "Fast Rise of "Neptune-size" Planets (4-8 $R_{\oplus}$) from P 0.5ex˜10 to 0.5ex˜250 Daysof Kepler Planet Candidates up to 0.5ex˜0.75 AU". In: *The Astrophysical Journal* 778, 53.

Dragomir, Diana et al. (2013). "MOST Detects Transits of HD 97658b, a Warm, Likely Volatile-rich Super-Earth". In: *The Astrophysical Journal Letters* 772, L2.

Dressing, Courtney D. and David Charbonneau (2013). "The Occurrence Rate of Small Planets around Small Stars". In: *The Astrophysical Journal* 767, 95.

— (2015). "The Occurrence of Potentially Habitable Planets Orbiting M Dwarfs Estimated from the Full Kepler Dataset and an Empirical Measurement of the Detection Sensitivity". In: *The Astrophysical Journal* 807, 45.

Dressing, Courtney D. et al. (2015). "The Mass of Kepler-93b and The Composition of Terrestrial Planets". In: *The Astrophysical Journal* 800, 135.

Eisner, N. L. et al. (2020). "Planet Hunters TESS I: TOI 813, a subgiant hosting a transiting Saturn-sized planet on an 84-day orbit". In: *Monthly Notices of the Royal Astronomical Society* 494, pp. 750–763.

Errmann, R. et al. (2014). "Investigation of a transiting planet candidate in Trumpler 37: An astrophysical false positive eclipsing spectroscopic binary star". In: *Astronomische Nachrichten* 335, p. 345.

Espinoza, Néstor et al. (2020). "7.9) star unveiled by TESS". In: *Monthly Notices of the Royal Astronomical Society* 491, pp. 2982–2999.

Essack, Zahra et al. (2020). "Low-albedo Surfaces of Lava Worlds". In: *The Astrophysical Journal* 898, 160.

Feinstein, Adina D. et al. (2019). "eleanor: An Open-source Tool for Extracting Light Curves from the TESS Full-frame Images". In: *Publications of the Astronomical Society of the Pacific* 131, p. 094502.

Fernandes, Rachel B. et al. (2022). "pterodactyls: A Tool to Uniformly Search and Vet for Young Transiting Planets in TESS Primary Mission Photometry". In: *The Astronomical Journal* 164.3, 78.

Fischer, Debra A. and Jeff Valenti (2005). "The Planet-Metallicity Correlation". In: *The Astrophysical Journal* 622, pp. 1102–1117.

Flock, Mario et al. (2019). "Planet formation and migration near the silicate sublimation front in protoplanetary disks". In: *Astronomy & Astrophysics* 630, A147.

Foreman-Mackey, Daniel et al. (2014). "Exoplanet Population Inference and the Abundance of Earth Analogs from Noisy, Incomplete Catalogs". In: *The Astrophysical Journal* 795, 64.

Foreman-Mackey, Daniel et al. (2021). "exoplanet: Gradient-based probabilistic inference for exoplanet data & other astronomical time series". In: *The Journal of Open Source Software* 6, 3285.

Fortney, J. J. et al. (2007). "Planetary Radii across Five Orders of Magnitude in Mass and Stellar Insolation: Application to Transits". In: *The Astrophysical Journal* 659, pp. 1661–1672.

Fressin, François et al. (2013). "The False Positive Rate of Kepler and the Occurrence of Planets". In: *The Astrophysical Journal* 766, 81.

Fried, D. L. (1978). "Probability of getting a lucky short-exposure image through turbulence". In: *Journal of the Optical Society of America (1917-1983)* 68, p. 1651.

Fulton, Benjamin J. and Erik A. Petigura (2018). "The California-Kepler Survey. VII. Precise Planet Radii Leveraging Gaia DR2 Reveal the Stellar Mass Dependence of the Planet Radius Gap". In: *The Astronomical Journal* 156, 264.

Fulton, Benjamin J. et al. (2017). "The California-Kepler Survey. III. A Gap in the Radius Distribution of Small Planets". In: *The Astronomical Journal* 154, 109.

Furlan, E. et al. (2017). "The Kepler Follow-up Observation Program. I. A Catalog of Companions to Kepler Stars from High-Resolution Imaging". In: *The Astronomical Journal* 153, 71.

Gagné, Jonathan et al. (2018). "BANYAN. XI. The BANYAN ΣMultivariate Bayesian Algorithm to Identify Members of Young Associations with 150 pc". In: *The Astrophysical Journal* 856, 23.

Gaia Collaboration et al. (2016). "The Gaia mission". In: *Astronomy & Astrophysics* 595, A1.

Gaia Collaboration et al. (2018). "Gaia Data Release 2. Summary of the contents and survey properties". In: *Astronomy & Astrophysics* 616, A1.

Gaia Collaboration et al. (2021). "Gaia Early Data Release 3. Summary of the contents and survey properties". In: *Astronomy & Astrophysics* 649, A1.

Galland, F. et al. (2005). "Extrasolar planets and brown dwarfs around A-F type stars. I. Performances of radial velocity measurements, first analyses of variations". In: *Astronomy & Astrophysics* 443, pp. 337–345.

Gan, Tianjun et al. (2022). "TESS discovery of a sub-Neptune orbiting a mid-M dwarf TOI-2136". In: *Monthly Notices of the Royal Astronomical Society* 514, pp. 4120–4139.

Gan, Tianjun et al. (2023). "Occurrence Rate of Hot Jupiters Around Early-type M Dwarfs Based on Transiting Exoplanet Survey Satellite Data". In: *The Astronomical Journal* 165, 17.

Garcia, Lionel J. et al. (2022). "PROSE: a PYTHON framework for modular astronomical images processing". In: *Monthly Notices of the Royal Astronomical Society* 509, pp. 4817–4828.

García Muñoz, A. and P. C. Schneider (2019). "Rapid Escape of Ultra-hot Exoplanet Atmospheres Driven by Hydrogen Balmer Absorption". In: *The Astrophysical Journal Letters* 884, L43.

Gaudi, B. Scott et al. (2017). "A giant planet undergoing extreme-ultraviolet irradiation by its hot massive-star host". In: *Nature* 546, pp. 514–518.

Gavel, Donald et al. (2014). "ShaneAO: wide science spectrum adaptive optics system for the Lick Observatory". In: *Adaptive Optics Systems IV*. Ed. by Enrico Marchetti et al. Vol. 9148. Society of Photo-Optical Instrumentation Engineers (SPIE) Conference Series, 914805.

Giacalone, Steven and Courtney D. Dressing (2020). *triceratops: Candidate exoplanet rating tool*. Astrophysics Source Code Library, record ascl:2002.004.

Giacalone, Steven et al. (2017). "A Test of the High-eccentricity Migration Scenario for Close-in Planets". In: *The Astronomical Journal* 154, 192.

Giacalone, Steven et al. (2021). "Vetting of 384 TESS Objects of Interest with TRICERATOPS and Statistical Validation of 12 Planet Candidates". In: *The Astronomical Journal* 161, 24.

Giacalone, Steven et al. (2022). "HD 56414 b: A Warm Neptune Transiting an A-type Star". In: *The Astrophysical Journal Letters* 935, L10.

Gibson, Steven R. et al. (2018). "Keck Planet Finder: preliminary design". In: *Ground-based and Airborne Instrumentation for Astronomy VII*. Ed. by Christopher J. Evans et al. Vol. 10702. Society of Photo-Optical Instrumentation Engineers (SPIE) Conference Series, 107025X.

Gilbert, Emily A. et al. (2020). "The First Habitable-zone Earth-sized Planet from TESS. I. Validation of the TOI-700 System". In: *The Astronomical Journal* 160, 116.

Gillon, M. et al. (2011). "TRAPPIST: a robotic telescope dedicated to the study of planetary systems". In: *European Physical Journal Web of Conferences*. Vol. 11. European Physical Journal Web of Conferences, 06002.

Gillon, Michaël et al. (2017a). "Seven temperate terrestrial planets around the nearby ultra-cool dwarf star TRAPPIST-1". In: *Nature* 542, pp. 456–460.

Gillon, Michaël et al. (2017b). "Two massive rocky planets transiting a K-dwarf 6.5 parsecs away". In: *Nature Astronomy* 1, 0056.

Ginsburg, Adam et al. (2019). "astroquery: An Astronomical Web-querying Package in Python". In: *The Astronomical Journal* 157, 98.

Ginzburg, Sivan et al. (2016). "Super-Earth Atmospheres: Self-consistent Gas Accretion and Retention". In: *The Astrophysical Journal* 825, 29.

— (2018). "Core-powered mass-loss and the radius distribution of small exoplanets". In: *Monthly Notices of the Royal Astronomical Society* 476, pp. 759–765.

Girardi, L. et al. (2005). "Star counts in the Galaxy. Simulating from very deep to very shallow photometric surveys with the TRILEGAL code". In: *Astronomy & Astrophysics* 436, pp. 895–915.

Grasset, O. et al. (2009). "A Study of the Accuracy of Mass-Radius Relationships for Silicate-Rich and Ice-Rich Planets up to 100 Earth Masses". In: *The Astrophysical Journal* 693, pp. 722–733.

Greene, Thomas P. et al. (2016). "Characterizing Transiting Exoplanet Atmospheres with JWST". In: *The Astrophysical Journal* 817, 17.

Greene, Thomas P. et al. (2023). "Thermal emission from the Earth-sized exoplanet TRAPPIST-1 b using JWST". In: *arXiv e-prints*, arXiv:2303.14849.

Griffin, R. E. M. et al. (2000). "Accuracy of radial-velocity measurements for early-type stars. II. Investigations of spectrum mismatch from high-resolution observations". In: *Astronomy and Astrophysics Supplement Series* 147, pp. 299–321.

Grunblatt, Samuel K. et al. (2019). "Giant Planet Occurrence within 0.2 au of Low-luminosity Red Giant Branch Stars with K2". In: *The Astronomical Journal* 158, 227.

Grunblatt, Samuel K. et al. (2022). "TESS Giants Transiting Giants. II. The Hottest Jupiters Orbiting Evolved Stars". In: *The Astronomical Journal* 163.3, 120.

Guerrero, Natalia M. et al. (2021). "The TESS Objects of Interest Catalog from the TESS Prime Mission". In: *The Astrophysical Journal Supplement Series* 254, 39.

Günther, Maximilian N. et al. (2019). "A super-Earth and two sub-Neptunes transiting the nearby and quiet M dwarf TOI-270". In: *Nature Astronomy* 3, pp. 1099–1108.

Gupta, Akash and Hilke E. Schlichting (2019). "Sculpting the valley in the radius distribution of small exoplanets as a by-product of planet formation: the core-powered mass-loss mechanism". In: *Monthly Notices of the Royal Astronomical Society* 487, pp. 24–33.

Habets, G. M. H. J. and J. R. W. Heintze (1981). "Empirical bolometric corrections for the main-sequence." In: *Astronomy and Astrophysics Supplement Series* 46, pp. 193–237.

Hallatt, Tim and Eve J. Lee (2022). "Sculpting the Sub-Saturn Occurrence Rate via Atmospheric Mass Loss". In: *The Astrophysical Journal* 924, 9.

Hara, N. C. et al. (2020). "The SOPHIE search for northern extrasolar planets. XVI. HD 158259: A compact planetary system in a near-3:2 mean motion resonance chain". In: *Astronomy & Astrophysics* 636, L6.

Harada, Caleb K. et al. (2023). "Stability and detectability of exomoons orbiting HIP 41378 f, a temperate Jovian planet with an anomalously low apparent density". In: *arXiv e-prints*, arXiv:2303.14294.

Hardegree-Ullman, Kevin K. et al. (2019). "Kepler Planet Occurrence Rates for Mid-type M Dwarfs as a Function of Spectral Type". In: *The Astronomical Journal* 158, 75.

Hayashi, C. (1961). "Stellar evolution in early phases of gravitational contraction." In: *Publications of the Astronomical Society of Japan* 13, pp. 450–452.

Hayward, T. L. et al. (2001). "PHARO: A Near-Infrared Camera for the Palomar Adaptive Optics System". In: *Publications of the Astronomical Society of the Pacific* 113, pp. 105–118.

Hedges, Christina (2021). "Vetting: A Stand-alone Tool for Finding Centroid Offsets in NASA Kepler, K2, and TESS, Alerting the Presence of Exoplanet False Positives". In: *Research Notes of the American Astronomical Society* 5, 262.

Hedges, Christina et al. (2020). "Systematics-insensitive Periodogram for Finding Periods in TESS Observations of Long-period Rotators". In: *Research Notes of the American Astronomical Society* 4, 220.

Hedges, Christina et al. (2021). "TOI-2076 and TOI-1807: Two Young, Comoving Planetary Systems within 50 pc Identified by TESS that are Ideal Candidates for Further Follow Up". In: *The Astronomical Journal* 162, 54.

Henden, A. A. et al. (2016). "VizieR Online Data Catalog: AAVSO Photometric All Sky Survey (APASS) DR9 (Henden+, 2016)". In: *VizieR Online Data Catalog* II/336.

Hillenbrand, Lynne et al. (2015). "Empirical Limits on Radial Velocity - Planet Detection for Young Stars". In: *18th Cambridge Workshop on Cool Stars, Stellar Systems, and the Sun*. Vol. 18. Cambridge Workshop on Cool Stars, Stellar Systems, and the Sun, pp. 759–766.

Hippke, Michael et al. (2019). "Wōtan: Comprehensive Time-series Detrending in Python". In: *The Astronomical Journal* 158, 143.

Hirano, Teruyuki et al. (2021). "Two Bright M Dwarfs Hosting Ultra-Short-Period Super-Earths with Earth-like Compositions". In: *The Astronomical Journal* 162, 161.

Hirsch, Lea A. et al. (2017). "Assessing the Effect of Stellar Companions from High-resolution Imaging of Kepler Objects of Interest". In: *The Astronomical Journal* 153, 117.

Hirsch, Lea A. et al. (2019). "Discovery of a White Dwarf Companion to HD 159062". In: *The Astrophysical Journal* 878, 50.

Holman, Matthew J. and Norman W. Murray (2005). "The Use of Transit Timing to Detect Terrestrial-Mass Extrasolar Planets". In: *Science* 307, pp. 1288–1291.

Hooton, M. J. et al. (2022). "Spi-OPS: Spitzer and CHEOPS confirm the near-polar orbit of MASCARA-1 b and reveal a hint of dayside reflection". In: *Astronomy & Astrophysics* 658, A75.

Horch, E. P. et al. (1996). "Speckle Interferometry of Southern Double Stars.I.First Results of the Yale-San Juan Speckle Interferometry Program". In: *The Astronomical Journal* 111, p. 1681.

Horch, Elliott P. et al. (2009). "Observations of Binary Stars with the Differential Speckle Survey Instrument. I. Instrument Description and First Results". In: *The Astronomical Journal* 137, pp. 5057–5067.

Horch, Elliott P. et al. (2012). "Observations of Binary Stars with the Differential Speckle Survey Instrument. IV. Observations of Kepler, CoRoT, and Hipparcos Stars from the Gemini North Telescope". In: *The Astronomical Journal* 144, 165.

Hormuth, Felix et al. (2008). "AstraLux: the Calar Alto lucky imaging camera". In: *Ground-based and Airborne Instrumentation for Astronomy II*. Ed. by Ian S. McLean and Mark M. Casali. Vol. 7014. Society of Photo-Optical Instrumentation Engineers (SPIE) Conference Series, 701448.

Houk, N. and A. P. Cowley (1975). *University of Michigan Catalogue of two-dimensional spectral types for the HD stars. Volume I. Declinations -90_ to -53_f0.*

Howard, Andrew W. et al. (2010). "The California Planet Survey. I. Four New Giant Exoplanets". In: *The Astrophysical Journal* 721, pp. 1467–1481.

Howard, Andrew W. et al. (2012). "Planet Occurrence within 0.25 AU of Solar-type Stars from Kepler". In: *The Astrophysical Journal Supplement Series* 201, 15.

Howell, Steve B. et al. (2011). "Speckle Camera Observations for the NASA Kepler Mission Follow-up Program". In: *The Astronomical Journal* 142, 19.

Howell, Steve B. et al. (2014). "The K2 Mission: Characterization and Early Results". In: *Publications of the Astronomical Society of the Pacific* 126, 938.

Hsu, Danley C. et al. (2018). "Improving the Accuracy of Planet Occurrence Rates from Kepler Using Approximate Bayesian Computation". In: *The Astronomical Journal* 155, 205.

Hsu, Danley C. et al. (2019). "Occurrence Rates of Planets Orbiting FGK Stars: Combining Kepler DR25, Gaia DR2, and Bayesian Inference". In: *The Astronomical Journal* 158, 109.

Hu, Renyu et al. (2012). "Theoretical Spectra of Terrestrial Exoplanet Surfaces". In: *The Astrophysical Journal* 752, 7.

Huang, Chelsea X. et al. (2020). "TESS Spots a Hot Jupiter with an Inner Transiting Neptune". In: *The Astrophysical Journal Letters* 892, L7.

Husser, T. -O. et al. (2013). "A new extensive library of PHOENIX stellar atmospheres and synthetic spectra". In: *Astronomy & Astrophysics* 553, A6.

Irwin, Jonathan M. et al. (2015). "The MEarth-North and MEarth-South Transit Surveys: Searching for Habitable Super-Earth Exoplanets Around Nearby M-dwarfs". In: *18th*

Cambridge Workshop on Cool Stars, Stellar Systems, and the Sun. Vol. 18. Cambridge Workshop on Cool Stars, Stellar Systems, and the Sun, pp. 767–772.

Jackson, Alan P. et al. (2012). "The coronal X-ray-age relation and its implications for the evaporation of exoplanets". In: *Monthly Notices of the Royal Astronomical Society* 422, pp. 2024–2043.

Jehin, E. et al. (2011). "TRAPPIST: TRAnsiting Planets and PlanetesImals Small Telescope". In: *The Messenger* 145, pp. 2–6.

Jenkins, Jon M. (2002). "The Impact of Solar-like Variability on the Detectability of Transiting Terrestrial Planets". In: *The Astrophysical Journal* 575, pp. 493–505.

Jenkins, Jon M. et al. (2010). "Transiting planet search in the Kepler pipeline". In: *Software and Cyberinfrastructure for Astronomy*. Ed. by Nicole M. Radziwill and Alan Bridger. Vol. 7740. Society of Photo-Optical Instrumentation Engineers (SPIE) Conference Series, 77400D.

Jenkins, Jon M. et al. (2016). "The TESS science processing operations center". In: *Software and Cyberinfrastructure for Astronomy IV*. Ed. by Gianluca Chiozzi and Juan C. Guzman. Vol. 9913. Society of Photo-Optical Instrumentation Engineers (SPIE) Conference Series, 99133E.

Jensen, E. (2013). *Tapir: A web interface for transit/eclipse observability*. Astrophysics Source Code Library, record ascl:1306.007.

Jin, Sheng and Christoph Mordasini (2018). "Compositional Imprints in Density-Distance-Time: A Rocky Composition for Close-in Low-mass Exoplanets from the Location of the Valley of Evaporation". In: *The Astrophysical Journal* 853, 163.

Jin, Sheng et al. (2014). "Planetary Population Synthesis Coupled with Atmospheric Escape: A Statistical View of Evaporation". In: *The Astrophysical Journal* 795, 65.

Johnson, John Asher et al. (2010). "Giant Planet Occurrence in the Stellar Mass-Metallicity Plane". In: *Publications of the Astronomical Society of the Pacific* 122, p. 905.

Kaltenegger, Lisa et al. (2020). "The White Dwarf Opportunity: Robust Detections of Molecules in Earth-like Exoplanet Atmospheres with the James Webb Space Telescope". In: *The Astrophysical Journal Letters* 901, L1.

Kane, Stephen R. et al. (2012). "The exoplanet eccentricity distribution from Kepler planet candidates". In: *Monthly Notices of the Royal Astronomical Society* 425, pp. 757–762.

Kass, Robert E and Adrian E Raftery (1995). "Bayes factors". In: *Journal of the American Statistical Association* 90, pp. 773–795.

Kempton, Eliza M. -R. et al. (2018). "A Framework for Prioritizing the TESS Planetary Candidates Most Amenable to Atmospheric Characterization". In: *Publications of the Astronomical Society of the Pacific* 130, p. 114401.

Kennedy, Grant M. and Scott J. Kenyon (2008). "Planet Formation around Stars of Various Masses: Hot Super-Earths". In: *The Astrophysical Journal* 682, pp. 1264–1276.

Kipping, D. M. (2013a). "Efficient, uninformative sampling of limb darkening coefficient". In: *Monthly Notices of the Royal Astronomical Society* 435, pp. 2152–2160.

— (2013b). "Parametrizing the exoplanet eccentricity distribution with the beta distribution." In: *Monthly Notices of the Royal Astronomical Society* 434, pp. L51–L55.

Kipping, David M. (2009). "Transit timing effects due to an exomoon". In: *Monthly Notices of the Royal Astronomical Society* 392, pp. 181–189.

Kirk, Brian et al. (2016). "Kepler Eclipsing Binary Stars. VII. The Catalog of Eclipsing Binaries Found in the Entire Kepler Data Set". In: *The Astronomical Journal* 151, 68.

Kite, Edwin S. et al. (2016). "Atmosphere-interior Exchange on Hot, Rocky Exoplanets". In: *The Astrophysical Journal* 828, 80.

Kolbl, Rea et al. (2015). "Detection of Stars Within ∼0.8 in of Kepler Objects of Interest". In: *The Astronomical Journal* 149, 18.

Koll, Daniel D. B. and Dorian S. Abbot (2016). "Temperature Structure and Atmospheric Circulation of Dry Tidally Locked Rocky Exoplanets". In: *The Astrophysical Journal* 825, 99.

Koll, Daniel D. B. et al. (2019). "Identifying Candidate Atmospheres on Rocky M Dwarf Planets via Eclipse Photometry". In: *The Astrophysical Journal* 886, 140.

Konacki, Maciej et al. (2003). "High-Resolution Spectroscopic Follow-up of OGLE Planetary Transit Candidates in the Galactic Bulge: Two Possible Jupiter-Mass Planets and Two Blends". In: *The Astrophysical Journal* 597, pp. 1076–1091.

Königl, Arieh et al. (2017). "On the Origin of Dynamically Isolated Hot Earths". In: *The Astrophysical Journal Letters* 846, L13.

Konopacky, Quinn M. et al. (2013). "Detection of Carbon Monoxide and Water Absorption Lines in an Exoplanet Atmosphere". In: *Science* 339, pp. 1398–1401.

Kostov, Veselin B. et al. (2019). "Discovery and Vetting of Exoplanets. I. Benchmarking K2 Vetting Tools". In: *The Astronomical Journal* 157, 124.

Kounkel, Marina and Kevin Covey (2019). "Untangling the Galaxy. I. Local Structure and Star Formation History of the Milky Way". In: *The Astronomical Journal* 158, 122.

Kovács, G. et al. (2002). "A box-fitting algorithm in the search for periodic transits". In: *Astronomy & Astrophysics* 391, pp. 369–377.

Kraft, Robert P. (1967). "Studies of Stellar Rotation. V. The Dependence of Rotation on Age among Solar-Type Stars". In: *The Astrophysical Journal* 150, p. 551.

Kraus, Adam L. et al. (2008). "Mapping the Shores of the Brown Dwarf Desert. I. Upper Scorpius". In: *The Astrophysical Journal* 679, pp. 762–782.

Kreidberg, Laura (2015). "batman: BAsic Transit Model cAlculatioN in Python". In: *Publications of the Astronomical Society of the Pacific* 127, p. 1161.

Kreidberg, Laura and Abraham Loeb (2016). "Prospects for Characterizing the Atmosphere of Proxima Centauri b". In: *The Astrophysical Journal Letters* 832, L12.

Kreidberg, Laura et al. (2019). "Absence of a thick atmosphere on the terrestrial exoplanet LHS 3844b". In: *Nature* 573, pp. 87–90.

Kunimoto, Michelle and Jaymie M. Matthews (2020). "Searching the Entirety of Kepler Data. II. Occurrence Rate Estimates for FGK Stars". In: *The Astronomical Journal* 159, 248.

Kunimoto, Michelle et al. (2022). "Predicting the Exoplanet Yield of the TESS Prime and Extended Missions through Years 1-7". In: *The Astronomical Journal* 163, 290.

Kunimoto, Michelle et al. (2023). "False Alarms Revealed in a Planet Search of TESS Light Curves". In: *Research Notes of the American Astronomical Society* 7, 7.

Kupke, Renate et al. (2012). "ShaneAO: an enhanced adaptive optics and IR imaging system for the Lick Observatory 3-meter telescope". In: *Adaptive Optics Systems III*. Ed. by Brent L. Ellerbroek et al. Vol. 8447. Society of Photo-Optical Instrumentation Engineers (SPIE) Conference Series, 84473G.

Kurucz, R. L. (1993a). *SYNTHE spectrum synthesis programs and line data*. Cambridge, MA: Smithsonian Astrophysical Observatory.

— (1993b). "VizieR Online Data Catalog: Model Atmospheres (Kurucz, 1979)". In: *VizieR Online Data Catalog* VI/39.

Lammer, H. et al. (2003). "Atmospheric Loss of Exoplanets Resulting from Stellar X-Ray and Extreme-Ultraviolet Heating". In: *The Astrophysical Journal Letters* 598, pp. L121–L124.

Lecavelier des Etangs, A. et al. (2004). "Atmospheric escape from hot Jupiters". In: *Astronomy & Astrophysics* 418, pp. L1–L4.

Lee, Eve J. and Eugene Chiang (2016). "Breeding Super-Earths and Birthing Super-puffs in Transitional Disks". In: *The Astrophysical Journal* 817, 90.

— (2017). "Magnetospheric Truncation, Tidal Inspiral, and the Creation of Short-period and Ultra-short-period Planets". In: *The Astrophysical Journal* 842, 40.

Lee, Eve J. et al. (2014). "Make Super-Earths, Not Jupiters: Accreting Nebular Gas onto Solid Cores at 0.1 AU and Beyond". In: *The Astrophysical Journal* 797, 95.

Lee, Eve J. et al. (2022). "Creating the Radius Gap without Mass Loss". In: *The Astrophysical Journal* 941, 186.

Léger, A. et al. (2009). "Transiting exoplanets from the CoRoT space mission. VIII. CoRoT-7b: the first super-Earth with measured radius". In: *Astronomy & Astrophysics* 506, pp. 287–302.

Li, Jie et al. (2019). "Kepler Data Validation II-Transit Model Fitting and Multiple-planet Search". In: *Publications of the Astronomical Society of the Pacific* 131, p. 024506.

Lightkurve Collaboration et al. (2018). *Lightkurve: Kepler and TESS time series analysis in Python*. Astrophysics Source Code Library, record ascl:1812.013.

Lillo-Box, J. et al. (2012). "Multiplicity in transiting planet-host stars. A lucky imaging study of Kepler candidates". In: *Astronomy & Astrophysics* 546, A10.

— (2014). "High-resolution imaging of Kepler planet host candidates. A comprehensive comparison of different techniques". In: *Astronomy & Astrophysics* 566, A103.

Lillo-Box, J. et al. (2023). "TOI-969: a late-K dwarf with a hot mini-Neptune in the desert and an eccentric cold Jupiter". In: *Astronomy & Astrophysics* 669, A109.

Lincowski, Andrew P. et al. (2018). "Evolved Climates and Observational Discriminants for the TRAPPIST-1 Planetary System". In: *The Astrophysical Journal* 867, 76.

Linsky, J. L. et al. (1979). "Stellar model chromospheres. X. High-resolution, absolute flux profiles of the Ca II H and K lines in stars of spectral types F0 - M2." In: *The Astrophysical Journal Supplement Series* 41, pp. 47–74.

Lissauer, Jack J. et al. (2012). "Almost All of Kepler's Multiple-planet Candidates Are Planets". In: *The Astrophysical Journal* 750, 112.

Lopez, Eric D. and Jonathan J. Fortney (2013). "The Role of Core Mass in Controlling Evaporation: The Kepler Radius Distribution and the Kepler-36 Density Dichotomy". In: *The Astrophysical Journal* 776, 2.

Lopez, Eric D. and Ken Rice (2018). "How formation time-scales affect the period dependence of the transition between rocky super-Earths and gaseous sub-Neptunesand implications for $\eta_{\oplus}$". In: *Monthly Notices of the Royal Astronomical Society* 479, pp. 5303–5311.

Lovis, Christophe and Debra Fischer (2010). *Exoplanets: Radial velocity techniques for exoplanets*. Ed. by Sara Seager. Tuscon, AZ: University of Arizona Press, pp. 27–53.

Lubin, Jack et al. (2022). "TESS-Keck Survey. IX. Masses of Three Sub-Neptunes Orbiting HD 191939 and the Discovery of a Warm Jovian plus a Distant Substellar Companion". In: *The Astronomical Journal* 163, 101.

Luger, R. and R. Barnes (2015). "Extreme Water Loss and Abiotic O2Buildup on Planets Throughout the Habitable Zones of M Dwarfs". In: *Astrobiology* 15, pp. 119–143.

Lund, M. B. and D. Ciardi (2020). "Reducing Errors in Derived Planetary Radii Caused by Undetected Stellar Companions". In: *American Astronomical Society Meeting Abstracts*. American Astronomical Society Meeting Abstracts, 249.06.

Lustig-Yaeger, Jacob et al. (2019). "The Detectability and Characterization of the TRAPPIST-1 Exoplanet Atmospheres with JWST". In: *The Astronomical Journal* 158, 27.

Lutgens, F. K. et al. (2014). *Essentials of Geology*. New York: Pearson.

MacDougall, Mason G. et al. (2021). "The TESS-Keck Survey. VI. Two Eccentric Sub-Neptunes Orbiting HIP-97166". In: *The Astronomical Journal* 162, 265.

MacDougall, Mason G. et al. (2022). "The TESS-Keck Survey. XIII. An Eccentric Hot Neptune with a Similar-mass Outer Companion around TOI-1272". In: *The Astronomical Journal* 164, 97.

Malavolta, Luca et al. (2018). "An Ultra-short Period Rocky Super-Earth with a Secondary Eclipse and a Neptune-like Companion around K2-141". In: *The Astronomical Journal* 155, 107.

Mann, Andrew W. et al. (2015). "How to Constrain Your M Dwarf: Measuring Effective Temperature, Bolometric Luminosity, Mass, and Radius". In: *The Astrophysical Journal* 804, 64.

Mansfield, Megan et al. (2019). "Identifying Atmospheres on Rocky Exoplanets through Inferred High Albedo". In: *The Astrophysical Journal* 886, 141.

Martinez, Cintia F. et al. (2019). "A Spectroscopic Analysis of the California-Kepler Survey Sample. I. Stellar Parameters, Planetary Radii, and a Slope in the Radius Gap". In: *The Astrophysical Journal* 875, 29.

Masuda, Kento and Daniel Tamayo (2020). "Revisiting the Architecture of the KOI-89 System". In: *The Astronomical Journal* 160, 224.

Mayo, Andrew W. et al. (2018). "275 Candidates and 149 Validated Planets Orbiting Bright Stars in K2 Campaigns 0-10". In: *The Astronomical Journal* 155, 136.

Mayor, Michel and Didier Queloz (1995). "A Jupiter-mass companion to a solar-type star". In: *Nature* 378, pp. 355–359.

Mazeh, T. et al. (2016). "Dearth of short-period Neptunian exoplanets: A desert in period-mass and period-radius planes". In: *Astronomy & Astrophysics* 589, A75.

McArthur, Barbara E. et al. (2004). "Detection of a Neptune-Mass Planet in the ρ^1 Cancri System Using the Hobby-Eberly Telescope". In: *The Astrophysical Journal Letters* 614, pp. L81–L84.

McCauliff, Sean D. et al. (2015). "Automatic Classification of Kepler Planetary Transit Candidates". In: *The Astrophysical Journal* 806, 6.

McCullough, P. R. et al. (2005). "The XO Project: Searching for Transiting Extrasolar Planet Candidates". In: *Publications of the Astronomical Society of the Pacific* 117, pp. 783–795.

McCully, Curtis et al. (2018). "Real-time processing of the imaging data from the network of Las Cumbres Observatory Telescopes using BANZAI". In: *Software and Cyberinfrastructure for Astronomy V*. Ed. by Juan C. Guzman and Jorge Ibsen. Vol. 10707. Society of Photo-Optical Instrumentation Engineers (SPIE) Conference Series, 107070K.

McLaughlin, D. B. (1924). "Some results of a spectrographic study of the Algol system". In: *The Astrophysical Journal* 60, pp. 22–31.

Moe, Maxwell and Rosanne Di Stefano (2017). "Mind Your Ps and Qs: The Interrelation between Period (P) and Mass-ratio (Q) Distributions of Binary Stars". In: *The Astrophysical Journal Supplement Series* 230, 15.

Montet, Benjamin T. et al. (2017). "Measuring the Galactic Distribution of Transiting Planets with WFIRST". In: *Publications of the Astronomical Society of the Pacific* 129, p. 044401.

Mori, Mayuko et al. (2022). "TOI-1696: A Nearby M4 Dwarf with a 3 $R_\oplus$ Planet in the Neptunian Desert". In: *The Astronomical Journal* 163, 298.

Moriarty, John et al. (2014). "Chemistry in an Evolving Protoplanetary Disk: Effects on Terrestrial Planet Composition". In: *The Astrophysical Journal* 787, 81.

Morley, Caroline V. et al. (2017). "Observing the Atmospheres of Known Temperate Earth-sized Planets with JWST". In: *The Astrophysical Journal* 850, 121.

Morris, Robert L. et al. (2020). *Kepler Data Processing Handbook: Photometric Analysis*. Kepler Science Document KSCI-19081-003, id. 6. Edited by Jon M. Jenkins.

Morton, T. D. (2015). *VESPA: False positive probabilities calculator*. Astrophysics Source Code Library, record ascl:1503.011.

Morton, Timothy D. (2012). "An Efficient Automated Validation Procedure for Exoplanet Transit Candidates". In: *The Astrophysical Journal* 761, 6.

Morton, Timothy D. and Jonathan Swift (2014). "The Radius Distribution of Planets around Cool Stars". In: *The Astrophysical Journal* 791, 10.

Morton, Timothy D. et al. (2016). "False Positive Probabilities for all Kepler Objects of Interest: 1284 Newly Validated Planets and 428 Likely False Positives". In: *The Astrophysical Journal* 822, 86.

Motalebi, F. et al. (2015). "The HARPS-N Rocky Planet Search. I. HD 219134 b: A transiting rocky planet in a multi-planet system at 6.5 pc from the Sun". In: *Astronomy & Astrophysics* 584, A72.

Muirhead, Philip S. et al. (2018). "A Catalog of Cool Dwarf Targets for the Transiting Exoplanet Survey Satellite". In: *The Astronomical Journal* 155, 180.

Mulders, Gijs D. et al. (2015a). "A Stellar-mass-dependent Drop in Planet Occurrence Rates". In: *The Astrophysical Journal* 798, 112.

— (2015b). "An Increase in the Mass of Planetary Systems around Lower-mass Stars". In: *The Astrophysical Journal* 814, 130.

Mulders, Gijs D. et al. (2018). "The Exoplanet Population Observation Simulator. I. The Inner Edges of Planetary Systems". In: *The Astronomical Journal* 156, 24.

Mullally, F. et al. (2016). "Identifying False Alarms in the Kepler Planet Candidate Catalog". In: *Publications of the Astronomical Society of the Pacific* 128, p. 074502.

Murray-Clay, Ruth A. et al. (2009). "Atmospheric Escape From Hot Jupiters". In: *The Astrophysical Journal* 693, pp. 23–42.

Narita, Norio et al. (2015). "MuSCAT: a multicolor simultaneous camera for studying atmospheres of transiting exoplanets". In: *Journal of Astronomical Telescopes Instruments and Systems* 1, 045001.

Narita, Norio et al. (2019). "MuSCAT2: four-color simultaneous camera for the 1.52-m Telescopio Carlos Sánchez". In: *Journal of Astronomical Telescopes Instruments and Systems* 5, 015001.

Narita, Norio et al. (2020). "MuSCAT3: a 4-color simultaneous camera for the 2m Faulkes Telescope North". In: *Society of Photo-Optical Instrumentation Engineers (SPIE) Conference Series*. Vol. 11447. Society of Photo-Optical Instrumentation Engineers (SPIE) Conference Series, 114475K.

Neil, Andrew R. and Leslie A. Rogers (2020). "A Joint Mass-Radius-Period Distribution of Exoplanets". In: *The Astrophysical Journal* 891, 12.

Newton, Elisabeth R. et al. (2019). "TESS Hunt for Young and Maturing Exoplanets (THYME): A Planet in the 45 Myr Tucana-Horologium Association". In: *The Astrophysical Journal Letters* 880.1, L17.

Newton, Elisabeth R. et al. (2022). "TESS Hunt for Young and Maturing Exoplanets (THYME). VII. Membership, Rotation, and Lithium in the Young Cluster Group-X and a New Young Exoplanet". In: *The Astronomical Journal* 164, 115.

Nielsen, Eric L. et al. (2019). "The Gemini Planet Imager Exoplanet Survey: Giant Planet and Brown Dwarf Demographics from 10 to 100 au". In: *The Astronomical Journal* 158, 13.

Niraula, Prajwal et al. (2017). "Three Super-Earths Transiting the Nearby Star GJ 9827". In: *The Astronomical Journal* 154, 266.

Nissen, P. E. (2015). "High-precision abundances of elements in solar twin stars. Trends with stellar age and elemental condensation temperature". In: *Astronomy & Astrophysics* 579, A52.

Nutzman, Philip and David Charbonneau (2008). "Design Considerations for a Ground-Based Transit Search for Habitable Planets Orbiting M Dwarfs". In: *Publications of the Astronomical Society of the Pacific* 120, p. 317.

Osborn, Ares et al. (2021). "TOI-431/HIP 26013: a super-Earth and a sub-Neptune transiting a bright, early K dwarf, with a third RV planet". In: *Monthly Notices of the Royal Astronomical Society* 507, pp. 2782–2803.

Otegi, J. F. et al. (2020). "Revisited mass-radius relations for exoplanets below 120 $M_{\oplus}$". In: *Astronomy & Astrophysics* 634, A43.

Owen, James E. and Dong Lai (2018). "Photoevaporation and high-eccentricity migration created the sub-Jovian desert". In: *Monthly Notices of the Royal Astronomical Society* 479, pp. 5012–5021.

Owen, James E. and Yanqin Wu (2013). "Kepler Planets: A Tale of Evaporation". In: *The Astrophysical Journal* 775, 105.

— (2017). "The Evaporation Valley in the Kepler Planets". In: *The Astrophysical Journal* 847, 29.

Penny, Matthew T. et al. (2019). "Predictions of the WFIRST Microlensing Survey. I. Bound Planet Detection Rates". In: *The Astrophysical Journal Supplement Series* 241, 3.

Pepper, Joshua et al. (2007). "The Kilodegree Extremely Little Telescope (KELT): A Small Robotic Telescope for Large-Area Synoptic Surveys". In: *Publications of the Astronomical Society of the Pacific* 119, pp. 923–935.

Perryman, Michael et al. (2014). "Astrometric Exoplanet Detection with Gaia". In: *The Astrophysical Journal* 797, 14.

Petigura, Erik A. et al. (2013). "Prevalence of Earth-size planets orbiting Sun-like stars". In: *Proceedings of the National Academy of Science* 110, pp. 19273–19278.

Petigura, Erik Ardeshir (2015). "Prevalence of Earth-size Planets Orbiting Sun-like Stars". PhD thesis. University of California, Berkeley.

Pinte, C. et al. (2008). "The Inner Radius of T Tauri Disks Estimated from Near-Infrared Interferometry: The Importance of Scattered Light". In: *The Astrophysical Journal Letters* 673, p. L63.

Piro, Anthony L. and Shreyas Vissapragada (Apr. 2020). "Exploring Whether Super-puffs can be Explained as Ringed Exoplanets". In: *AJ* 159.4, 131, p. 131. DOI: 10.3847/1538-3881/ab7192. arXiv: 1911.09673 [astro-ph.EP].

Pollacco, D. L. et al. (2006). "The WASP Project and the SuperWASP Cameras". In: *Publications of the Astronomical Society of the Pacific* 118, pp. 1407–1418.

Pollack, James B. et al. (1996). "Formation of the Giant Planets by Concurrent Accretion of Solids and Gas". In: *Icarus* 124, pp. 62–85.

Psaridi, Angelica et al. (2022). "Three new brown dwarfs and a massive hot Jupiter revealed by TESS around early-type stars". In: *Astronomy & Astrophysics* 664, A94.

Quinn, Samuel N. et al. (2019). "Near-resonance in a System of Sub-Neptunes from TESS". In: *The Astronomical Journal* 158, 177.

Ramırez, I. et al. (2014). "The Solar Twin Planet Search. I. Fundamental parameters of the stellar sample". In: *Astronomy & Astrophysics* 572, A48.

Rauer, H. et al. (2014). "The PLATO 2.0 mission". In: *Experimental Astronomy* 38, pp. 249–330.

Ribas, Álvaro et al. (2015). "Protoplanetary disk lifetimes vs. stellar mass and possible implications for giant planet populations". In: *Astronomy & Astrophysics* 576, A52.

Ribas, Ignasi et al. (2005). "Evolution of the Solar Activity over Time and Effects on Planetary Atmospheres. I. High-Energy Irradiances (1-1700)". In: *The Astrophysical Journal* 622, pp. 680–694.

Rice, K. et al. (2019). "Masses and radii for the three super-Earths orbiting GJ 9827, and implications for the composition of small exoplanets". In: *Monthly Notices of the Royal Astronomical Society* 484, pp. 3731–3745.

Rice, Malena and John M. Brewer (2020). "Stellar Characterization of Keck HIRES Spectra with The Cannon". In: *The Astrophysical Journal* 898, 119.

Rice, Malena et al. (2022). "Origins of Hot Jupiters from the Stellar Obliquity Distribution". In: *The Astrophysical Journal Letters* 926, L17.

Ricker, George R. et al. (2010). "Transiting Exoplanet Survey Satellite (TESS)". In: *American Astronomical Society Meeting Abstracts #215*. Vol. 215. American Astronomical Society Meeting Abstracts, 450.06.

Rodriguez, Joseph E. et al. (2018). "A System of Three Super Earths Transiting the Late K-Dwarf GJ 9827 at 30 pc". In: *The Astronomical Journal* 155, 72.

Rodriguez, Joseph E. et al. (2021). "TESS Delivers Five New Hot Giant Planets Orbiting Bright Stars from the Full-frame Images". In: *The Astronomical Journal* 161, 194.

Rogers, Leslie A. (2015). "Most 1.6 Earth-radius Planets are Not Rocky". In: *The Astrophysical Journal* 801, 41.

Rossiter, R. A. (1924). "On the detection of an effect of rotation during eclipse in the velocity of the brigher component of beta Lyrae, and on the constancy of velocity of this system". In: *The Astrophysical Journal* 60, pp. 15–21.

Rouan, D. et al. (2011). "The Orbital Phases and Secondary Transits of Kepler-10b. A Physical Interpretation Based on the Lava-ocean Planet Model". In: *The Astrophysical Journal Letters* 741, L30.

Rubenzahl, Ryan A. et al. (2021). "The TESS-Keck Survey. IV. A Retrograde, Polar Orbit for the Ultra-low-density, Hot Super-Neptune WASP-107b". In: *The Astronomical Journal* 161, 119.

Safonov, B. S. et al. (2017). "The speckle polarimeter of the 2.5-m telescope: Design and calibration". In: *Astronomy Letters* 43, pp. 344–364.

Samuel, B. et al. (2014). "Constraining physics of very hot super-Earths with the James Webb Telescope. The case of CoRot-7b". In: *Astronomy & Astrophysics* 563, A103.

Sanchis-Ojeda, Roberto et al. (2013). "Transits and Occultations of an Earth-sized Planet in an 8.5 hr Orbit". In: *The Astrophysical Journal* 774, 54.

Sanchis-Ojeda, Roberto et al. (2014). "A Study of the Shortest-period Planets Found with Kepler". In: *The Astrophysical Journal* 787, 47.

Sandoval, Angeli et al. (2021). "The Influence of Age on the Relative Frequency of Super-Earths and Sub-Neptunes". In: *The Astrophysical Journal* 911, 117.

Santerne, A. et al. (2012). "SOPHIE velocimetry of Kepler transit candidates. VII. A false-positive rate of 35% for Kepler close-in giant candidates". In: *Astronomy & Astrophysics* 545, A76.

Santerne, A. et al. (2015). "PASTIS: Bayesian extrasolar planet validation - II. Constraining exoplanet blend scenarios using spectroscopic diagnoses". In: *Monthly Notices of the Royal Astronomical Society* 451, pp. 2337–2351.

Saunders, Nicholas et al. (2022). "TESS Giants Transiting Giants. I.: A Noninflated Hot Jupiter Orbiting a Massive Subgiant". In: *The Astronomical Journal* 163.2, 53.

Savel, Arjun B. et al. (2020). "A Closer Look at Exoplanet Occurrence Rates: Considering the Multiplicity of Stars without Detected Planets". In: *The Astronomical Journal* 160, 287.

Scarsdale, Nicholas et al. (2021). "TESS-Keck Survey. V. Twin Sub-Neptunes Transiting the Nearby G Star HD 63935". In: *The Astronomical Journal* 162, 215.

Schaefer, Laura et al. (2012). "Vaporization of the Earth: Application to Exoplanet Atmospheres". In: *The Astrophysical Journal* 755, 41.

Schlichting, Hilke E. et al. (2015). "Atmospheric mass loss during planet formation: The importance of planetesimal impacts". In: *Icarus* 247, pp. 81–94.

Schröder, C. and J. H. M. M. Schmitt (2007). "X-ray emission from A-type stars". In: *Astronomy & Astrophysics* 475, pp. 677–684.

Schwarz, Gideon (1978). "Estimating the Dimension of a Model". In: *Annals of Statistics* 6, pp. 461–464.

Scott, Nicholas J. and Steve B. Howell (2018). "NESSI and 'Alopeke: two new dual-channel speckle imaging instruments". In: *Optical and Infrared Interferometry and Imaging VI*. Ed. by Michelle J. Creech-Eakman et al. Vol. 10701. Society of Photo-Optical Instrumentation Engineers (SPIE) Conference Series, 107010G.

Scott, Nicholas J. et al. (2018). "The NN-explore Exoplanet Stellar Speckle Imager: Instrument Description and Preliminary Results". In: *Publications of the Astronomical Society of the Pacific* 130, p. 054502.

Seager, S. and D. Deming (2009). "On the Method to Infer an Atmosphere on a Tidally Locked Super Earth Exoplanet and Upper Limits to GJ 876d". In: *The Astrophysical Journal* 703, pp. 1884–1889.

Seager, S. et al. (2007). "Mass-Radius Relationships for Solid Exoplanets". In: *The Astrophysical Journal* 669, pp. 1279–1297.

Selsis, F. et al. (2011). "Thermal phase curves of nontransiting terrestrial exoplanets. I. Characterizing atmospheres". In: *Astronomy & Astrophysics* 532, A1.

Shabram, Megan et al. (2016). "The Eccentricity Distribution of Short-period Planet Candidates Detected by Kepler in Occultation". In: *The Astrophysical Journal* 820, 93.

Shallue, Christopher J. and Andrew Vanderburg (2018). "Identifying Exoplanets with Deep Learning: A Five-planet Resonant Chain around Kepler-80 and an Eighth Planet around Kepler-90". In: *The Astronomical Journal* 155, 94.

Shporer, Avi et al. (2011). "Detection of KOI-13.01 Using the Photometric Orbit". In: *The Astronomical Journal* 142, 195.

Shporer, Avi et al. (2020). "GJ 1252 b: A 1.2 $R_\oplus$ Planet Transiting an M3 Dwarf at 20.4 pc". In: *The Astrophysical Journal Letters* 890, L7.

Shuvalov, V. (2009). "Atmospheric erosion induced by oblique impacts". In: 44, pp. 1095–1105.

Sing, David K. et al. (2016). "A continuum from clear to cloudy hot-Jupiter exoplanets without primordial water depletion". In: *Nature* 529, pp. 59–62.

Skrutskie, M. F. et al. (2006). "The Two Micron All Sky Survey (2MASS)". In: *The Astronomical Journal* 131, pp. 1163–1183.

Smith, A. M. S. et al. (2018). "K2-137 b: an Earth-sized planet in a 4.3-h orbit around an M-dwarf". In: *Monthly Notices of the Royal Astronomical Society* 474, pp. 5523–5533.

Smith, Jeffrey C. et al. (2012). "Kepler Presearch Data Conditioning II - A Bayesian Approach to Systematic Error Correction". In: *Publications of the Astronomical Society of the Pacific* 124, p. 1000.

Sorahana, S. et al. (2013). "On the Radii of Brown Dwarfs Measured with AKARI Near-infrared Spectroscopy". In: *The Astrophysical Journal* 767, 77.

Spake, J. J. et al. (2018). "Helium in the eroding atmosphere of an exoplanet". In: *Nature* 557, pp. 68–70.

Spergel, D. et al. (2015). "Wide-Field InfrarRed Survey Telescope-Astrophysics Focused Telescope Assets WFIRST-AFTA 2015 Report". In: *arXiv e-prints*, arXiv:1503.03757.

Stassun, Keivan G. and Guillermo Torres (2016). "Eclipsing Binaries as Benchmarks for Trigonometric Parallaxes in the Gaia Era". In: *The Astronomical Journal* 152, 180.

Stassun, Keivan G. et al. (2017). "Accurate Empirical Radii and Masses of Planets and Their Host Stars with Gaia Parallaxes". In: *The Astronomical Journal* 153, 136.

Stassun, Keivan G. et al. (2018a). "Empirical Accurate Masses and Radii of Single Stars with TESS and Gaia". In: *The Astronomical Journal* 155, 22.

Stassun, Keivan G. et al. (2018b). "The TESS Input Catalog and Candidate Target List". In: *The Astronomical Journal* 156, 102.

Stassun, Keivan G. et al. (2019). "The Revised TESS Input Catalog and Candidate Target List". In: *The Astronomical Journal* 158, 138.

Strehl, K. (1902). "die Bildschder Fernrohre". In: *Astronomische Nachrichten* 158, p. 89.

Struve, O. (1952). "Proposal for a project of high-precision stellar radial velocity work". In: *The Observatory* 72, pp. 199–200.

Stumpe, Martin C. et al. (2012). "Kepler Presearch Data Conditioning Iand Algorithms for Error Correction in Kepler Light Curves". In: *Publications of the Astronomical Society of the Pacific* 124, p. 985.

Stumpe, Martin C. et al. (2014). "Multiscale Systematic Error Correction via Wavelet-Based Bandsplitting in Kepler Data". In: *Publications of the Astronomical Society of the Pacific* 126, p. 100.

Swift, Jonathan J. et al. (2013). "Characterizing the Cool KOIs. IV. Kepler-32 as a Prototype for the Formation of Compact Planetary Systems throughout the Galaxy". In: *The Astrophysical Journal* 764, 105.

Szentgyorgyi, A. H. and G. Furész (2007). "Precision Radial Velocities for the Kepler Era". In: *Revista Mexicana de Astronomia y Astrofisica Conference Series*. Ed. by Stanley Kurtz. Vol. 28. Revista Mexicana de Astronomia y Astrofisica Conference Series, pp. 129–133.

Talens, G. J. J. et al. (2017). "The Multi-site All-Sky CAmeRA (MASCARA). Finding transiting exoplanets around bright (m_V ¡ 8) stars". In: *Astronomy & Astrophysics* 601, A11.

Telting, J. H. et al. (2014). "FIES: The high-resolution Fiber-fed Echelle Spectrograph at the Nordic Optical Telescope". In: *Astronomische Nachrichten* 335, p. 41.

Teske, Johanna et al. (2021). "The Magellan-TESS Survey. I. Survey Description and Mid-survey Results". In: *The Astrophysical Journal Supplement Series* 256, 33.

Teske, Johanna K. et al. (2018). "The Effects of Stellar Companions on the Observed Transiting Exoplanet Radius Distribution". In: *The Astronomical Journal* 156, 292.

Thompson, Susan E. et al. (2018). "Planetary Candidates Observed by Kepler. VIII. A Fully Automated Catalog with Measured Completeness and Reliability Based on Data Release 25". In: *The Astrophysical Journal Supplement Series* 235, 38.

Thorngren, Daniel P. et al. (2023). "Removal of Hot Saturns in Mass-Radius Plane by Runaway Mass Loss". In: *The Astrophysical Jounral Letters* 945, L36.

Tinetti, G. et al. (2016). "The science of ARIEL (Atmospheric Remote-sensing Infrared Exoplanet Large-survey)". In: *Space Telescopes and Instrumentation 2016: Optical, Infrared, and Millimeter Wave*. Ed. by Howard A. MacEwen et al. Vol. 9904. Society of Photo-Optical Instrumentation Engineers (SPIE) Conference Series, 99041X.

Tokovinin, Andrei et al. (2013). "CHIRONFiber Fed Spectrometer for Precise Radial Velocities". In: *Publications of the Astronomical Society of the Pacific* 125, p. 1336.

Torres, G. et al. (2010). "Accurate masses and radii of normal stars: modern results and applications". In: *The Astronomy and Astrophysics Review* 18, pp. 67–126.

Torres, Guillermo et al. (2004). "Testing Blend Scenarios for Extrasolar Transiting Planet Candidates. I. OGLE-TR-33: A False Positive". In: *The Astrophysical Journal* 614, pp. 979–989.

— (2005). "Testing Blend Scenarios for Extrasolar Transiting Planet Candidates. II. OGLE-TR-56". In: *The Astrophysical Journal* 619, pp. 558–569.

Torres, Guillermo et al. (2011). "Modeling Kepler Transit Light Curves as False Positives: Rejection of Blend Scenarios for Kepler-9, and Validation of Kepler-9 d, A Super-earth-size Planet in a Multiple System". In: *The Astrophysical Journal* 727, 24.

Trifonov, T. et al. (2021). "A nearby transiting rocky exoplanet that is suitable for atmospheric investigation". In: *Science* 371, pp. 1038–1041.

Tucci Maia, M. et al. (2016). "The Solar Twin Planet Search. III. The [Y/Mg] clock: estimating stellar ages of solar-type stars". In: *Astronomy & Astrophysics* 590, A32.

Turtelboom, Emma V. et al. (2022). "The TESS-Keck Survey. XI. Mass Measurements for Four Transiting Sub-Neptunes Orbiting K Dwarf TOI-1246". In: *The Astronomical Journal* 163, 293.

Twicken, Joseph D. et al. (2010). "Photometric analysis in the Kepler Science Operations Center pipeline". In: *Software and Cyberinfrastructure for Astronomy*. Ed. by Nicole M. Radziwill and Alan Bridger. Vol. 7740. Society of Photo-Optical Instrumentation Engineers (SPIE) Conference Series, 774023.

Twicken, Joseph D. et al. (2018). "Kepler Data Validation I, Diagnostic Tests, and Data Products for Vetting Transiting Planet Candidates". In: *Publications of the Astronomical Society of the Pacific* 130, p. 064502.

Valencia, Diana et al. (2006). "Internal structure of massive terrestrial planets". In: *Icarus* 181, pp. 545–554.

Valencia, Diana et al. (2007a). "Detailed Models of Super-Earths: How Well Can We Infer Bulk Properties?" In: *The Astrophysical Journal* 665, pp. 1413–1420.

— (2007b). "Radius and Structure Models of the First Super-Earth Planet". In: *The Astrophysical Journal* 656, pp. 545–551.

Valizadegan, Hamed et al. (2022). "ExoMiner: A Highly Accurate and Explainable Deep Learning Classifier That Validates 301 New Exoplanets". In: *The Astrophysical Journal* 926, 120.

Van Eylen, V. et al. (2018). "An asteroseismic view of the radius valley: stripped cores, not born rocky". In: *Monthly Notices of the Royal Astronomical Society* 479, pp. 4786–4795.

van Leeuwen, F. (2007). "Validation of the new Hipparcos reduction". In: *Astronomy & Astrophysics* 474, pp. 653–664.

Van Zandt, Judah et al. (2023). "TESS-Keck Survey. XIV. Two Giant Exoplanets from the Distant Giants Survey". In: *The Astronomical Journal* 165, 60.

Vanderburg, Andrew and Joseph E. Rodriguez (2021). "First Doppler Limits on Binary Planets and Exomoons in the HR 8799 System". In: *The Astrophysical Journal Letters* 922, L2.

Vanderburg, Andrew et al. (2016). "Two Small Planets Transiting HD 3167". In: *The Astrophysical Journal Letters* 829, L9.

Vanderburg, Andrew et al. (2018). "Detecting Exomoons via Doppler Monitoring of Directly Imaged Exoplanets". In: *The Astronomical Journal* 156, 184.

Vanderburg, Andrew et al. (2019). "TESS Spots a Compact System of Super-Earths around the Naked-eye Star HR 858". In: *The Astrophysical Journal Letters* 881, L19.

Vanderspek, Roland et al. (2019). "TESS Discovery of an Ultra-short-period Planet around the Nearby M Dwarf LHS 3844". In: *The Astrophysical Journal Letters* 871, L24.

Vidal-Madjar, A. et al. (2003). "An extended upper atmosphere around the extrasolar planet HD209458b". In: *Nature* 422, pp. 143–146.

Vogt, S. S. et al. (1994). "HIRES: the high-resolution echelle spectrometer on the Keck 10-m Telescope". In: *Instrumentation in Astronomy VIII*. Ed. by David L. Crawford and Eric R. Craine. Vol. 2198. Society of Photo-Optical Instrumentation Engineers (SPIE) Conference Series, p. 362.

Weiss, Lauren M. et al. (2021). "The TESS-Keck Survey. II. An Ultra-short-period Rocky Planet and Its Siblings Transiting the Galactic Thick-disk Star TOI-561". In: *The Astronomical Journal* 161, 56.

Wells, R. D. et al. (2021). "A large sub-Neptune transiting the thick-disk M4 V TOI-2406". In: *Astronomy & Astrophysics* 653, A97.

Werner, M. W. et al. (2004). "The Spitzer Space Telescope Mission". In: *The Astrophysical Journal Supplement Series* 154, pp. 1–9.

Wheatley, Peter J. et al. (2018). "The Next Generation Transit Survey (NGTS)". In: *Monthly Notices of the Royal Astronomical Society* 475, pp. 4476–4493.

Winn, Joshua N. (2010). *Exoplanets: Exoplanet transits and occultations*. Ed. by Sara Seager. Tuscon, AZ: University of Arizona Press, pp. 55–77.

Winn, Joshua N. et al. (2010). "Hot Stars with Hot Jupiters Have High Obliquities". In: *The Astrophysical Journal Letters* 718, pp. L145–L149.

Winn, Joshua N. et al. (2011). "A Super-Earth Transiting a Naked-eye Star". In: *The Astrophysical Journal Letters* 737, L18.

Winn, Joshua N. et al. (2017). "Absence of a Metallicity Effect for Ultra-short-period Planets". In: *The Astronomical Journal* 154, 60.

Wu, Yanqin (2019). "Mass and Mass Scalings of Super-Earths". In: *The Astrophysical Journal* 874, 91.

Yan, Fei and Thomas Henning (2018). "An extended hydrogen envelope of the extremely hot giant exoplanet KELT-9b". In: *Nature Astronomy* 2, pp. 714–718.

Yee, Samuel W. et al. (2017). "Precision Stellar Characterization of FGKM Stars using an Empirical Spectral Library". In: *The Astrophysical Journal* 836, 77.

Yee, Samuel W. et al. (2022). "The TESS Grand Unified Hot Jupiter Survey. I. Ten TESS Planets". In: *The Astronomical Journal* 164, 70.

Yi, Sukyoung et al. (2001). "Toward Better Age Estimates for Stellar Populations: The Y2 Isochrones for Solar Mixture". In: *The Astrophysical Journal Supplement Series* 136, pp. 417–437.

Zeng, Li and Dimitar Sasselov (2013). "A Detailed Model Grid for Solid Planets from 0.1 through 100 Earth Masses". In: *Publications of the Astronomical Society of the Pacific* 125, p. 227.

Zeng, Li and S. Seager (2008). "A Computational Tool to Interpret the Bulk Composition of Solid Exoplanets based on Mass and Radius Measurements". In: *Publications of the Astronomical Society of the Pacific* 120, p. 983.

Zeng, Li et al. (2016). "Mass-Radius Relation for Rocky Planets Based on PREM". In: *The Astrophysical Journal* 819, 127.

Zhou, G. et al. (2019a). "HATS-70b: A 13 MJ Brown Dwarf Transiting an A Star". In: *The Astronomical Journal* 157, 31.

Zhou, G. et al. (2019b). "Two New HATNet Hot Jupiters around A Stars and the First Glimpse at the Occurrence Rate of Hot Jupiters from TESS". In: *The Astronomical Journal* 158, 141.

Zieba, S. et al. (2022). "K2 and Spitzer phase curves of the rocky ultra-short-period planet K2-141 b hint at a tenuous rock vapor atmosphere". In: *Astronomy & Astrophysics* 664, A79.

Ziegler, Carl et al. (2020). "SOAR TESS Survey. I. Sculpting of TESS Planetary Systems by Stellar Companions". In: *The Astronomical Journal* 159, 19.

Ziegler, Carl et al. (2021). "SOAR TESS Survey. II. The Impact of Stellar Companions on Planetary Populations". In: *The Astronomical Journal* 162, 192.

Zilinskas, M. et al. (2022). "Observability of evaporating lava worlds". In: *Astronomy & Astrophysics* 661, A126.

Zilinskas, Mantas et al. (2020). "Atmospheric compositions and observability of nitrogen-dominated ultra-short-period super-Earths". In: *Monthly Notices of the Royal Astronomical Society* 494, pp. 1490–1506.